



**Universiteit
Leiden**
The Netherlands

Interventional molecular imaging, a hybrid approach

Buckle, T.

Citation

Buckle, T. (2012, October 17). *Interventional molecular imaging, a hybrid approach*. Retrieved from <https://hdl.handle.net/1887/19979>

Version: Corrected Publisher's Version

License: [Licence agreement concerning inclusion of doctoral thesis in the Institutional Repository of the University of Leiden](#)

Downloaded from: <https://hdl.handle.net/1887/19979>

Note: To cite this publication please use the final published version (if applicable).

Interventional

Interventional molecular imaging,

molecular imaging,

a hybrid approach

a hybrid approach

Tessa Buckle

Interventional molecular imaging, a **hybrid** approach

Tessa Buckle

Design and layout by: Margo Verduin | www.mvvormendtp.nl

Printed by: Proefschriftmaken.nl | Uitgeverij BOXPress

Published by: Uitgeverij BOXPress, 's-Hertogenbosch

© T. Buckle, 2012

ISBN 978-90-8891-473-7

Interventional molecular imaging, a hybrid approach

Proefschrift

ter verkrijging van
de graad van Doctor aan de Universiteit Leiden,
op gezag van Rector Magnificus prof.mr. P.F. van der Heijden,
volgens besluit van het College van Promoties
te verdedigen op woensdag 17 oktober 2012
klokke 16.15 uur

door

Tessa Buckle

geboren te Utrecht in 1979

Promotiecommissie

Promotores: Prof. dr. J.L. Bloem
Prof. dr. C.J.H. van de Velde

Co-promotor: Dr. F.W.B. van Leeuwen

Overige leden: Prof. dr. H.J. Tanke
Dr. H.G. van der Poel (NKI/AvL)
Dr. R.A. Valdés-Olmos

Financial support by J.E. Jurriaanse Foundation, Intuitive Surgical, Karl Storz GMBH and Oncovision for the publication of this thesis is greatly acknowledged.

Content

Chapter 1	General introduction	9
Part I	Hybrid guidance for sentinel lymph node biopsy	13
Chapter 2	(Non-targeted) radioactive/fluorescent nanoparticles and their potential in combined pre- and intraoperative imaging during sentinel lymph node resection	15
Chapter 3	A self-assembled hybrid complex for combined pre- and intraoperative imaging of the sentinel lymph node	37
Chapter 4	Tracer-cocktail injections for combined pre- and intraoperative hybrid imaging of lymph nodes in a spontaneous mouse prostate tumor model	61
Chapter 5	Comparing the hybrid fluorescent-radioactive tracer indocyanine green- ^{99m} Tc-nanocolloid with ^{99m} Tc-nanocolloid for sentinel lymph node identification: A validation study using lymphoscintigraphy and SPECT/CT	87
Chapter 6	Intraoperative laparoscopic fluorescence guidance to the sentinel lymph node in prostate cancer patients: clinical proof of concept of an integrated functional imaging approach using a hybrid tracer	105
Chapter 7	Relation between intraprostatic tracer deposits and sentinel lymph node mapping in prostate cancer patients	123

Part II	Chemokine receptor (CXCR4) targeting applications	145
Chapter 8	Imaging agents for the chemokine receptor 4 (CXCR4)	147
Chapter 9	Immunohistochemical detection of the CXCR4 expression in tumor tissue using the fluorescent peptide antagonist Ac-TZ14011-FITC	179
Chapter 10	Non-invasive longitudinal imaging of tumor progression using an ¹¹¹ Indium labeled CXCR4 peptide antagonist	203
Chapter 11	Synthesis and evaluation of a hybrid CXCR4 antagonistic peptide	223
Chapter 12	Hybrid peptide dendrimers for imaging of chemokine receptor 4 (CXCR4) expression	245
Chapter 13	Integrating target validation with in vivo and ex vivo imaging of mouse tumor lesions resembling human DCIS using a single hybrid imaging agent	273
Chapter 14	Future perspectives	297
Chapter 15	Summary	305
Chapter 16	Dutch summary / Nederlandse samenvatting	313
	List of publications	321
	Curriculum Vitae	329
	Acknowledgements / Dankwoord	330

Interventional molecular imaging, a hybrid approach

General introduction

Chapter 1

General Introduction

Accurate detection of tumor tissue is a key feature in the diagnosis of cancer, and surgery is one of the major pillars in further management of the disease. Using preoperatively obtained images, the area of interest can be linked to the anatomy of the patient, enabling planning of the surgical intervention.

During surgical exploration morbidity may be caused by the unnecessary removal of healthy tissue and/or the unintentional damage to delicate anatomical structures. Furthermore, the inability to completely excise the cancerous tissue increases the need for invasive re-excisions. More accurate surgical visualization of the area's of interest can supplement the surgeons eyes and help improve surgical outcome.

Accurate preoperative identification, surgical planning, and intraoperative visualization can be integrated using hybrid imaging agents that contain both a radio- and fluorescent label. This hybrid interventional molecular imaging concept was initially validated in sentinel lymph node (SLN) biopsies, but can be further expanded by the implementation of imaging agents that specifically visualize tumor cells. In this thesis both the preclinical and clinical introduction of this hybrid concept is described.

Part I of this thesis is focused on combined pre- and intraoperative imaging of the SLN. **Chapter 2** provides an overview of radioactive, fluorescent and size-dependent properties of non-targeted hybrid nanoparticles and their (potential) value in SLN detection.

In **Chapter 3** conventional preoperative lymphoscintigraphy with technetium labeled albumin colloids is quantitatively compared with optical intraoperative guidance using the near-infrared dye indocyanine green (ICG) in a mouse model for metastatic breast cancer. A self-assembled hybrid complex (ICG-^{99m}Tc-nanocolloid) is applied, in order to attain identical dynamics of the radioactive and fluorescent components.

In a spontaneous mouse prostate tumor model (**Chapter 4**), the lymphatic distribution pattern of the hybrid imaging agent ICG-^{99m}Tc-nanocolloid was quantitatively compared to that of the visible dye patent blue, ICG, and dual labeled human serum albumin particles (ICG-^{99m}Tc-Vasculosis).

In a clinical reproducibility study, described in **Chapter 5**, lymphoscintigraphic drainage patterns of ^{99m}Tc-nanocolloid and ICG-^{99m}Tc-nanocolloid are compared, showing that the addition of ICG does not alter the drainage properties of the radiocolloid.

Chapter 6 describes the added value of combined pre- and intraoperative imaging

using ICG-^{99m}Tc-nanocolloid in patients who underwent robot assisted laparoscopic prostatectomy (RALP) with (S)LN dissection for prostate cancer.

An additional feature of ICG-^{99m}Tc-nanocolloid is demonstrated in **Chapter 7**, wherein the location of the ICG-^{99m}Tc-nanocolloid tracer deposit in embedded prostate samples is related to the lymphatic drainage pattern as seen on lymphoscintigraphy.

In **Part II** of this thesis the preclinical evaluation of a number of differently labeled Ac-TZ14011-based CXCR4 targeting imaging agents, including hybrid derivatives, are described.

In **Chapter 8** expression of CXCR4 in preclinical (tumor) models is compared to the clinical situation. Furthermore, peptide structures and receptor affinities of CXCR4 targeting T140 peptide derivatives are evaluated.

The ability to accurately stain the CXCR4 receptor in both cells and tumor tissue using a fluorescently labeled version of Ac-TZ4011 (Ac-TZ14011-FITC) is compared to CXCR4 targeting antibodies in **Chapter 9**.

In a mouse tumor model resembling human ductal carcinoma in situ (DCIS; **Chapter 10**), an indium labeled version of Ac-TZ14011 (¹¹¹In-Ac-TZ14011) is used to longitudinal monitor lesion development by way of CXCR4 expression levels.

Chapter 11 describes the synthesis and evaluation of hybrid Ac-TZ14011 derivatives that contain both a DTPA chelate and a fluorescent dye. Like the untargeted hybrid agent ICG-^{99m}Tc-nanocolloid, the hybrid version of the targeting peptide (MSAP-Ac-TZ14011) enables integration of pre- and intraoperative imaging.

The effect of multimerization; increasing the amount of targeting peptides per molecule to reduce the negative influence of the hybrid label on the receptor affinity and distribution is studied in **Chapter 12**.

An expansion of the targeted hybrid imaging approach is discussed in **Chapter 13** wherein MSAP-Ac-TZ14011 is used to assess the CXCR4 expression pattern in fresh tumor tissue specimens. This approach enables target validation and accurate staging of the lesions prior to imaging.

In the future perspectives (**Chapter 14**), additional suggestions for expansion of the hybrid surgical guidance concept are given.

Interventional **Hybrid guidance for** **molecular imaging,** **sentinel lymph node biopsy** **a hybrid approach**

Part I

Interventional **(Non-targeted) radioactive/fluorescent** **molecular imaging,** **nanoparticles and their potential in combined** **a hybrid approach** **pre- and intraoperative imaging during** **sentinel lymph node resection**

Chapter 2

Adapted from:

Buckle T, van Leeuwen AC, Chin PT, Janssen H, Muller SH, Jonkers J, van Leeuwen FWB.

Nanotechnology. 2010; 21: 355101

Abstract

A clear clinical precedent for the use of nano-sized imaging agents is localization of the tumor draining sentinel lymph nodes (SLNs). Specific removal of the SLN during breast cancer surgery presents physicians with the opportunity to detect early metastatic disease. In this application, radiocolloids such as ^{99m}Tc -nanocolloid are commonly used to plan the surgical procedure and to provide acoustic gamma guidance to the SLN during the intervention. An additional injection of a (visible) dye is used to provide optical surgical guidance. Hybrid nanoparticles, which contain both a radioactive and fluorescent label, provide the potential to combine both radioactivity based surgical planning and intraoperative fluorescence guidance. In this chapter an overview is provided of the radioactive, fluorescent, and size properties of such (non-targeted) hybrid nanoparticles, and their (potential) value in SLN detection.

Introduction

In oncology, the presence of (lymphatic) metastases is considered an important predictor of distant tumor spread and consequently the life expectancy of the patient. The sentinel lymph node ((S)LN) is the first tumor draining lymph node and is generally the first LN affected by metastasizing tumor cells draining from a primary tumor. Based on the presence of tumor cells within the SLN, the likelihood of metastatic spread throughout the lymphatic system can be predicted and further treatment can be adapted accordingly.¹ Evaluation of the tumor presence in SLNs is a standard procedure during the clinical management of breast cancer patients and is also being investigated for many other tumor types e.g. melanoma and prostate cancer.¹⁻³ Accurate pathological analysis of the SLN depends on their accurate removal during surgical resection, which in turn relies heavily on the guidance provided during the surgical procedure.

Clinically, for SLN mapping lymphoscintigraphy is most frequently performed using radioactive colloidal particles.⁴⁻⁶ In Europe, ^{99m}Tc-nanocolloid is the current clinical standard, whereas in the US ^{99m}Tc-sulfurcolloids are most frequently used.⁷ Peritumoral/subdermal injection of these non-targeted colloidal particles results in transport via the lymphatic system, followed by accumulation in the SLN.⁸

Surgical resection of the SLN requires combined pre- and intraoperative imaging.⁹⁻¹¹ Commonly, the surgical procedure is planned according to preoperatively acquired lymphoscintigraphy using the radiocolloid.¹² Intraoperative surgical guidance is then obtained using an acoustic gamma probe and/or via co-injected dyes.¹³⁻¹⁵ Such dyes offer the potential to add (superficial) optical intraoperative guidance. Unfortunately, the small organic dyes, such as methylene blue¹⁵, patent blue¹⁴, fluorescein ($\lambda_{em} = 530$ nm)¹⁵, and the near-infrared (NIR) dye indocyanine green (ICG; $\lambda_{em} = 808$ nm)¹⁶ do not appear to accumulate in the SLNs, limiting their use in real-time lymphatic mapping studies.¹⁷ Differences in lymphatic migration translate to a different effective time window for both the radioactivity based and optical procedures. Hence in clinical practice pre- and intraoperative imaging consists out of two separate diagnostic approaches (radiocolloid and dye based), rather than a single integrated approach. Nano-sized hybrid imaging agents can, however, be used to combine radioactive and fluorescence properties in a single particle.¹⁸ In such particle the radiolabel will enable surgical planning and guidance during the excision in the dm - cm range, while fluorescence will enable accurate intraoperative localization (cm - mm range; Figure 1).

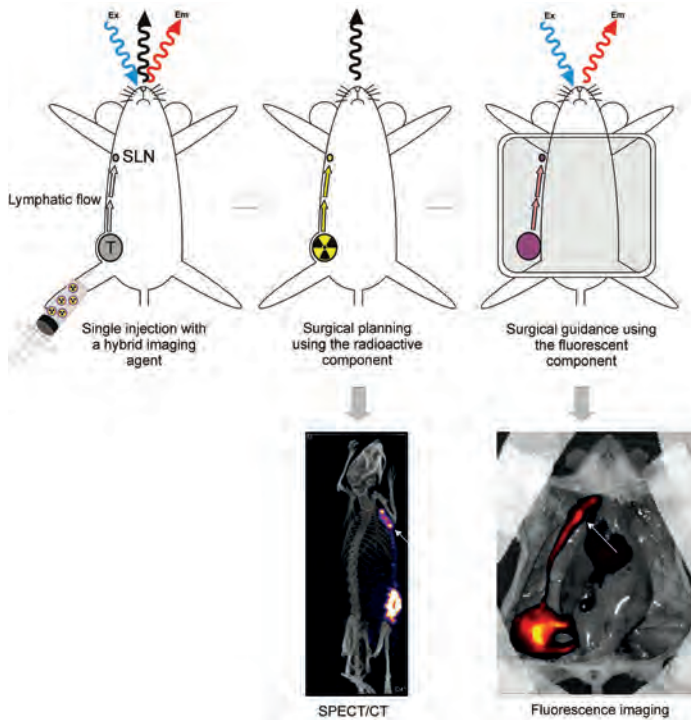


Figure 1. Schematic presentation of combined pre- and intraoperative imaging of the SLN using hybrid imaging agents that contain both a radioactive and fluorescent label (Figure adapted from Buckle et al.²⁴) Both the SPECT/CT and the fluorescence image show the injection site (tumor), the draining lymphatic vessel (arrows) and the SLN.

Pre- and intraoperative imaging can be combined using non-targeted radioactive/fluorescent nano-sized materials. The physical requirements of these particles are considered to be a good guideline for the future development of nanotechnology-based imaging agents and their implementation in SLN imaging. Several reviews have been written discussing hybrid imaging agents.¹⁸⁻²⁰ Moreover, there are a number of reviews that discuss the use of nanoparticles for SLN imaging that also include MRI/optical hybrid particles.^{21,22,23} As the standard clinical SLN procedure is based on radioactivity-based 3D imaging, rather than MRI, this Chapter is focused on the combination of radioactive and fluorescent antennae. We discuss the chemical properties of a variety of non-targeted hybrid nanoparticles and discuss their (potential) value in combined pre- and intraoperative SLN imaging applications.

Radioactive/fluorescent nanoparticles

Protein based

In Europe, the most widely applied protein-based nanoparticle in nuclear medicine is ^{99m}Tc (Technetium (^{99m}Tc ; 140 keV; SPECT) labeled colloidal human serum albumin (nanocolloid; average diameter 14 nm).²⁴ Although it is not accurately described, the ^{99m}Tc -radiolabeling randomly occurs at the many available nitrogen- and/or sulfur-groups. We have recently shown that self-assembly can be used to generate a hybrid derivative of this compound, namely ICG- ^{99m}Tc -nanocolloid (Figure 2a).^{24,25} Due to the large number of non-covalent binding sites,²⁶ a single albumin particle can contain a number of non-covalently bound guest molecules.²⁷ As nanocolloid consists out of multiple albumin particles, this results in a further concentration of dye molecules.

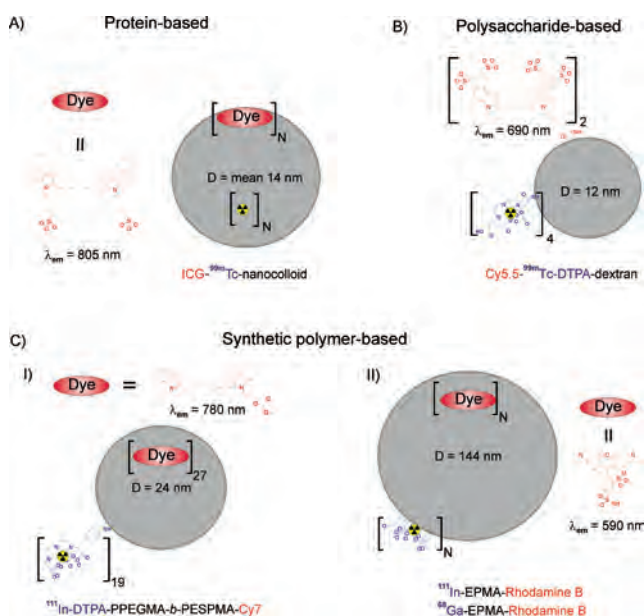


Figure 2. Schematic representation of non-targeted radioactive/fluorescent organic nanoparticles. A) Protein-based self-assembled ICG- ^{99m}Tc -nanocolloid particles.²⁴ B) Polysaccharide-based dextran particles covalently functionalized with Cy5.5 and a ^{99m}Tc -DTPA label.²⁸ C) Synthetic polymer-based nanoparticles: I) hybrid co-block polymers with an ^{111}In -DTPA label and a covalently linked fluorescent label (Cy7)³¹ and II) EPMA-based latex nanoparticles with non-covalently internalized dye (RhB) and surface coordinated radiolabels.³² The radiolabels are represented in blue, the fluorescent antennae in red and the carrier molecules in gray.

Combined pre- and intraoperative imaging of the SLN with ICG-^{99m}Tc-nanocolloid has been validated in mouse models for metastatic breast and prostate cancer.^{24,25} The migration properties of the hybrid derivative was found to be highly similar, if not identical to ^{99m}Tc-nanocolloid (Figure 1). Incorporation of multiple ICG molecules on the nanocolloid resulted in a huge improvement in the signal-to-background-ratio compared to free ICG.

Polysaccharide based

Polysaccharides like dextran contain a large number of reactive hydroxy groups that can be utilized for covalent functionalization. Vera et al.²⁸ generated 12 nm dextran particles (Mw = 70 kDa), labeled with four DTPA moieties and two Cy5.5 (λ_{em} 690 nm) dye molecules (Figure 2b). In theory any type of dye functionalized with a reactive group can be linked to this dextran backbone, allowing the generation of particles with emission wavelengths ranging from visual to the NIR. The large number of appropriate reactive groups allows introduction of increasing numbers of fluorescent antennae and radioactive labels. Unfortunately in vivo examples using these hybrid nanoparticles are not described.

Although not (commonly) used for clinical applications, dextran particles with a 7 nm size have proven their value in lymphatic (flow) imaging; both radioactive (^{99m}Tc) and fluorescent derivatives have been described.^{29,30} Since the dextran scaffold is the driving factor for these properties, a dual-labeled derivative should perform equally well. Moreover, size alteration of the dextran-scaffold can be used to improve the accumulation in SLNs.

Synthetic polymer-based

Synthetic polymeric nanoparticles, such as polymer micelles³¹ and latex³² with combined radioactive/fluorescent labels have also been reported (Figure 2c). For example, PEG-coated core-crosslinked polymer micelles (24 nm) can be formed by crosslinking the block copolymer poly(PEG-methacrylate)-b-poly triethoxysilyl propylmethacrylate (PPEGMA-b-PESPMA) and 3-(triethoxysilyl)propyl-Cy7 (λ_{em} 780 nm).³¹ Crosslinking resulted in incorporation of approximately 27 Cy7 molecules into the particle core. Primary amine groups available on the (cross-linked) polymer surface were subsequently functionalized with 19 chelating DTPA-moieties per particle, which in turn allowed efficient incorporation of ¹¹¹In at the particle surface. When linked to a 3-(triethylsilyl)propyl group other dyes can potentially also be incorporated in a similar manner. Again the number of dye molecules and radiolabels can be varied in this set-up, but no in vivo data is described.

Emulsion copolymerization of poly-2,3-epoxypropylmethacrylate (EPMA) and Rhodamine B (RhB; λ_{em} 590 nm) has been used to form latex particles with a diameter of 144 nm.³² The dye, which does not contain a reactive end group, remains trapped within the particle structure after crosslinking of the EPMA molecules. As RhB incorporation does not appear to be based on a specific interaction between the polymer and the dye, a similar procedure could be performed using other dyes. These latex particles contain a large number of carboxyl end groups on their surface and the authors have shown that these can function as chelating moiety for radioisotopes such as ⁶⁸Ga and ¹¹¹In. However, no data on the stability of these alternative metal-complexes has been reported, nor is an *in vivo* application mentioned.

Fluorescent polystyrene microspheres (20 - 200 nm) have shown potential value in lymphatic mapping procedures.³³ However, the hybrid derivatives have not yet been studied in this particular application. These polymeric hybrid particles (24 nm or 144 nm) can most likely provide synthetic alternatives to the albumin- or dextran-based nanoparticles. In addition to the possibility to chemically optimize the different polymer components of these synthetic derivatives, their size can potentially also be exploited to optimize lymphatic migratory properties even further.

Inorganic nanoparticles

In the last few decades a popular new class of inorganic dyes has been developed, referred to as quantum dots (QDs). In contrast to the earlier discussed protein-, saccharide-, and synthetic polymer-based nanoparticles, QDs do not rely on the inclusion of a dye for fluorescence. These nano-sized inorganic semiconductor crystals are inorganic fluorophores on their own. QD fluorescence induces great flexibility; alterations in size and materials allows tuning of the fluorescence from the visible part of the spectrum into the NIR.³⁴

Introduction of a radioactive group on the surface of a QD is relatively easy, resulting in direct generation of a hybrid particle. This introduction commonly occurs via covalent attachment of a precoordinated reactive chelate complex to the polymer-, lipid- or surfactant coating of the QDs (Figure 3). The surface of CdSe/ZnS QDs has been radiolabeled with different isotopes, e.g. ^{99m}Tc and ⁶⁴Cu.^{35,36,37} An advantage of surface modification is that it can easily be extrapolated to alternative QDs, e.g. InAs/ZnS.³⁸ A radiolabel *viz.* fluorine (¹⁸F; PET) attached to a reactive organic molecule can be introduced onto a phospholipid coating.³⁹ Of course the value of such a non-covalent coating relies heavily on a good particle stability *in vivo*. Alternatively, a radioactive isotope can be

introduced in the crystal core during the QD synthesis. In this manner CdTe/ZnS QDs containing ^{125m}Te have been generated (Figure 3d).⁴⁰ This latter type of radiolabeling is very elegant as it requires no physical alteration to the QD. However, it appears to be less practical than a final-step introduction of a radioactive moiety on preprepared QDs.

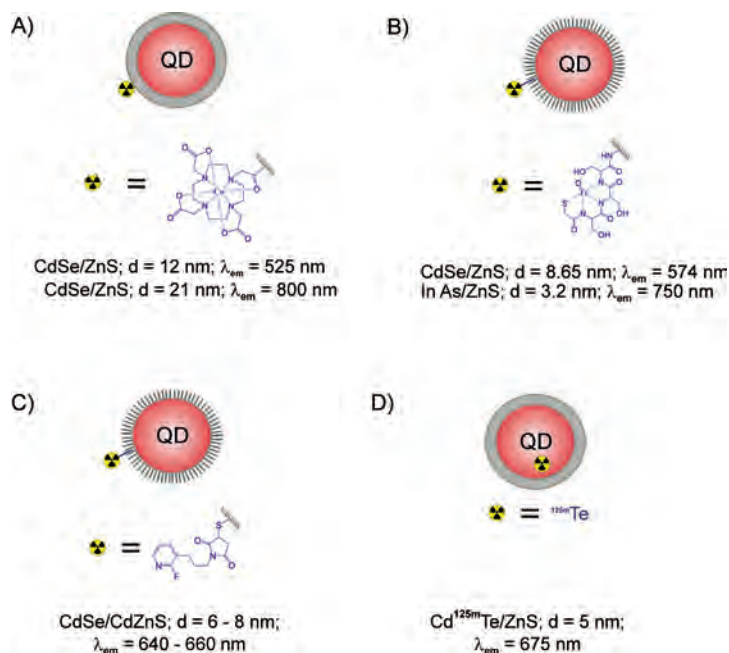


Figure 3. Schematic representation of non-targeted inorganic nanoparticles. A) Polymer coated QDs functionalized with a ^{64}Cu radiolabel³⁶ B) Thiol-based lipid coated QDs functionalized with a ^{99m}Tc radiolabel.^{35,38} C) Lipid coated QDs functionalized with a radiolabel (^{18}F).³ D) Core radiolabeled (^{125m}Te) QDs.⁴⁰ The radiolabels are represented in blue and the fluorescent antennae in red.

The potential value of QDs in SLN imaging was initially been reported by Kim et al.⁴¹ and Ballou et al.⁴² and has later underlined by a number of different groups.⁴³ While none of the SLN studies using QDs included the use of a radiolabel, there is no reason why radioactive/fluorescent QDs could not be equally suitable for such an application. Such hybrid QDs will also allow quantification of the kinetics in the lymphatic system, a feature that is currently lacking. QDs with a covalent coating functionalized with a radiolabel are more likely to remain stable under the desired conditions than those coated with lipid micelles.

Dendrimers

Signal enhancement can be achieved via the creation of molecules that have multiple available reactive groups. In such compounds, so called dendrimers, increasing generations contain increasing amounts of reactive end groups and an increase in size. Moreover, the number of end groups can be well documented and accurately tuned for a particular application. While a number of MRI/fluorescent dendrimers have been reported^{44,45} there is, to the best of our knowledge, only one single example of dendritic structures labeled with both a radionuclide and a fluorescent dye (Figure 4).⁴⁶ After the introduction of chelating DTPA moieties, generation-6 PAMAM dendrimers containing 256 end groups were functionalized with Cy5 or one of four different Alexa dyes (Alexa660, Alexa680, Alexa700, or Alexa750). This resulted in particles of approximately 8 nm in size with a PAMAM/dye/DTPA ratio of 1:4:120. A single indium isotope (¹¹¹In) was introduced to one of the 120 DTPA moieties on the dendrimer. The use of five different derivatives, all containing a different dye covered an application from 670 to 780 nm. Moreover, the 120 chelating moieties present can be used to increase the radioactive signal intensity.

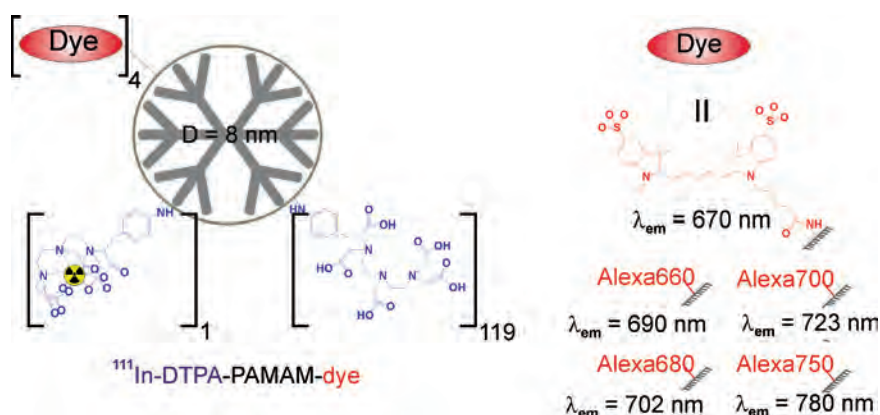


Figure 4. Schematic representation of non-targeted hybrid generation 6 PAMAM dendrimers functionalized with a radiolabel (¹¹¹In) and one of five different dyes; Cy5, Alexa660, Alexa680, Alexa700, or Alexa750.⁴⁶ The radiolabels are represented in blue, the NIR fluorescent antennae in red, and the linker molecule in black/gray.

After injection of five differently 'colored' dendrimers into the front paw of mice, Kobayashi et al.⁴⁴ were able to obtain accurate information with respect to the location of five separate lymphatic basins. In turn, the radiolabel provided a quantitative read out on

the lymphatic migration. When sufficient retention of these relatively small dendrimers in the SLN is obtained over time, this type of molecule is a good candidate for combined pre- and intraoperative imaging. This is strengthened by the large degree of synthetic control and the simultaneous use of differently colored dyes. The latter may be used to simultaneously identify the lymphatic draining sites of e.g. multifocal tumors.

General design guidelines that can be derived from literature examples

Based on the different radioactive/fluorescent nanostructures that have been reported, a number of general design guidelines can be derived, of which the most important are listed below.

Detection sensitivity: Radioactivity vs. fluorescence

Recent developments in sensitive surgical fluorescence cameras,⁴⁷ and the ability to optimize both the color and intensity of the fluorescence signal, make fluorescence imaging an attractive optical supplement to acoustic (intraoperative) radioactivity based detection. Despite the similar contrast sensitivity,⁴⁸ the signal penetration through tissue of radioactivity- and fluorescence-based imaging techniques differs quite dramatically.⁴⁹ The 25 - 511 keV gamma emission used in gamma camera imaging, single photon emission computed tomography (SPECT), and positron emission tomography (PET) provides total body penetration. In fluorescence imaging, the penetration of emitted photons remains confined within the cm - mm range, even those with NIR wavelengths. This difference influences the (clinical) application of these modalities. Whereas gamma camera imaging, SPECT, and PET are extremely suitable for non-invasive total body imaging (e.g. 3D surgical planning), fluorescence imaging is predominately suitable for superficial detection (e.g. intraoperative imaging).

In SLN applications dye concentrations used are generally much higher than the concentration of radiocolloids. The hybrid imaging agent ICG-^{99m}Tc-nanocolloid, enables detection of the SLNs using both radioactivity- and fluorescence-based imaging without changing the administered nanocolloid dose. While in ICG-^{99m}Tc-nanocolloid multiple dye molecules are present per particle, a 1:1 ratio between the radioactive and fluorescent imaging label was also proven sufficient in a recent review on peptide based tumor specific hybrid imaging agents.²⁰

Chemical properties and SLN retention

The optimal particle size for SLN imaging applications is estimated to be approximately 40 nm. Smaller particles are expected to migrate throughout the complete lymphatic trajectory while migration speed of larger particles will possibly be too slow.⁵⁰ Nunezet et al. underlined that nanometer sized particles are more preferable than microsized particles.⁵¹ Nanocolloid is said to have a favorable hydrodynamic diameter for SLN imaging⁵¹; via TEM analysis a mean particle size of 14 nm was found.²⁴ The diagnostic value of nanocolloid particles suggests that perhaps there is more to the accumulation in the SLN than size alone. Recognition of nanoparticles by the immune system may play a role in the accumulation of particles in the SLN.⁸ The administered concentration of nanocolloid was also shown to be of influence on the visualization of SLNs.¹⁰ Combined, size, recognition by the immune system, and injected concentration, seem to be the most dominant features in the feasibility of visualization of SLNs.

Radiolabel

The choice of a radiolabel is largely dictated by the radioactive half-life of the isotope. Due to the time needed for lymphatic migration and to bridge the timespan between pre- and intraoperative imaging, isotopes that can still be detected 4 - 6 hrs after administration, e.g. ^{99m}Tc and ¹¹¹In, are preferred. Several of the chelating moieties can complex different isotopes, rendering the compound suitable for a use in either SPECT or PET imaging, depending on the demand of the user. In general a single radiolabel is sufficient for accurate detection.

Dyes

Different to radioactivity based imaging procedures that directly detect the emitted gamma photons from the imaging agent, fluorescence imaging requires an external excitation light source (λ_{ex}) to obtain a fluorescent signal (λ_{em} ; Figure 1). In the body significant tissue absorption and a strong autofluorescence is observed between 400 and 650 nm. As a consequence, NIR fluorescent dyes ($\lambda_{em} > 700$ nm) are considered most suitable for 'deep' tissue imaging (cm range) in vivo, explaining the mainstream focus on NIR dyes for surgical image guidance.⁵³

In combined radioactive and fluorescent imaging agents, the radioactive component already allows for initial guidance towards the lesion. The fluorescent component is only required for superficial visualization of the SLN (Figure 5).⁴⁴

An interesting expansion of the radioactive/fluorescent labeling technology was suggested by Liu et al., who demonstrated that ^{131}I -isotopes can also be used to excite QDs.⁵⁴ Although not performed on the same molecule, such a hybrid cocktail application can be of use in, for example, tumor marker seeds,⁵⁵ which in turn can be used to mark lymph nodes (LNs).⁵⁶

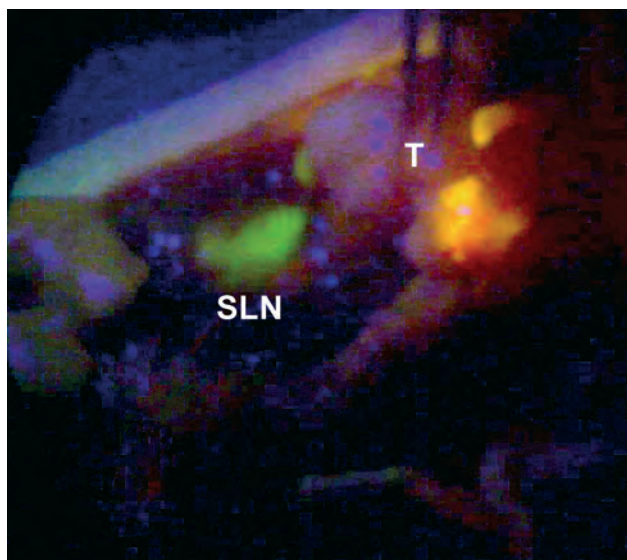


Figure 5. Example of superficial visual fluorescence guidance towards the SLN using InP/ZnS QDs (Figure adapted from Chin et al.).⁴³

In general, the type of organic dye used on the nanoparticles is not expected to alter the lymphatic distribution. This is mainly due to the dominance of the parental scaffold molecule. However, an important feature to keep in mind is the loading rate of the dye. When dyes are not physically separated in the hybrid particles, (self-)quenching of the fluorescence signal may occur. For the inorganic QD-based systems, the size related properties are used to tune the fluorescence to the desired wavelength. The fluorescence of QDs can be further tuned by inclusion of a dopant⁵⁷ in to the QD core or by the creations of QD hetero structures, which are often referred to as type II QDs.⁵⁸

Particle stability

Especially for the (non-covalent) self-assembled systems, the type of linkage between the radiolabel and the fluorophore may be instrumental for final in vivo stability of the complex. For example, in self-assembled amphiphilic lipids, the most investigated (hybrid) nano-platforms for biomedical purposes⁵⁹, dissociation may occur during SLN applications via exchange with fatty tissue leading to particle aggregation.³⁹ Unfortunately in vivo monitoring of the stability of non-covalent assembled particles can be difficult. To validate the value of non-covalent complexes in SLN applications, it is important that the distribution of all the individual components of these imaging agents can be monitored (Figure 1).²⁴

Toxicity

This Chapter is predominantly focused on the fluorescent, radioactive, and size properties of hybrid nanoparticles. However, the clearance and resulting toxicity profile will be decisive for clinical implementation of these nanoparticles. The synthetic structures that are not based on endogenous proteins, e.g. dendrimers and (inorganic) nanoparticles, may suffer from toxic side effects. The highly toxic cadmium in many of the commercial available QDs is a prime example of a property that currently stands in the way of clinical translation. Significant effort is required to generate hybrid nanoparticles with advantageous properties but with a readily translatable toxicity profile. For example the combination of clinically applied radiocolloids and a clinically applied NIR dye (ICG) yielded a good translational character; currently the hybrid imaging agent ICG-^{99m}Tc-nanocolloid is being clinically evaluated for use in SLN procedures in patients with melanoma in the head and neck area or on the trunk, penile or prostate carcinoma, and oral cavity cancer.⁶⁰⁻⁶⁴

Conclusion

Non-targeted hybrid nanoparticles that contain both a radioactive and fluorescent label represent a relatively unexploited area of chemical/nanotechnological development, with only a minor amount of compounds being produced. Despite the limited examples in literature, the potential to initiate a novel route for medical diagnostics, namely combined (preoperative) 3D radioactive imaging and (intraoperative) 2D fluorescence imaging is eminent. Diagnostics of the SLN provides a logical clinical application where size matters and nano actually performs better than sub nanometer sized molecules. As long as the size of the parental scaffold particle induces sufficient lymphatic retention, a variety of dyes and radiolabels can be introduced. This allows finetuning to the specific demands of a user.

References

- 1 Rutgers EJT. Sentinel node biopsy: interpretation and management of patients with immunohistochemistry-positive sentinel nodes and those with micrometastases. *J Clin Oncol* 2008; 26: 698-702
- 2 Morton DL, Thompson JF, Cochran AJ, Mozzillo N, Elashoff R, Essner R, Nieweg OE, Roses DF, Hoekstra HJ, Karakousis CP, Reintgen DS, Coventry BJ, Glass EC, Wang HJ. Sentinel node biopsy or nodal observation in melanoma. *N Engl J Med*. 2006; 355: 1307-1317
- 3 Vermeeren L, Valdés-Olmos RA, Meinhardt W, Bex A, van der Poel HG, Vogel WV, Sivro F, Hoefnagel CA, Horenblas S. Value of SPECT/CT for detection and anatomic localization of sentinel lymph nodes before laproscopic sentinel node lymphadenectomy in prostate carcinoma. *J Nucl Med*. 2009; 50: 865-870
- 4 Valdés-Olmos RA, Vidal-Sicart S, Nieweg OE. SPECT/CT and real-time intraoperative imaging: new tools for sentinel node localization and radioguided surgery? *Eur J Nucl Med Mol Imaging*. 2009; 36: 1-5
- 5 Krag D, Weaver D, Ashikaga T, Moffat F, Klimberg VS, Shriver C, Feldman S, Kusminsky R, Gadd M, Kuhn J, Harlow S, Beitsch P. The sentinel node in breast cancer - a multicenter variation study. *New Engl J Med*. 1998; 339: 941-946
- 6 Fujii H, Kitagawa Y, Kitajima M, Kubo A. Sentinel nodes of malignancies originating in the alimentary tract. *Ann Nucl Med*. 2004; 18: 1-2
- 7 Wilhelm AJ, Mijnhout GS and Franssen EJ. Radiopharmaceuticals in sentinel lymph-node detection - an overview. *Eur J Nucl Med*. 1999; 26: 536-42
- 8 Faries MB, Bedrosian I, Reynolds C, Nguyen HQ, Alavi A, Czerniecki BJ. Active macromolecule uptake by lymph node antigen-presenting cells: a novel mechanism in determining sentinel lymph node status. *Ann Surg Oncol*. 2000; 7: 98-105
- 9 Argon AM, Duygun U, Acar E, Daglitz G, Yenjay L, Zekioglu O, Kapkac M. The use of periareolar intradermal Tc-^{99m} tin colloid and peritumoral intraparenchymal isosulfan blue dye injection for determination of the sentinel lymph node. *Clin Nucl Med*. 2006; 31: 795-800
- 10 Valdés-Olmos RA, Tanis PJ, Hoefnagel CJ, Nieweg OE, Muller SH, Rutgers EJT, Kooi MLK, Kroon BBR. Improved sentinel node visualization in breast cancer by optimizing the colloid particle concentration and tracer dosage. *Nucl Med Comm*. 2001; 22: 579-586
- 11 Valdés-Olmos RA, Jansen L, Hoefnagel CA, Nieweg OE, Muller SH, Rutgers EJT, Kroon BBR. Evaluation of mammary lymphoscintigraphy by a single intratumoral injection for sentinel node identification. *J Nucl Med*. 2000; 41: 1500-1506

- 12 Hung WK, Chan WK, Ying M, Chong SF, Mak KL, Yip AWC. Randomized clinical trial comparing blue dye with combined dye and isotope for sentinel lymph node biopsy in breast cancer. *Br J Surg.* 2005; 92: 1494-1497
- 13 Cserni G, Rajtár M, Boross G, Sinkó M, Svébis M, Baltás B. Comparison of vital dye-guided lymphatic mapping and dye plus gamma probe-guided sentinel node biopsy in breast cancer. *World J Surg.* 2002; 26: 592-597
- 14 Simmons R, Thevarajah S, Brennan MB, Christos P, Osborne M. Methylene blue dye as an alternative to isosulfan blue dye for sentinel node localization. *Ann Surg Oncol.* 2003; 10: 242-247
- 15 Meyer A, Cheng C, Antonescu C, Pezzetta E, Bischof-Delaloye A, Ris HB. Successful migration of three tracers without identification of sentinel nodes during intraoperative lymphatic mapping for non-small cell lung cancer. *Interact Cardiovasc Thorac Surg.* 2007; 6: 214-218
- 16 Kitai T, Inomoto T, Miwa M, Shikayama T. Fluorescence navigation with indocyanine green for detecting sentinel lymph nodes in breast cancer. *Breast Cancer* 2005; 12: 211-215
- 17 Fujii H, Kitagawa Y, Kitajima M, Kubo A. Sentinel nodes of malignancies originating in the alimentary tract. *Ann Nucl Med.* 2004; 18: 1-12
- 18 Culver J, Akers W, Achilefu S. Multimodality molecular imaging with combined optical and SPECT/PET modalities. *J Nucl Med.* 2008; 49: 169-172
- 19 Jennings LE, Long NJ. 'Two is better than one' - probes for dual-modality molecular imaging. *Chem Commun.* 2009: 3511-3524
- 20 Kuil J, Velders AH, van Leeuwen. FWB Multimodal tumor-targeting peptides functionalized with both a radio- and a fluorescent-label. *Bioconjugate Chem.* 2010; 21: 1709-19
- 21 Ravizzini G, Turkbey B, Barrett T, Kobayashi H, Choyke PL. Nanoparticles in sentinel lymph node mapping. *Wiley Interdiscip Rev Nanomed Nanobiotechnol.* 2009; 1: 610-623
- 22 Jain R, Dandekar P, Patravale V. Diagnostic nanocarriers for sentinel lymph node imaging. *J Control Release.* 2009; 138: 90-102
- 23 Josephson L, Kircher MF, Mahmood U, Tang Y, Weissleder R. Near-infrared fluorescent nanoparticles as combined MR/optical imaging probes. *Bioconjugate Chem.* 2002; 13: 554-560
- 24 Buckle T, van Leeuwen AC, Chin PTK, Janssen H, Muller S, Jonkers J, van Leeuwen FWB. A self-assembled multimodal complex for combined pre- and intraoperative imaging of the sentinel lymph node. *Nanotechnology.* 2010; 21: 355101

- 25 van Leeuwen AC, Buckle T, Vermeeren L, Valdés-Olmos RA, van der Poel HG, van Leeuwen FWB. "Cocktail" injections for combined pre- and intraoperative multimodal imaging, of the tumor draining lymph nodes in a spontaneous mouse prostate tumor model. *Journal of Biomedical Optics*. 2011; 16: 016004
- 26 Kragh-Hansen U, Chuang VT, Otagiri M. Practical aspects of the ligand-binding and enzymatic properties of human serum albumin. *Biol Pharm Bull*. 2002; 25: 695-704
- 27 Simard JR, Zunszain PA, Ha CE, Yang JS, Bhagavan NV, Petipas I, Curry S, Hamilton JA. Locating high-affinity fatty acid-binding sites on albumin by x-ray crystallography and NMR spectroscopy. *Proc Nat Acad Soc USA*. 2005; 102: 17958-17963
- 28 Vera DR, Hall DJ, Hoh CK, Gallant P, McIntosh LM, Mattrey RF. Cy5.5-DTPA-galactosyl-dextran: a fluorescent probe for in vivo measurement of receptor biochemistry. *Nucl Med Biol*. 2005; 32: 687-693
- 29 Vera DR, Wakkace AM, Hoh CK, Mattrey RF. A synthetic macromolecule for sentinel node detection: ^{99m}Tc-DTPA-Mannosyl-dextran. *J Nucl Med*. 2001; 42: 951-959
- 30 von Andrian UH, Mempel TR. Homing and cellular traffic in lymph nodes. *Nature Rev Immunol*. 2003; 3: 867-878
- 31 Yang Z, Zheng S, Harrison WJ, Harder J, Wen X, Gelovani JG, Qiao A, Li C. Long-circulating near-infrared fluorescence core-cross-linked polymer micelles: synthesis, characterization, and dual nuclear/optical imaging. *Biomacromolecules* 2007; 8: 3422-3428
- 32 Cartier R, Kaufner L, Paulke BR, Wustneck R, Pietschmann S, Michel R, Bruhn H, Pison U. Latex nanoparticles for multimodal imaging and detection in vivo. *Nanotechnology*. 2007; 18: 195102-195114
- 33 Nakajima M, Takeda M, Kobayashi M, Suzuki S, Ohuchi N. Nano-sized fluorescent particles as new tracers for sentinel node detection: experimental model for decision of appropriate size and wavelength. *Cancer Sci*. 2005; 96: 353-356
- 34 Weissleder R, Ntziachristos V. Shedding light onto live molecular targets. *Nature Med*. 2009; 9: 123-128
- 35 Choi HS, Liu W, Misra P, Tanaka E, Zimmer JP, Ipe BI, Bawendi M, Frangioni JV. Renal clearance of quantum dots. *Nature Biotech*. 2007; 25: 1165-1170
- 36 Schipper ML, Cheng Z, Lee SW, Bentolila LA, Iyer G, Rao J, Chen X, Wu AM, Weiss S, Gambhir SS. MicroPET-based biodistribution of quantumdots in living mice. *J Nucl Med*. 2007; 48: 1511-1518
- 37 Cai W, Chen W, Li ZB, Gambhir SS, Chen X. Dual-function probe for PET and near-infrared fluorescence imaging of tumor vasculature. *J Nucl Med*. 2007; 48: 1862-1870

- 38 Choi HS, Ipe BI, Misra P, Lee JH, Bawendi MG, Frangioni JV. Tissue- and organ-selective biodistribution of NIR fluorescent quantum dots. *Nano Lett.* 2009; 9: 2354-2359
- 39 Duconge F, Pons T, Pestourie C, Herin L, Theze B, Gombert K, Mahler B, Hinnen F, Kuhnast B, Dolle F, Dubertret B, Tavittain B. Fluorine-18-labeled phospholipid quantum dot micelles for in vivo multimodal imaging from whole body to cellular scales. *Bioconjugate Chem.* 2008; 19: 1921-1926
- 40 Woodward JD, Kennel SJ, Mirzadeh S, Dai S, Wall JS, Richey T, Avenell J, Rondinone AJ. In vivo SPECT/CT imaging and biodistribution using radioactive Cd125mTe/ZnS nanoparticles. *Nanotechnology.* 2007; 18: 175103
- 41 Kim S, Lim YT, Soltesz EG, De Grand AM, Lee J, Nakayama A, Parker JA, Mihaljevic T, Laurence RG, Dor DM, Cohn LH, Bawendi MG, Frangioni JV. Near-infrared fluorescent type II quantum dots for sentinel lymph node mapping. *Nature Biotech.* 2004; 22: 93-97
- 42 Ballou B, Lagerholm BC, Ernst LA, Bruchez MP, Waggoner AS. Noninvasive imaging of quantum dots in mice. *Bioconjugate Chem.* 2004; 15: 79-86
- 43 Chin PTK, Buckle T, Aguirre de Miguel A, Meskers SCJ, Janssen RAJ, van Leeuwen FWB. Dual emissive quantum dots for multispectral intraoperative fluorescence imaging. *Biomaterials.* 2010; 31: 6823-6832
- 44 Talanov VS, Regino CAS, Kobayashi H, Bernardo M, Choyke PL, Brechbiel MW. Dendrimer-based nanoprobe for dual modality magnetic resonance and fluorescence imaging. *Nano Lett.* 2006; 6: 1459-1463
- 45 Xu H, Regino CA, Koyama Y, Hama Y, Gunn AJ, Bernardo M, Kobayashi H, Choyke PL, Brechbiel MW. Preparation and preliminary evaluation of a biotin-targeted, lectin-targeted dendrimer-based probe for dual-modality magnetic resonance and fluorescence imaging. *Bioconjugate Chem.* 2007; 18: 1474-1482
- 46 Kobayashi H, Koyama Y, Barret T, Hama Y, Regino CAS, Shin IS, Jang BS, Paik CH, Choyke PL, Urano Y. Multimodal nanoprobe for radionuclide and five color near-infrared optical lymphatic imaging. *ACS Nano.* 2007; 1: 258-264
- 47 Troyan SL, Kianzad V, Gibbs-Strauss SL, Gioux S, Matsui A, Oketokoun R, Ngo L, Khamene A, Azar F, Frangioni JV. The FlareTM intraoperative near-infrared fluorescence imaging system: A first-in-human clinical trial in breast cancer sentinel lymph node mapping. *Ann Surg Oncol.* 2009; 16: 2943-2952
- 48 Meikle SR, Kench P, Kassiou M, Banati RB. Small animal SPECT and its place in the matrix of molecular imaging technologies. *Phys. Med. Biol.* 2005; 50: R45-61
- 49 Weissleder R, Pittet MJ. Imaging in the era of molecular oncology. *Nature.* 2008; 452: 580-589

-
- 50 Nakajima M, Takeda M, Kobayashi M, Suzuki S, Ohuchi N. Nano-sized fluorescent particles as new tracers for sentinel node detection: experimental model for decision of appropriate size and wavelength. *Cancer Sci.* 2005; 96: 353-356
 - 51 Nunez EGF, Faintuch BL, Teodoro R, Wiecek DP, Martinelli JR, da Silva NG, Castanheira CE, de Oliveira Filho RS, Pasqualini R. Influence of colloid particle profile on sentinel lymph node uptake. *Nucl Med Biol.* 2009; 36: 741-747
 - 52 Ohnishi S, Lomnes SJ, Laurence RG, Gogbashian A, Mariani G, Frangioni JV. Organic alternatives to quantum dots for intraoperative near-infrared fluorescent sentinel lymph node mapping. *Mol Imaging.* 2005; 4: 172-181
 - 53 Frangioni JV. In vivo near-infrared fluorescence imaging. *Curr Op Chem Biol.* 2003; 7: 626-634
 - 54 Liu H, Zhang X, Xing B, Han P, Gambir SS, Cheng Z. Radiation-luminescence-excited quantum dots for in vivo multiplexed optical imaging. *Small.* 2010; 6: 1087-1091
 - 55 Buckle T, Chin PTK, van den Berg NS, Loo C, Koops W, Gilhuijs KG, van Leeuwen FWB. Tumor bracketing and safety margin estimation using multimodal marker seeds; a proof of concept. *J Biomedical Optics.* 2010; 15: 056021.
 - 56 Straveren ME, Loo CE, Alderliesten T, Rutgers EJT, Vrancken Peeters MT. Marking the axilla with radioactive iodine seeds (MARI procedure) may reduce the need for axillary dissection after neoadjuvant chemotherapy for breast cancer. *Br J Surg.* 2010; 97: 1226-1231
 - 57 Bhargava RN, Gallagher D, Hong X, Nurmikko A. Optical properties of manganese-doped nanocrystals of ZnS. *Phys Rev Lett.* 1994; 72: 416-419
 - 58 Hatami F, Grundmann M, Ledentsov NN, Heinrichsdorff F, Heitz R, Böhrer J, Bimberg D, Ruvimov SS, Werner P, Ustinov VM, Kopev PS, Alferov ZHL. Carrier dynamics in type-II GaSb/GaAs quantum dots. *Phys Rev B.* 1998; 57: 4635-4641
 - 59 Mulder WJL, Strijkers GJ, van Tilborg GAF, Cormode DP, Fayad ZA, Nicolay K. Nanoparticulate assemblies of amphiphiles and diagnostically active materials for multimodality imaging. *Acc Chem Res.* 2009; 42: 904-914
 - 60 Brouwer OR, Klop MWC, Buckle T, van den Brekel MWM, Balm AJM, Nieweg OE, Valdés-Olmos RA, van Leeuwen FWB. Feasibility of sentinel node biopsy in head and neck melanoma using a hybrid radioactive and fluorescent tracer. *Ann Surg Oncol.* 2012; 19(6): 1988-1994
 - 61 van der Poel HG, Buckle T, Brouwer OR, Valdés-Olmos RA, van Leeuwen FWB. Intraoperative laparoscopic fluorescence guidance to the sentinel lymph node in prostate cancer patients; clinical proof of concept of an integrated functional imaging approach using a multimodal tracer. *Eur Urol* 2011; 60: 826-833

- 62 Buckle T, Brouwer OR, Valdés-Olmos RA, van der Poel HG, van Leeuwen FWB. Relation between intraprostatic tracer deposits and sentinel lymph node mapping in prostate cancer patients. *J Nucl Med.* 2012; 53: 1026-1033
- 63 Brouwer OR, Buckle T, Vermeeren L, Klop MWC, Balm AJM, van der Poel HG, van Rhijn BW, Horenblas S, Nieweg OE, van Leeuwen FWB, Valdés-Olmos RA. Comparing the hybrid fluorescent-radioactive tracer indocyanine green-^{99m}Tc-nanocolloid with ^{99m}Tc-nanocolloid for sentinel lymph node identification: A validation study using lymphoscintigraphy and SPECT/CT. *J Nucl Med.* 2012; 53(7): 1-34-1040
- 64 van den Berg NS, Brouwer OR, Klop MWC, Balm AJ, van den Brekel MWM, Valdés-Olmos RA, van Leeuwen FWB. A hybrid tracer for concomitant radio- and fluorescence guided sentinel lymph node biopsy in oral cavity cancer. *Eur J Nucl Med Mol Imaging.* 2012; 39(7): 1128-1136

Interventional

**A self-assembled hybrid complex
molecular imaging,
for combined pre- and intraoperative
a hybrid approach
imaging of the sentinel lymph node**

Chapter 3

Adapted from:

Buckle T, van Leeuwen AC, Chin PTK, Janssen H, Muller SH, Jonkers J, van Leeuwen FWB.

Nanotechnology. 2010; 21(35): 3

Abstract

To increase the accuracy of intraoperative sentinel lymph node (SLN) detection, new methods with higher sensitivity and specificity are required. To facilitate this, conventional detection procedures based on preoperative lymphoscintigraphy with technetium labeled albumin radiocolloids (^{99m}Tc -nanocolloid) and optical intraoperative guidance using the near-infrared dye indocyanine green (ICG) were quantitatively compared in an orthotopic mouse model for metastatic breast cancer. Furthermore, a self-assembled hybrid complex was evaluated. In this complex ICG was non-covalently bound to ^{99m}Tc -nanocolloid to attain identical dynamics of the radioactive and optical components. The SLN specificity of the hybrid complex was similar to that of the parental ^{99m}Tc -nanocolloid, and the fluorescent signal-to-noise ratio was found to be improved compared to ICG alone. Consequently, ICG- ^{99m}Tc -nanocolloid has the potential to be used for both lymphoscintigraphy and surgical visualization via intraoperative fluorescence imaging.

Introduction

One of the main challenges in surgical oncology is the intraoperative detection of preoperatively diagnosed lesions. At present, (molecular) imaging is a rapidly growing research field aiming at accurate and non-invasive diagnosis of disease.¹ Consequently it becomes of increasing importance to develop strategies that enable incorporation of such novel imaging approaches into surgical procedures. To achieve surgical incorporation, intraoperative imaging procedures must be developed that depict identical features as defined during the preoperative image acquisition. The latter is used to plan the surgical procedure. The sentinel lymph node (SLN) procedure in breast cancer patients is a good example of a clinical application where combined pre- and intraoperative detection is desired.²⁻⁴ Based on the histological status of the SLN, the possible presence of metastasis in the (axillary) lymph nodes can be assessed. The outcome of this assessment is used to select further therapeutic approaches. Accuracy of removal of the SLN, however, relies heavily on the accuracy of the functional guidance provided during the excision.

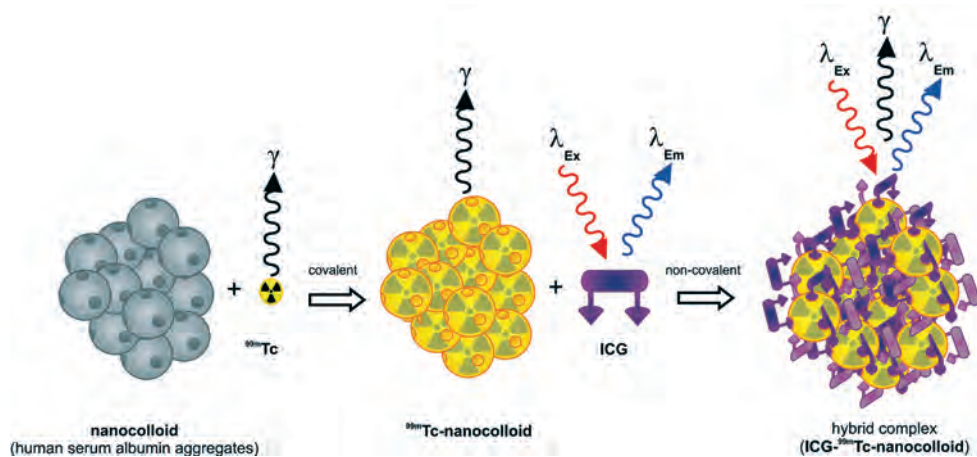
Preoperative lymphoscintigraphy following injection of radiopharmaceuticals such as nano-sized radiocolloids (e.g. ^{99m}Tc-nanocolloid) accurately visualizes the SLN in the majority of patients.^{3,4} However, in some settings the intraoperative use of radiocolloids is cumbersome due to high background signals coming from the injection site. Therefore, visible blue dyes such as methylene blue and patent blue⁵⁻⁹ are often added to provide real time visual guidance during the surgical procedure. A potential downside of this additional visual detection approach is the low detection sensitivity. Accordingly, high concentrations (10 mg/mL) of visible dyes are required, which frequently results in cosmetically undesirable blue colored residues that remain visible for a long period of time after the operation.⁶ Together, these limitations call for alternative methods that yield a higher sensitivity and improve detection rates during optical intraoperative guidance.

Near-infrared (NIR) fluorescence signals in the 700 - 900 nm range allow for increased tissue penetration and therefore can be detected with a much higher sensitivity than visible dyes.^{1,10} Although tissue penetration of the NIR dyes is insufficient for accurate preoperative planning in 3D, it is adequate for superficial intraoperative fluorescence imaging procedures.

The NIR fluorescent dye indocyanine green (ICG) has been applied during SLN procedures in lung cancer,¹¹ gastrointestinal cancer¹²⁻¹⁴ and breast cancer.¹⁵⁻¹⁸ However, a limitation in these studies is the lack of a quantitative and dynamic comparison between the ICG technique to conventional approaches.

By combining the radiopharmaceutical- and dye-based methods, the SLN can be detected both pre- and intraoperatively.^{8,19} Herein is the variation in lymphatic transport velocity of the individual agents a limiting factor as differences in dynamic properties and/or injection procedures do occur. A hybrid approach using a single imaging agent that can be detected both with optical and radioactive methods can overcome these problems.²⁰ The use of radiolabeled dyes (e.g. iodinated methylene blue) has been described previously.²¹ However, no application of such an imaging agent has been reported for combined pre- and intraoperative imaging procedures.

In this Chapter several approaches for pre- and intraoperative imaging of the SLN were evaluated in an orthotopic mouse model for metastatic breast cancer. Preoperative SPECT/CT procedures using radiocolloids (^{99m}Tc-nanocolloid) were quantitatively compared to fluorescence-based intraoperative procedures using ICG. In addition, the utility of an integrated approach based on a supramolecular hybrid imaging agent consisting of a self-assembled complex comprising of ICG and ^{99m}Tc-nanocolloid (Scheme 1) was demonstrated.



Scheme 1. Schematic representation of the subsequent albumin colloid radiolabeling with ^{99m}Tc and fluorescent labeling with ICG.

Materials and methods

Animals

Female [FVB x 129/Ola] F1 animals (6 - 12 weeks of age) were used. By means of orthotopic transplantation, 1×10^5 KEP1-Luc cells were injected into the fat pad of the left fourth mammary gland.²² The incision was closed and mice received an intraperitoneal (i.p.) injection of 10 μ l of Temgesic (0.3 mg/mL buprenorfin; Schering Plough) in 1 mL of 5% glucose/saline solution for postoperative pain relief. Tumor progression and spread was monitored by bioluminescence imaging (BLI). When the tumors reached a size of 4 - 5 mm in diameter, initial metastasis could be observed in the axillary region. At this time animals were deemed suitable for experiments. Mice were included until tumors reached 7 - 9 mm or when lung metastasis occurred. Prior to SPECT/CT and fluorescence imaging experiments the animals were anesthetized with a 1:1:2 mixture of Hypnorm (Vetapharma), Dormicum (Roche) and water (5 μ L/g i.p.). BLI scans were performed using isoflurane inhalation anesthesia (Forene; Abbott). Experiments were conducted in tumor-bearing (n = 15) and control animals (n = 10), where the imaging agent was injected into the tumor or mammary fat pad, respectively. The axillary, brachial and the right inguinal lymph nodes (LN) were dissected and renamed as (S)LN1, LN2, LN3, LN4 and LN5 (Figure 1). All animal experiments were performed in accordance with Dutch animal welfare regulations and were approved by the local ethics committee.

Imaging agents

One gram of luciferin (substrate for luciferase; Xenogen Corp., Alameda, CA, USA) was dissolved in 66.7 mL phosphate buffered saline (PBS). After filtration using a 22 μ m filter (Millipore), this resulted in a sterile 15 mg/mL solution. A 1 mg/mL (1.3×10^{-3} mmol/mL) Cardiogreen (indocyanine green (ICG); Sigma Aldrich) solution was prepared in a 0.9% saline solution. Clinical grade human serum albumin nanocolloid (NanoColl; 0.5 mg human serum albumin (7.5×10^{-6} mmol); GE Healthcare) was radiolabeled with ^{99m}Tc (2 mL) according to standard clinical preparation procedures.

Preparation of the hybrid imaging agent

A self-assembled supramolecular complex of ICG and nanocolloid was made according to a slightly modified procedure for human serum albumin (HSA) labeling.⁴ To a clinical grade solution of ^{99m}Tc -labeled nanocolloid (200 μ L; 80 - 100 MBq), 60 μ l of a 1 mg/mL ICG solution

was added. After 30 min incubation, the ICG-^{99m}Tc-nanocolloid complex was separated from unbound reagents using a C-18 column, leading to a yield of 59% of the ICG-^{99m}Tc-nanocolloid complex [elution 9 g/L NaCl and 9 g/L NaCl (10% acetonitrile)]. For the imaging experiments a micron centrifugal filter (Millipore) with a molecular weight cut off at 30,000 Mw was used to isolate the complex from free dye. After this size-selective separation, the concentrate containing the ICG-nanocolloid complex was resuspended in 200 μ L saline solution.

Electron microscopy

Nanocolloid powder (0.5 mg; not radiolabeled) was dissolved in 0.9% NaCl from which 5 μ L was placed on a glow discharged Formvar/carbon coated copper grid (H100). It was allowed to attach to the surface whereafter the excess fluid was blotted off. The grid was negatively stained with a 1% phosphotungstic acid (w/v) in water solution for 30 sec, blotted off and air dried. Specimens were examined with a Philips CM10 electron microscope. Size measurements were performed on prints from negatives at a final magnification of 119 600 x, by means of a vernier caliper gauge.

UV-VIS spectroscopy

Absorption spectra were recorded using a Perkin Elmer Lambda Bio 20 spectrophotometer, equipped with an in-house made glass cuvette with an optical path length of 0.13 mm. For this experiment 1 mg/mL free ICG and ICG-nanocolloid (not radiolabeled) solutions in demi water were used. To determine the concentration an ICG absorption trend line was made. From a 1 mg/mL ICG solution (1.3 mmol/L) dilutions were made in demi water down to 6.5 μ mol/L. The obtained trend line (absorption measured at 700 nm) had a slope of 9536.5 L/mol/cm.

Fluorescence and bioluminescence imaging

Tumor-bearing mice (n = 5) or control animals (n = 5) were anesthetized and injected i.p. with 150 mg/kg Luciferin. After 10 min a BLI scan was performed. A blank fluorescence scan, performed at standard ICG settings (excitation 710 - 760 nm and emission 810 - 875 nm) was directly followed by an intratumoral (i.t.) injection of 6 μ L ICG solution (7.8×10^{-6} mmol). Before initiating dynamic scans, a single total body scan was taken, after which the torso and injection site were covered. Sequential fluorescence images were recorded during a period of 30 min. After the imaging experiments the animals were sacrificed and LNs were removed. Explanted LNs were imaged using the IVIS camera prior to histological

analysis. Signal intensities were quantified as the sum of detected photons per second within the region of interest (ROI) using the Living Image software package. In each image the fluorescent signal intensity (photons/s/cm²) was measured in the four axillary and brachial LNs with four respective ROIs. The fluorescent signal intensity in the right inguinal LN (LN5) was used as the background measurement. Increase in signal intensity in the SLN compared to the background signal was then calculated [100% x (signal/background)].

Single photon emission computed tomography/computed tomography (SPECT/CT imaging)

Immediately after injection of the imaging agent the mice were placed in a temperature controlled (37°C) animal holder (Equipment Veterinaire MINERVE). Based on a (sagittal) tomographic planning X-ray image, a field of view (FOV) was selected in such a way that the complete body of the mouse was incorporated. SPECT/CT imaging was performed on a NanoSPECT/CT system (Bioscan Inc.) equipped with four collimators, each containing nine 1.4 mm diameter pinholes. After the acquisition, the data were reconstructed using HiSPECT software (Scivis GmbH).

SPECT/CT imaging of ^{99m}Tc-nanocolloid

Tumor-bearing mice (n = 5) or control animals (n = 5) were anesthetized and injected intratumorally (i.t.) with 20 µL (8 - 10 MBq; 7.4 x 10⁻⁸ mmol) ^{99m}Tc-nanocolloid. Sequential total body SPECT scans of the total FOV were performed, taking 30 min in total. Directly after the SPECT imaging sequence, a helical 3D CT acquisition of the same FOV was performed for 12 min. The relative signal intensity of the tracer in the SLN was analyzed using InVivoScope post-processing software (Bioscan, Inc.). The total activity measured in the SLN (MBq) was divided by the total activity measured in the animal (MBq) and multiplied by 100%.

SPECT/CT and fluorescence imaging of the ICG-^{99m}Tc-nanocolloid complex

After injection of tumor-bearing mice (n = 5) with 20 µL (7.4 x 10⁻⁸ mmol) hybrid ICG-^{99m}Tc-nanocolloid, SPECT/CT imaging was performed as described above with the difference that only a single SPECT scan was made (30 min in total), followed by a CT scan (12 min; total scan time: 45 min). Immediately after the SPECT procedure the animal was sacrificed and the skin was dissected. Single fluorescence images were recorded as described before. LNs were removed and checked for fluorescence. Ex vivo BLI measurements were performed by

incubating the LN in Luciferin solution for several minutes before performing a BLI scan. Subsequently, ^{99m}Tc activity (counts per minute; cpm) in all dissected LNs was determined with a gamma counter (Wizard3 1480 automatic gamma counter; Perkin Elmer).

Correlation between fluorescent and radioactive signal intensities

In order to establish a direct correlation between the fluorescent signal and the radioactive signal in the hybrid complex the individual signals were corrected for the maximum signal intensity and converted into percentages according to: $100\% \times (\text{signal} - \text{background}) / (\text{maximum signal} - \text{background})$. Statistical analysis was performed by means of a Student's t-test.

Histology

After imaging, the LNs and tumor were removed and fixed in 4% formaldehyde solution overnight, embedded in paraffin and cut into 4 μm sections. Following deparaffinization and rehydration, sections were stained with hematoxylin and eosin (H&E). The pathological findings were used to cross validate the BLI findings.

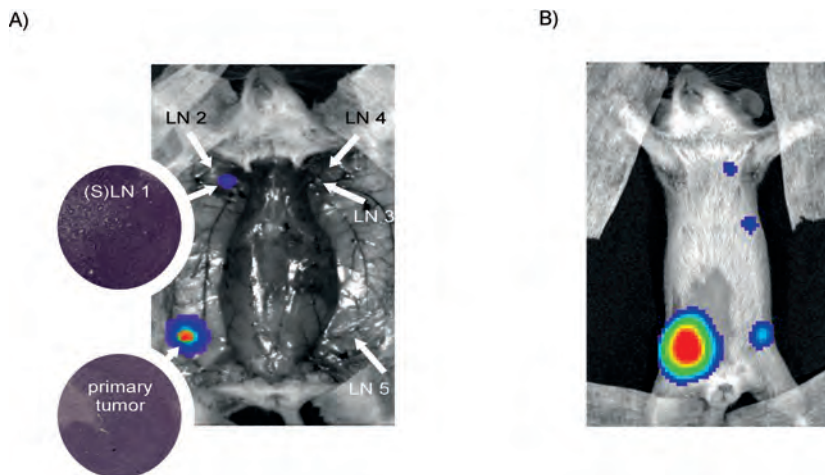


Figure 1. Biology of the mammary mouse tumor model: A) Representation of the lymphatic tumor spread in a mouse in the surgical position. BLI depicts the location of the primary tumor (seeded in the left fourth mammary fat-pad) and early metastatic spread to the left axillary LN (LN1; defined as the SLN). Histological investigation of the primary tumor, (S)LN 1, LN 2, LN 3, LN 4 and LN5 validate the tumor spread. B) Advanced metastatic spread resulted in tumor presence in LN's other than the SLN, namely the right axillary LN (LN 3) and the right inguinal LN (LN5).

Results

In the clinical setting, pathological investigations are required to establish the presence of metastases in the SLN. Here a mammary mouse tumor model was used, which is based on the orthotopic transplantation of luciferase expressing mouse invasive lobular carcinoma (ILC) cells (KEP1-Luc cells) derived from an E-cadherin and p53-deficient mouse mammary tumor.²² The bioluminescence signal emitted by the tumor cells permitted accurate intra- and postoperative detection of the primary tumor in the mammary gland and detection of metastatic tumor cells in the primary tumor-draining LN located in the axillary region (Figure 1A). Due to the high bioluminescent signal emitted from the primary tumor and the attenuating effect of the fur and skin, non-invasive BLI of small clusters of metastatic tumor cells in the axillary region is quite difficult. However, when the primary tumor was covered and the skin dissected, it became possible to identify even small metastasis in the axillary LN (LN 1; Figure 1A). Depending on the progression of the tumor development in individual animals, additional metastases in other LNs could be observed (Figure 1B). In all cases examined (n=3), metastases were first observed in LN 1, defining it as the primary lymph node, the so-called SLN for tumor drainage in this tumor model. Pathological examination of the LNs verified the BLI findings, showing clusters of tumor cells embedded within the lymphatic structures (Figure 1A). The tumor morphology and physiology of this model have previously been described by van Leeuwen et al.²⁴

Formation of the supramolecular hybrid complex

A hybrid complex comprising of the lymphatic imaging agents ICG and ^{99m}Tc-nanocolloid was generated and its efficacy was compared to the individual components.

To create an agent for hybrid imaging of the SLN, ICG was non-covalently bound to ^{99m}Tc-nanocolloid via self-assembly. This resulted in a supramolecular complex that is both fluorescent and radioactive (Scheme 1).²⁵ Equimolar amounts of ^{99m}Tc-nanocolloid and ICG that were used in the free agent studies below were mixed to form the complex. Under these conditions approximately 59% of ICG was bound to ^{99m}Tc-nanocolloid. Nanocolloid is an aggregate of HSA particles, and its particle size was determined using transmission electron microscopy (TEM). During TEM examination an average diameter of 14 nm (n = 100; Figure 2) was found, whereas the reported diameter of single HSA particles is 7 nm.²⁵ In order to determine an average molecular weight for nanocolloid, a spherical structure with a volume of $1.8 \times 10^3 \text{ nm}^3$ was assumed; the volume of HSA was calculated to be 179.59 nm^3 . Based on this volumetric difference, on average a nanocolloid particle consists

out of approximately ten HSA particles and the molecular weight is therefore expected to be 10 times larger than that of HSA (67,000 Mw). Accordingly, an average molar ICG : ^{99m}Tc -nanocolloid ratio in the hybrid complex of 61 : 1 was obtained. It is important to note that the nanocolloid samples were not mono-disperse and contained particles in a size range of 7 - 30 nm, which resulted in different loading rates (Figure 2C).

The degree of functionalization of nanocolloid increased exponentially with the particle size and showed a clear similarity to that reported for the surface modification of other nanoparticles, e.g. polystyrene beads (70 nm; $5 \times 10^3 : 1$ molar ratio)²⁵; a similar sized nanocolloid particle (70 nm) could be functionalized to a ratio of $6 \times 10^3 : 1$. The ICG- ^{99m}Tc -nanocolloid complex formation was further studied using UV-VIS spectroscopy. Figure 2D shows the absorption spectra of free ICG and ICG- ^{99m}Tc -nanocolloid, both at an ICG concentration of 1 mg/mL. Apart from the decrease in intensity of the 700 nm absorption peak (representative for stacking of ICG dye molecules) an extra absorption peak emerged at 780 nm for ICG- ^{99m}Tc -nanocolloid (representative for non-aggregated ICG dye molecules). This result is similar to previously reported data that use this change in the absorption spectrum of ICG to validate that ICG is bound to a protein.²⁷

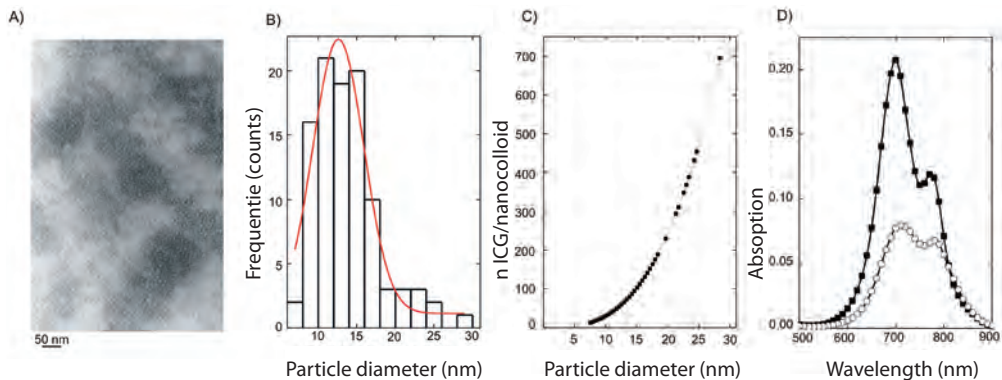


Figure 2. Complex formation between ICG and nanocolloid: A) TEM image of nanocolloid; B) Corresponding size distribution histogram revealing a maximum frequency at 14 nm particle diameter, the red line represents a Gaussian distribution fit. C) The calculated average ICG loading per nanocolloid plotted as function of the particle diameter. D) Absorbance spectra of 'free' ICG in water (solid squares) and nanocolloid bound ICG (open spheres).

Preoperative SPECT/CT imaging of the SLN

Using a dedicated small animal SPECT/CT system it is possible to mimic the standard clinical SPECT/CT assessment of the SLN in mice with metastatic breast tumors. Analogous to the human situation, ^{99m}Tc -nanocolloid (Figure 3) was injected i.t. but, rather than in human patients where SPECT/CT images are taken up to four hrs after injection^{3,4} the nanocolloid dynamics in KEP1-Luc tumor-bearing mice were imaged during the first 30 min after injection. In control animals, where 20 μL of tracer was directly injected into the mammary gland, no tracer migration into the axillary region could be detected during the scan period (Figure 3A). Longer scan times (up to one hr) did not provide additional information. This suggests that lymphatic migration is partly dependent on the tumor presence. In contrast, all tumor-bearing mice showed highly reproducible tracer uptake in the SLN (Figure 3B and C) starting at around 6 min post-injection. This initial uptake was followed by a gradual increase, giving maximum values at 30 min ($2.1 \pm 1.5\%$). BLI measurements in these animals showed only minor degree of metastatic spread within the SLN. The only amount of background signal observed, apart from a significant amount of radioactivity at the injection site, was a small quantity of radioactivity in the liver, which was possibly caused by leakage of the tracer into the bloodstream. This confirmed that this procedure is highly selective for the preoperative visualization of the SLN.

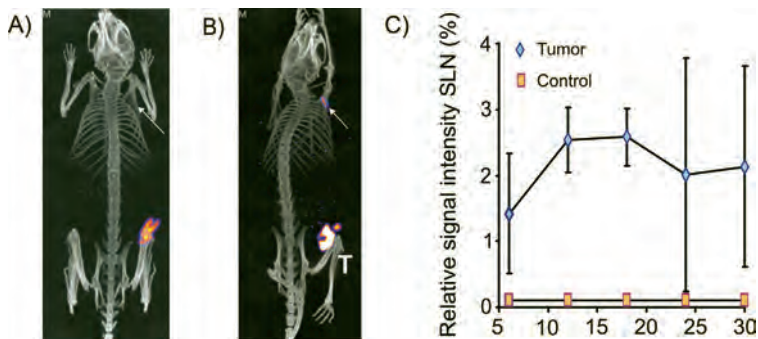


Figure 3. Nanocolloid-based imaging of the SLN. A) SPECT/CT imaging after nanocolloid injection in the mammary gland of a non-tumor-bearing animal, does not show any accumulation of radioactivity in (S)LN 1 indicated with an arrow. B) SPECT/CT image after intra tumoral nanocolloid injection in tumor-bearing animals clearly revealing accumulation in (S)LN 1 (top arrow) and the left inguinal LN (bottom arrow). The location of the primary tumor is indicated with T. C) Relative signal intensities (percentage injected dose) measured in the (S)LN 1 of the different animals from 5 - 30 min after injection.

Intraoperative imaging of the SLN with ICG

After an initial blank scan, mice injected with ICG were examined by dynamic whole-body fluorescence imaging to visualize the uptake kinetics of ICG in the LNs. Figure 4A clearly shows the lymphatic tract running from the tumor to the SLN, which could be seen almost directly after injection. The lymphatic tract also remained fluorescent during the full duration of the experiment. The dynamics of ICG uptake in the SLN of three different animals showed that in all animals the effective imaging time window for ICG could be set at 20 - 30 min post-injection. However, the relation between the injection time and the SLN uptake was not identical for all five mice.

The quantified ICG data showed that in four different tumor-bearing mice (numbers 1, 2, 4, and 5) the fluorescent signal intensity increased by $52\% \pm 17\%$ compared to the background (Figure 4B). In all these mice BLI showed early metastasis in the SLN. A fifth mouse (no. 3) showed much more pronounced metastatic tumor spread in the lymphatic system. This also resulted in much higher ICG flow rates towards the SLN, resulting in a signal-to-background ratio increasing to 190% (Figure 4B).

In the other LNs no clear increase over the background could be detected (Figure 4). Covering the injection site and background signal from the abdomen improved the intraoperative fluorescence detection of the SLN, as it allowed optimization of the scan and threshold settings. Similar to ^{99m}Tc -nanocolloid, non tumor-bearing animals did not show any ICG uptake above background level for any of the four LNs studied after injection in the mammary gland (Figure 4C). In tumor-bearing animals only the (S)LN1 gave a signal increase above background level (Figure 4D). Together, these findings suggest that, in this tumor model, the inter-mouse variation is linked to differences in the extent of metastatic disease between individual animals.

Hybrid imaging with the ICG- ^{99m}Tc -nanocolloid complex

To achieve identical dynamics for the radioactive and fluorescent signal a supramolecular hybrid imaging agent comprising ICG non-covalently bound to ^{99m}Tc -nanocolloid was used.

Using an i.t. injection procedure, the hybrid imaging complex depicted identical features in the SPECT/CT scan as in the experiments where ^{99m}Tc -nanocolloid was injected (compare Figure 3 and 5). Other than described for the 5 x 6 min scan times used to determine the uptake of ^{99m}Tc -nanocolloid the continuous 30 min scan used for the ICG- ^{99m}Tc -nanocolloid complex did allow visualization of the radiotracer throughout the

lymphatic tract. The fluorescence signals emerging from the SLN and draining lymph vessels were also clearly visible by eye. At 45 min post-injection, the correlation between the fluorescent and radioactive signal of the hybrid complex proved to be very high (Figure 5C). The maximum corrected intensity patterns of the radioactive and fluorescence signals were very similarly distributed over the four LNs. This demonstrates that the supramolecular complex has a good stability in the lymphatic system at 45 min post-injection. The normalized signal intensities in the different LNs were very similar for the radioactive and fluorescent component and the SLN specificity was reproducible in the five different animals.

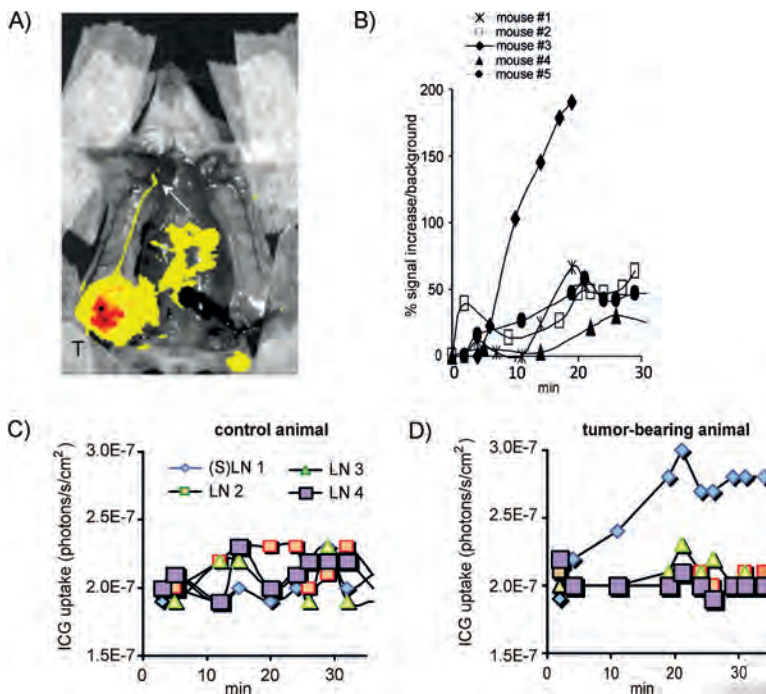


Figure 4. ICG-based NIR fluorescence imaging of the SLN. A) Lymphatic flow in the tumor draining lymphatic vessel can be visualized in the first minutes after injection using NIR fluorescence imaging. The SLN is indicated by the arrow and the primary tumor indicated with T. B) The dynamic increase in the percentage of fluorescent signal intensity/background measured in the (S)LN 1 varies between different animals and is markedly higher in the animal with the most advanced metastatic tumor spread. C) Quantified signal intensities (photon/s/cm²) show no relative increase in any of the four LN's after ICG injection in the mammary gland of a non-tumor-bearing control animal (example n = 1). D) In a tumor-bearing animal, the quantified signal intensities show that only (S)LN 1 gives a signal increase above background after ICG injection into the tumor (example n = 1; mouse #1).

An additional advantage of this hybrid imaging agent is the enhanced signal intensity that is obtained compared to free ICG. Using the same molar amount of dye (7.8×10^{-6} mmol), free ICG achieved a signal intensity of 30 - 200%, whereas the hybrid imaging agent performed significantly better (1252 - 8080%; $p = 0.027$). None of the animals in which the hybrid agent was tested showed signs of advanced metastatic spread outside of the SLN. Excluding the animal with advanced metastatic spread from the free ICG-group, this results in an average 86-fold increase in signal-to-background ratio with the hybrid agent. This dramatic increase in the signal-to-noise ratio is most likely due to the increased nodal retention. The hybrid complex also improved the accuracy of detecting tumor draining lymphatic vessels, as evidenced by the fact that a secondary tumor draining lymphatic vessel could be detected visually during dissection of one of the animals. The hybrid ICG- ^{99m}Tc -nanocolloid complex allowed for highly specific intraoperative visualization of both the tumor draining lymphatic vessel(s) and the SLN (Figure 6).

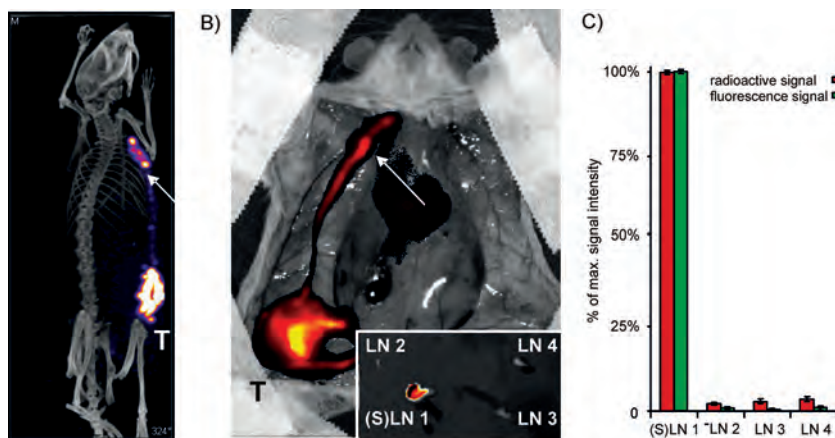


Figure 5. Hybrid imaging of the SLN. A) Preoperative SPECT/CT (directly after i.t. injection) of the SLN using the radioactive component of the complex. B) Intraoperative visualization of the SLN and lymphatic tract using the fluorescent component of the complex (45 min after injection), ex vivo fluorescence of the individual LNs shows the high specificity for the (S)LN 1 (bottom right corner). The SLN is indicated by the white arrow and the primary tumor by T. C) Normalized uptake ratios in the different LNs showing a good correlation between the radioactive and fluorescent signal intensities. This figure has been modified from the scientific annual report of the NKI-AVL Division of Diagnostic Oncology (SAR2009).



Figure 6. Visibility of the tumor draining lymphatics. The ICG-^{99m}Tc-nanocolloid complex enables the visualization of multiple tumor draining lymphatic vessels.

Discussion

Histopathological diagnosis of early lymphatic metastases in the SLN is widely used in the management of breast cancer patients. Using a preclinical breast cancer model that metastasizes via the lymphatic system, the efficacy of SLN detection by ^{99m}Tc-nanocolloid, ICG and a complex formed by the two compounds was quantitatively compared demonstrating the great potential of the hybrid ICG-^{99m}Tc-nanocolloid complex for combined pre- and intraoperative imaging of the (S)LN.

Imaging agent migration in a preclinical breast cancer model for lymphatic metastasis

Preclinical imaging of lymphatic migration with fluorescent dyes in mice is most commonly performed by injecting the agent intravenously or into the footpad.²⁹⁻³³ To increase clinical relevance, here the lymphatic migration was studied using injection procedures similar to those applied in the clinical situation.^{3,4} This was combined with a mouse mammary tumor model that resembles lymphatic metastasis of human breast cancer.

Orthotopic injection of KEP1-Luc mouse mammary tumor cells in syngeneic, immunocompetent mice resulted in the formation of a primary tumor in the mammary gland and subsequent metastatic spread of tumor cells to the SLN (Figure 1A), which

accurately mimics metastatic invasive lobular breast carcinoma (ILC). Furthermore, the low vascular density of the KEP1-Luc tumor core reduced the background signal caused by non-specific uptake of an imaging agent in the vascular system. This is beneficial for the accuracy of the data interpretation. Consequently, the KEP1-Luc mammary tumor model allowed accurate comparative analysis of different imaging agents for the visualization of lymphatic migration.

To determine the influence of the tumor presence on the migratory properties of the imaging agents, a series of control experiments in non-tumor-bearing animals were performed. These findings did not reveal any transport of ICG or ^{99m}Tc -nanocolloid (data not shown). Furthermore, imaging of free ICG in the animals with advanced lymphatic metastatic spread showed an approximate three-fold increase in fluorescence intensity (Figure 4B; mouse 3). Since the injection procedure was identical for all mice, the increased metastatic spread (determined by BLI) seemed to correlate with increase in outflow. This observation was also made by Dadiani et al. and Ruddell et al.^{34,35}

SLN imaging with ^{99m}Tc -nanocolloid or ICG separately

Clinically the preoperative radiopharmaceutical (^{99m}Tc -nanocolloid) guided method has shown a high accuracy for detecting SLNs.⁴ Our preclinical data showed comparable transport of ^{99m}Tc -nanocolloid in preoperative SPECT/CT images. Similar experiments with ^{99m}Tc -nanocolloid in Balb/c nude mice transplanted with MDAMB231 cells showed comparable migration patterns (data not shown). The high signal penetration of the radiolabel (140 keV; ^{99m}Tc) makes ^{99m}Tc -nanocolloid very suitable for non-invasive planning of surgical procedures, but also makes it difficult to accurately determine the origin of the signal due to interfering signals from the injection site,^{3,7,8,36} making it difficult to distinguish lymph nodes with the gamma probe. To explore complementary intraoperative imaging procedures, we investigated the NIR fluorescent dye ICG.

NIR fluorescence imaging with ICG enabled specific detection of the SLN and it permitted intraoperative visualization of the tumor draining lymphatic vessels. However, the relatively low signal-to-background ratio makes the interpretation of the images dependent on the expertise of the operator and on the threshold settings of the scanner. Quantification by way of ROI measurements and subtraction of the background signal intensity was found to be the best way to reduce interpretation bias. Results from several clinical studies indicated that a combination of radiopharmaceutical- and dye-based methods improved SLN detection rates, compared to the individual technique.^{2,8,35,37-39}

Intraoperative use of ICG was found to be complementary to the preoperative situation, which is in accordance with previous report on the lack of surgical planning with ^{99m}Tc -nanocolloid. However, these preclinical results differ from the clinical experience. Compared to mice, a much larger volume of imaging agent is injected in patients, which might result in a local increase in interstitial fluid pressure, thereby providing a driving force for lymphatic transport. This is not expected to occur after a maximal injection of 20 μL in mice.

Migration of the imaging agents via the tumor draining lymphatic vessels to the SLN clearly occurred in tumor-bearing mice with lymph node metastasis. In tumor-bearing animals visualization of the tumor draining lymphatic vessel(s) was considered highly beneficial. However, a comparative dynamic study showed that the lymphatic flow rates of both ICG and ^{99m}Tc -nanocolloid varied and, more importantly, the signal-to-noise ratios obtained with free ICG were vastly inferior to those obtained with ^{99m}Tc -nanocolloid.

Hybrid imaging agents for combined pre- and intraoperative SLN imaging

Ohnishi et al. previously showed the potential of intraoperative SLN imaging using CW800 labeled albumin nanocolloids (not functionalized with technetium).²⁵ However, a limitation of this method is that it does not allow for a preoperative readout similar to ^{99m}Tc -nanocolloid. Furthermore, each albumin nanocolloid was reported to contain only 2.7 CW800 dye molecules. As an alternative, a supramolecular complex consisting out of two clinically approved imaging agents was generated. This approach was based on the work of Moody et al. describing the non-covalent interaction between ICG and albumin.²³ The major differences of our approach are: (i) the presence of a radiolabel, resulting in a hybrid particle, (ii) the application of this interaction on albumin nanocolloids, and (iii) the significantly increased loading rate.

Whereas the injection of separate imaging agents still leaves some doubt regarding the overlap of the findings, the hybrid imaging agent ICG- ^{99m}Tc -nanocolloid allowed accurate intraoperative fluorescence detection of features identical to those detected during preoperative SPECT imaging.

Preoperative SPECT/CT imaging of ICG- ^{99m}Tc -nanocolloid showed comparable lymphatic dynamics, distribution, and specificity as compared to ^{99m}Tc -nanocolloid alone. The hybrid imaging approach provided supplementary information to the existing clinical ^{99m}Tc -nanocolloid procedure, without changing its in vivo behavior.

Conclusion

Quantitative comparative studies between ^{99m}Tc -nanocolloid and ICG revealed the drawbacks of NIR fluorescence imaging with ICG alone. Compared to the high signal specificity found with ^{99m}Tc -nanocolloid a relatively low signal-to-background ratio was obtained with free ICG. ICG- ^{99m}Tc -nanocolloid retained the optimal imaging properties of ^{99m}Tc -nanocolloid, and complemented them with fluorescent properties. Use of this hybrid imaging agent may, therefore, significantly improve the feasibility of intraoperative SLN imaging via fluorescence.

References

- 1 Weissleder R, Pittet MJ. Imaging in the era of molecular oncology. *Nature*. 2008; 452: 580-589
- 2 Argon AM, Duygun U, Acar E, Daglitz G, Yenjay L, Zekioglu O, Kapkac M. The use of periareolar intradermal Tc-^{99m} tin colloid and peritumoral intraparenchymal isosulfan blue dye injection for determination of the sentinel lymph node. *Clin Nucl Med*. 2006; 31: 795-800
- 3 Valdés-Olmos RA, Tanis PJ, Hoefnagel CJ, Nieweg OE, Muller SH, Rutgers EJTh, Kooi MLK, Kroon BBR. Improved sentinel node visualization in breast cancer by optimizing the colloid particle concentration and tracer dosage. *Nucl Med Commun*. 2001; 22: 579-586
- 4 Valdés-Olmos RA, Jansen L, Hoefnagel CA, Nieweg OE, Muller SH, Rutgers EJTh, Kroon BBR. Evaluation of mammary lymphoscintigraphy by a single intratumoral injection for sentinel node identification. *J Nucl Med*. 2000; 41: 1500-1506
- 5 Simmons R, Thevarajah S, Brennan MB, Christos P, Osborne M. Methylene blue dye as an alternative to isosulfan blue dye for sentinel node localization. *Ann Surg Oncol*. 2003; 10: 242-247
- 6 Varghese P, Abdel-Rahman AT, Akberali S, Mostafa A, Gattuso JM, Carpenter R. Methylene blue dye - a safe and effective alternative for sentinel lymph node localization. *Breast J*. 2008; 14: 61-67
- 7 Goyal A, Newcombe RG, Chharbra A, Mansel RE. Factors affecting failed localization and false-negative rates of sentinel node biopsy in breast cancer-results of the ALMANAC validation phase. *Breast Cancer Res Treat*. 2006; 99: 203-208
- 8 Cserni G, Rajtár M, Boross G, Sinkó M, Svébis M, Baltás B. Comparison of vital dye-guided lymphatic mapping and dye plus gamma probe-guided sentinel node biopsy in breast cancer. *World J Surg*. 2002; 26: 592-597
- 9 Hung WK, Chan WK, Ying M, Chong SF, Mak KL, Yip AWC. Randomized clinical trial comparing blue dye with combined dye and isotope for sentinel lymph node biopsy in breast cancer. *Br J Surg*. 2005; 92: 1494-1497
- 10 Frangioni JV. In vivo near-infrared fluorescence imaging. *Curr Opin Chem Biol*. 2003; 7: 626-634
- 11 Ito N, Fukuta M, Tokushima T, Nakai K, Ohgi S. Sentinel node navigation surgery using indocyanine green in patients with lung cancer. *Surg. Today*. 2004; 34: 581-585

- 12 Ichikura T, Chochi K, Sugawasa H, Yaguchi Y, Sakamoto N, Takahata R, Kosuda S, Mochizuki H. Individualized surgery for early gastric cancer guided by sentinel node biopsy. *Surgery*. 2006; 139: 501-507
- 13 Nimura H, Narimiya N, Mitsumori N, Yamazaki Y, Yanaga K, Urashima M. Infrared ray electronic endoscopy combined with indocyanine green injection for detection of sentinel nodes of patients with gastric cancer. *Br J Surg*. 2004; 91: 575-579
- 14 Kusano M, Tajima Y, Yamazaki K, Kato M, Watanabe M, Miwa M. Sentinel node mapping guided by indocyanine green fluorescence imaging; a new method for sentinel node navigation surgery in gastrointestinal cancer. *Dig Surg*. 2008; 25: 103-108
- 15 Tagaya N, Yamazaki R, Nakagawa A, Abe A, Hamada K, Kubota K, Oyama T. Intraoperative identification of sentinel lymph nodes by near-infrared fluorescence imaging in patients with breast cancer. *Am J Surg*. 2008; 195: 850-853
- 16 Kitai T, Inomoto T, Miwa M, Shikayama S. Fluorescence navigation with indocyanine green for detecting sentinel lymph nodes in breast cancer. *Breast Cancer*. 2005; 12: 211-214
- 17 Ogasawara Y, Ikeda H, Takahashi M, Kawasaki K, Doihara H. Evaluation of breast lymphatic pathways with indocyanine green fluorescence in patients with breast cancer. *World J Surg*. 2008; 32: 1924-1929
- 18 Sevick-Muraca EM, Sharma R, Rasmussen JC, Marshall MV, Wendt JA, Pham HQ, Bonefas E, Houston JP, Sampath L, Adams KE, Blanchard DK, Fisher RE, Chiang SB, Elledge R, Mawad ME. Imaging of lymph flow in breast cancer patients after microdose administration of a near-infrared fluorophore: feasibility study. *Radiology*. 2008; 246: 734-741
- 19 Valdés-Olmos RA, Vidal-Sicart S, Nieweg OE. SPECT/CT and real time intraoperative imaging: new tools for sentinel node localization and radioguided surgery? *Eur J Med Mol Imaging*. 2009; 36: 1-5
- 20 Culver J, Akers W, Achilefus S. Multimodality molecular imaging with combined optical and SPECT/PET modalities. *J Nuc. Med*. 2008; 49: 169-172
- 21 Link EM, Blower PJ, Costa DC, Lane DM, Lui D, Brown RSD, Ell PJ, Spittle MF. Early detection of melanoma metastases with radioionidated methylene blue. *Eur J Nucl Med*. 1998; 25: 1322-1329

- 22 Derksen PW, Liu X, Saridin F, van der Gulden H, Zevenhoven J, Evers B, van Beijnum JR, Griffioen AW, Vink J, Krimpenfort P, Peterse JL, Cardiff RD, Berns A, Jonkers J. Somatic inactivation of E-cadherin and p53 in mice leads to metastatic lobular mammary carcinoma through induction of aneuploidy resistance and angiogenesis. *Cancer Cell*. 2006; 10: 437-449
- 23 Moody ED, Viskari PJ, Colyer CL. Non-covalent labeling of human serum albumin with indocyanine green: a study by capillary electrophoresis with diode laser-induced fluorescence detection. *J Chromatogr B*. 1999; 729: 55-64
- 24 van Leeuwen FWB, Buckle T, Pool B, Sinaasappel M, Jonkers J, Gilhuijs K. Potential value of color-coded dynamic breast-specific gamma-imaging; comparing ^{99m}Tc (V)-DMSA, ^{99m}Tc -MIBI, and ^{99m}Tc -HDP in a mouse mammary tumor model. *Appl. Rad. Isotopes* 2010; 12: 2117-2124.
- 25 Ohnishi S, Lomnes SJ, Laurence RG, Gobashian A, Mariani G, Frangioni FV. Organic alternatives to quantum dots for intraoperative near-infrared fluorescent sentinel lymph node mapping. *Mol Imaging*. 2005; 4: 172-181
- 26 Kragh-Hansen U, Chuang VTG, Otagiri M. Practical aspects of the ligand binding and enzymatic properties of human serum albumin. *Biol Pharm Bull*. 2002; 25: 695-704
- 27 Haritoglou C, Freyer W, Priglinger SG, Kampik A. Light absorbing properties of indocyanine green (ICG) in solution and after adsorption to the retinal surface: an ex vivo approach. *Graefes Arch Clin Exp Ophthalmol*. 2006; 244: 1196-1202
- 28 Bergqvist L, Strand S, Persson BR. Particle size and biokinetics of interstitial lymphoscintigraphic agents. *Semin Nucl Med*. 1983; 13: 9-19
- 29 Wunderbaldinger P, Turetschek K, Bremer C. Near-infrared fluorescence imaging of lymph nodes using a new enzyme sensing activatable macromolecular optical probe. *Eur Radiol*. 2003; 13: 2006-2211
- 30 Faries MB, Bedrosian I, Reynolds C, Nguyen HQ, Alavi A, Czerniecki BJ. Active macromolecule uptake by lymph node antigen-presenting cells: a novel mechanism in determining sentinel lymph node status. *Ann Surg Oncol*. 2000; 7: 98-105
- 31 Mahmood U, Weissleder R. Near-infrared optical imaging of proteases in cancer. *Mol Cancer Ther*. 2003; 2: 489-496
- 32 Harrell MI, Iritani BM, Ruddell A. Lymph node mapping in mouse. *J Immunol Methods*. 2008; 332: 170-174

- 33 Ballou B, Ernst L A, Andreko S, Harper T, Fitzpatrick JAJ, Waggoner AS, Bruchez MP. Sentinel lymph node imaging using quantum dots in mouse tumor models. *Bioconjug Chem.* 2007; 18: 389-396
- 34 Dadiani M, Kalchenko V, Yosepovich A, Margalit R, Hassid Y, Degani H, Seger D. Real-time imaging of lymphogenic metastasis in orthotopic human breast cancer. *Cancer Res.* 2006; 66: 8037-8041
- 35 Ruddell A, Harrell MI, Minoshima S, Maravilla KR, Iritani BM, White SW, Partridge SC. Dynamic contrast-enhanced magnetic resonance imaging of tumor-induced lymph flow. *Neoplasia.* 2008; 10: 706-713
- 36 Motamura K, Inaji H, Komoike Y, Hasegawa Y, Kasugai T, Noguchi T, Koyama H. Combination technique is superior to dye alone in identification of the sentinel node in breast cancer patients. *J Surg Oncol.* 2001; 76: 95-99
- 37 Takei H, Suemasu K, Kurosumi M, Horii Y, Ninomiya J, Kamimura M, Naganuma R, Uchida K, Igarashi K, Inoue K, Tabei T. Added value of the presence of blue nodes or hot nodes in sentinel lymph node biopsy of breast cancer. *Breast Cancer.* 2006; 13: 179-185
- 38 Sato K, Tamaki K, Shigekawa T, Tsuda H, Kosuda S, Kusano S, Hiraide H, Mochizuki H. Clinically useful detection criteria for sentinel nodes in patients with breast cancer using a radioisotope technique. *Japan. J Clin Oncol.* 2002; 32: 403-406
- 39 Yen R-F, Kuo W H, Lien H-C, Chen T H-H, Jan I-S, Wu Y-W, Wang M-Y, Chang K-J, Huang C-S. Radio-guided sentinel lymph node biopsy using periareolar injection technique for patients with early breast cancer. *J Formos Med Assoc.* 2007; 106: 44-50

Interventional

Tracer-cocktail injections for combined
molecular imaging,
pre- and intraoperative hybrid imaging
a hybrid approach
of lymph nodes in a spontaneous mouse

prostate tumor model

Chapter 4

Adapted from:

van Leeuwen AC#, Buckle T#, Bendle G, Vermeeren L, Valdés-Olmos RA, van der Poel HG, van Leeuwen FWB.

J Biomed Opt. 2011; 16(1): 016004

authors contributed equally

Abstract

In this Chapter evaluation of a more clinically translatable formulation of the hybrid tracer ICG-^{99m}Tc-nanocolloid is discussed. In order to achieve surgical guidance towards prostate draining sentinel lymph nodes (SLNs), TRAMP mice with spontaneous prostate tumors were injected intratumorally with: 1) a cocktail of patent blue (Pb) and indocyanine green (ICG); 2) a cocktail of albumin radiocolloids (^{99m}Tc-nanocolloid), Pb, and ICG; or 3) a cocktail of radiolabeled albumin (^{99m}Tc-HSA), Pb, and ICG. The lymphatic distribution of these imaging agents was studied at various time points after injection. At 60 min post injection the SLN detection rate using Pb was only 7%, whereas the detection rate using ICG was significantly higher (53%). Moreover, a cocktail of ICG and ^{99m}Tc-nanocolloid, which yields the ICG-^{99m}Tc-nanocolloid complex, improved the fluorescent detection rate to 86%, equalling that of the clinically applied ^{99m}Tc-nanocolloid. Fluorescence detection of the SLNs using a cocktail containing ^{99m}Tc-HSA gave similar results as free ICG (58%; 60 min). In conclusion, a ^{99m}Tc-nanocolloid, Pb, and ICG cocktail enriched the standard ^{99m}Tc-nanocolloid approach by adding fluorescent detection of the SLNs. Furthermore, this approach improved the fluorescent based guidance and enabled both accurate surgical planning and intraoperative detection, based on a single injection. Clinical pilot data revealed this approach is also potentially valuable in patients.

Introduction

The presence of metastasis in the tumor draining sentinel lymph nodes (SLNs) in the pelvic region is considered a strong predictor of treatment failure in patients with prostate cancer.¹ Postoperative histopathological examination of tissue samples obtained during surgery is the 'golden standard' to assess the metastatic spread. To obtain these samples, extensive dissection of lymphatic tissue is required. In up to 51% of procedures, this can lead to post-operative complications such as lymphoceles, injuries to the obturator nerve and/or the ureter, and lymphedema of the lower extremity.^{2,3} Surgical pelvic lymphadenectomy procedures such as extended pelvic lymphadenectomy^{4,5,6} can be improved by relying on better surgical guidance towards the tumor draining lymphatic tract and SLN(s). Ideally, an intraoperative imaging approach will enable the surgeon to visualize and excise the SLNs accurately, which may shorten overall procedure time and decrease complication levels.

Innovations in SLN mapping mainly find their origin in the evaluation of metastatic spread in melanoma and breast cancer.^{7,8} At present, SLN mapping in e.g. the breast is generally performed with a combination of preoperative ^{99m}Tc-labelled colloid injection and intraoperative injection of blue dyes (e.g. patent blue; Pb) for optical guidance.⁹ For breast cancer this combined approach considerably increased the detection rate compared to the dye based (from 79.6% to 93.5%) and for the colloid based method (from ≈ 95% to 97.7 - 99.2%).^{10,11} However, these values may be lower for more complex resections such a laparoscopic SLN biopsy.

Lymphoscintigraphy at 15 minutes and two hrs after injection of ^{99m}Tc-labelled colloidal particles enables visualization of the SLNs.¹² Integrated single photon emission tomography combined with computed tomography (SPECT/CT) is also used to provide superior 3D visualization and to provide anatomical data for surgical planning with a detection rate of 98%.¹³ We were not able to find any literature examples of blue dye based detection of the SLN in the prostate.

The intraoperative translation of the radiocolloid procedure requires the use of a gamma probe or camera to monitor the transit of a ^{99m}Tc-labelled colloid from the injection site into the SLN, which can then be dissected and histologically examined.^{14,15} Unfortunately, the tracer deposits in the prostate may cause a high background signal when the highly sensitive gamma probe is placed on or near the pelvic lymph nodes (LNs).

The use of near-infrared (NIR) fluorescence imaging is rapidly advancing in medical optical imaging.¹⁶ Even when much lower concentrations are used, excitation and emission

wavelengths in the 800 nm range provide higher tissue penetration than the reflected blue light of a visible dye (400 nm).¹⁷ Recently, several promising new trials using the NIR fluorescent dye indocyanine green (ICG) have been published for SLN biopsy in breast- and gastrointestinal cancer.^{18,19} A limiting factor in these studies is the effective time window, which appears to be similar to that of the visible blue dyes.¹⁸ Furthermore, this approach requires an additional ICG injection next to the lymphoscintigraphic approach. In a feasibility study, the US Food and Drug Administration (FDA) suggested that a 'cocktail' injection of fluorescent and radioactive agents would be preferable over multiple single injections.¹⁹ However, this study revealed that a cocktail injection of ICG with ^{99m}Tc-labeled sulfur radiocolloid reduced the fluorescence intensity by a factor ten and yielded poor imaging results.²¹ Although ^{99m}Tc-labeled sulfur colloid is the most widely used radiotracer for lymphatic mapping in the United States, ^{99m}Tc-colloidal albumin (^{99m}Tc-nanocolloid) is more frequently used for identical procedures in European countries.^{20,21} The SLN specificity of hybrid ICG-^{99m}Tc-nanocolloid complexes was shown to be similar to that of conventional lymphoscintigraphy in a preclinical setting (see Chapter 3).²²

Animal models are useful tools for investigation of the pathogenesis of cancers and the development of new imaging procedures.^{23,24} One of the best-characterized and widely used mouse models of prostate cancer is the transgenic adenocarcinoma of the mouse prostate (TRAMP) model. This tumor model provides an ideal preclinical starting point to study combined pre- and intraoperative imaging procedures in prostate cancer.

The goal of this study was to improve the accuracy of the intraoperative detection of SLNs in prostate cancer. Using the TRAMP model, a cocktail of ^{99m}Tc-nanocolloid, Pb, and ICG was evaluated and compared to a cocktail of ^{99m}Tc labelled albumin (human serum albumin; HSA), Pb and ICG. To underline the potential of combined pre- and intraoperative imaging, the first results of an ongoing clinical pilot study wherein the ICG-^{99m}Tc-nanocolloid cocktail was used in 6 patients with prostate carcinoma are presented.

Material and Methods

Imaging agents

Pb solutions were obtained as clinical grade dye solution (Guerbet). ICG (preclinical: Sigma Aldrich; clinical: ICG-Pulsion, Pulsion Medical Systems AG) solution was prepared by dissolving 1.0 mg in 1.0 mL 1% Pb solution. For dye injections, ten mL of this solution [Pb (1.76×10^{-4} mmol); ICG (1.29×10^{-5} mmol)] was diluted in 30 mL of a 0.9% sodium chloride solution (B Braun).

^{99m}Tc -labeled human serum albumin (^{99m}Tc -HSA; Vasculosis, 7 nm;²⁵ IBA) and ^{99m}Tc -labeled human serum albumin colloids (^{99m}Tc -nanocolloid; Nanocoll, median particle size 14nm; 22 GE Healthcare) were of clinical grade and produced following standard preparation protocols (pH 6 - 7). ^{99m}Tc -HSA was prepared by adding 2 mL pertechnetate solution (2500 MBq) to a clinical grade kit, followed by 30 min incubation at room temperature. ^{99m}Tc -nanocolloid was prepared by adding 2 mL pertechnetate (1500 MBq) to a vial, followed by 30 min incubation at room temperature. The efficacy of both labeling procedures was determined via thin layer chromatography using MeOH/water (85 : 15).

Cocktail injections were prepared by diluting 10 mL of the Pb/ICG solution in 30 mL of the respective tracer solution (^{99m}Tc -HSA: 1.14×10^{-6} mmol albumin; 12 MBq, ^{99m}Tc -nanocolloid: 1.11×10^{-7} mmol albumin; 8 MBq). For the clinical procedures cocktails were prepared under GMP and without the presence of Pb.

To confirm the insitu formation of self-assembled hybrid complexes,²⁶ protein separations were performed on the albumin particle containing cocktails in micron centrifugal filters (Millipore) with a molecular weight cut of at 30,000 Da. Solutions were centrifuged for 8 min at 7×10^3 rpm after which the fluorescent content of the residue and the filtrate was determined.

Mice

Male TRAMP mice expressing the SV40 T antigen (TRAMP+) spontaneously develop autochthonous prostate tumors following the onset of puberty.²⁷ Lymphatic metastases occur at 24 - 28 weeks of age and by the age of 28 weeks, 100% harbor metastatic prostate cancer in the lymph nodes or lungs.²⁸ Previous studies described the caudal and lumbar lymph nodes as the preferential sites for metastasis in orthotopic and genetically engineered mouse models for prostate cancer.^{29,30} The lymphatic pathway from the prostate drains via the lumbar LNs to the renal LNs, all these LNs were investigated for their imaging agent content and no discrimination was made between SLNs and possible higher echelon LNs (Figure 1). In this study, TRAMP+ mice between 25 and 30 weeks of age were used. Age matched non transgenic (TRAMP-) mice served as control. All animal experiments were performed in accordance with Dutch animal welfare regulations and approved by the local animal ethics committee of the Netherlands Cancer Institute - Antoni van Leeuwenhoek Hospital.

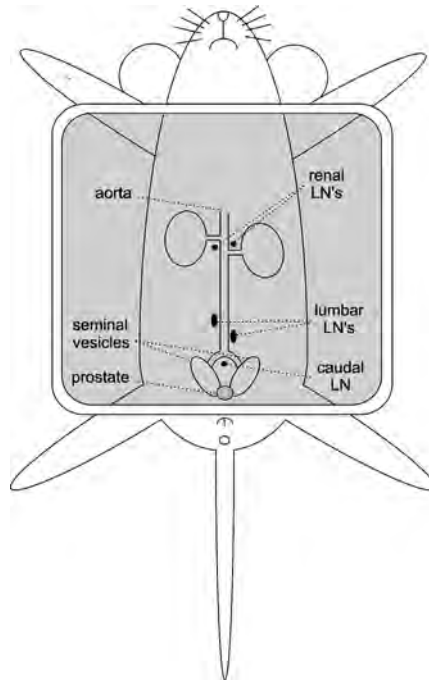


Figure 1. Schematic representation of a mouse with an exposed abdominal cavity (in gray). Herein the five (caudal, lumbar and renal) LNs are depicted that potentially function as the SLNs for the prostate tumors formed in the TRAMP mice.

Injection procedures

Animals were anaesthetized with a mixture of hypnorm (Vetapharma), dormicum (Roche) and water (suitable for injection; 1:1:2; 5 μ l/gr i.p.). An incision of approximately 1 cm was made in the skin of the lower abdomen of the mice. Subsequently mice were injected intratumorally (i.t.; TRAMP+) or into the prostate (TRAMP-) with the respective imaging agents using a 29G needle. The injected cocktail solutions were abbreviated as: ICG (Pb/ICG), NC (^{99m}Tc -nanocolloid/Pb/ICG), and HSA (^{99m}Tc -HSA/Pb/ICG). Non-tumor-bearing mice were used as control; abbreviated as NC control (Table1). Abbreviations are followed by the time after injection when the SLNs were dissected (e.g. 15 min) in subscript.

After injection, the injection site was massaged for 5 min to stimulate the lymphatic migration. With exception of the animals that were sacrificed 15 min post injection, the incision was closed directly after the injection and massage.

Table 1. Different study groups and time points used for tumor draining SLN imaging experiments.

Name group	Number of animals	Imaging agents used	Imaging time point (min after injection)	Detection method
ICG15	n = 6	Pb/ICG	15	Visual/ NIR fluorescence
ICG60	n = 6	Pb/ICG	60	Visual/NIR fluorescence
NC60	n = 6	^{99m} Tc-nanocolloid/Pb/ICG	60	SPECT/ Visual/ NIR fluorescence
NC240	n = 6	^{99m} Tc-nanocolloid/Pb/ICG	240	SPECT/ Visual/NIR fluorescence
HSA60	n = 6	^{99m} Tc-HSA/Pb/ICG	60	SPECT/ Visual/ NIR fluorescence
NC60 control	n = 6	^{99m} Tc-nanocolloid/Pb/ICG	60	SPECT/ Visual/ NIR fluorescence

Imaging procedures

Migration of the imaging agents to the SLNs was assessed at different time points after injection (Table 1). These specific time points were chosen as they enclose a wide time window in which the pro's and cons of the individual agents can be reviewed. The shortest time interval was set at 15 min post injection as this time interval is clinically used for dye-based methods. A 60 min time-point was used as previous experiments have shown that this time point is optimal for the evaluation of the migration of nanocolloid to the SLNs of mice.²⁴ The 4 hrs (240 min) time point was added to show the value of approach at later time points.

Fluorescent and visual detection of the ICG and Pb was conducted alone or directly following the SPECT/CT scan. Hereafter, SLNs were dissected using a surgical microscope (Universal S3; Zeiss). At 15 and 60 min post injection, the level of blue staining in the SLNs was visually evaluated. SLNs were staged as not blue (0), light blue (1) or blue (2) before fluorescence imaging of the ICG component was conducted (Table 2). The distribution of the fluorescence and radioactivity over the SLNs was studied postoperatively (Table 3).

Fluorescence imaging

In vivo fluorescence imaging was conducted after the mice were sacrificed, using a preclinical fluorescence scanner (IVIS 200; Xenogen Corp.) using Living Imaging Acquisition and Analysis software (Xenogen Corp.). Images were acquired with standard ICG settings (excitation 710 - 760 nm and emission 810 - 875 nm). A whole body fluorescence scan was performed before dissection of the five involved LNs (Figure 1). To decrease background levels and increase the visibility of the SLNs, the prostate and intestines were removed prior to imaging. After dissection, the SLNs were scanned and their fluorescent content was quantified (photons/s/cm²) and corrected for the background signal in that measurement. As the background signal showed some small deviations, subtraction of the background sometimes lead to negative values. As only positive fluorescent signals can be used in the experimental set-up the negative fluorescent signals were set at the minimum of zero. Trendline based linear regression correlations (Excel) were used to establish the correlation between the fluorescence intensities and the radioactive count rate findings.

SPECT/CT imaging

After the injection procedure, the mice were placed in a temperature controlled (37°C) animal holder (Equipment Veterinaire MINERVE) before performing a SPECT/CT scan on a preclinical SPECT/CT system (nanoSPECT/CT; Bioscan Inc.) A region of interest incorporating the whole body was selected, based on a (sagital) tomographic planning X-ray image. One sequential total body SPECT scan of the same field of view was initialized taking 30 min in total. Directly after the SPECT imaging sequence, a helical 3D CT acquisition of the animal was performed during 12 min. After acquisition, the CT data was reconstructed with HiSPECT software (Scivis GmbH). The SPECT and CT data sets were automatically co-registered. The images were analyzed using InVivoScope post processing software (Bioscan Inc.).

Ex vivo radioactivity counting

After dissection, the amount of ^{99m}Tc in the individual SLNs was determined (gamma counts per minute; cpm) using a Wizard 3 1480 automatic gamma counter (Perkin Elmer). Specimens were counted for 120 seconds using a 126 - 159 keV energy window, automatically including background signal measurements. For normalization, the individual radioactive count rates were corrected for the background and radioactive decay. Correlations with the fluorescent intensity were made using the decay corrected signal intensities.

Clinical study

During a clinical pilot study, the nanocolloid-ICG cocktail was evaluated in six patients with prostate carcinoma. The criteria for inclusion were the presence of one or more of the following characteristics: clinical stage greater than T2b, or Gleason sum score greater than six. The cocktail solution (240 MBq; 0.4 mL) was injected peri- and intratumorally; 0.1 mL was injected in each quadrant of the prostate. Administration was guided by transrectal ultrasonography, and each injection was followed by flushing with approximately 0.7 mL of saline. During surgical pelvic lymphadenectomy, both the prostate and SLNs were excised at about 60 min post injection. In all cases the nodal areas of the interna and obturator LNs were included. Intraoperative detection of the SLNs was conducted using a gamma probe. Ex vivo examination of the radioactive signal in the excised SLNs was detected using a portable gamma camera equipped with a pinhole collimator (Sentinella, Oncovision). Distribution of the radioactivity was evaluated by placing the head of the gamma camera at a distance of 5 cm above each excised specimen (acquisition time 1 min). Furthermore, an overview of the radioactivity within all excised nodes was made by placing the detector of the camera 10 cm above all excised nodes. Here after fluorescence imaging was conducted on the excised specimens (See Fluorescence imaging section). Distribution of radioactivity was correlated to the distribution of the fluorescence; presence of radioactivity in each node was compared to the presence of fluorescence in the node. Patient studies were performed conform protocol after approval by the local Medical Ethics Committee comity of the Netherlands Cancer Institute - Antoni van Leeuwenhoek Hospital and were carried out after obtaining informed consent.

Results

Lymphatic migration studies

The lymphatic migration towards the SLNs was studied with visible, fluorescent and radioactive imaging agents. Similar to the clinical situation,³¹ lymphatic migration of the imaging agents from the injection site greatly improved by massaging the injection site, whereas almost no drainage was observed when no massage was applied (data not shown). This was found to be especially important for the 15 and 60 min groups. These animals remained anesthetized until imaging, thus limiting the spontaneous massage by movement. In the 240 min groups, the animals awoke from their initial anesthetics, and were able to walk around freely in the cage (hereby also spontaneously massaging the prostate).

As lymphatic migration depends on the site of injection and may vary between individual animals, the measured signal intensities (Table 2, 3 and 4) showed some fluctuations within the different groups. The radioactive count rates obtained with ^{99m}Tc-nanocolloid tended to vary (Table 3 and 4), which could, in part, be attributed to a variation in particle size as a single ^{99m}Tc-nanocolloid preparation consists out of a wide range of particle sizes with a reported median of 50 nm. However, in different ^{99m}Tc-nanocolloid batches the distribution of particle sizes can vary in theory.

Distribution Pb/ICG

To create an imaging approach that would allow both visible and NIR fluorescence detection, a cocktail of Pb and ICG was prepared (defined as ICG - cocktail; Table 1). The distribution of the visual component, Pb, was first assessed. When massage of the injection site was performed after injection, SLNs stained blue and the lymphatic tract became visible. At 15 and 60 min post injection, the visible blue LNs were less blue than observed directly after massage (the first 5 min post injection), indicating a quick wash-out of Pb (Figure 2A and B; Table 2). The visible blue dye could best be observed in SLNs in the ICG₁₅ group, wherein Pb uptake was seen in at least two SLNs in five of the six animals. However, only 42% of all the excised SLNs were stained blue. After 60 min the detection efficacy was found to be reduced to 7% (Figure 2E).

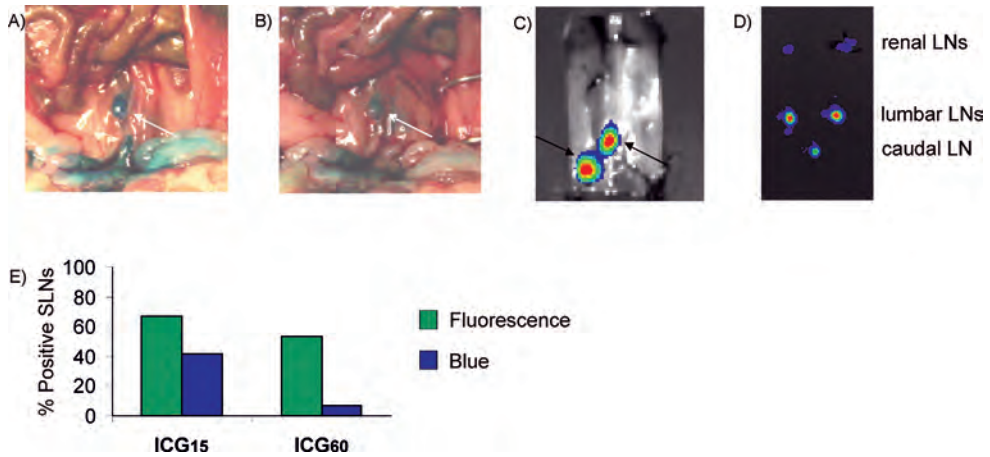


Figure 2. Imaging of the SLN with visible Pb and NIR fluorescent ICG: A) Intraoperative detection of Pb in the right lumbar LN, directly after massage of the injection site and B) after 15 min, showing the washout of the dye during this time period. C) Intraoperative NIR fluorescence imaging of the lumbar LNs with free ICG, which was visible up to 60 min after injection. D) The fluorescent content could be detected and quantified in excised SLNs. E) Percentages of imaging agent containing (positive) SLNs in the ICG₁₅ and ICG₆₀ groups. In the graphs the percentages of the fluorescent component in the cocktail are depicted in green and the percentages for the visible component in blue; percentages were calculated using Table 2.

Within the ICG groups all blue SLNs contained fluorescence. Overall the fluorescence intensities in the ICG₆₀ group were lower compared to those in the ICG₁₅ group (Table 2). The ability to specifically detect the SLNs using the fluorescence signal of ICG also decreased over time. After 15 min 67% of the SLNs could be detected, whereas after 60 min this was only 53%.

Even though the injected concentration of ICG was 14 times lower than that of Pb, fluorescence detection of ICG enabled a much longer functional imaging time period post injection. Multiple LNs contained fluorescence with varying intensities. In ten out of twelve animals the maximal fluorescence intensity was measured in one or both of the lumbar SLNs (Table 2).

Table 2. Fluorescence signal intensity and visibility (blue) after injection of ICG cocktails in tumor-bearing animals. Non-evaluated LNs are marked by x.

	Fluorescence intensity (photons/s/cm ² /sr * 10 ⁶ ; background corrected))						Visibility blue dye (0: no colour, 1: light blue, 2: blue)					
	caudal	lumbar R	lumbar L	renal R	renal L	renal L	caudal	lumbar R	lumbar L	renal R	renal L	
ICG ₁₅ mouse #1	0	6	1	0	0	0	0	1	1	0	0	
ICG ₁₅ mouse #2	5	3	4	5	0	0	0	1	1	0	0	
ICG ₁₅ mouse #3	0	57	65	0	0	0	0	0	0	0	0	
ICG ₁₅ mouse #4	x	1598	278	0	4	4	x	2	1	0	0	
ICG ₁₅ mouse #5	37	453	859	173	9	9	2	2	2	1	0	
ICG ₁₅ mouse #6	282	772	877	25	0	0	1	1	1	0	0	
ICG ₆₀ mouse #1	1	59	66	12	0	0	0	0	0	0	0	
ICG ₆₀ mouse #2	2	7	5	4	3	3	0	0	0	0	0	
ICG ₆₀ mouse #3	24	461	254	x	48	48	1	1	1	x	1	
ICG ₆₀ mouse #4	0	31	0	3	0	0	0	0	0	0	0	
ICG ₆₀ mouse #5	0	40	0	0	4	4	0	0	0	0	0	
ICG ₆₀ mouse #6	0	55	1	1	1	1	0	0	0	0	0	

Table 3. Fluorescence and radioactive signal intensity. Signals were measured ex vivo. Non-evaluated SLNs were marked by x. In addition, the correlation between the radioactive and fluorescent signal intensities after injection of NC and HSA cocktails in TRAMP+ animals is depicted in the last column.

	Fluorescence intensity (photons/s/cm ² /sr x 10 ⁶ ; background corrected))						Radioactive intensity (10 ³ cpm; decay corrected)						Correlation fluorescence and radioactive intensities (R ²)								
	caudal		lumbar R		lumbar L		renal R		renal L		caudal			lumbar R		lumbar L		renal R		renal L	
NC ₆₀ mouse #1	54	18	209	4	0	481	142	4468	10	16	0.98										
NC ₆₀ mouse #2	49	0	2	2	0	3	1	1	0	0	0.92										
NC ₆₀ mouse #3	4	43	2	3	6	83	2927	46	57	267	1										
NC ₆₀ mouse #4	413	163	354	49	20	194	55	112	7	4	0.94										
NC ₆₀ mouse #5	0	40	103	0	0	1	226	620	2	0	1										
NC ₆₀ mouse #6	94	13	105	10	24	1200	469	2816	80	813	0.76										
NC ₂₄₀ mouse #1	7	19	12	15	5	3	243	54	55	68	0.52										
NC ₂₄₀ mouse #2	30	237	17	22	1	54	906	34	95	0	1										
NC ₂₄₀ mouse #3	449	105	61	0	5	1235	454	1317	0	167	0.41										
NC ₂₄₀ mouse #4	2	15	50	0	9	7	1	146	1	8	0.90										
NC ₂₄₀ mouse #5	5	15	20	0	4	3	5	71	1	16	0.54										
NC ₂₄₀ mouse #6	0	5	7	0	1	0	0	2	0	0	0.79										
HSA ₆₀ mouse #1	5	5	10	2	1	1	0	1	0	2	0.14										
HSA ₆₀ mouse #2	0	0	0	0	0	3	4	2	0	1	0.00										
HSA ₆₀ mouse #3	0	0	2	0	0	1	2	3	0	0	0.42										
HSA ₆₀ mouse #4	3	33	170	0	6	4	24	107	0	2	1										
HSA ₆₀ mouse #5	0	102	0	3	15	0	50	9	1	3	0.94										
HSA ₆₀ mouse #6	13	480	480	x	140	4	7	6	x	1	0.53										

Table 4. Fluorescence and radioactive signal intensity and their correlation after injection of a NC cocktail in TRAMP- control animals.

	Fluorescence intensity (photons/s/cm ² /sr x 10 ⁶ ; background corrected))						Radioactive intensity (10 ³ cpm; decay corrected)						Correlation fluorescence and radioactive intensities (R ²)		
	caudal		lumbar L		renal R		caudal		lumbar R		lumbar L			renal R	
NC ₆₀ control #1	5	4	20	0	0	0	8	215	396	0	0	0	0	0	0.80
NC ₆₀ control #2	0	8	45	38	2	23	2	2	589	0	2	0	2	0.45	
NC ₆₀ control #3	0	6	0	0	2	0	0	25	1	1	51	0	1	0.33	
NC ₆₀ control #4	6	9	108	6	0	4	109	789	5	1	0.99	0	1	0.99	
NC ₆₀ control #5	82	172	54	0	10	9	186	8	0	17	0.78	0	17	0.78	
NC ₆₀ control #6	15	17	0	0	0	2	39	437	0	1	0.82	0	1	0.82	

Combined SPECT and fluorescence imaging

Radiotracer experiments (^{99m}Tc -nanocolloid or ^{99m}Tc -HSA) were performed using cocktail solutions that also contained Pb and ICG. Separation of the albumin from the cocktail with a size exclusion filter revealed that while no ICG had passed the filter, Pb was present in the filtrate. In the presence of a 14-fold excess of Pb, the ICG had formed a complex with the albumin via self-assembly. Since this binding could not have been established in a covalent manner, complex formation was based on non-covalent interactions caused by the charges and lipophilic groups on ICG and albumin.³² This binding is unique to ICG as we could not observe any binding of Pb to the albumin colloids. If a small amount of binding between Pb and the albumin did occur, it was not enough to aid in visual detection of the SLNs. Hence in the cocktail injections, a hybrid complex is present that comprises of a radioactive (^{99m}Tc -HSA or ^{99m}Tc -nanocolloid) and a fluorescent (ICG) component. Based on the results obtained with the ICG-cocktails, it could be concluded that > 60 min, the free Pb component in this NC-cocktail only attributes to the evaluation of the injection accuracy (e.g. leakage of the injected volume out of the injection site), which is not possible with non-dye containing radiopharmaceutical injections.

Preoperative SPECT/CT imaging, using a dedicated small animal SPECT/CT system made it possible to mimic the standard preoperative clinical lymphoscintigraphy based assessment in mice. Next to lymphatic migration, the injected radiopharmaceuticals showed distribution throughout the tumor and seminal vesicles. In combination with the relatively small migratory distances and the one mm SPECT resolution, the preclinical SPECT/CT scans only allowed for the preoperative determination of uptake in the lumbar and renal LNs. Therefore, to quantitatively study the radioactive content in all SLNs postoperative scintillation counting was used. This predominantly revealed the highest uptake values in either the caudal and/or lumbar LNs (Table 3).

Within the NC_{60} group the correlation between the radioactive and the fluorescent signal intensities was good (Table 3); in five out of six animals a correlation of $R^2 > 0.92$ was obtained. On average, the fluorescence intensities in the NC_{60} group were higher than those with ICG alone at 60 min post injection. Furthermore, in four out of six animals all the SLNs could be identified based on both their radioactive and fluorescence signature. Of all the SLNs in this group, 86% and 91% contained fluorescence or radioactivity respectively (Figure 3A).

To study the effective time window for imaging and to provide an indication of the stability of the cocktail-approach the uptake in the SLNs was also investigated at 240 min post injection (NC_{240} ; Table 3). Although a correlation of $R^2 > 0.79$ was only obtained in 50% of animals, the SLN with the highest radioactive content also contained the highest

amount of fluorescence. Within this group 95% of the SLNs contained fluorescence and 86% contained radioactivity (Figure 3A).

Within the HSA₆₀ group noticeably lower average signal intensities were measured compared to the NC₆₀ group. Furthermore, the correlation between the normalized radioactive and the fluorescence intensities in these animals was quite poor as only two out of six mice showed a good correlation ($R^2 > 0.78$). Furthermore, only 58% and 71% of all SLNs contained, respectively fluorescence or radioactivity.

As can be seen in Figure 3A, the correlation between the percentage of SLNs that contained fluorescence and the SLNs that contained radioactivity was highest at 60 min after injection in the NC group. This correlation remained high at 240 min after injection. Therefore this complex can be considered stable over the time period measured.

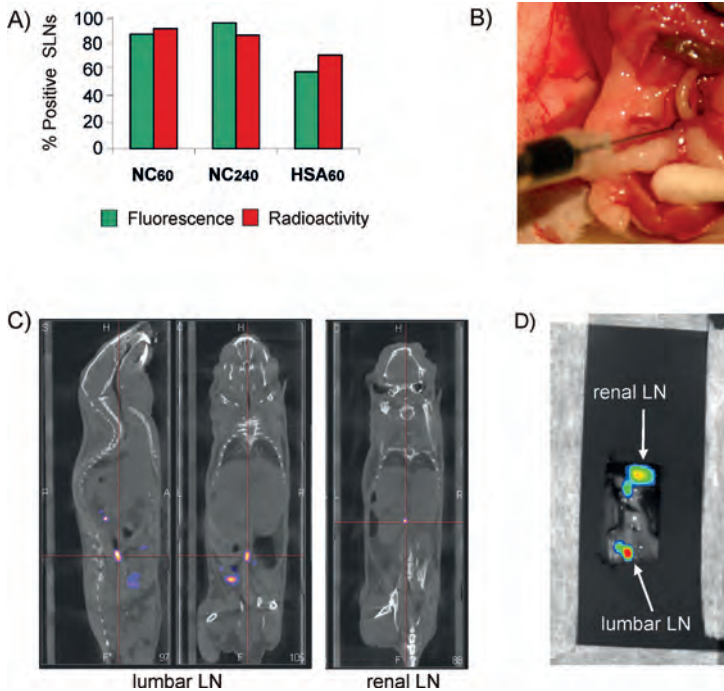


Figure 3. NC₆₀ cocktail based imaging of SLNs: A) Percentages of imaging agent containing LNs in the ICG₁₅ and ICG₆₀ groups. In the graphs the percentages of the fluorescent component in the cocktail were depicted in green and the percentages for the radioactive component in yellow; percentages are calculated from Table 3. B) Visualization of the injection accuracy via the visible Pb component. C) Preoperative SPECT/CT imaging via the radioactive nanocolloid component, depicting a.o. a lumbar and a renal LN. D) Intraoperative NIR fluorescence imaging of the fluorescent ICG component animal revealing only lumbar and renal LNs. To minimize the background signal the animal was covered except for the ROI.

Preliminary clinical data

The concept of using the NC-cocktail (without Pb) in clinical procedures involving the excision of both the prostate and the nearby SLNs is currently under investigation. Here initial ex vivo results (n = 6) were reported to substantiate the translational nature of the presented preclinical data. Patients were injected with the cocktail solution in the operating theatre and the prostate and SLNs were excised at approximately 60 min after injection, hence mimicking the preclinical NC₆₀ conditions. Examination of the excised tissue sections (Figure 4), demonstrated the overlap between the fluorescent and radioactive signals. All fluorescence containing SLNs contained radioactivity and vice versa. Although this is preliminary data, the results indicate that the approach can also be of value in the clinical situation.

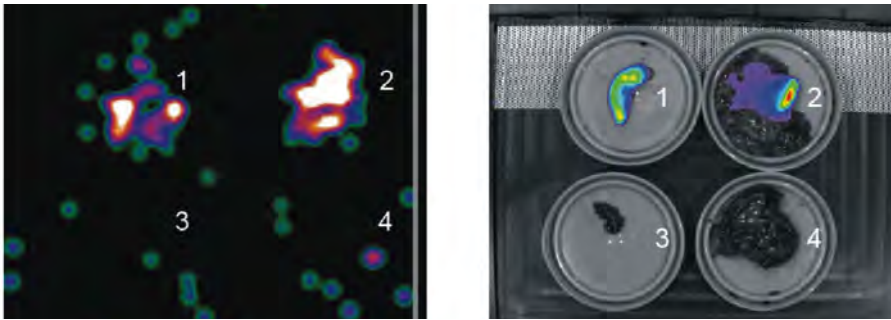


Figure 4. Ex vivo analysis of excised SLNs. SLNs situated in the extended pelvic lymphadenectomy area (LN 1-4) were excised during a laparoscopic procedure, approximately 60 min after the cocktail solution was injected into the prostate. Ex vivo evaluation of the excised tissue using a gamma camera (left image) showed a radioactive signal in two of the four excised nodes. Fluorescence imaging (right image) resulted in visualization of a fluorescence signal in the same LNs as wherein the radioactive signal could be detected.

Discussion

In the clinic it is important to identify the SLN or group of SLNs infiltrated by metastasizing cancer cells via lymph flow. As it has been shown that lymph flow is increased in tumor-bearing animals³³, experiments were conducted in TRAMP+ mice that develop spontaneous tumors in the prostate accompanied by metastatic spread.²⁵ Although in the TRAMP model the prostate dependant drainage pathways resemble the clinical situation, the lymphatic drainage pattern differs slightly from that seen in patients. Lymphatic drainage logically occurs via the caudal and lumbar LNs to the renal LNs and can occur via either the left or right drainage path.

Histological evaluation of lymphatic tissue after surgical pelvic lymphadenectomy procedures is acknowledged as 'golden standard' in the assessment of LN metastasis in the field of prostate cancer. In order to simplify the excision of the SLNs, accurate surgical guidance is crucial. Unfortunately, very little intraoperative imaging techniques are described for prostate cancer and techniques for combined pre- and intraoperative visualization of the tumor draining SLNs are lacking. The TRAMP model can serve as a good model for the development and validation of new (intraoperative) SLN imaging procedures.

Visual (Pb) vs. fluorescence (ICG) detection

Pb and ICG show chemical similarities; both contain aromatic units with a cationic nitrogen atom and two anionic-groups for water solubility. As a result, similar lymphatic migration and thus a similar effective time window were foreseen. Unexpectedly, no direct correlation could be observed between the detection of Pb and ICG (Table 2). Visible blue dye guided SLN dissection in the ICG₁₅ group only resulted in the removal 42% of all the SLNs, while via fluorescent detection this percentage improved to 67%. Moreover, at 60 min after injection the fluorescent dye still enabled visualization 53% of the SLNs compared to only 7% with Pb. Since both imaging agents were injected as a cocktail, an explanation for the differences in identification of SLNs could be the higher detection sensitivity obtained with the NIR dye ICG. This is especially interesting, considering that the Pb/ICG-cocktails contain 14-fold excess of Pb compared to ICG. As a result of the poor visualization rate, Pb was eliminated from the clinical cocktail as surgery was initiated at approximately 60 min post injection.

Diagnostic value radioactive albumin(colloid) containing cocktail injections

Preoperative SPECT/CT with radiocolloids is a reliable method to detect the tumor draining LNs of the prostate. By doing so the surgical procedure can be planned and the operating time reduced.³⁴ With the NC- and HSA-cocktail injections the radioactive component could be used for surgical planning based on preoperative SPECT/CT images. The other two components complemented this clinically proven technique by adding the possibility to: 1) validate the accuracy of the injection site via visual detection of Pb; and 2) guide the surgical procedure by intraoperative NIR fluorescence imaging (Figure 3). As a result the cocktail approach combined the advantages of three different separate detection procedures in one single injection.

Lymphatic migration studies using differently sized imaging agents have led to questions regarding the optimal particle size for optimal migration in the lymphatic tract. Fujil et al.³⁵ describe that molecules with a hydrodynamic diameter less than approximately 10 nm (viz. Pb, ICG, ^{99m}Tc-HSA) have the potential to travel beyond the SLN, while larger molecules <100 nm diameter (viz. ^{99m}Tc-nanocolloid) are retained in the SLN. Furthermore, Faries et al.³⁶ demonstrated that albumin colloids are actively accumulated by macrophages in the LN's. Indeed, we found that at 60 and 240 min post injection the radioactive count rates obtained with the albumin colloids (^{99m}Tc-nanocolloid) are, on average, higher than those obtained with single albumin particles (^{99m}Tc-HSA; Tabel 3).

Crucial for combined pre- and intraoperative visualization of the hybrid nature of the approach is the ability to identify all SLNs based on both their radioactive and fluorescent content. Not only was a high correlation found between the fluorescence signal intensities and radioactive count rates in the NC-groups (Table 3 and 4), both modalities also showed highly similar SLN detection rates, 86% and 95%, respectively (Figure 3A). The overall fluorescence intensities in the NC₆₀ group were highly similar to those obtained with free ICG at 60 min (Table 2, 3, and 4), suggesting that the emission of fluorescence was not negatively influenced by the interaction with albumin. Moreover, the ability to detect the SLNs via fluorescence imaging in the NC₆₀ group increased with 33% compared to that with free ICG. The HSA-cocktail, on the other hand, did not show an improvement in fluorescence detection of SLNs compared to the free ICG at 60 min post injection (Figures 2E and 3A). The similarity in distribution of fluorescence and the low correlation between fluorescence signal intensities and radioactive count rates found for the HSA-cocktail suggests that the complex stability in the latter is lower than in the NC-cocktails.

While all animals in the NC₆₀ group showed a correlation > 0.76 between radioactivity and fluorescence content, such a correlation was only obtained in three animals in the HSA60 group. Based on the molar ratios used in the cocktails, the ICG : ^{99m}Tc-HSA ratio is much lower than the ratio between the nanocolloid and ICG. Clearly, the hybrid nature of the non-covalent complex is less influenced by dissociation of ICG compared to the complexes formed between ICG and HSA (Table 3). At a later time point (NC₂₄₀) dissociation of ICG from ^{99m}Tc-nanocolloid also became detectable; only three animals give a correlation > 0.79. Even though the correlation decreased, it was still possible to also see the radioactivity containing LNs via NIR fluorescence imaging procedures. As long as some of the ICG remained bound to the radioactive albumin particles, the SLNs could be detected via fluorescence imaging. In these instances the self-assembled complexes could still help

guide the surgical resection via intra-operative NIR imaging.

In the NC₆₀ control group a slightly lower correlation between the fluorescence and radioactive signal was found in TRAMP- animals that were injected in the prostate (Table 3). It seemed that the self-assembled complexes were less stable after injection into the highly vascularised prostate. This is in agreement with findings that these self-assembled complexes are not stable in the blood stream after intravenous injection (data not shown). The efficacy of the self-assembled complexes after intratumoral injections, however, is an indication that the physiology in the tumor is favorable for the complex stability. Combined this suggests that the physiological conditions of the injection site are of influence on the stability of the non-covalent self-assembled complex. Nevertheless, it warrants their use in intratumoral injections and lymphatic migration studies.

Clinical applicability

Similar to the suggestion of the FDA,²¹ the local ethical committee of the Netherlands Cancer Institute acknowledged that a single cocktail injection of fluorescent and radioactive agents would be preferable over multiple injections. The use of ICG and ^{99m}Tc-nanocolloid containing cocktail was approved for use in a clinical pilot study. It was shown that the combination of ICG and ^{99m}Tc-nanocolloid yielded the in situ formation of a non-covalent complex comprising of two clinically approved imaging agents. Hence, different from what was found with sulphur radiocolloids, here a cocktail injection provided clear added value over free ICG alone.

In this Chapter, only ex vivo validation data were shown to demonstrate the excellent correlation between the radioactive and the fluorescence signal in this selected group of patients. Further studies will be conducted using an intraoperative fluorescence camera, allowing intraoperative visualization of the nodes during the surgical procedure. The preliminary clinical data are promising and substantiate the potential the approach might have in a clinical application. The clinical value of this approach is being further evaluated in Chapters 5, 6 and 7.

Conclusion

In addition of the conventional preoperative SPECT/CT guidance, SLN imaging with a cocktail solution of Pb, ICG, and ^{99m}Tc -nanocolloid provides additional visual information regarding the accuracy of the injection (Pb) and provides the possibility of optical fluorescence guidance during the surgical procedure (ICG). Due to the self-assembly of ICG and ^{99m}Tc -nanocolloid a hybrid complex was generated that enabled both pre- and intraoperative detection of the SLNs up to 240 min post injection.

References

- 1 Fujisawa M, Miyake H. Significance of micrometastases in prostate cancer. *Surg Oncol.* 2008; 154: 247-252
- 2 Heidenreich A, Ohlmann CH, Polyakov S. Anatomical extent of pelvic lymphadenectomy in patients undergoing radical prostatectomy. *Eur Urol.* 2007; 52: 29-37
- 3 Briganti A, Chun FK-H, Salonia A, Suardi N, Gallina A, Da Pozzo LF, Roscigno M, Zanni G, Valiquette L, Rigatti P, Montorsi F, Karakiewicz PI. Complications and other surgical outcomes associated with extended pelvic lymphadenectomy in men with localized prostate cancer. *Eur Urology.* 2006; 50: 1006-1013
- 4 Link RE, Morton RA. Indications for pelvic lymphadenectomy in prostate cancer. *Urol Clin North Am.* 2001; 28: 491-498
- 5 Wilkinson BA, Hamdy FC. State-of-the-art staging in prostate cancer. *BJU Int.* 2001; 87: 423-431
- 6 Bader P, Bukhard FC, Markwalder R, Studer UE. Is a limited lymph node dissection an adequate staging procedure for prostate cancer? *J. Urol.* 2002; 168: 514-518
- 7 Giuliano AE, Kirgan DM, Guenther JM, Morton DL. Lymphatic mapping and sentinel lymphadenectomy for breast cancer. *Ann Surg.* 1994; 220: 391-398
- 8 Morton DL, Thompson JF, Cochran AJ, Mozzillo N, Elashoff R, Essner R, Nieweg OE, Roses DF, Hoekstra HJ, Karakousis CP, Reintgen DS, Coventry BJ, Glass EC, Wang HJ. Sentinel node biopsy or nodal observation in melanoma. *N Engl J Med.* 2006; 355: 1307-1317
- 9 Mariani G, Erba P, Villa G, Gipponi M, Manca G, Boni G, Buffoni F, Castagnola F, Paganelli G, Strauss HW. Lymphoscintigraphic and intraoperative detection of the sentinel lymph node in breast cancer patients: the nuclear medicine perspective. *J Surg Oncol.* 2004; 85: 112-122
- 10 Pelosi E, Ala A, Bellò M, Douroukas A, Migliaretti G, Berardengo E, Varetto T, Bussone R, Bisi G. Impact of axillary nodal metastasis on lymphatic mapping and sentinel lymph node identification rates in patients with early stage breast cancer. *Eur J Nucl Med Biol Imaging.* 2005; 32: 937-942
- 11 Hayashida T, Jinno H, Sakata M, Takahashi M, Onishi T, Seki H, Sato T, Nakahara T, Shigematsu N, Mukai M, Hibi T, Kitajima M, Kitagawa Y. Superiority of radioisotope over blue dye for sentinel lymph node detection in breast cancer. *Eur Surg Res.* 2010; 44: 111-116

- 12 Warncke SH, Mattei A, Fuechsel FG, Z'Burn S, Krause T, Studer UE. Detection rate and operating time required for γ probe-guided sentinel lymph node resection after injection of Technetium-99m nanocolloid into the prostate with and without preoperative imaging. *Eur.Urol.* 2007; 52: 126-133
- 13 Vermeeren L, Valdés-Olmos RA, Meinhardt W, Bex A, van der Poel HG, Vogel WV, Sivo F, Hoefnagel CA, Horenblas S. Value of SPECT/CT for detection and anatomic localization of sentinel lymph nodes before laproscopic sentinel node lymphadenectomy in prostate carcinoma. *J Nucl Med.* 2009; 50: 865-870
- 14 Meinhardt W, Valdés-Olmos RA, van der Poel HG, Bex A, Horenblas S. Laparoscopic sentinel node dissection for prostate carcinoma: technical and anatomical observations. *BJU Int.* 2008; 102: 714-717
- 15 Valdés-Olmos RA, Vidal-Sicart S, Nieweg OE. SPECT-CT and real-time intraoperative imaging: new tools for sentinel node localization and radioguided surgery? *Eur J Nucl Med Mol Imaging* 2009; 36: 1-5
- 16 Frangioni JV. In vivo near-infrared fluorescence imaging. *Curr Op Chem Biol.* 2003; 7: 626-634
- 17 Lim YT, Kim S, Nakayama A, Stott NE, Bawendi MG, Frangioni JV. Selection of quantum dot wavelengths for biomedical assays and imaging. *Mol Imaging.* 2003; 2: 50-64
- 18 Ogasawara Y, Ikeda H, Takahashi M, Kawasaki K Doihara H. Evaluation of breast lymphatic pathways with indocyanine green fluorescence imaging in patients with breast cancer. *World J Surg.* 2008; 32: 1924-1929
- 19 Kusano M, Tajima Y, Yamazaki K, Kato M, Watanabe M, Miwa M. Sentinel node mapping guided by indocyanine green fluorescence imaging: a new method for sentinel node navigation surgery in gastrointestinal cancer. *Dig Surg.* 2008; 25: 103-108
- 20 Ohshini S, Lomnes SJ, Laurence RG, Gogbashian A, Mariani G, Frangioni JV. Organic alternatives for quantum dots for intraoperative near-infrared fluorescent sentinel lymph node mapping. *Mol Imaging.* 2005; 4: 172-181
- 21 Sevick-Muraca EM, Sharma R, Rasmussen JC, Marshall MV, Wendt JA, Pham HQ, Bonefas E, Houston JP, Sampath L, Adams KE, Blanchard DK, Fisher RE, Chiang SB, Elledge R, Mawad ME. Imaging of lymph flow in breast cancer patients after microdose administration of a near-infrared fluorophore. *Radiology.* 2008; 246: 734-741
- 22 Newman EA, Newman LA. Lymphatic mapping techniques and sentinel lymph node biopsy in breast cancer. *Surg Clin North Am.* 2007; 87: 353-364

- 23 Newman LA. Lymphatic mapping and sentinel lymph node biopsy in breast cancer patients: a comprehensive review of variations in performance and technique. *J Am Coll Surg.* 2004; 199: 804–816
- 24 Buckle T, van Leeuwen AC, Chin PTK, Janssen H, Muller S, Jonkers J, van Leeuwen FWB. A self-assembled multimodal complex for combined pre- and intraoperative imaging of the sentinel lymph node. *Nanotechnology.* 2010; 21: 355101
- 25 Weissleder R. Scaling down imaging: molecular mapping of cancer in mice. *Nature Rev.* 2001; 2: 1-8
- 26 Winter SF, Cooper AB, Greenberg NM. Models of metastatic prostate cancer: a transgenic perspective. *Prostate Cancer Prostatic Dis.* 2003; 6: 204-211
- 27 Ohshini S, Lomnes SJ, Laurence RG, Gogbashian A, Mariani G, Frangioni JV. Organic alternatives for quantum dots for intraoperative near-infrared fluorescent sentinel lymph node mapping. *Mol Imaging.* 2005; 4: 172-181
- 28 Moody ED, Viskari PJ, Colyer CJ. Non-covalent labeling of human serum albumin with indocyanine green: a study by capillary electrophoresis with diode laser-induced fluorescence detection. *J Chrom B.* 1999; 729: 55-64
- 29 Hurwitz AA, Foster BA, Allison JP, Greenberg NM, Kwon ED. The TRAMP mouse as a model for prostate cancer. *Curr Protoc Immunol.* 2001; 20: unit 20.5
- 30 Gupta S, Ahmad N, Marengo SR, Maclennan GT, Greenberg NM, Mukhtar H. Chemoprevention of prostate carcinogenesis by α -difluoromethylornithine in TRAMP mice. *Cancer Res.* 2000; 60: 5125-5133
- 31 Rubio N, Villacampa MM, El Hilali N, Blanco J. Metastatic burden in nude mice organs measured using prostate tumor PC-3 cells expressing the luciferase gene as quantifiable tumor cell marker. *Prostate.* 2002; 44: 133-143
- 32 Shappell SB, Thomas GV, Roberts RL, Herbert R, Ittmann MM, Rubin MA, Humphrey PA, Sundberg JP, Rozengurt N, Barrios R, Ward JM, Cardiff RD. Prostate pathology of genetically engineered mice: definitions and classification. The consensus report from the bar harbor meeting of the mouse models of human cancer consortium prostate pathology committee. *Cancer Res.* 2004; 64: 2270-2305
- 33 Bass SS, Cox CE, Salud CJ, Lyman GH, McCann C, Dupont E, Berman C, Reintgen DS. The effects of postinjection massage on the sensitivity of lymphatic mapping in breast cancer. *J Am Coll Surg.* 2001; 192: 9-16
- 34 Kragh-Hansen U. Molecular aspects of ligand binding to serum albumin. *Pharm Rev.* 1981; 33: 17-53

- 35 Ruddell A, Harrell MI, Minoshima S, Iritani BM, White SW, Partridge SC. Dynamic contrast-enhanced magnetic resonance imaging of tumor-induced lymph flow. *Neoplasia*. 2007; 10: 706-713
- 36 Studer UE. Detection rate and operating time required for gamma probe-guided sentinel lymph node resection after injection of technetium-99m nanocolloid into the prostate with and without preoperative imaging. *Eur Urol*. 2007; 52: 126-132
- 37 Fujil H, Kitagawa Y, Kumbo A. Sentinel nodes of malignancies originating in the alimentary tract. *Ann Nucl Med*. 2004; 18: 1-12
- 38 Faries MB, Bedrosian I, Reynolds C, Nguyen HQ, Alavi A, Czerniecki BJ. Active macromolecule uptake by lymph node antigen-presenting cells: a novel mechanism in determining sentinel lymph node status. *Ann Surg Onc*. 2000; 7: 98-105

Interventional

**Comparing the hybrid fluorescent-radioactive
molecular imaging,
tracer indocyanine green-^{99m}Tc-nanocolloid
a hybrid approach
with ^{99m}Tc-nanocolloid for sentinel
lymph node identification: A validation study
using lymphoscintigraphy and SPECT/CT**

Chapter 5

Adapted from:

*Brouwer OR, Buckle T, Vermeeren L, Klop WMC, Balm AJM, van der Poel HG,
van Rhijn BW, Horenblas S, Nieweg OE, van Leeuwen FWB, Valdés-Olmos RA.*

J Nucl Med 2012; 53(7): 1034-1040

Abstract

Before the hybrid tracer ICG-^{99m}Tc-nanocolloid can be widely applied during sentinel lymph node (SLN) imaging in patients, lymphoscintigraphic drainage patterns of ICG-^{99m}Tc-nanocolloid need to be compared to the parental compound ^{99m}Tc-nanocolloid, which is the standard tracer for lymphoscintigraphy in many European countries. To this end, 25 patients with either a melanoma in the head and neck region (n = 10), on the trunk (n = 6), or with penile carcinoma (n = 9) were prospectively included in a reproducibility study. First, the standard ^{99m}Tc-nanocolloid procedure was performed. After injection at the lesion site, static and dynamic lymphoscintigraphy was performed, followed by SPECT/CT. The scintigraphic procedure was repeated after injection of hybrid ICG-^{99m}Tc-nanocolloid on the same day (ten patients), or the next morning (15 patients). The paired images of both injections were evaluated and count rates in the SLN were calculated and compared. SLNs were surgically localized using blue dye, a gamma ray detection probe, a portable gamma camera and a fluorescence camera. Lymphatic drainage was visualized in all 25 patients. All SLNs detected with ^{99m}Tc-nanocolloid were also identified with ICG-^{99m}Tc-nanocolloid. Moreover, a high correlation between the radioactive counts rates in the SLNs of both scintigraphic studies was observed (mean $R^2 = 0.83$). Intraoperatively, all preoperatively identified SLNs could be localized using radio- and fluorescence guidance combined. Ex vivo, all radioactive SLNs were found to be fluorescent and vice versa. From these data can be concluded that the lymphatic drainage pattern of ICG-^{99m}Tc-nanocolloid is identical to that of ^{99m}Tc-nanocolloid.

Introduction

Based on the hypothesis of sequential tumor spread, sentinel lymph node (SLN) biopsy is increasingly being used as a staging procedure for various malignancies.¹⁻⁷ In the preoperative setting, the lymphatic drainage pattern can be gradually visualized using sequential lymphoscintigraphy, enabling identification of the tumor draining (S)SLNs.⁸ Single photon emission computed tomography combined with computed tomography (SPECT/CT) complements lymphoscintigraphy with three-dimensional anatomical data, and can reveal additional SLNs in some occasions.⁹⁻¹¹

Intraoperative SLN identification traditionally relies on the combination of acoustic signals generated by a gamma ray detection probe and optical SLN visualization using a visible blue dye.^{12,13} Since the gamma probe has a limited spatial resolution and SLNs are not always stained blue, SLNs can be difficult to localize in areas with a complex anatomy and when SLNs are located close to the injection site.^{14,15} The incorporation of a portable gamma camera in the intraoperative procedure partially addresses these limitations by increasing the detection sensitivity and providing an intraoperative overview image of the (radioactive) SLNs. Nevertheless this device does not depict the surrounding anatomical structures in the surgical field.¹⁶⁻¹⁸

Near-infrared (NIR) fluorescence imaging has the potential to address the drawbacks of radioguided SLN detection by providing better spatial resolution and allowing for real-time optical detection of the SLN within the surrounding anatomy.¹⁹⁻²² As the signal penetration of fluorescent probes is limited by tissue attenuation, radio-guidance to the general area of interest is still indispensable.²³ To combine the beneficial properties of both modalities, a hybrid tracer comprising the fluorescent dye indocyanine green (ICG) and the human serum albumin based radiocolloid ^{99m}Tc-nanocolloid was developed.^{24,25} Recently, hybrid ICG-^{99m}Tc-nanocolloid was introduced for laparoscopic and open SLN biopsies in patients with prostate cancer, head and neck melanoma or oral cavity carcinoma.^{23,26-28}

Before this hybrid tracer can be used routinely, it is imperative to ensure that the addition of the fluorescent moieties does not alter the biological properties of the parental radiocolloid. Therefore, the main purpose of the present study was to assess the concordance between the lymphatic drainage pattern of ^{99m}Tc-nanocolloid and ICG-^{99m}Tc-nanocolloid, using lymphoscintigraphy and SPECT/CT. In addition, this study further evaluate the value of combined radio- and fluorescence-guided SLN biopsy in various malignancies with superficial lymphatic drainage to areas such as the groin, axilla, and neck.

Methods

Patients

Twenty-five patients with either a melanoma in the head and neck region ($n = 10$), on the trunk ($n = 6$), or with penile carcinoma ($n = 9$) scheduled for SLN biopsy were prospectively enrolled in the study. Patient characteristics are listed in Table 1. The mean age of the patients was 54 years (range 26 - 74 years). All patients were clinically node-negative at the time of SLN biopsy. The study protocol was approved by the medical ethical committee of the Netherlands Cancer Institute - Antoni van Leeuwenhoek Hospital (NKI-AvL) and all patients provided written informed consent.

Tracer preparation

^{99m}Tc -nanocolloid was prepared by adding 2 mL pertechnetate in saline (approx. 1125 MBq) to a commercial vial of nanocolloid containing 0.5 mg of albumin colloid (Nanocoll; GE Healthcare). Following 30 min of incubation at room temperature, the ^{99m}Tc -nanocolloid solution (pH 6 - 7) was exposed to air via a needle to get rid of any excess reactive elements. Subsequently, a dose of 0.25 mg ICG (ICG-Pulsion, Pulsion Medical Systems) was added to form hybrid ICG- ^{99m}Tc -nanocolloid as described previously.²³ All preparations were performed under good manufacturing practice and with approval of The Netherlands Cancer Institute's pharmacist.

Preoperative procedure and image analysis

To determine the concordance between the lymphatic drainage patterns of ICG- ^{99m}Tc -nanocolloid and ^{99m}Tc -nanocolloid, both tracers were injected in consecutive order in the same patients, and the lymphoscintigraphic findings of both tracers were directly compared. Firstly ^{99m}Tc -nanocolloid was injected, in a volume of 0.4 mL containing 0.05 mg human serum albumin. Before tracer injection, the planned sites of injection were carefully marked with an indelible felt-tip pen (Figure 1). In the melanoma patients, four injections were placed intradermally around the scar of the primary melanoma excision. For penile carcinoma, the tracer was intradermally administered divided into three injections proximally surrounding the tumor. The mean radioactivity dose of the first injection calculated on the basis of net administered doses was 71 MBq (range 54 - 88 MBq). Immediately after injection, anterior and lateral dynamic images were obtained with a dual-head gamma camera (Symbia T, Siemens) over ten minutes to visualize the

lymphatic flow and to identify lymph nodes (LNs) on a direct lymphatic drainage pathway. Subsequently, static planar images were acquired at 15 min. Two hrs after injection of ^{99m}Tc -nanocolloid, delayed planar images were obtained to further differentiate first-echelon nodes from higher-echelon nodes and to identify SLNs in other basins. In the same session, SPECT/CT (Symbia T, Siemens) was performed. The LNs draining directly from the injection site were classified as SLNs.⁸ The first node appearing in the basin was considered to be the SLN in case of multiple visible nodes without visible afferent vessels.

The same afternoon (ten patients: one-day protocol), or the next morning (fifteen patients: two-day protocol), the complete scintigraphic sequence was repeated after injection of hybrid ICG- ^{99m}Tc -nanocolloid. Shortly before injection, a five min static image was obtained as a point of reference for the second injection in six patients. Hybrid tracer administration was then performed at the locations previously marked on the skin, by the same nuclear physician, using a similar tracer concentration (0.05 mg HSA in 0.4 mL, mean 74 MBq, range 57 - 97 MBq). The mean interval between the two injections was 19 hrs (median 21, range 2.5 - 24, Table 1). Paired images of both injections were evaluated with regard to similarity of the depicted draining LN basins and the location and number of the SLNs. Count rates (maximum counts per pixel) were measured from the planar anterior images at two hrs after each injection and the reference images before the second injection using regions of interest drawn around the SLN(s). Trendline-based linear regression correlations (Excel) were used to establish the correlation between the radioactive count rates of both scintigraphic studies in patients with more than two preoperatively identified SLNs.

Intraoperative procedure

Shortly before surgery, 1.0 mL patent blue dye (Laboratoire Guerbet) was injected in all patients except those with melanoma located in the face to prevent unaesthetic long lasting skin marks. Next, a portable gamma camera (Sentinella, Oncovision) was used to guide the skin incisions and to obtain a pre-excision overview image of the SLNs. Intraoperatively, the SLNs were firstly pursued using the acoustic guidance provided by a gamma ray detection probe (Neoprobe, Johnson & Johnson Medical). During this initial exploration, attempts were made to visually detect the SLNs via the blue dye and the hybrid tracer's fluorescent component (ICG) using a hand-held near-infrared fluorescence camera (PDE, Hamamatsu). After excision of each SLN, a post-excision image was acquired with the portable gamma camera to ensure its complete removal.

Patient	Age (yrs)	Sex	Primary tumor	Interval between injections (hrs)	Study 1 Dose (MBq)	Study 1 No. of SLNs	Study 1 No. of basins	Study 2 Dose (MBq)	Study 2 No. of SLNs	Study 2 No. of basins	Correlation SLN count rates both studies (R ²)
1	33	M	Melanoma trunk	24	71	2	1	80	2	1	*
2	66	M	Melanoma trunk	21	88	3	2	77	3	2	0.91
3	26	F	Melanoma trunk	24	74	2	2	79	2	1	*
4	65	M	Melanoma trunk	20	78	2	1	80	2	2	*
5	50	F	Melanoma trunk	5	71	2	2	68	2	2	*
6	30	F	Melanoma trunk	4	68	3	3	73	3	3	0.99
7	74	M	Head/Neck melanoma	23	61	3	3	70	3	3	0.99
8	55	M	Head/Neck melanoma	3	59	2	2	76	2	2	*
9	32	F	Head/Neck melanoma	2.5	54	1	1	67	1	1	*
10	39	M	Head/Neck melanoma	4.5	87	2	2	86	2	2	*
11	70	F	Head/Neck melanoma	22	64	3	3	67	3	3	0.93
12	32	F	Head/Neck melanoma	2.5	64	3	2	72	3	2	0.85
13	49	M	Head/Neck melanoma	23	67	1	1	60	1	1	*
14	66	F	Head/Neck melanoma	20	61	2	2	58	2	2	*
15	56	F	Head/Neck melanoma	2.5	82	6	6	98	6	6	0.58
16	67	F	Head/Neck melanoma	22	74	2	2	96	2	2	*
17	57	M	Penile carcinoma	2.5	80	2	2	87	2	2	*
18	61	M	Penile carcinoma	2.5	69	5	2	57	5	2	0.96
19	72	M	Penile carcinoma	19	70	3	2	73	3	2	0.93
20	72	M	Penile carcinoma	24	61	3	2	83	3	2	0.71
21	48	M	Penile carcinoma	20	70	3	1	59	3	1	0.51
22	34	M	Penile carcinoma	20	69	3	2	71	3	2	0.99
23	64	M	Penile carcinoma	23	67	3	1	66	3	1	0.99
24	71	M	Penile carcinoma	20	75	3	2	81	3	2	0.49
25	65	M	Penile carcinoma	2.5	83	2	2	74	2	2	*

Table 1. Patient characteristics and lymphoscintigraphy results

SLN	= sentinel lymph node
Study 1	= First examination using ^{99m}Tc -nanocolloid
Study 2	= Second examination using ICG- ^{99m}Tc -nanocolloid
*	= Correlation (R^2) between count rates measured two hrs after each injection could only be calculated in patients with > 2 SLNs

Ex vivo analyses and histopathological examination

Excised LNs were postoperatively analyzed for the presence of a radioactive and/or fluorescence signal using the portable gamma camera and an ex vivo fluorescence camera system (IVIS 200, Caliper Lifesciences), respectively. All harvested nodes were fixed in formalin, bisected, embedded in paraffin, and cut at a minimum of six levels at 50 to 150 μm intervals. Pathological evaluation included haematoxylin-eosin and immunohistochemical staining (anti-cytokeratin; CAM 5.2; Becton Dickinson).

Results

Preoperative image analysis

Lymphoscintigraphy and SPECT/CT after injection of ^{99m}Tc -nanocolloid showed at least one SLN in all 25 patients. The conventional lymphoscintigrams depicted 65 SLNs, of which 89% were visualized on the early static planar images. SPECT/CT showed the anatomical location of these nodes and revealed one additional SLN that was not visualized on the conventional lymphoscintigrams. The 66 SLNs were distributed over 51 nodal basins (Table 1; average of 2.6 SLNs per patient). In the ten patients with a melanoma in the head and neck region, 25 SLNs were observed in various neck LN basins ($n = 17$), the parotid gland ($n = 2$), submandibular region ($n = 2$), and suboccipital region ($n = 3$). In the six patients with a melanoma on the trunk, 14 SLNs were identified in nine axillae and two groins. In the nine patients with penile carcinoma, 27 SLNs were visualized in 16 groins.

The second scintigraphic study using ICG- ^{99m}Tc -nanocolloid yielded an identical drainage pattern with the same number of SLNs in the corresponding nodal basins for all patients (Table 1, illustrated in Figure 1, 2 and 3). A comparison of the radioactive count rates in the individual SLNs at two hrs after both injections revealed a high correlation (R^2) of 0.85 ± 0.20 for the patients injected twice on the same day (one-day protocol) and 0.83

± 0.19 for the patients within the two-day protocol (Table 1). In the one-day protocol, radioactive count rates measured two hrs after the second injection (ICG-^{99m}Tc-nanocolloid) were higher compared to count rates measured two hrs after the first injection (^{99m}Tc-nanocolloid) in 90% of the SLNs. For the two-day protocol this was 66%. Furthermore, in the six patients in whom a reference image had been acquired shortly before the second scintigraphic procedure (both one and two-day protocol), an increased radioactive count rate was found in each SLN two hrs after the second injection (average 85%, range 47 - 96%).

Intraoperative results

On average, SLN biopsy was initiated six hrs after injection of the hybrid tracer (range 4 - 23, median five hrs; Figure 4, Table 2). Intraoperatively, all scintigraphically visualized SLNs could be localized and excised using radio- and fluorescence guidance combined. In six patients, postexcision imaging with the portable gamma camera identified considerable residual radioactivity at the original location of the SLN, resulting in the pursuit and removal of a total of 13 additional SLNs. 74 of the total of 79 SLNs (94%) could be localized using the gamma ray detection probe. The remaining five nodes were identified using the fluorescence camera (Table 2). Three of these SLNs concerned melanomas in the temporal region and were located in front of the ear, where the overwhelming radioactive signal from the nearby injection site hampered probe guidance. Two SLNs in the inguinal region in penile carcinoma patients were difficult to localize using the probe due to the low radioactive count rate in the SLNs relative to the (high) background.

A total of 75 SLNs (95%) could be visualized by fluorescence imaging after initial surgical exploration, whereas only 54% of the SLNs were stained when patent blue was used (Table 2). The four SLNs that eluded fluorescence imaging were probably not sufficiently exposed to enable detection of the fluorescence signal. Nevertheless, a fluorescence signal could be visualized in all SLNs (including the four nodes mentioned above) *ex vivo* using the more sensitive IVIS fluorescence imaging system, underlining the stability of the ICG-^{99m}Tc-nanocolloid complex.

Histopathological examination revealed metastases in six excised SLNs in four patients (Table 2). The use of ICG-^{99m}Tc-nanocolloid was not associated with adverse reactions.

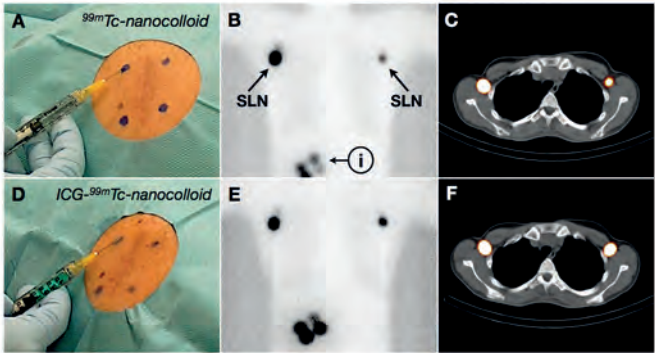


Figure 1. Comparison of the lymphatic drainage pattern of ^{99m}Tc-nanocolloid and ICG-^{99m}Tc-nanocolloid in a patient with a melanoma on the right posterior flank. A) Firstly ^{99m}Tc-nanocolloid was injected after the planned sites of injection were carefully marked with an indelible felt-tip pen. B) Planar lymphoscintigram two hrs post injection showing the four deposits at the injection site (i) and two SLNs, one in each axilla. C) axial SPECT/CT image revealing the anatomical information of both SLNs. D) The same patient was injected with ICG-^{99m}Tc-nanocolloid 24 hrs later at the previously marked locations. E) The planar lymphoscintigram two hrs post injection reveals the same two axillary SLNs. F) axial SPECT/CT image confirming that both SLNs are located at exactly the same locations compared to the first scintigraphic study using ^{99m}Tc-nanocolloid.

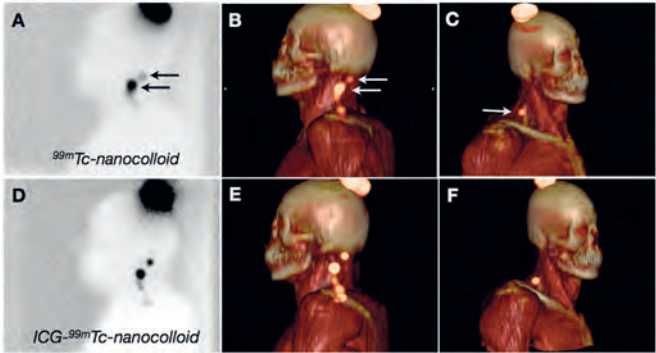


Figure 2. Comparison of the lymphatic drainage pattern of ^{99m}Tc-nanocolloid and ICG-^{99m}Tc-nanocolloid in a patient with a melanoma on the parietal scalp. A) Planar lymphoscintigram two hrs after injection of ^{99m}Tc-nanocolloid showing two SLNs (arrows) in the left neck region with second-echelon activity in caudal direction. B) 3D volume-rendered SPECT/CT image revealing the two SLNs (arrows) in level V of the (left) neck and a second-echelon node located more caudally C) 3D volume-rendered SPECT/CT revealing a SLN in level V on the right side (which was also visible on the anterior planar image, not shown). D) Planar lymphoscintigram two hrs after injection of ICG-^{99m}Tc-nanocolloid (23 hrs after the ^{99m}Tc-nanocolloid injection) showing the same two SLNs on the left side, with increased higher-echelon activity. E) 3D volume-rendered SPECT/CT image showing the same SLNs at the same location compared to the first scintigraphic study, with more notable higher-echelon activity. F) Injection of ICG-^{99m}Tc-nanocolloid also led to the identification of the same SLN on the right side, as seen on the 3D volume-rendered SPECT/CT image.

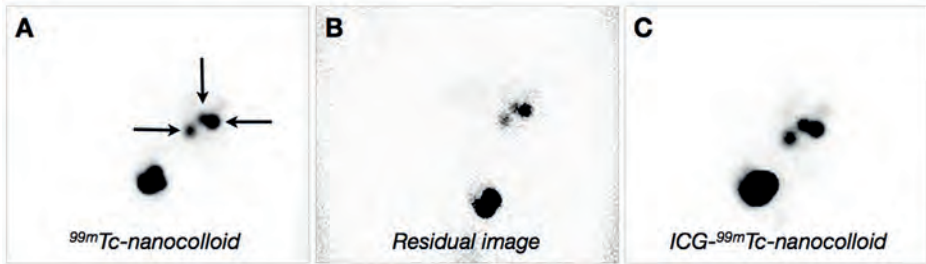


Figure 3. Comparison of the lymphatic drainage pattern of ^{99m}Tc -nanocolloid and ICG- ^{99m}Tc -nanocolloid in a patient with penile carcinoma. A) Planar lymphoscintigram two hrs after injection of ^{99m}Tc -nanocolloid showing drainage to three SLNs in the left inguinal region (arrows). B) The next morning, the residual image before ICG- ^{99m}Tc -nanocolloid injection showed decreased activity in the three nodes due to radioactive decay. C) Planar lymphoscintigram two hrs after injection of ICG- ^{99m}Tc -nanocolloid showed drainage to the same three SLNs in the left inguinal region (later confirmed by SPECT/CT).

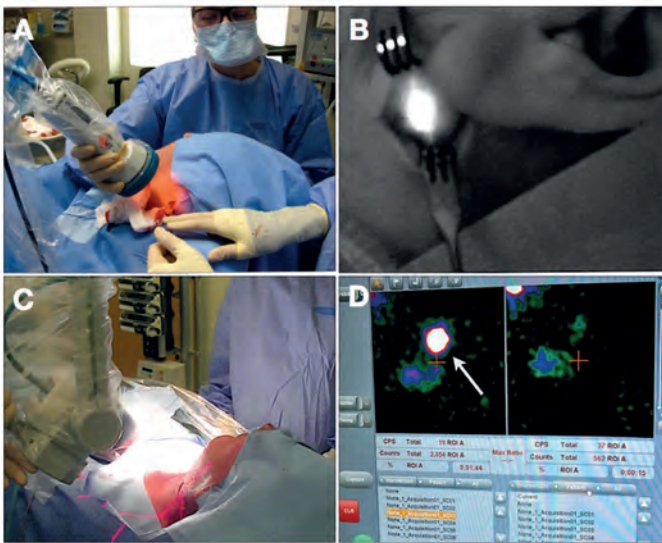


Figure 4. Combined intraoperative radio- and fluorescence-guided SLN biopsy in a head and neck melanoma patient. A) After initial exploration guided by the gamma probe and portable gamma camera, the hand-held fluorescence camera was used to visualize the SLN. B) Near-infrared fluorescence image showing the exact location and margins of the SLN within exposure of an infra-auricular SLN. C) The portable gamma camera was used to make a pre- and postexcision image of the (radioactive) SLNs. D) By comparing the preexcision (left) and postexcision (right) image on the screen of the portable gamma camera, successful removal of each SLN (arrow) could be confirmed in the operation room.

Table 2 Intraoperative SLN and pathology results

Tumour type	Patients	Preoperatively identified SLNs with SPECT/CT	Time-interval between Injection 2* and operation (range)	Excised SLNs	SLNs localized with probe	% SLNs blue	% Intraoperatively fluorescent SLNs	SLN metastases
Melanoma (trunk)	6	14	4 – 23	15	100% (15/15)	74% (11/15)	93% (14/15)	1
Melanoma (head/neck)	10	25	4 – 6	27	89% (24/27)	37% (7/19)**	93% (25/27)	0
Penile carcinoma	9	27	4 – 7.5	37	95% (35/37)	54% (20/37)	97% (36/37)	5
TOTAL	25	66	4 – 23	79	94%	54%	95%	6

* Injection of hybrid ICG-^{99m}Tc-nanocolloid

** Patent blue was injected in six patients with a head and neck melanoma outside the facial area (19 SLNs)

Discussion

This study shows that the lymphatic drainage pattern of the hybrid radioactive and fluorescent tracer ICG-^{99m}Tc-nanocolloid and ^{99m}Tc-nanocolloid, the current standard radiopharmaceutical in most European countries are identical. Lymphoscintigraphy and SPECT/CT after injection of ICG-^{99m}Tc-nanocolloid did not reveal any SLNs at other locations, and all preoperatively identified SLNs were found to contain ICG after excision. This confirms that ICG-^{99m}Tc-nanocolloid drains to the same SLNs as ^{99m}Tc-nanocolloid, and accumulates in the SLNs accordingly. The high correlation between count rates measured in the SLNs on the lymphoscintigrams two hrs after each tracer injection in both the one-day and two-day protocol further substantiated these findings. Combined with the absence of adverse reactions, these findings validate the use of ICG-^{99m}Tc-nanocolloid as a tracer for preoperative lymphatic mapping and SLN identification.

The reproducibility of repeated lymphoscintigraphy with ^{99m}Tc-nanocolloid has been studied for penile carcinoma and melanoma.^{29,30} While our present results are in agreement with the 100% reproducibility rate found for penile carcinoma, a discordance in lymphoscintigraphy results after the second scintigraphic study could have been anticipated for melanoma, as Kapteijn et al. found a reproducibility rate of 88% after repeat lymphoscintigraphy after 2-4 weeks in melanoma patients.³¹ A possible explanation for the high reproducibility observed in the current study may lie in the significantly shorter interval between both injections. The placement of the second injection at the exact same locations previously marked on the skin is also likely to have had a positive influence on the high reproducibility rate found in the current study (Figure 1).

In recent years, the fluorescent dye ICG has been evaluated as a single agent for intraoperative lymphatic mapping and SLN identification.^{19,20,31} Like vital blue dyes, ICG is a small molecule organic dye and migrates quickly through the lymphatic system resulting in a relatively short detection window after injection and the necessity for careful timing to intraoperatively identify the SLNs. In practice, this may require the use of 50-fold higher ICG dosages than the one used in the current study.²⁰ Moreover, rather than visualizing lymph flow with fluorescence imaging, the hybrid approach individually illuminated the very nodes identified on lymphoscintigrams and SPECT/CT. The high rate of fluorescence containing SLNs visualized in the operating room (95%) compared to the relatively low percentage of SLNs that were stained blue (54%) underline how the fluorescent component of ICG-^{99m}Tc-nanocolloid can improve optical identification of the SLNs. In addition, the time window for fluorescence detection was possible up to 23 hrs post-injection. The improved

tissue penetration fluorescence imaging offers over vital blue dyes and the high resolution that can be obtained compared to gamma tracing modalities help enhance (optical) identification of the SLNs. This proved to be especially helpful when high radioactive background signals impeded SLN localization using the probe, in accordance with previous findings in head and neck melanoma and prostate cancer patients.^{23,27}

In the present study, the application of hybrid ICG-^{99m}Tc-nanocolloid has successfully been extended to anatomical areas such as the axilla and the groin. This encourages further extension of this technique to other areas where radioguided surgery can be challenging. The introduction of hybrid tracers also poses new technological challenges for manufacturers of imaging systems. In the current study, separate devices for radioguided and optical sentinel detection were used. In the future, the development of hybrid devices combining both techniques may further improve the logistics in daily clinical practice.

Conclusion

The lymphatic drainage pattern of hybrid ICG-^{99m}Tc-nanocolloid is identical to that of ^{99m}Tc-nanocolloid. These findings, together with the added value of intraoperative fluorescence guidance, warrant further evaluation of hybrid ICG-^{99m}Tc-nanocolloid as a tracer for SLN procedures.

References

- 1 Jansen L, Koops HS, Nieweg OE, Doting MH, Kapteijn BA, Balm AJ, Vermey A, Plukker JT, Hoefnagel CA, Piers DA, Kroon BB. Sentinel node biopsy for melanoma in the head and neck region. *Head Neck*. 2000; 22: 27-33
- 2 Saha S, Dan AG, Bilchik AJ, Kitagawa Y, Schochet E, Choudhri S, Saha LT, Wiese D, Morton D, Kitajima M. Historical review of lymphatic mapping in gastrointestinal malignancies. *Ann Surg Oncol*. 2004; 11: 2455-95
- 3 Aikou T, Kitagawa Y, Kitajima M, Uenosono Y, Bilchik AJ, Martinez SR, Saha S. Sentinel lymph node mapping with GI cancer. *Cancer Metastasis Rev*. 2006; 25: 269-277
- 4 Meinhardt W, Valdés-Olmos RA, van der Poel HG, Bex A, Horenblas S. Laparoscopic sentinel node dissection for prostate carcinoma: technical and anatomical observations. *Brit J Urol Int*. 2008; 102: 714-717
- 5 Leijte JA, Hughes B, Graafland NM, Kroon BK, Valdés-Olmos RA, Nieweg OE, Corbishley C, Heenan S, Watkin N, Horenblas S. Two-center evaluation of dynamic sentinel node biopsy for squamous cell carcinoma of the penis. *J Clin Oncol*. 2009; 27: 3325-3329
- 6 Bex A, Vermeeren L, de Windt G, Prevoo W, Horenblas S, Olmos RAV. Feasibility of sentinel node detection in renal cell carcinoma: a pilot study. *Eur J Nucl Med Mol Imaging*. 2010; 37: 1117-1123
- 7 Brouwer OR, Valdés-Olmos RA, Vermeeren L, Hoefnagel CA, Nieweg OE, Horenblas S. SPECT/CT and a portable gamma-camera for image-guided laparoscopic sentinel node biopsy in testicular cancer. *J Nucl Med*. 2011; 52: 551-554
- 8 Nieweg OE, Tanis PJ, Kroon BB. The definition of a sentinel node. *Ann Surg Oncol*. 2001; 8: 538-541
- 9 van der Ploeg IMC, Valdés-Olmos RA, Kroon BBR, Nieweg OE. The Hybrid SPECT/CT as an additional lymphatic mapping tool in patients with breast cancer. *World J Surg*. 2008; 32: 1930-1934
- 10 Vermeeren L, van der Ploeg IM, Valdés-Olmos RA, Meinhardt W, Klop WM, Kroon BB, Nieweg OE. SPECT/CT for preoperative sentinel node localization. *J Surg Oncol*. 2010; 101: 184-190
- 11 Vermeeren L, Valdés-Olmos RA, Klop WM, van der Ploeg IM, Nieweg OE, Balm AJ, van den Brekel MW. SPECT/CT for sentinel lymph node mapping in head and neck melanoma. *Head Neck*. 2011; 33: 1-6
- 12 Nieweg OE, Jansen L, Kroon BB. Technique of lymphatic mapping and sentinel node biopsy for melanoma. *Eur J Surg Oncol*. 1998; 24: 520-524

- 13 Kapteijn BA, Nieweg OE, Liem I, Mooi WJ, Balm AJ, Muller SH, Peterse JL, Valdés-Olmos RA, Hoefnagel CA, Kroon BB. Localizing the sentinel node in cutaneous melanoma: gamma probe detection versus blue dye. *Ann Surg Oncol.* 1997; 4: 156-160
- 14 Tanis PJ, Nieweg OE, van den Brekel MWM, Balm AJM. Dilemma of clinically node-negative head and neck melanoma: outcome of “watch and wait” policy, elective lymph node dissection, and sentinel node biopsy-a systematic review. *Head Neck.* 2008; 30: 380-389
- 15 Kroon BK, Horenblas S, Meinhardt W, van der Poel HG, Bex A, van Tinteren H, Valdés-Olmos RA, Nieweg OE. Dynamic sentinel node biopsy in penile carcinoma: evaluation of 10 years experience. *Eur Urol.* 2005; 47: 601-606
- 16 Vermeeren L, Valdés-Olmos RA, Meinhardt W, Horenblas S. Intraoperative imaging for sentinel node identification in prostate carcinoma: its use in combination with other techniques. *J Nucl Med.* 2011; 52: 741-744
- 17 Vermeeren L, Valdés-Olmos RA, Klop WMC, Balm AJM, van den Brekel MWM. A portable gamma-camera for intraoperative detection of sentinel nodes in the head and neck region. *J Nucl Med.* 2010; 51: 700-703
- 18 Vermeeren L, Valdés-Olmos RA, Meinhardt W, Bex A, van der Poel HG, Vogel WV, Sivo F, Hoefnagel CA, Horenblas S. Intraoperative radioguidance with a portable gamma camera: a novel technique for laparoscopic sentinel node localisation in urological malignancies. *Eur J Nucl Med Mol Imaging.* 2009; 36: 1029-1036
- 19 Mieog JS, Troyan SL, Hutteman M, Donohoe KJ, van der Vorst JR, Stockdale A, Liefers GJ, Choi HS, Gibbs-Strauss SL, Putter H, Gioux S, Kuppen PJ, Ashitate Y, Löwik CW, Smit VT, Oketokoun R, Ngo LH, van de Velde CJ, Frangioni JV, Vahrmeijer AL. Toward optimization of imaging system and lymphatic tracer for near-infrared fluorescent sentinel lymph node mapping in breast cancer. *Ann Surg Oncol.* 2011; 18: 2483-2491
- 20 Hutteman M, Mieog JS, van der Vorst JR, Liefers GJ, Putter H, Löwik CW, Frangioni JV, van de Velde CJ, Vahrmeijer AL. Randomized, double-blind comparison of indocyanine green with or without albumin premixing for near-infrared fluorescence imaging of sentinel lymph nodes in breast cancer patients. *Breast Cancer Res Tr.* 2011; 127: 163-170
- 21 Crane LM, Themelis G, Arts HJ, Buddingh KT, Brouwers AH, Ntziachristos V, van Dam GM, van der Zee AG. Intraoperative near-infrared fluorescence imaging for sentinel lymph node detection in vulvar cancer: first clinical results. *Gynecol Oncol.* 2011; 120: 291-295

- 22 Hayashi T, Furukawa H, Oyama A, Funayama E, Saito A, Yamao T, Yamamoto Y. Sentinel lymph node biopsy using real-time fluorescence navigation with indocyanine green in cutaneous head and neck/lip mucosa melanomas. *Head Neck*. 2012; 34(5): 758-761
- 23 van der Poel HG, Buckle T, Brouwer OR, Valdés-Olmos RA, van Leeuwen FWB. Intraoperative laparoscopic fluorescence guidance to the sentinel lymph node in prostate cancer patients: clinical proof of concept of an integrated functional imaging approach using a multimodal tracer. *Eur Urol*. 2011; 60: 826-833
- 24 van Leeuwen AC, Buckle T, Bendle G, Vermeeren L, Valdés-Olmos RA, van de Poel HG, van Leeuwen FWB. Tracer-cocktail injections for combined pre- and intraoperative multimodal imaging of lymph nodes in a spontaneous mouse prostate tumor model. *J Biomed Opt*. 2011; 16: 016004
- 25 Buckle T, van Leeuwen AC, Chin PT, Janssen H, Muller SH, Jonkers J, van Leeuwen FWB. A self-assembled multimodal complex for combined pre- and intraoperative imaging of the sentinel lymph node. *Nanotechnology*. 2010; 21: 355101
- 26 Buckle T, Brouwer OR, Valdés-Olmos RA, van der Poel HG, van Leeuwen FWB. Relation between intraprostatic tracer deposits and sentinel lymph node mapping in prostate cancer patients. *J Nucl Med*. 2012; 53: 1-8
- 27 Brouwer OR, Klop WM, Buckle T, Vermeeren L, van den Brekel MW, Balm AJ, Nieweg OE, Valdés Olmos RA, van Leeuwen FWB. Feasibility of Sentinel Node Biopsy in Head and Neck Melanoma Using a Hybrid Radioactive and Fluorescent Tracer. *Ann Surg Oncol*. 2012 Jun; 19(6): 1988-1994
- 28 van den Berg NS, Brouwer OR, Klop WM, Karakullucku B, Zuur CL, Tan IB, Balm AJ, van den Brekel MW, Valdés-Olmos RA, van Leeuwen FWB. Concomitant radio- and fluorescence-guided sentinel lymph node biopsy of the oral cavity using ICG-(99m) Tc-nanocolloid. *Eur J Nucl Med Mol Imaging*. 2012; 39(7): 1128-1136
- 29 Kroon BK, Valdés-Olmos RA, van Tinteren H, Nieweg OE, Horenblas S. Reproducibility of lymphoscintigraphy for lymphatic mapping in patients with penile carcinoma. *J Urol*. 2005; 174: 2214-2217
- 30 Kapteijn BA, Nieweg OE, Valdés-Olmos RA, Liem IH, Panday RK, Hoefnagel CA, Kroon BB. Reproducibility of lymphoscintigraphy for lymphatic mapping in cutaneous melanoma. *J Nucl Med*. 1996; 37: 972-975
- 31 Bredell MG. Sentinel lymph node mapping by indocyanin green fluorescence imaging in oropharyngeal cancer - preliminary experience. *Head Neck Oncol*. 2010; 2: 31

Interventional

**Intraoperative laparoscopic fluorescence
molecular imaging,**

**guidance to the sentinel lymph node
a hybrid approach**

in prostate cancer patients; clinical proof of

concept of an integrated functional imaging

approach using a hybrid imaging agent

Chapter 6

Adapted from:

van der Poel HG, Buckle T, Brouwer OR, Valdés-Olmos RA, van Leeuwen FWB.

Eur Urol. 2011; 60(4): 826-33

The Surgery in Motion video accompanying this article can be found in the online version at doi:10.1016/j.eururo.2011.03.024

and via www.europeanurology.com or www.youtube.com/watch?v=wEoE5NkLxeQ.

Abstract

Integration of molecular imaging and in particular intraoperative image guidance is expected to improve surgical accuracy of minimally invasive procedures such as laparoscopic sentinel lymph node (SLN) biopsy. The applicability of combined pre- intra-, and postoperative SLN imaging using an integrated diagnostic approach was evaluated using the hybrid imaging agent ICG-^{99m}Tc-nanocolloid. Eleven patients with prostate carcinoma scheduled for robot-assisted laparoscopic prostatectomy (RALP) with an increased risk of nodal metastasis participated in a pilot assessment. ICG-^{99m}Tc-nanocolloid was injected into the prostate prior to surgery. Preoperatively, SLNs were identified using lymphoscintigraphy and single photon emission computed tomography combined with computed tomography (SPECT/CT). During the surgical procedure a fluorescence laparoscope, optimized for detection in the near-infrared range, was used to visualize the preoperatively identified SLNs. Fluorescence particularly improved surgical guidance in areas with a high radioactive background signal such as the injection site. Ex vivo analysis revealed a strong correlation between the radioactive and fluorescent content in the excised SLNs. These results indicate that the hybrid imaging agent ICG-^{99m}Tc-nanocolloid, can be used to facilitate and optimize dissection of SLNs during laparoscopic procedures.

Introduction

Functional (optical) imaging holds great promise to supplement the surgeons' eye and to help improve the surgical outcome.^{1,2} One practical clinical application where imaging can help guide the surgical intervention is the identification of lymph nodes (LNs) draining directly from the tumor (referred to as sentinel lymph nodes; SLNs). Functional imaging of SLNs depends on lymphatic migration and nodal accumulation of an imaging agent.^{3,4} Because imaging agents which visualize lymphatic drainage do not require targeting moieties, they can be relatively simple in design, improving their translational character. For this reason SLN imaging provides a platform for the introduction of new surgical guidance technologies that may later be expanded to other surgical applications.

The identification of SLNs is common practice in for example breast cancer and melanoma.^{5,6} Although the role of SLN dissection in prostate cancer is still under debate, lymphadenectomy does enable accurate staging of the lymphatic tumor spread.^{7,8} SLNs outside the area of extended pelvic lymphadenectomy have also been described, underlining the need to document lymphatic drainage pathways for each individual patient.⁹ We reason that more accurate removal of prostate cancer associated SLNs will help identify the value of SLN biopsy in prostate cancer patients and may provide more accurate staging. Preoperative single photon emission computed tomography/computed tomography (SPECT/CT) imaging provides useful anatomical information regarding the location of the SLNs and allows for the identification of SLNs that lie beyond the standard dissection margins.¹⁰ In addition to their diagnostic purposes, these preoperative images can act as a guide during surgery.

Prostatectomy procedures have shifted from use of an open approach towards less invasive laparoscopic and robot-assisted techniques.¹¹ Although advances in surgical instrumentation have been made, fluorescence guided (robotic) surgery is still in its infancy. Integration of optical imaging modalities that specifically visualize the areas of interest may provide the next step in the technical evolution of surgical interventions. Most clinical studies regarding optical surgical guidance to the SLNs focused on the use of the fluorescent dye indocyanine green (ICG).^{12,13} Limiting in this approach is that the rapidly migrating ICG has to be administered intraoperatively and its pharmacokinetics and distribution cannot be accurately monitored. To circumvent these problems a hybrid imaging agent (ICG-^{99m}Tc-nanocolloid) that contains both a radioactive and a fluorescent component was developed. The principal advantage of this hybrid imaging agent is that

it retains the well-established functional properties of ^{99m}Tc -nanocolloid, including accumulation in the SLNs, while providing complementary optical properties.¹⁴⁻¹⁷

In this Chapter the first clinical results of an integrated method that enables combined preoperative detection and intraoperative visualization of the SLNs in prostate cancer patients were presented.

Materials and Methods

Patients

Between June 2010 and Januari 2011, eleven patients with prostate carcinoma scheduled for robot-assisted laparoscopic prostatectomy (RALP) with an increased risk of nodal metastasis, based on MSKCC/Kattan nomogram estimation were included. Inclusion criteria comprised the presence of one or more of the following characteristics: clinical stage greater than T2b, prostate serum antigen (PSA) level greater than 10.0 ng/mL, or Gleason sum score greater than 6. Patient characteristics are shown in Table 1. The surgical intervention was performed using a da Vinci S robotic system (Intuitive Surgical). During this procedure, both the prostate and SLNs were excised. Additionally, the nodal areas of the internal, obturator, and external LNs were dissected. LNs proximal to the ureter vessel crossing were only removed when SLNs were detected in this area. The study was performed conform protocol (N09IGF) after receiving approval from the local ethics committee of the NKI-AvL and after written patient consent was obtained.

Tracer preparation

^{99m}Tc -nanocolloid was prepared by adding 1 mL pertechnetate (approximately 700 MBq) in saline to a vial containing albumin nanocolloid (NanoColl; GE-Healthcare). ICG-PULSION (Pulsion Medical Systems) was prepared by dissolving 25 mg of solid ICG in 5 mL demineralized water. The ICG- ^{99m}Tc -nanocolloid solution was prepared by adding 0.05 mL (0.25 mg ICG) of the ICG-PULSION solution to 1 mL ^{99m}Tc -nanocolloid solution (pH 6 - 7). ICG- ^{99m}Tc -nanocolloid was formed via non-covalent interactions between ICG and albumin molecules.¹⁴⁻¹⁶ All procedures were performed under the Kern Energie Wet (Nuclear Energy Law) using Dutch guidelines for good manufacturing practice and with approval of the local pharmacist.

Tracer administration and imaging

Patients (n = 11) were injected with ICG-^{99m}Tc-nanocolloid (\approx 280 MBq; 0.4 mL) in the peripheral zone of the prostate three hrs prior to surgery (Figure 1).⁸ The imaging agent was injected under transrectal ultrasound guidance (Hitachi) in both lobes of the prostate; each injection was followed by flushing of the needle and tubing with approximately 0.7 mL of saline. A portable gamma camera equipped with a pinhole collimator (Sentinella; Oncovision) was used to confirm adequate concentration of the hybrid imaging agent in the prostate using its radioactive ^{99m}Tc label. Static planar gamma camera images were acquired at 15 min and two hrs post injection. These were used to distinguish between SLNs and second echelon nodes as well as to identify unexpected drainage patterns. SPECT/CT (Siemens) was performed directly after planar imaging at two hrs post injection. SLNs were anatomically localized after image fusion. The first LN in each nodal basin appearing on early planar imaging was considered to be the SLN. LNs appearing later in the same basin were considered to be higher-echelon nodes. SPECT/CT images were displayed in the operation room to guide laparoscopic detection during RALP.

Surgical technique

Intraoperatively, the SLNs were visualized using a dedicated laparoscopic D-light NIR fluorescence camera (Karl Storz). Herein light, emitted by an internal light source (760 nm) is guided through a special fluid light cable to a 30 degrees infrared-optimized rigid laparoscope containing an optical filter system. The image was recorded using a CCD-camera. Intraoperative fluorescence imaging was performed through two 12 mm laparoscopy ports positioned 5 cm lateral to the umbilicus or 2 cm medial from the anterior iliac spine. The fluorescence signal was depicted in green on an additional screen attached to the laparoscope (Figure 1,3 I). During fluorescence imaging the laparoscopic image was projected into the surgeons goggles of the da Vinci S using the systems Tile/Pro function (Figure 1,3 II; fluorescence in blue). After removal of the preoperatively localized SLNs, dissection was guided by a laparoscopic gamma probe (Europrobe) and the fluorescence laparoscope.

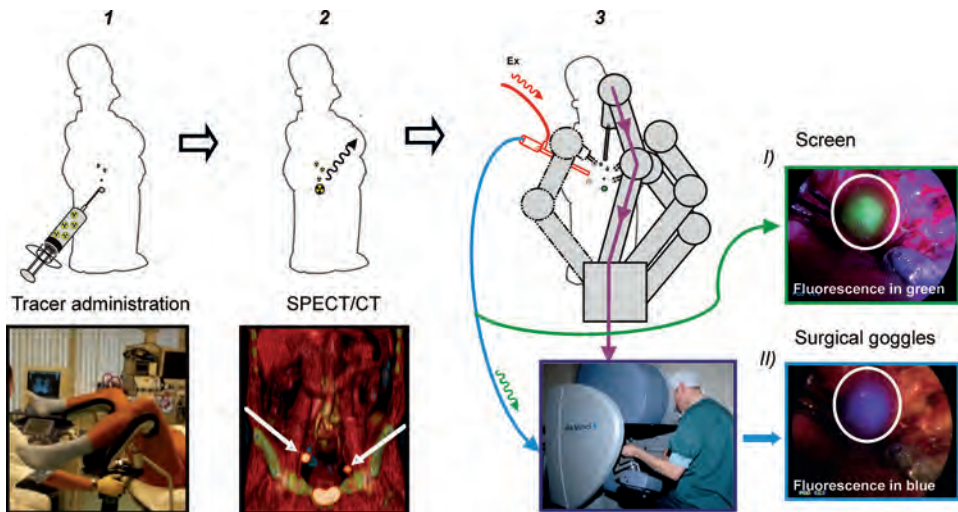


Figure 1. 1. Transrectal ultrasound guided intraprostatic injection of ICG-^{99m}Tc-nanocolloid. 2. Preoperative SPECT-CT showing the anatomical localization of the SLNs (arrows) and 3. intraoperative SLN detection using a laparoscopic near-infrared camera (fluorescence depicted in green). Surgical goggles were used to simultaneously depict the 3D surgical field and the intraoperative laparoscopic fluorescence image in blue (blue arrow; II). White circles highlight the fluorescent area.

Ex vivo specimen analysis

Ex vivo examination of the radioactive signal in the excised LNs was performed using a portable gamma camera (Figure 2A). The radioactive content of the excised tissue was evaluated by placing the head of the gamma camera at a standardized distance of 10 cm above each excised specimen. Radioactive counts were measured using an acquisition time of one min and were quantified using Sentinella Suite software (Oncovision). Fluorescence signal intensities were measured using a preclinical fluorescence scanner (IVIS 200; Xenogen Corp.; Figure 2A). Images were acquired with standard ICG (excitation: 710 - 760 nm; emission: 810 - 875 nm) filter settings. Measured intensities (photons/s/cm²/sr) were quantified using Living Imaging Acquisition and Analysis software (Xenogen Corp.). Trend line based linear regression correlations (Excel) were used to establish the correlation between the fluorescence intensities and the radioactive count rate findings (Table 1).¹⁶ Fluorescence imaging of paraffin-embedded material was used to visualize the location of the tracer injection and its distribution throughout the prostate (Figure 2B). Lymphoid tissue specimens were analyzed in a similar manner to evaluate their fluorescent content and the location of the imaging agent in the SLNs (Figure 2C).

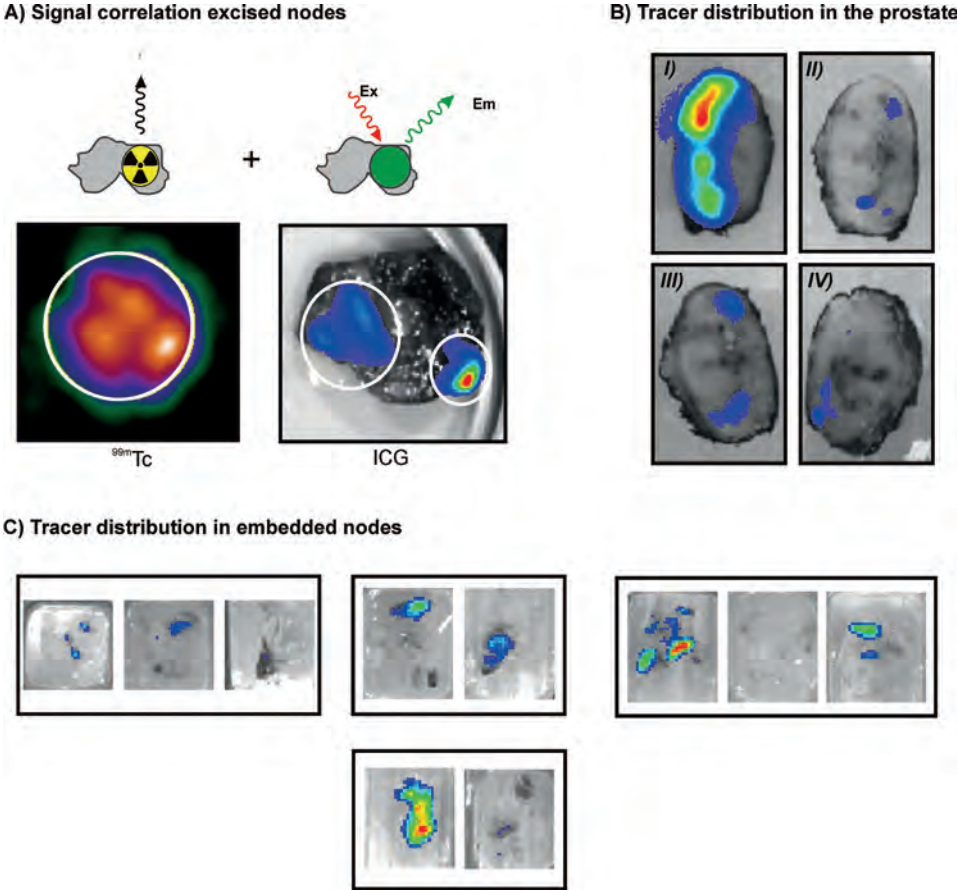


Figure 2. Ex vivo analysis. A) Comparison of ICG-^{99m}Tc-nanocolloid signal in an excised tissue specimen containing SLNs. The radioactive signal was detected using a portable gamma camera and the fluorescence emission was detected using a preclinical fluorescence scanner. B) Fluorescence imaging of paraffin-embedded prostate samples (order I - IV) depicted the injection site and the distribution of ICG-^{99m}Tc-nanocolloid throughout the prostate. C) Fluorescence analysis also allowed detection of the imaging agent accumulation in embedded SLNs.

Results

In Chapters 3 and 4 it was shown that the lymphatic migration of ICG can be positively influenced by the carrier molecule ^{99m}Tc -nanocolloid after formation of the ICG- ^{99m}Tc -nanocolloid complex.¹⁴⁻¹⁶ This hybrid complex provides gradual and specific migration of the imaging agent from the primary injection site into the SLNs (Figure 1). At 15 min post injection SLNs could be visualized in 55% of the patients. This visualization rate increased to 91% at two hrs post injection which is in agreement to previous reports by Jeschke et al.¹⁷ and Vermeeren et al.¹⁰ Preoperatively, 27 SLNs were detected (Table 1) with a median number of two SLNs per patient (range 0 - 4).

During the surgical procedure SLNs were identified in real-time using a combination of a gamma probe and a NIR-optimized fluorescence laparoscope. The radioactive background signal coming from the injection site prevented accurate gamma probe guidance to some of the preoperatively defined SLNs. In these cases, SLNs could be identified with the fluorescence laparoscope. In areas where the radioactive background signal was less prominent, fluorescence imaging provided additional high resolution guidance during the last cm - mm of the SLN identification process. The fluorescence signal output of the NIR-optimized fluorescence laparoscope was presented in both blue and green (Figure 1). For proper detection of the fluorescence signal the white-light intensity of the da Vinci System was dimmed. Overlying tissue (e.g. fat, vessels etc.) had to be removed as it generally obscured the fluorescence image. One of the 27 preoperatively detected SLNs was only detected on SPECT/CT and could not be identified during surgery using either the gamma probe or fluorescence laparoscope (Figure 3). Four of 27 SLNs (15%) could not be detected intraoperatively with the fluorescence laparoscope, but were found to contain fluorescence ex vivo (Table 1, Figure 3). In these cases the SLNs were completely embedded in tissue/fat, resulting in a significant attenuation of the fluorescent signal. Overall, no background staining of free ICG was observed.

Table 1. Patient characteristics and ex vivo correlation between the radioactive and fluorescence signal intensities in the excised nodes.

Age (yrs)	Preop. PSA (ng/ml)	Prostate size (cc)	cT pT	cN pN	cM	cG pG	cG1 pG1	cG2 pG2	SLNs	LN's removed	SLNs with tumor	R ²
1	16,3	41	cT2b pT3a	cN0 pN0	cMx	7 7	3 3	4 4	3	8	0	0.97
2	8,4	78	cT2c pT2c	cN0 pN0	cMx	7 6	3 3	4 3	0	11	0	0.79/0.97 [§]
3	12,2	46	cT2b pT3a	cN0 pN0	cMx	7 8	3 3	4 5	2	11	0	0.91
4	16	26	cT2b pT2c	cN0 pN0	cM0	7 9	3 4	4 5	2	13	0	0.98
5	4,3	40	cT2b pT2c	cNx pN0	cMx	6 7	3 4	3 3	3	9	0	0.81
6	9,8	47	cT2a pT3a	cN0 pN0	cM0	7 7	3 3	4 4	4	10	0	0.99
7	27	40	cT2b pT3a	cN0 pN1	cM0	8 10	5 5	3 5	2	6	1	0.91
8	24	77	cT2c pT3a	cN0 pN0	cM0	6 6	3 3	3 3	3	16	0	0.71*
9	17	35	cT2c pT2c	cN0 pN0	cM0	7 7	3 3	4 4	2	12	0	0.64/0.99*
10 [§]	5,1	22	cT3b	cN0 pN1	cMx	7	4	3	3	4	2 [§]	0.95
11	7,9	23	cT2c pT2c	cN0 pN0	cMx	7 7	3 3	4 3	3	12	0	0.80

TNM staging 2010; T = tumor N = nodes, M = metastases, G = Gleason sum score; c and p represent the clinical and pathological values respectively; SLNs = sentinel lymph nodes; R² = ex vivo correlation between the radioactive and fluorescence signal intensities. * One large piece of excised tissue in which the LN was fully surrounded by a thick layer of tissue was omitted in the correlation; the fluorescence signal could not be accurately detected in this specimen. § This patient did not undergo prostatectomy and due to a lack of lymphatic drainage, no SLN was detected. § Metastases had a tumor size of 0.15 mm and 0.02 mm.

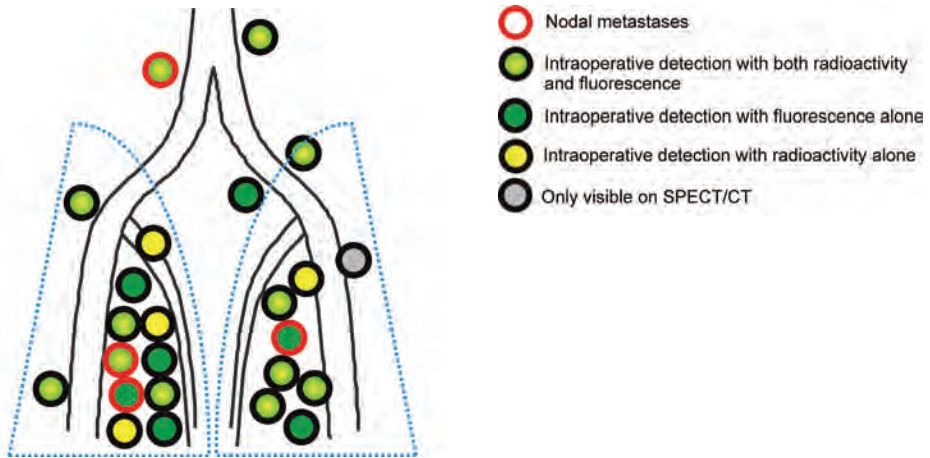


Figure 3. Schematic representation of the excised SLNs based on the preoperative SPECT/CT images, and the modalities with which they could be accurately identified during surgery. The red circles represent metastases containing SLNs. The blue dotted lines encompass the extended dissection field. Note: The inability to detect some of the SLNs in real-time using either the fluorescence laparoscope or the gamma probe is a technical limitation related to the emission type and the modality used as the correlation between fluorescence and radioactive content was high in all excised specimens (Table 1).

Ex vivo gamma- and fluorescence imaging of the dissected specimens (Figure 2A) showed a high signal intensity correlation for all the individual patient samples ($R^2 \geq 0.71$; total 112 LNs investigated; Table 1). This underlines that all radioactive nodes contained fluorescence and to a similar extend. Consequently, visualization difficulties encountered during the surgical procedure were not related to the hybrid imaging agent and its migration.

As expected, the improved spatial resolution of fluorescence imaging allowed identification of the (superficial) SLNs within the resected tissue specimens (Figure 2A). Ex vivo fluorescence imaging can, therefore, also provide pathological guidance towards the SLNs embedded in the excised tissue specimens. The fluorescent signal could still be detected in the embedded samples up until twelve months after the decay of the radioactive signal (Figure 2B and C).

Anatomical locations of the by preoperative and surgically identified SLNs were documented (Figure 3). In 36% of the patients SLNs outside of the extended dissection field were found (obturator fossa + internal iliac + bifurcation iliac vessels + common iliac vessels; Figure 3).^{18,19}

Discussion

The integrated laparoscopic surgical guidance concept that was presented here is based on a hybrid imaging agent (ICG-^{99m}Tc-nanocolloid) that allows both surgical planning via lymphoscintigraphy and/or SPECT/CT and real-time fluorescence-based surgical guidance (Figure 1). Herein the radioactive antenna (^{99m}Tc) was used for preoperative imaging and intraoperative guidance to the region of interest. The fluorescent antenna (ICG) was used for improved intraoperative identification of the SLNs.

We have previously shown that nanocolloid-based procedures were superior over those based on free ICG or ICG bound to (radiolabeled) human serum albumin.¹⁶ In the described procedure any free ICG present during injection will thus already have been cleared at the time of dissection.

The radioactive component in ICG-^{99m}Tc-nanocolloid enabled accurate preoperative assessment of the distribution of the hybrid imaging agent via lymphoscintigraphy and/or SPECT/CT. The anatomical information provided by the CT component was previously shown to improve the SLN detection accuracy up to 98%.¹⁰ During the surgical procedure the SPECT/CT image provided guidance towards the area of the SLN. Still, the spatial orientation is often related to large anatomical structures such as vessels and bone. Movement of internal anatomy of the patient during the surgical procedure limits the accuracy of sole SPECT/CT-based navigation. Real-time gamma probe detection allows acoustic tracing of the SLN location. This technique, however, suffers from background signals coming from the injection site (e.g. prostatic fossa) and collimator issues that hamper depth perception. The use of ICG-^{99m}Tc-nanocolloid enabled us to integrate the advantages of optical fluorescence guidance into these procedures. We found that fluorescence imaging was especially valuable for the intraoperative identification of the SLNs in areas where acoustic gamma tracing was inefficient (Figure 3). In other areas fluorescence helped identify the location of the SLNs with a higher spatial resolution.

One of the shortcomings of fluorescence imaging is the limited tissue penetration of the fluorescence signal. In the current study this prevented real-time surgical detection of the SLNs via fluorescence imaging alone in 15% of the cases; only fully exposed nodes could be accurately detected. This result underlines that fluorescence techniques benefit from additional guidance toward the areas of interest. The next challenge will be to investigate if SPECT/CT based image-navigation can help guide the laparoscope to the SLNs.^{20,21}

The majority of the clinically used intraoperative fluorescence cameras are designed for open surgery, e.g. Photodynamic Eye (Hamamatsu Photonics), the self-built fluorescence-assisted resection and exploration-system (FLARE) and the light-absorption corrected (multispectral) real-time surgical guidance-system (Surgoptics).^{22,23} Due to the less invasive character of laparoscopic surgery there is a clear need to also translate the fluorescence guidance technology into laparoscopic surgery. This translation was facilitated by the D-light fluorescence laparoscope. We found that integration of this laparoscope into the RALP procedures was feasible. The laparoscope could be inserted through one of the existing access ports and the read out of the fluorescence laparoscope could be integrated into the surgical da Vinci goggles. A limitation of the current setting is that the surgical assistant still has to manually guide the fluorescence laparoscope toward the lesions. Future developments that allow the surgeon to independently guide the laparoscope towards the lesion via integration in the robotic-system are expected to improve the accuracy even further.

In our opinion, the widespread development of surgical fluorescence cameras and the development and clinical implementation of new imaging agents are all essential in improving the surgical efficacy. Additionally, integration of these developments into technical surgical procedures such as minimally invasive robot guided surgery will be crucial. The hybrid approach presented here can easily be expanded into other surgical guidance applications such as tumor bracketing²⁴ and receptor targeted tumor imaging.²⁵⁻²⁷ Limiting for these extended applications, however, is obtaining approval for the clinical use of new imaging agents. ICG-^{99m}Tc-nanocolloid circumvents this problem as a cocktail of the in Europe clinically approved ICG and ^{99m}Tc-nanocolloid results in the formation of a hybrid complex without the requirement of any chemical modifications or altering the toxicological profile. As such, ICG-^{99m}Tc-nanocolloid facilitates the clinical introduction of the hybrid surgical guidance concept.

Conclusion

The hybrid radiocolloid ICG-^{99m}Tc-nanocolloid, which contains both a radioactive and fluorescent component, enabled us to link preoperative SPECT/CT guidance with intraoperative NIR-fluorescence laparoscopy. Initial data showed the feasibility of integrating surgical fluorescence guidance into the robot assisted laparoscopic prostatectomy. Real-time fluorescence guidance proved particularly valuable in areas where accurate gamma tracing was hindered by background signal.

References

- 1 Pleijhuis RG, Graafland M, de Vries J, Bart J, de Jong JS, van Dam GM. Obtaining adequate surgical margins in breast-conserving therapy for patients with early-stage breast cancer: current modalities and future directions. *Ann Surg Oncol.* 2009; 16: 2717-2730
- 2 Keereweer S, Kerrebijn JD, van Driel PB, Xie B, Kaijzel E, Snoeks TJ, Que I, Hutteman M, van der Vorst JR, Mieog JS, Vahrmeijer AL, van de Velde CJ, Baatenburg de Jong RJ, Löwik CW. Optical Image-guided Surgery-Where Do We Stand. *Mol Imaging Biol.* 2010; 9: 223-231
- 3 Nunez EGF, Faintuch BL, Teodoro R, Wiecek DP, Martinelli JR, da Silva NG, Castanheira CE, de Oliveira Filho RS, Pasqualini R. Influence of colloid particle profile on sentinel lymph node uptake. *Nucl Med Biol.* 2009; 36: 741-747
- 4 Faries MB, Bedrosian I, Reynolds C, Nguyen HQ, Alavi A, Czerniecki BJ. Active macromolecule uptake by lymph node antigen-presenting cells: a novel mechanism in determining sentinel lymph node status. *Ann Surg Oncol.* 2000; 7: 98-105
- 5 Giuliano AE, Kirgan DM, Guenther JM, Morton DL. Lymphatic mapping and sentinel lymphadenectomy for breast cancer. *Ann Surg.* 1994; 22: 391-398
- 6 Morton DL, Thompson JF, Cochran AJ, Mozzillo N, Elashoff R, Essner R, Nieweg OE, Roses DF, Hoekstra HJ, Karakousis CP, Reintgen DS, Coventry BJ, Glass EC, Wang HJ. Sentinel-node biopsy or nodal observation in melanoma. *N Engl J Med.* 2006; 355: 1307-1317
- 7 Weckermann D, Holl G, Wagner T, Harzmann R. Reliability of preoperative diagnostics and location of lymph node metastases in presumed unilateral prostate cancer. *BJU Int.* 2007; 99: 1036-1040
- 8 Meinhardt W, Valdés-Olmos RA, van der Poel HG, Bex A, Horenblas S. Laparoscopic sentinel node dissection for prostate carcinoma: technical and anatomical observations. *BJU Int.* 2008; 102: 714-717
- 9 Holl G, Dorn R, Wengenmair H, Weckermann D, Sciuk J. Validation of sentinel lymph node dissection in prostate cancer: experience in more than 2,000 patients. *Eur J Nucl Med Mol Imaging.* 2009; 36: 1377-1382
- 10 Vermeeren L, Valdés-Olmos RA, Meinhardt W, Bex A, van der Poel HG, Vogel WV, Sivro F, Hoefnagel CA, Horenblas S. Value of SPECT/CT for detection and anatomical localization of sentinel lymph nodes before laparoscopic sentinel node lymphadenectomy in prostate carcinoma. *J Nucl Med.* 2009; 50: 865-870

- 11 Skolarus TA, Zhang Y, Hollenbeck BK. Robotic surgery in urologic oncology: gathering the evidence. *Expert Rev Pharmacoecon Outcomes Res.* 2010; 10: 421-432
- 12 Crane LM, Themelis G, Budding T, Harlaar NJ, Pleijhuis PG, Sarantopoulos A, van der Zee AG, Ntzicristos V, van Dam GM. Multispectral real-time fluorescence imaging for intraoperative detection of the sentinel node in gynecologic oncology. *J Vis Exp.* 2010; 44: 2225
- 13 Sevick-Muraca EM, Sharma R, Rasmussen JC, Marshall MV, Wendt JA, Pham HQ, Bonefas E, Houston JP, Sampath L, Adams KE, Blanchard DK, Fisher RE, Chiang SB, Elledge R, Mawad ME. Imaging of lymph flow in breast cancer patients after micro-dose administration of a near-infrared fluorophore. *Radiology.* 2008; 246: 734-741
- 14 Buckle T, van Leeuwen AC, Chin PTK, Janssen H, Muller S, Jonkers J, van Leeuwen FWB. A self-assembled multimodal complex for combined pre- and intraoperative imaging of the sentinel lymph node. *Nanotechnology.* 2010; 21: 355101
- 15 Buckle T, Chin PTK, van Leeuwen FWB. (Non-targeted) nanosized radioactive/fluorescent imaging agents for combined pre- and intraoperative imaging of the lymphatic system. *Nanotechnology.* 2010; 21: 482001
- 16 van Leeuwen AC, Buckle T, Vermeeren L, Valdés-Olmos RA, van der Poel HG, van Leeuwen FWB. "Cocktail" injections for combined pre- and intraoperative multimodal imaging of the tumor draining lymph nodes in a spontaneous mouse prostate tumor model. *J Biomed Opt.* 2010; 16: 016004
- 17 Jeschke S, Beri A, Grull M, Ziegerhofer J, Prammer P, Leeb K, Segal W, Janetschek G. Laparoscopic radioisotope-guided sentinel lymph node dissection in staging of prostate cancer. *Eur Urol.* 2008; 53: 126-133
- 18 Brouwer OR, Klop WM, Buckle T, Vermeeren L, van den Brekel MW, Balm AJ, Nieweg OE, Valdés-Olmos RA, van Leeuwen FWB. Feasibility of sentinel node biopsy in head and neck melanoma using a hybrid radioactive and fluorescent tracer. *Ann Surg Oncol.* 2012; 19(6): 1988-1994
- 19 Briganti A, Blute ML, Eastham JH, Graefen M, Heidenreich A, Karnes JR, Montorsi F, Struder UE. Pelvic lymph node dissection in prostate cancer. *Eur Urol.* 2009; 55: 1251-1265
- 20 Brouwer OR, Buckle T, Bunschoten A, Kuil J, Vahrmeijer AL, Wendler T, Valdés-Olmos RA, van der Poel HG, van Leeuwen FWB. Image navigation as a means to expand the boundaries of fluorescence-guided surgery. *Phys Med Biol.* 2012; 57(10): 3123-3136

- 21 Ukimura O. Image-guided surgery in minimally invasive urology. *Curr Opin Urol.* 2010; 20: 136-140
- 22 De Grand GM, Frangioni JV. An operational near-infrared fluorescence imaging system prototype for large animal surgery. *Technol Cancer Res Treat.* 2003; 2: 553-562
- 23 Themelis G, Yoo JS, Soh KS, Schiltz R, Ntziachristos V. Real-time intraoperative fluorescence imaging system using light-absorption correction. *J Biomed Opt.* 2009; 14: 064012
- 24 Buckle T, Chin PTK, van den Berg NS, Loo C, Koops W, van Leeuwen FWB. Tumor bracketing and safety margin estimation using multimodal marker seeds; a proof of concept. *J Biomed Opt.* 2010; 15: 056021
- 25 Kuil J, Velders AH, van Leeuwen FWB. Multimodal tumor-targeting peptides functionalized with both a radio-and a fluorescent-label. *Bioconjugate Chem.* 2010; 21: 1709-1719
- 26 Kuil J, Buckle T, Yuan H, van den Berg NS, Oishi S, Fujii N, Josephson L, van Leeuwen FWB. Synthesis and evaluation of a bimodal CXCR4 antagonistic peptide. *Bioconjugate Chem.* 2011; 22: 859-864
- 27 Sampath L, Kwon S, Hall MA, Price RE, Sevick-Muraca EM. Detection of Cancer metastases with a dual-labeled near-infrared/positron emission tomography imaging agents. *Transl Oncol.* 2010; 3: 307-317

Interventional

Relation between intraprostatic molecular imaging, tracer deposits and sentinel lymph node a hybrid approach mapping in prostate cancer patients

Chapter 7

Adapted from:

Buckle T, Brouwer OR, Valdés-Olmos RA, van der Poel HG, van Leeuwen FWB.

J Nucl Med 2012; 53(7): 1026-1033

Abstract

Intraprostatic injection of the hybrid tracer ICG-^{99m}Tc-nanocolloid has been shown to enable both preoperative sentinel lymph node (SLN) identification and intraoperative visualization of the SLN. By relating the fluorescence deposits in embedded prostate tissue specimens to the preoperatively detected SLNs, the relation between the site of deposition and the lymphatic drainage pattern can be studied. 19 patients with prostate carcinoma scheduled for robot assisted laparoscopic prostatectomy and lymph node (LN) dissection were included to study this effect. ICG-^{99m}Tc-nanocolloid was injected intraprostatically guided by ultrasound. SLN biopsy was performed using a combination of radio- and fluorescence-guidance. Tracer distribution was visualized in paraffin-embedded prostate samples using ex vivo fluorescence imaging. Tracer distribution was correlated to the number and location of the (S)LNs identified on preoperative lymphoscintigraphy and SPECT/CT. Ex vivo fluorescence imaging revealed a large variation in the distribution of the intraprostatic tracer deposits among individual patients. Tracer deposition in the peripheral zone could be correlated to a higher amount of visualized LNs compared to tracer deposition in the central zone (on average 4.7 vs. 2.4 LNs per patient). Furthermore, tracer deposits in the mid gland could be correlated to more visualized LNs compared to deposits located near the base or apex of the prostate (on average 6 vs. 3.5 LNs per patient). In conclusion, the hybrid nature of the tracer does not only enable surgical guidance, but also provides the opportunity to study the correlation between the location of the tracer deposits within the prostate and the number and location of the preoperatively visualized LNs. The acquired data suggests that the location where a tracer deposit is placed is of influence on the lymphatic drainage pattern.

Introduction

Lymph node (LN) metastases are often the initial step in the cascade of metastatic (prostate) cancer spread. Unfortunately, diagnostic imaging modalities such as CT, MRI and ^{18}F -FDG PET lack sensitivity for identification of metastases.^{1,2} Currently, laparoscopic sentinel lymph node (SLN) biopsy followed by histopathological examination of the excised tissue is used to assess the nodal status in prostate cancer patients.^{3,4}

The concept of SLN biopsy has been studied extensively in breast cancer and melanoma.⁵⁻⁷ For prostate cancer, the principle of SLN detection is based on the assumption that accurate SLN identification is possible after intraprostatic injection of a radioactive tracer guided by ultrasound.^{8,9} As the majority of adenocarcinomas arise in the peripheral zone of the prostate,^{10,11} placement of tracer deposits at this location in the prostate is considered favorable for the detection of the tumor draining SLNs. Accurate placement of the intraprostatic tracer deposits may increase the reliability of the entire SLN procedure. However, monitoring of the injection accuracy using the radioactive signature of the injected tracer is difficult.

The extent of lymph node dissection in prostate cancer is a topic of debate.^{8,12} Where some have argued that sole excision of the SLN is a sensitive method to detect (micro) metastases, others favor extensive nodal dissection. Since unexpected locations of SLNs outside the field of an extended pelvic lymphadenectomy are not rare, it is crucial that SLNs are accurately identified preoperatively as well as intraoperatively.⁹

As radioguided intraoperative localization of SLNs based on the acoustic signal generated by a gamma probe has its drawbacks, the surgical guidance concept was previously expanded with the use of fluorescence imaging (Chapter 2 - 6). To achieve this, a hybrid radiocolloid that can be visualized with a gamma camera, single photon emission computed tomography/computed tomography (SPECT/CT) imaging and via near infrared (NIR) fluorescence imaging was developed.^{13,14} This hybrid radiocolloid enabled linking of preoperative SLN identification to intraoperative visualization of the SLNs in patients with prostate carcinoma.¹⁵ Ex vivo assessment of embedded tissue specimens revealed that the fluorescence signal could still be detected long after the radioactivity had decayed.¹⁵ Reasoning that the fluorescent beacon could also be used to analyze intraprostatic tracer distribution in retrospect, we have analyzed the fluorescence signal in prostate specimens. Hereafter, the location of the tracer deposit in the prostate was correlated to the number and location of the (S)LN identified by lymphoscintigraphy and SPECT/CT.

Materials and Methods

Patients

The protocol (N09IGF, NL28143.031.09) was approved by the local ethics committee of the Netherlands Cancer Institute - Antoni van Leeuwenhoek Hospital. Between June 2010 and February 2011, 19 patients with prostate carcinoma of intermediate prognosis scheduled for robot-assisted laparoscopic prostatectomy (RALP) and retroperitoneal lymph node dissection (RPLND) were included after obtaining written informed consent. Inclusion criteria were the presence of one or more of the following characteristics: clinical stage > T2b, prostate serum antigen level > 10.0 ng/mL, or Gleason sum score > 6. The complete patient characteristics are listed in Table 1. In the current study *ex vivo* analyses were performed on the prostate specimens obtained during the surgical intervention described below.

Tracer preparation

^{99m}Tc -nanocolloid was prepared by adding 1 mL pertechnetate (approximately 700 MBq) in saline to a vial containing albumin nanocolloid (NanoColl; GE-Healthcare). ICG-PULSION (Pulsion Medical Systems) was prepared by dissolving 25 mg of solid ICG in 5 mL demineralized water. The ICG- ^{99m}Tc -Nanocolloid solution was prepared by adding 0.05 mL (0.25 mg ICG) of the ICG-PULSION solution to 1 mL ^{99m}Tc -nanocolloid solution (pH 6 - 7). ICG- ^{99m}Tc -nanocolloid was formed via non-covalent interactions between ICG and albumin molecules.¹³⁻¹⁵ All procedures were performed under the Kern Energie Wet (Nuclear Energy Law) using Dutch guidelines for good manufacturing practice and with approval of the local pharmacist.

Table 1. Patient characteristics

	Age (yrs)	PSA (ng/ml)	cT/pT	cN/pN	cM	cG/pG	cG1/pG1	cG2/pG2
1	60	41	cT2b/pT3a	cN0/pN0	cMx	7/7	3/3	4/4
2	64	78	cT2c/pT2c	cN0/pN0	cMx	7/6	3/3	4/3
3	67	46	cT2b/pT3a	cN0/pN0	cMx	7/8	3/3	4/5
4	63	26	cT2b/pT2c	cN0/pN0	cM0	7/9	3/4	4/5
5	50	40	cT2b/pT2c	cNx/pN0	cMx	6/7	3/4	3/3
6	74	47	cT2a/pT3a	cN0/pN0	cM0	7/7	3/3	4/4
7	63	40	cT2b/pT3a	cN0/pN1	cM0	8/10	5/5	3/5
8	62	77	cT2c/pT3a	cN0/pN0	cM0	6/6	3/3	3/3
9	63	35	cT2c/pT2c	cN0/pN0	cM0	7/7	3/3	4/4
10	62	23	cT2c/pT2c	cN0/pN0	cMx	7/7	3/3	4/3
11	63	27	cT2b/pT3b	cN0/pN0	cM0	8/10	5/5	3/5
12	62	27	cT2a/pT2c	cNx/pN0	cM0	6/6	3/3	3/3
13	63	35	cT3c/pT2c	cN0/pN0	cM0	7/7	3/3	4/4
14	67	107	cT2a/pT2b	cN0/pN0	cM0	8/9	5/4	3/5
15	61	37	cT3b/pT3c	cN0/pN1	cM0	6/7	3/3	3/4
16	62	22	cT2c/pT2c	cN0/pN0	cMx	7/7	3/3	4/4
17	56	39	cT2b/pT2c	cNx/pN0	cMx	7/7	3/3	3/4
18	65	42	cT3a/pT2c	cN0/pN0	cM0	7/7	3/3	4/4
19	49	19	cT3a/pT2c	cN0/pN0	cM0	6/6	3/3	3/3

PSA = prostate-specific antigen (determined preoperatively); G = Gleason sum score; c = clinical values; p = pathologic values; T = tumor status; N = nodal status; M = distant metastases.

Tracer administration and preoperative imaging

Tracer was administered approximately three hrs prior to surgery (Figure 1). Transrectal positioning of the needle into the prostate was guided by ultrasound (Hitachi). Injections were performed by three different urologists. Subsequently, both lobes of the prostate were injected with two tracer deposits of 0.1 mL each (total volume 0.4 mL, average dose 280 MBq). The needle and tubing were flushed with approximately 0.7 mL of saline after placement of each tracer deposit. To assess the adequacy of delivery each tracer deposit, intraprostatic tracer retention was monitored using a portable gamma camera equipped with a pinhole collimator (Sentinella; Oncovision).

Planar lymphoscintigraphy (anterior and lateral 5 min images) was performed at the nuclear medicine department at 15 min and two hrs post injection using a hybrid dual-head camera (Symbia T, Siemens). The first LN in each nodal basin appearing on early planar imaging was considered to be the SLN (SLN1), whereas LNs appearing later in the same basin were considered higher echelon nodes. For anatomical localization of the SLNs, SPECT/CT was performed directly after planar imaging at two hrs post injection using the same hybrid camera system. If SPECT/CT revealed additional hot spots in caudal areas or on a side without previous drainage, these hotspots were also considered to be SLNs. The amount of radioactivity in the SLNs was determined by measuring the counts/cm² per LN using Osirix software. The total activity on the left and right side of the body was determined by calculating the sum of the measured counts in all visualized LNs. Using these count rates, the total percentage of radioactivity (%RA) per patient and the mean percentage of radioactivity on each side were calculated. To determine the mean percentage of radioactivity in SLN1, only count rates in that SLN were used.

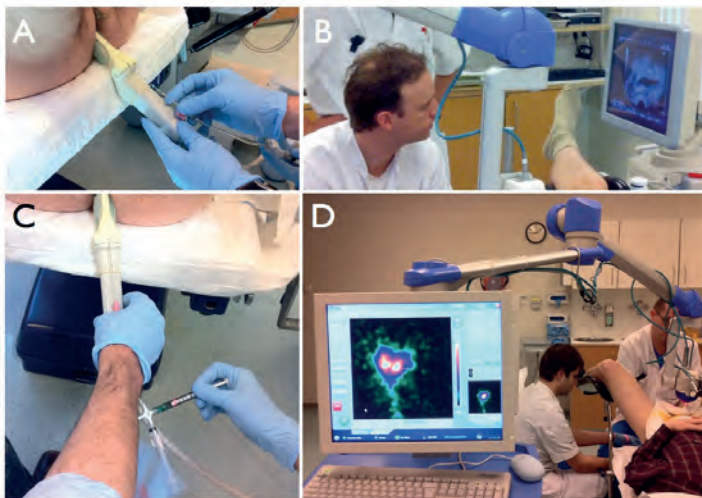


Figure 1. Intraprostatic injection procedure. A, B) Placement of the needle was conducted guided by ultrasound. C) ICG-^{99m}Tc-nanocolloid was injected into the prostate. D) A portable gamma camera was used to confirm adequate concentration of the tracer in the prostate using its radioactive ^{99m}Tc label.

Surgical procedure

SLNs were intraoperatively localized and excised after prostatectomy using a laparoscopic gamma probe (Europrobe, Euro Medical Instruments; Figure 2) and a fluorescence laparoscope (D-light system, Karl Storz Endoscopes, Germany). A RPLND was performed after SLN excision in all patients. When no SLNs were identified preoperatively, a LN dissection was performed comprising the internal/external iliac and obturator nodes.¹⁵

Ex vivo specimen analysis

Fluorescence imaging of paraffin-embedded prostate tissue was used to visualize the location of the tracer deposits. For each patient, 2 - 6 sections were analyzed. An overview of the tracer deposits throughout the prostate was created by combining of the sections of each patient. Figure 3 illustrates the different zones and the orientation of the prostate; the x-axis visualizes the difference between the left and right side of the prostate, the y-axis follows the path from the bottom (peripheral zone) to the top (central zone) and the z-axis follows the base to the apex of the prostate. No discrimination was made between the transition and central zone; both are specified as the central zone. Fluorescence signal intensities were measured using a preclinical fluorescence camera (IVIS 200 camera; Xenogen Corp.). Images were acquired with standard ICG filter settings (excitation 710 - 760 nm and emission 810 - 875 nm). Measured intensities (photons/s/cm²/sr) were quantified using Living Imaging Acquisition and Analysis software (Xenogen Corp.). For analysis, the prostate was divided into four quadrants (Q1-Q4, Figure 1B); Q1 and Q3 representing the left side of the prostate and Q2 and Q4 representing the right side. Q1 and Q2 were deemed to include the largest part of the central zone of the prostate, whereas Q3 and Q4 were deemed to mostly represent the peripheral zone. Per section, distribution of the fluorescence signal was evaluated and the (mean) percentage of fluorescence in each quadrant was calculated.

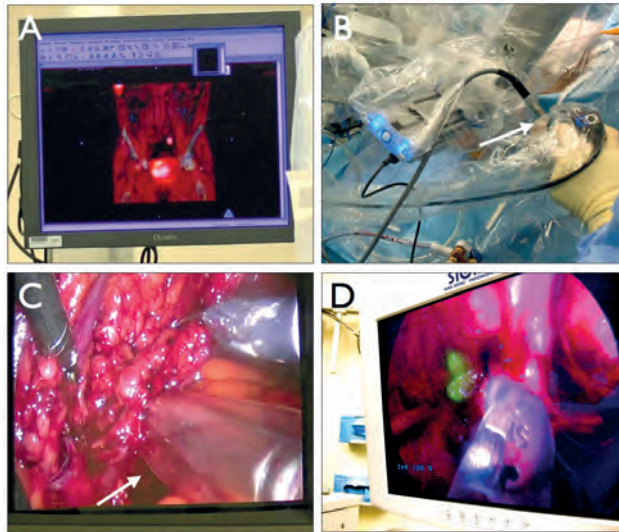


Figure 2. Robot-assisted intraoperative SLN biopsy. A) The SPECT/CT image was acquired to preoperatively determine the exact location of the SLN and is displayed in the operation room. B) During the surgical procedure, a gamma probe and fluorescence laparoscope (arrow) were inserted through one of the access ports. C) The acoustic signal produced by the gamma probe (arrow) was used to roughly guide the surgeon towards the location of the SLN. D) The SLNs (depicted in green) were visualized using the fluorescence laparoscope.

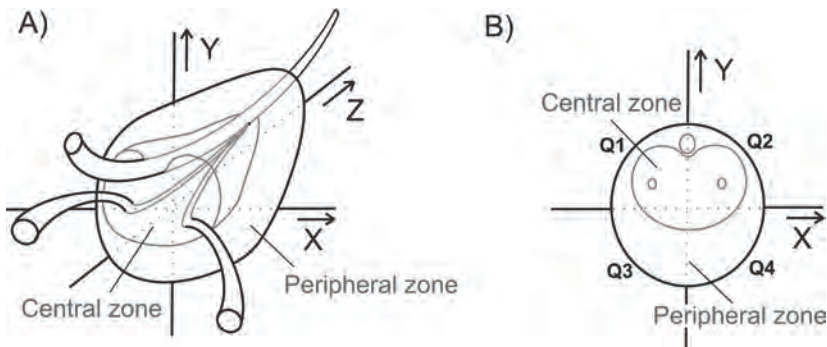


Figure 3. Schematic representation of the prostate. A) Within the prostate, discrimination can be made between the peripheral and central zone due to differences in tissue morphology. The base of the prostate is wider than the apex and is located next to the bladder. B) For quantification purposes, the embedded sections of the prostate samples were divided into four quadrants (Q1-4). Q1 and Q2 represent the central zone whereas Q3 and Q4 represent the peripheral zone.

Results

In Chapter 6 the use of ICG-^{99m}Tc-nanocolloid for combined preoperative detection and image guided dissection of SLNs in eleven patients with prostate carcinoma using radio- and fluorescence guidance was described.¹⁵ In the 19 patients reported here (eight additional patients included) the possibility to ex vivo assess the placement of the tracer deposit with fluorescence imaging was explored. The efficacy of the hybrid guidance procedure in this enlarged patient population remained similar to the previous report.

Pathological analysis of the embedded prostate samples showed that in all prostate samples tumor tissue was mainly present in Q3 and Q4 (84%), which corresponds with the peripheral zone of the prostate (Figure 3). Tumor spread was determined during pathologic analysis of the embedded prostate sections. In all patients tumor was found in the third quadrant (Q3; Figure 3, Table 2). In 16 patients tumor was also present in Q4. In three prostate samples tumor was present in Q1 or Q2 next to presence of tumor in Q3 and/or Q4 and in three patients tumor was present in all quadrants.

Table 2. Tumor presence

Patient nr	Q1	Q2	Q3	Q4
1			X	
2			X	X
3	X	X	X	X
4			X	X
5	X		X	
6	X		X	X
7			X	X
8		X	X	X
9	X	X	X	X
10	X		X	X

Patient nr	Q1	Q2	Q3	Q4
11	X	X	X	X
12			X	X
13			X	X
14			X	
15			X	X
16			X	X
17	X	X	X	X
18			X	X
19			X	X

X= presence of tumor. Q1-4 depict the different quadrants in the prostate.

Ex vivo fluorescence imaging of the tracer deposits

Within the paraffin-embedded sections of the prostate, fluorescence could still be detected more than twelve months after prostatectomy and embedding of the tissue. Overlay pictures wherein the fluorescence image was superimposed on a photograph of

that specific section of the prostate were used to determine the location of the tracer deposits. Figure 4 illustrates the variations that were found. Figure 4A depicts the fluorescence signal in the different sections of the prostate and the corresponding lymphoscintigraphy image in two representative patients; in patient 8 the tracer was injected into the peripheral zone, while in patient 6 the tracer was injected into the central zone of the prostate. The location of tracer deposits for all individual patients are graphically represented in Figure 4B. Clearly, deposits vary in size, intensity (light green deposits depict identical or low intensities, dark green deposits depict deposits with high fluorescent intensity) and location.

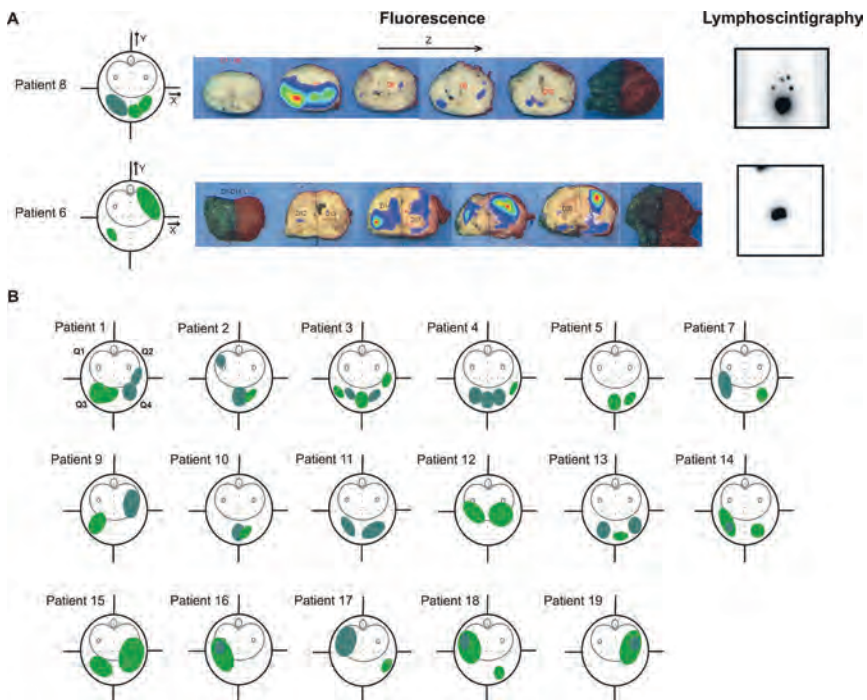


Figure 4. Variations in tracer distribution throughout the prostate. A) Two representative patients examples wherein the tracer was injected evenly distributed over the left and right side of the peripheral zone (patient number 8), and mostly in the central zone on the right with a single deposit in the peripheral zone on the left (patient number 6). These images also illustrate the variation in the z-direction. B) A schematic overview of the tracer deposits per prostate sample. Fluorescence deposits are depicted in green (light green for deposits with comparable or low intensity; dark green for deposits with high intensity).

Table 3. Fluorescence distribution observed ex vivo

Patient nr	Q1	Q2	Q3	Q4	Injection site #	Tracer distribution throughout the prostate (base-mid gland-apex) *
1	12 ± 5	16 ± 5	34 ± 8	37 ± 15	L peripheral zone, R peripheral and central zone	No FL in mid gland; deposits near base and apex
2	19 ± 3	13 ± 1	40 ± 9	28 ± 7	Central in prostate, mostly peripheral zone	FL mostly in mid gland; hotspot L central zone
3	12 ± 4	17 ± 8	36 ± 6	37 ± 7	Central in prostate, peripheral zone	Evenly over all sections
4	11 ± 2	13 ± 3	35 ± 13	41 ± 11	Central in prostate, peripheral zone	FL mostly in central section
5	13 ± 3	26 ± 8	23 ± 6	36 ± 4	Central in prostate, peripheral zone	Evenly over all sections
6	15 ± 4	35 ± 18	23 ± 6	33 ± 12	Mostly central zone	Evenly over all sections
7	16 ± 8	12 ± 5	52 ± 16	20 ± 4	Mostly peripheral zone	FL in all sections; largest deposit near base
8	12 ± 2	12 ± 5	44 ± 9	32 ± 7	Peripheral zone	FL mostly in mid gland
9	12 ± 6	21 ± 13	43 ± 19	27 ± 14	L peripheral zone, R mostly central zone	FL in all sections; largest deposit near apex
10	13 ± 5	15 ± 5	31 ± 4	41 ± 7	Central in prostate, peripheral zone	Evenly over all sections
11	10 ± 3	9 ± 2	55 ± 5	26 ± 4	Peripheral zone	No FL in mid gland; deposits near base and apex
12	14 ± 4	25 ± 12	24 ± 4	37 ± 12	Peripheral and central zone	Evenly over all sections
13	12 ± 4	13 ± 3	44 ± 14	30 ± 12	Peripheral zone	No FL in mid gland; deposits near base (L) and apex (R)
14	23 ± 11	19 ± 9	34 ± 15	24 ± 10	Peripheral zone	FL in all sections; largest deposit near base
15	6 ± 1	24 ± 11	32 ± 12	37 ± 11	Peripheral zone and R central zone	Evenly over all sections
16	28 ± 13	16 ± 5	40 ± 13	16 ± 5	L central zone and peripheral zone	Evenly over all sections
17	43 ± 13	8 ± 3	41 ± 12	8 ± 2	L central zone	Evenly over all sections
18	18 ± 8	10 ± 5	52 ± 9	20 ± 7	L mostly central zone	Evenly over all sections
19	7 ± 3	40 ± 12	12 ± 5	48 ± 11	R mostly central zone	FL in all sections; largest deposit near base of prostate

In Q1-Q4 the mean percentage of fluorescence per quadrant is shown. The injection site was determined by evaluation of the fluorescence signal in the different zones of the prostate (central zone: Q1-Q2; peripheral zone: Q3-Q4). Distribution throughout the prostate was determined evaluating the fluorescence in each section of the prostate L = left, R = right, FL = fluorescence. * For a schematic overview of the distribution of the signal throughout the prostate per patient, see Figure 2.

Table 4. Radioactivity based distribution in preoperatively defined (S)LN.

Patient nr	SLNs on lymphoscintigraphy	Number of LN L	SLN1 L (counts)	Total L (counts)	Number of LN R	SLN1 R (counts)	Total R (counts)
1	L: 2 (ext. + int.) R: 1 (ext.)	4	1971 †	3943 ‡	1	1573	1573
2	L: 2 (int., presacral) R: 1 (ext.)	4	1808 †	4714 ‡	1	1705	1705
3	L: 3 (obt.) R: 1 (obt.)	2	1973 †	2928 ‡	1	799	799
4	L: 3 (obt.) R: 1 (obt.)	3	553	1435 ‡	1	1051 †	1051
5	L: 1-2 (obt.) R: 1 (comm. bif)	1	796	796	1	1367 †	1367 ‡
6	L: - R: -	-	-	-	-	-	-
7	L: 1 (ext.) R: 1 (comm.)	1	2292 †	2292 ‡	1	1505	1505
8	L: 2 (obt., aortabifurcation) R: 1 (obt.)	3	4087 †	10008 ‡	2	2998	4022
9	L: 1 (obt.) R: 2 (obt., paracaval)	5	2396 †	6507 ‡	5	1772	5622
10	L: 2 (ext., int.) R: 2 (ext., int.)	4	3050 †	5053 ‡	2	1576	2084
11	L: 1 (obt.) R: 1 (ext.)	2	639	1134	1	1784 †	1784 ‡
12	L: 2 (ext., int.) R: 1 (ext.)	4	3233 †	7787 ‡	2	1188	3128
13	L: 1 (obt.) R: 1 (obt.)	1	585	585	2	982 †	1324 ‡
14	L: 2 (obt., comm.) R: -	3	1851 †	3967 ‡	1	-	632
15	L: - R: 1 (obt.)	-	-	371	-	-§ †	404 ‡
16	L: 2 (obt., int., ext.) R: 1 (obt.)	2	4005 †	5775 ‡	2	877	1745
17	L: 2 (int., comm.) R: -	2	1305 †	2131 ‡	-	-	772
18	L: 1 (obt.) R: 1 (obt.)	2	691 †	1120 ‡	1	454	454
19	L: - R: 1 (externa)	-	-	760	2	1227 †	2093 ‡

Highest number of visualized LNs (L or R) are depicted in bold. † highest amount of counts in SLN1 (L or R). ‡ highest activity (total; L or R). § SLN visualized only on SPECT/CT. Ext. = external iliac; int. = internal iliac; obt. = obturator; comm. bif. = common iliac bifurcation; comm. = common iliac

To provide a more quantitative readout, the mean percentage of fluorescence in each quadrant of the prostate (Q1-Q4; Figure 3) per patient is shown in Table 3. In most patients the sum of Q3 and Q4 was higher than the sum of Q1 and Q2. In 68% of the patients a clear difference in signal presence was observed between the left and right side. In 53% of patients, the tracer was injected into the peripheral zone of the prostate, in 31% in the peripheral and central zone and in 16% only in the central zone (Figure 4; y-axis).

Evaluation of the distribution from the base to the apex of the prostate (Table 3 and Figure 3; z-axis) revealed that in 47% of patients the fluorescence signal was evenly distributed over all sections. In 21% of patients a larger deposit near the base or the apex was detected. In 16% of patients the fluorescence signal was only present near the base and apex whereas in another 16% the fluorescence signal was only present in the mid gland of the prostate.

Radioactivity based evaluation of lymphatic drainage

Immediately after injection a scan was made using a portable gamma-camera to evaluate possible loss of tracer during the injection, e.g. into the bladder or the bloodstream. In patient number 7 and 14 an upcoming signal in the bladder was observed. Loss of tracer could also be evaluated using the SPECT/CT images, which visualize loss of tracer via the bloodstream; in six patients (patient number 6, 9, 12, 13, 15 and 16) a signal in the liver could be detected at 15 min post injection. In one patient this resulted in non-visualization of the SLN (patient number 6). Overall the height of the signal in the SLN seems not to be influenced by the loss of tracer during the injection as the amount of counts/cm² detected did not differ significantly between patients wherein loss of tracer to the bladder or liver was observed (see above) and patients wherein no loss of tracer occurred.

Lymphoscintigraphy and subsequent SPECT/CT imaging were used to visualize the SLNs and second echelon LNs. Except for patient number 6, where no SLNs could be visualized, SLNs were predominantly found in the region of the obturator nerve and internal iliac/external iliac vessels. It must be noted that in patient number 15 the SLN could only be visualized with SPECT/CT at two hrs post injection whereas in all other patients a SLN was visualized with lymphoscintigraphy at 15 min post injection. In six patients (32%; patient number 2, 5, 7, 9, 14 and 17), SLNs situated further along the obturator- internal/external iliac drainage route were identified.

As listed in Table 4, the lymphatic drainage was not equally distributed over both sides of the patients. In eleven patients more LNs were found on the left side (61%) whereas in three patients more LNs were found on the right side (17%). In four patients,

the same amount of LNs was found on both sides (22%). Besides the number of LNs visualized, the activity measured in the first SLN (SLN1) on each side was also slightly different. In Table 4 the side with the highest activity in SLN1 is noted as †. In twelve patients a higher signal was measured in SLN1 on the left side (67%), whereas in six patients a higher signal was measured in SLN1 on the right side (33%). This same trend was seen when the total activity per side was assessed (See ‡ in Table 4 for the highest activity); in 13 patients the total activity was higher on the left side compared to the right side (72%).

Relation between tracer deposit location (fluorescence-based) and the lymphatic drainage pattern (radioactivity-based)

To evaluate the relation between the location of the tracer deposits and the drainage to the LNs, the fluorescence signals were directly correlated to the measured activity in the visualized LNs. Patient 6 was excluded from the comparison as preoperatively no drainage was observed in this patient.

Comparison of the fluorescence detected on the left and right side of the prostate (Figure 3; x-axis) with the radioactivity intensities measured on each side of the body (Table 5) resulted in a positive trend in ten patients (56%). In these patients the highest percentage of fluorescence was found on the side where the highest count rates were detected. When the fluorescence and the radioactivity in SLN1 were compared, this percentage increased to 67%. This, and the fact that in patients wherein tracer was deposited mostly on one side of the prostate a larger number of LNs could be visualized on that side (Table 4) suggests that lymphatic drainage may be influenced by the site of injection (x-axis).

The influence of the injection site is underlined by the eight patients wherein no positive correlation between deposit distribution and the drainage pattern was found (Table 5). In two patients the lack of a correlation could not be explained, whereas in the remaining six patients a clear deposit in the central zone of the prostate (patient number 1, 3, 7 and 12-14; Figure 4 and Table 3) was observed. The possible link between placement of deposits at different locations in the prostate (Fig. 3; y-axis) and the drainage pattern was further evaluated. The location of fluorescent deposits in the prostate (Table 3) was correlated to the amount of LNs detected on lymphoscintigraphy (Table 4). Presence of fluorescence in the central zone of all prostate sections resulted in visualization of a mean of 2.4 LNs per patient (patient number 15 - 19). However, when the fluorescence was

predominantly situated in the peripheral zone of all sections of the prostate the number of visualized LNs increased to an average of 4.7 per patient (patient number 3, 5, 7, 9, 10, 12 and 14). Apparently, the drainage is reduced when the injection is placed partly or completely in the central zone.

A difference in drainage was also observed after injection in different sections of the prostate (Figure 3; z-axis). When tracer deposits were unevenly distributed between the different sections, no positive correlation between the site of the fluorescent deposit and the radioactivity in the LNs was found (Table 5). Placement of tracer deposits in the peripheral zone near the base or apex resulted in visualization of on average 3.5 LNs per patient (patient number 1, 7, 11 and 14). When tracer deposits were placed in the peripheral zone in the mid gland of the prostate the number of visualized LNs per patient increased to an average of 6 (patient number 2, 4, 8 and 9).

In addition to the number of visualized LNs, a clear correlation between the distribution of the tracer deposits (Table 3) and the location of the visualized SLN (Table 4) was observed. Injection into the peripheral zone near the base of the prostate resulted in visualization of a SLN in the common iliac area (patient number 7, 14 and 17), whereas in one patient the injection was localized near the apex of the prostate, yielding a paracaval SLN (patient number 9).

Table 5: Relation between location of fluorescent tracer deposits and lymphatic drainage.

Patient nr	FL% L	FL% R	RA% Total L	RA% Total R	Correlation between FL%/ %RA total	RA% SLN L	RA% SLN1 R	Correlation between FL%/ %RA SLN1
1	47 ± 11	53 ± 11	71	29	No (inverted)	55	45	Yes (large variance FL)
2	59 ± 6	41 ± 6	73	27	Yes (larger difference RA)	52	48	Yes
3	49 ± 7	54 ± 4	79	21	No (inverted)	71	29	No (inverted)
4	46 ± 13	54 ± 13	58	42	Yes (larger difference RA)	35	65	Yes (difference RA larger)
5	39 ± 7	61 ± 7	37	63	Yes	37	63	Yes
6	38 ± 6	69 ± 9	-	-	No (no drainage)	-	-	No (no drainage)
7	68 ± 8	32 ± 8	37	63	No (inverted)	60	40	Yes
8	56 ± 9	44 ± 9	71	29	Yes (larger difference RA)	58	42	Yes
9	55 ± 21	48 ± 24	54	46	Yes	58	42	Yes
10	45 ± 4	55 ± 4	71	29	No	66	34	
11	65 ± 4	35 ± 4	39	61	No (inverted)	26	74	No (inverted)
12	38 ± 0	66 ± 0	71	29	No (inverted)	73	27	No (inverted)
13	57 ± 13	43 ± 13	31	69	No (inverted)	37	63	No
14	57 ± 18	43 ± 18	86	14	No	100	-	Yes
15	38 ± 12	61 ± 12	48	52	Yes	-	-	Yes§
16	68 ± 4	32 ± 4	77	23	Yes	82	18	Yes (difference RA larger)
17	84 ± 3	16 ± 3	73	27	Yes	100	-	Yes
18	70 ± 11	30 ± 11	71	29	Yes	60	40	Yes
19	20 ± 5	87 ± 16	27	73	Yes	-	100	Yes

In each patient the fluorescence within the different sections of the prostate was determined and the mean percentage of fluorescence (FL%) was calculated on both sides of the body (L/R). To evaluate the relation between the presence of fluorescence and radioactivity, the percentages on the L and R were compared. When the highest percentage of FL and RA was measured on one side of the body (L or R), this was noted as a positive correlation. § SLN visualized with SPECT/CT instead of lymphoscintigraphy.

Discussion

Although a relatively small patient group was evaluated, the results obtained in this study underline the value of the hybrid surgical guidance technology. The present study shows that the position where a tracer deposit is placed in the prostate is of influence on the lymphatic drainage pattern and that large variations in placement do occur in practice. The first point is underlined by Wawroschek et al. who showed that in canines, the site of injection influences the drainage pattern from the prostate.¹⁶

Overall, our data suggests that drainage from the peripheral zone seems to be higher than from the central zone; injection into the peripheral zone of the prostate resulted in visualization of more LNs per patient (Tables 3 and 4). This is in line with the hypothesis stated by Brössner et.al that different zones of the prostate follow a different lymphatic drainage pattern.¹¹ Possibly this difference in lymphatic drainage can be explained by the fact that the structure of the peripheral zone is more densely packed.¹¹ As such, injection of the radiotracer may result in a local increase in the interstitial fluid pressure leading to an increase in lymphatic drainage. The relation between increased fluid pressure after injection and lymphatic drainage may also explain why deposits situated only on the left or right side of the prostate result in a greater number of visualized SLNs (Table 4).

Placement of deposits in different regions (along the z-axis; Figure 3) of the prostate also resulted in visualization of LNs in different basins (Table 4). Deposits clearly situated near the base of the prostate led to the visualization of LNs in the common iliac region, whereas a deposit near the apex of the prostate resulted in visualization of a paracaval SLN. In all cases lymphatic drainage tended to occur via the standard drainage route of the prostate including the obturator, internal iliac, external iliac, common iliac and presacral nodes.¹⁷ These basins are also the most frequent sites of lymphatic metastatic spread.¹⁸

Ideally, SLNs are identified during surgery as these nodes are most likely to harbor possible metastases. Unfortunately, actual visualization of prostate tumor tissue *in vivo* is difficult using current standard imaging methods. When taken into account that prostate cancer predominantly develops in the peripheral zone,^{9,10} which is in line with the results shown in Table 4, we suggest that distribution of tracer over the peripheral zone (Q3-Q4) yields the highest chance of visualizing the SLNs. To compensate for injection errors such as loss of tracer to the bladder resulting in less drainage to one side, it can be recommended to always perform a contralateral RPLND in case of unilateral SLN detection by preoperative imaging.

In the current setting, the tracer was deposited into the prostate under ultrasound guidance, which has a poor sensitivity for tumor visualization. Zonal anatomy of the prostate can be visualized using T2-weighted MR images.^{19,20} Therefore, fusion of MR images with real-time transrectal ultrasound may provide a solution for more accurate injection procedures, without resulting in major adaptations to current patient logistics. Also, as MR guided biopsies and MR guided focal therapy allow real-time visualization of needle placement, methods for MR guided tracer injections could be explored.^{21,22}

The recently developed hybrid radiocolloid allowed us to accurately document tracer locations in archived prostate material. These findings may have implications for SLN biopsies in prostate cancer patients, but more extensive research in this area is necessary.

Conclusion

Besides the potential to improve surgical guidance during (robot-assisted) SLN biopsy, hybrid ICG-^{99m}Tc-nanocolloid provides a unique tool to postoperatively monitor the location of tracer deposits in the prostates of individual patients. This study suggests that the location of intraprostatic tracer deposition may influence the preoperatively visualized lymphatic drainage patterns and as such, the SLN procedure in prostate cancer patients as a whole.

References

- 1 Weckermann D, Dorn R, Trefz M, Wagner T, Wawroschek F, Harzmann R. Sentinel lymph node dissection for prostate cancer: experience with more than 1,000 patients. *J Urol.* 2007; 177: 916-920
- 2 Briganti A, Karnes RJ, Da Pozzo LF, Cozzarini C, Capitanio U, Gallina A, Suardi N, Bianchi M, Tutolo M, Salonia A, Di Muzio N, Rigatti P, Montorsi F, Blute M. Combination of adjuvant hormonal and radiation therapy significantly prolongs survival of patients with pT2-4 pN+ prostate cancer: results of a matched analysis. *Eur Urol.* 2001; 59: 832-840
- 3 Jeschke S, Beri A, Grüll M, Ziegerhofer J, Prammer P, Leeb K, Segal W, Janetschek G. Laparoscopic radioisotope-guided sentinel lymph node dissection in staging of prostate cancer. *Eur Urol.* 2008; 53: 126-132
- 4 Meinhardt W, Valdés-Olmos RA, van der Poel HG, Bex A, Horenblas S. Laparoscopic sentinel node dissection for prostate carcinoma: technical and anatomical observations. *BJU Int.* 2008; 102: 714-717
- 5 Valsecchi ME, Silbermins D, de Rosa N, Wong SL, Lyman GH. Lymphatic mapping and sentinel lymph node biopsy in patients with melanoma: A meta analysis. *J Clin Oncol.* 2011; 29: 1479-1487
- 6 Giuliano AE, Kirgan DM, Guenther JM, Morton DL. Lymphatic mapping and sentinel lymphadenectomy for breast cancer. *Ann Surg.* 1994;220: 391-398; discussion 398-401
- 7 Morton DL, Wen DR, Wong JH, Economou JS, Cagle LA, Storm FK, Foshag LJ, Cochran AJ. Technical details of intraoperative lymphatic mapping for early stage melanoma. *Arch Surg.* 1992; 127: 392-399
- 8 Meinhardt W. Sentinel node evaluation in prostate cancer. *EAU-EBU update series* 5. 2007; 223-231
- 9 Holl G, Dorn R, Wengenmair H, Weckermann D, Sciuk J. Validation of sentinel lymph node dissection in prostate cancer: experience in more than 2,000 patients. *Eur J Nucl Med Mol Imaging.* 2009; 36: 1377-1382
- 10 Coackley F.V., Hrivak H. Radiologic anatomy of the prostate gland: a clinical approach. *Radiol Clin North Am.* 2000; 38: 15-30
- 11 Brössner C, Ringhofer H, Hernady T, Kuber W, Madersbacher S, Pycha A. Lymphatic drainage of prostatic transition and peripheral zones visualized on a three-dimensional workstation. *Urology.* 2001; 57: 389-393

- 12 Briganti A, Blute ML, Eastham JH, Graefen M, Heidenreich A, Karnes JR, Montorsi F, Studer UE. Pelvic lymph node dissection in prostate cancer. *Eur Urol.* 2009; 55: 1251-1265
- 13 Buckle T, van Leeuwen AC, Chin PT, Janssen H, Muller SH, Jonkers J, van Leeuwen FWB. A self-assembled multimodal complex for combined pre- and intra-operative imaging of the sentinel node. *Nanotechnology.* 2010; 21: 355101
- 14 van Leeuwen AC, Buckle T, Bendle G, Vermeeren L, Valdés Olmos R, van de Poel HG, van Leeuwen FWB. Tracer cocktail injections for combined pre- and intraoperative multimodal imaging of lymph nodes in a spontaneous mouse prostate model. *J Biomed Opt.* 2011; 16: 016004
- 15 van der Poel HG, Buckle T, Brouwer OR, Valdés Olmos RA, van Leeuwen FWB. Intraoperative laparoscopic fluorescence guidance to the sentinel lymph node in prostate cancer patients: Clinical proof of concept of an integrated functional imaging approach using a multimodal tracer. *Eur Urol.* 2011; 60: 826-833
- 16 Wawroschek F, Wengenmair H, Senekowitsch-Schmidtke R, Hamm M, Henke J, Schönberger T, Hauser A, Erhardt W, Harzmann R. Prostate lymphoscintigraphy for sentinel lymph node identification in canines: reproducibility, uptake, and biokinetics depending on different injection strategies. *Urol Res.* 2003; 31: 152-158
- 17 Park JM, Charnsangavej C, Yoshimitsu K, Herron D, Robinson TJ, Wallace S. Pathways of nodal metastasis from pelvic tumors. *Radiographics.* 1994; 14: 1309-1321
- 18 Yu KK, Hawkins RA. The prostate: diagnostic evaluation of metastatic disease. *Radiol Clin North Am.* 2000; 38: 139-157
- 19 Mazaheri Y, Shukla-Dave A, Muellner A, Hricak H. MRI of the prostate: Clinical relevance and emerging applications. *J Magn Reson Imaging.* 2011; 33: 258-274
- 20 Verma S, Rajesh A. A clinically relevant approach to imaging prostate cancer: Review. *AJR Am J Roentgenol.* 2011; 196: S1-10
- 21 Haker SJ, Mulkern RV, Roebuck JR, Barnes AS, Dimaio S, Hata N, Tempany CM. Magnetic resonance-guided prostate interventions. *Top Magn Reson Imaging.* 2005; 16: 355-368
- 22 Lundner U, Lawrentschuk N, Trachtenberg J. Image guidance for focal therapy of prostate cancer. *World J Urol.* 2010; 28: 727-734

Interventional Chemokine receptor 4 (CXCR4) molecular imaging, targeting applications a hybrid approach

Part II

Interventional Imaging agents for molecular imaging, the chemokine receptor 4 (CXCR4) a hybrid approach

Chapter 8

Adapted from:

*Kuil J, Buckle T, van Leeuwen FWB.
Chem Soc Rev. 2012; 41(15): 5239-61*

Abstract

The interaction between the chemokine receptor 4 (CXCR4) and stromal cell-derived factor 1 (SDF-1, also known as CXCL12) is a natural regulatory process in the human body. CXCR4 overexpression is found in diseases such as cancer, where it plays a role in, amongst others, metastatic spread. For this reason CXCR4 is an interesting biomarker for the field of diagnostic oncology, and is gaining increasing interest for applications in molecular imaging. In this Chapter small molecule imaging agents based on the CXCR4 targeting T140 peptide are discussed based on their receptor affinity/specificity and/or distribution. The level wherein CXCR4 is upregulated in cancer patients and its relation to the different cell lines and animal models used to evaluate the efficacy of the imaging agents is discussed.

Introduction

The chemokine receptor 4 (CXCR4) is a 7-transmembrane G protein-coupled receptor consisting of 352 amino acids (40 kDa). The interaction between CXCR4 and its natural ligand stromal cell-derived factor-1 (SDF-1, also known as CXCL12, which is an extracellular chemokine consisting of 72 amino acids, 8 kDa) is considered important for directional cell migration (i.e. chemotaxis).¹

CXCR4 is expressed by adult CD34⁺ bone marrow progenitor cells, vascular smooth muscle cells, endothelial cells, retinal pigment epithelial cells, intestinal and alveolar endothelial cells, microglia, neurons and astrocytes, and several types of immune response related cells.² On the other hand, SDF-1 is expressed/secreted by tissues/organs such as fibroblasts, liver and kidney cells and regions in the central nervous system.¹ The cell migratory function of the SDF-1 - CXCR4 chemotactic axis is instrumental during the development of embryos and in the attraction of inflammatory cells.²

Besides its expression in normal tissues, CXCR4 overexpression has also been related to a number of diseases. CXCR4 was first reported as a co-receptor for CD4⁺ T-cell infection of human immunodeficiency virus (HIV) type 1.³⁻⁴ More recently, a role for CXCR4 has been described in the pathogenesis of rheumatoid arthritis.⁵⁻⁷ Upregulation of CXCR4 has been reported in at least 23 different epithelial, mesenchymal and haematopoietic types of cancer.⁸ However, not every cancerous lesion is CXCR4 positive and CXCR4 expression within a tumor is generally heterogeneous with clear positive and negative subpopulations.⁸

In cancer, CXCR4-based chemotaxis acts directly on tumor cell migration and invasion towards an SDF-1 gradient. High expression levels of SDF-1 have been found at the most common sites of breast cancer metastasis: axillary lymph nodes, lungs, liver and bone marrow.^{1,8} CXCR4 overexpression in tumor tissue has been correlated to poor survival,⁹⁻¹⁴ tumor aggressiveness,^{10,11,15,16} increased risk of metastasis^{11,16-18} and a higher probability of recurrence.¹⁹ Due to the important role of CXCR4 in oncology, CXCR4 is a candidate target for therapeutic purposes.⁸ For this reason a number of (small molecule-based) CXCR4 inhibitors have been developed, which have been previously reviewed in several publications.²⁰⁻²⁵ A specific subset of antagonistic peptides is formed by the T140 family. Recently it was found that these CXCR4 targeting moieties also provide versatile platforms for the development of imaging agents (Figure 1).²⁶ The underlying rationale here is that (non-invasive) imaging of CXCR4 can potentially be used to detect tumors and/or highly aggressive subpopulations of tumor cells.

Receptor-targeted²⁷⁻³¹ and enzyme-targeted^{32,33} molecular imaging of cancer had

been reviewed extensively. Furthermore, targets such as somatostatin,^{34,35} $\alpha_v\beta_3$ integrin^{36,37} and bombesin^{38,39} have been published. To date, no comprehensive review involving the emerging target CXCR4 has been published; only a short overview was reported.²⁶ In the following overview CXCR4 targeting imaging agents of the T140 family that are luminescent and/or radioactive are discussed with the parental compounds as a reference. Firstly the clinical situation and preclinical models are described to provide crucial background information. Secondly the potential of the different compounds for (pre)clinical use is assessed.

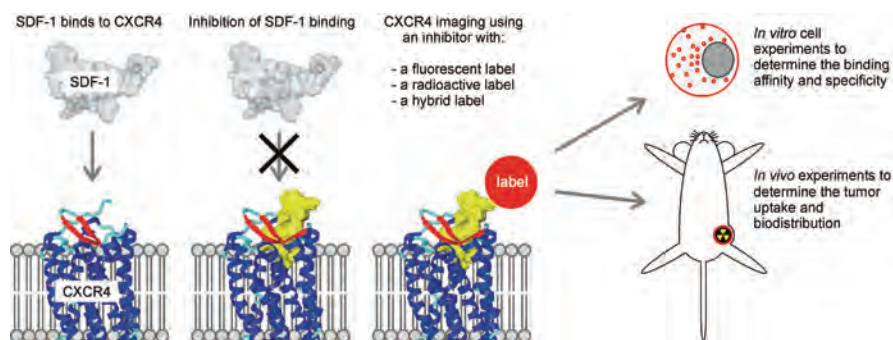


Figure 1. Schematic representation of the interaction between CXCR4 (protein data bank (PDB) code 3OE0) and SDF-1 (PDB code 2K05) and the use of CXCR4 as a target for therapy (inhibitor in yellow) and imaging.

CXCR4 expression levels in oncology: the clinical situation

Immunohistochemical analysis of patient samples, using a variety of different antibodies, revealed staining of CXCR4 in the cytoplasm, on the cell membrane and in the nucleus of the cell (Table 1). The percentage of CXCR4 positive samples ranged from 12% in early breast cancer to > 90% in ductal carcinoma in situ (DCIS), non small cell lung cancer (NSCLC), renal cell carcinoma, mesothelioma, gastric cancer and prostate cancer (Table 1). In metastatic lesions in breast cancer, NSCLC, gastric cancer and renal cell carcinoma the percentages of CXCR4 positive cells ranged between 63.3 and 100% (Table 1).

Overexpression levels of CXCR4 determined with (quantitative) real-time PCR ((Q-)RT-PCR), western blot, immunoblot or immunohistochemistry (IHC) revealed variance in expression between cancer types and stages of tumor progression (Table 2). With the exception of CXCR4 expression levels in renal cell carcinoma, the average expression of CXCR4 in tumor tissue samples was 4.5-fold (range between 2.5 - 6.6-fold; Table 2) higher compared to normal tissue or low CXCR4 expressing cells.

Preclinical models for the evaluation of imaging agents for CXCR4

In the development and evaluation of a new CXCR4 targeting imaging agent a few important challenges have to be met. Firstly, a compound has to bind to the CXCR4 receptor with a high affinity.²⁷ The receptor affinity of a compound is described by the dissociation constant (K_D) or by the half maximum inhibitory concentration (IC_{50}), the latter being more experiment dependent than the K_D .⁶² Both values have to be determined in vitro using cell lines with intrinsic CXCR4 expression or cell lines that overexpress the CXCR4 receptor after transfection with the (human) CXCR4 gene. Secondly, a high specificity is required for differentiation between CXCR4 positive and negative cells, which can also be determined in vitro.³⁰ Especially possible binding to the closely related CXCR7 receptor can cause non-CXCR4 mediated cell binding.⁶³ Thirdly, for a clinical translation, the most ideal imaging agent should provide high tumor uptake, which can be evaluated in vivo in (mouse) tumor models.^{30,64} For toxicity reasons (nonspecific) retention in vital organs should be minimal. This may be especially important for imaging studies wherein high doses of potentially radiotoxic radionuclides are injected.³¹ Fourthly, as CXCR4 is also natively expressed in immune-related cells residing in tissues as the lymph nodes,⁶⁵ background staining in these tissues must be taken into consideration when evaluating both distribution and in vivo imaging results.

Besides challenges during the development of the imaging agents, the preclinical evaluation set-up used can also have a large influence on the obtained data. The CXCR4 expression level in the cells used for in vitro evaluation can be of influence on the determined affinity and even more on the specificity. Similarly, for in vivo evaluation, the (mouse) tumor model, in particular the CXCR4 expression level in the tumor, can influence the tumor accumulation of an imaging agent. All tumor models used for CXCR4 imaging agents are listed in Table 3. The cell line-based tumor models DU4475 and MDAMB231^{CXCR4+} and the transplantation-based MIN-O model show the closest resemblance to the clinical situation, since the level of upregulation is comparable to the average factor of 4.5 measured in patient samples. For the other tumor models the CXCR4 expression level was not specified or higher, due to the use of transfected cell lines (Table 3). As the uptake of an imaging agent is also influenced by tumor morphology and vascular physiology, a transplantation-based model will generally provide a closer resemblance to the human situation than a cell line-based model. Tumor models based on transfected cell lines resemble the clinical situation to a lesser extent,^{31,66} but they are valuable in order to provide an indication whether an imaging agent can be used for tumor visualization at all.

Table 1. Percentage of CXCR4 positive tumor cells in patient samples, determined with immunohistochemistry.

Tissue	Percentage positive samples	Staining	Antibody	
Breast DCIS	92	cytoplasm cell membrane	Anti-human CXCR4 specific mouse monoclonal antibody; 12G5	40
Breast	67	cytoplasm nucleus	Anti-human CXCR4 specific mouse monoclonal antibody; MAB173 clone 44716	41
Pancreatic adeno carcinoma	84.5	cytoplasm cell membrane nucleus	Mouse monoclonal anti human CXCR4; clone not specified	13
Colorectal carcinoma	62	cytoplasm	Goat polyclonal anti-human CXCR4 antibody; AB1671	42
Non small cell lung cancer	95	cytoplasm	Monoclonal mouse anti-human CXCR4; clone not specified	43
Papillary thyroid carcinoma	82	cytoplasm	Anti-human CXCR4 specific mouse monoclonal antibody; 12G5	16
Metastatic prostate cancer	94.2	no localization of staining specified	Goat anti-human polyclonal; SC-6191	9
Renal cell carcinoma	100	cytoplasm cell membrane	Anti-CXCR4; clone not specified	44
Hormonal receptor negative breast cancer	60	cytoplasm nucleus	Anti-human CXCR4 specific mouse monoclonal antibody; MAB172 clone 44716	45
Non small cell lung cancer + brain metastasis	68.8 - 90.6 brain metastasis: 63.3 - 100	cytoplasm cell membrane	Mouse anti-human CXCR4 monoclonal; clone not specified	46
Primary invasive duct breast cancer	77	cytoplasm nucleus	Rabbit polyclonal anti- CXCR4; clone not specified	12
Early breast cancer	12	cytoplasm cell membrane	Anti-human CXCR4 specific mouse monoclonal antibody; clone 44716	17
Stage I-III breast cancer	DCIS 54 Tumors 47	cytoplasm nucleus	pCXCR4	47
Squamous cell carcinoma	40	not specified	Anti-human CXCR4 specific mouse monoclonal antibody; 12G5	48
Thyroid carcinoma	34.3	cytoplasm nucleus	Anti-human CXCR4 specific mouse monoclonal antibody; clone SC53534	49

Gastric cancer	80.0 88.9 in metastatic lymph nodes	cytoplasm	not specified	not specified	50
Mesothelioma	97.6	not specified		Anti-human CXCR4 specific mouse monoclonal antibody; 12G5	51
Renal cell carcinoma	81.4 95.2 in metastasis	cytoplasm (metastasis) cell membrane (primary tumor)		Anti-human CXCR4 antibody; clone not specified	52
Advanced breast cancer	41 67 in bone metastasis	cytoplasm cell membrane nucleus		Clone 44.11; no details about antibody provided	19
Gastric cancer	96.8	cytoplasm cell membrane		Anti-human CXCR4 specific mouse monoclonal antibody; MAB172	11
Node negative breast cancer	81 (cytoplasm) 25 (membrane)	cytoplasm cell membrane		CXCR4 monoclonal antibody; clone not specified	53
Inflammatory breast cancer	40.9	cytoplasm cell membrane nucleus		Anti-human CXCR4 specific mouse monoclonal antibody; 44717.111	54
Esophageal squamous cell (SC) and adenocarcinoma (AC)	SCC 94.1 AC 89.1	cytoplasm cell membrane (weak)		Anti-human CXCR4 specific goat monoclonal antibody; CIO115	55
Non small cell lung cancer	100 (low or high)	cytoplasm		Anti-human CXCR4 specific monoclonal; UMB2	14
Glioblastoma multiforma	66 ± 11	nucleus		Anti-CXCR4; clone not specified	56
Breast cancer	not specified	cytoplasm cell membrane		Anti-human CXCR4 specific rabbit polyclonal antibody; clone not specified	18
Chondrosarcoma	not specified	cytoplasm nucleus		Anti-human CXCR4 specific mouse monoclonal; clone not specified	15
Renal cell carcinoma	not specified	cytoplasm		Anti-human CXCR4 specific goat polyclonal antibody; clone A-17	57
Advanced colorectal cancer	not specified	cytoplasm cell membrane nucleus		Anti-human CXCR4 specific mouse monoclonal antibody; 12G5	58
Renal cell carcinoma	100	cytoplasm cell membrane nucleus		Anti-human CXCR4 specific mouse monoclonal antibody; MAB172 clone 44716	59

Table 2. Quantitative analysis of overexpression levels of CXCR4 in patient samples

Tissue	Screening method	Overexpression (-fold)	n-fold expression related to	Reference
Breast	RT-PCR	3-5	corresponding mammary tissue	60
Colorectal carcinoma colorectal liver-metastasis	Q-RT-PCR	4-5	corresponding normal tissue	42
HER2 negative breast cancer	Western blot	6.6 ± 4.7	a known concentration of HeLa cells	10
Breast	RT-PCR	5	corresponding normal tissue	18
Chondrosarcoma	IHC	2.7	integrated optical density measurements	15
Glioblastoma multiforme	RT-PCR	2.5 (Grade III)-4.9 (GBM)	non-neoplastic controls	56
Renal cell carcinoma	RT-PCR	29.5 (2.3 - 85.2)	normal tissue	57
Hormone receptor positive, node-negative breast cancer	Western blot	6.4 ± 3.4	a concentration of HeLa cells	61
Renal cell carcinoma	immunoblot	1.4 - 46 (average ≈ 5.5)	normal tissue	59

RT-PCR = real-time PCR. Q-RT-PCR = quantitative real-time PCR. GBM = glioblastoma multiforme

Table 3. Level of upregulation of CXCR4 in tumor models

Cell line/ tumor model	Origin	Manor of overexpression	Receptors/cell	Level of upregulation (-fold)	Control cell line	Reference
CHO-CXCR4	Chinese hamster ovary	transfected with human CXCR4	6.8×10^5	186 ^a	U87	67-72
U87 stb CXCR4	Human glioblastoma cell line	transfected with human CXCR4	1.3×10^5	37 ^a 36 ^b	U87	73-74
DU4475	Human breast cancer cell line	intrinsic	1.6×10^4	4.6 ^a	U87	74
MDAMB231 CXCR4	Human breast cancer cell line	upregulation CXCR4 after culture under hypoxic conditions	-	4.4 ^b	MDAMB231	75-76
MDAMB231	Human breast cancer cell line	intrinsic	6.8×10^3	1.9 ^a	U87	74-76
MIN-O	Spontaneous mouse tumor model resembling human ductal carcinoma in situ	intrinsic	-	4.0 ^b	4T1	75,77

^a Mean fluorescence intensity ratio (MFIR) between cell line/tumor model in question and low expressing control cells determined with flow cytometry using antibodies. Please note: the level of upregulation based on MFIRs may be less accurate than comparison of the number of receptors in different cell lines. ^b Ratio between the number of receptors on each cell of the cell line in question and the control cell line.

T140 derivatives

In 1992 Fujii et al. reported on an 18 amino acid-containing peptide that possesses two disulfide bridges that was designed based on the antimicrobial peptides Tachyplesin and polyphemusin.⁷⁸⁻⁸⁰ The potent peptide analog, T140, consists of 14 amino acids and one disulfide bridge (Figure 2A).⁸¹ T140 is an inverse agonist of CXCR4⁸² and its derivatives are one of the most widely studied classes of CXCR4 imaging agents. T140 derivatives have a low nanomolar affinity for CXCR4 and are proven to be specific; they solely bind to CXCR4 and not to CXCR7.^{68,81}

Binding mode

The N- and C-terminus of T140 bind into the cavity of the seven transmembrane helices of CXCR4.⁸³ The pharmacophore of T140 consists of residues Arg², Nal³, Tyr⁵, and Arg¹⁴. Furthermore, residues 7 - 10 in the β -turn of T140 are located at more than 3.0 Å from the CXCR4 receptor.⁸³ This CXCR4 binding model has been corroborated using a crystal structure of the T140 analog CXV15 (Figure 2B; protein data bank (PDB) structure ID: 3OE0).⁸⁴ The crystal structure showed that the binding cavity of CXCR4 is larger, more open and located closer to the extracellular surface compared to other G protein-coupled receptors (GPCRs). Furthermore, it was shown that the peptide CXV15 fills most of the binding pocket: Arg¹-Cys⁴ of CXV15 has interaction with Asp¹⁹⁷-Tyr¹⁹⁰ of CXCR4. Arg² of the peptide also interacts with Thr¹¹⁷, Asp¹⁷¹ and His¹¹³ of CXCR4, Arg¹⁴ of the peptide makes a salt bridge with Asp²⁶² and the C-terminus of the peptide interacts with Asp²⁸⁸.

Based on the location of the pharmacophore in T140, imaging labels can be attached to the N-terminus and the side chains of Lys⁷ and D-Lys⁸ (Figure 2B). During binding, the N-terminus is positioned in the binding cavity of CXCR4, limiting the space for label attachment at this position. Lys⁷ and D-Lys⁸ in the β -turn are directed away from the binding cavity, therefore these residues appear to be the most suited for functionalization.

Inhibitors

T140 has been used as a starting point and reference compound during the development of many derivatives.⁸⁵⁻⁹⁵ One compound in particular, Ac-TZ14011, (Figure 2A), showed a higher binding affinity for CXCR4 and a higher in vivo stability compared to T140. Furthermore, only one amine group is present (D-Lys⁸) in Ac-TZ14011, instead of three in T140, enabling controlled functionalization.^{68,71,96}

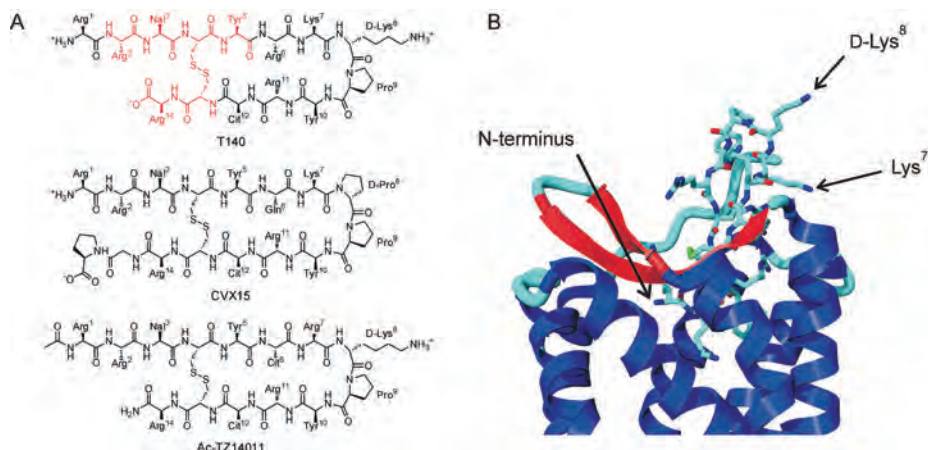


Figure 2. A) T140, CVX15 and Ac-TZ14011. The pharmacophore of the T140 derivatives is indicated in red in T140. B) Model of T140 binding to CXCR4 based on the protein data bank (PDB) structure 3OE0.

Monomeric derivatives

Three versions of imaging agents have been reported: fluorescent, radioactive and hybrid/multimodal (combined fluorescent and radioactive).

Ac-TZ14011 has been labeled on D-Lys⁸ with several fluorescent dyes,^{68,96-99} including FITC ($\lambda_{\text{ex}} = 495 \text{ nm}$, $\lambda_{\text{em}} = 520 \text{ nm}$; Figure 3). The CXCR4 affinity of Ac-TZ14011-FITC is 24-fold lower than that of Ac-TZ14011 (Table 4) despite the fact that molecular modeling demonstrated that D-Lys⁸ is the favored functionalization point. Nevertheless, the binding affinity remained in the nanomolar range and Ac-TZ14011-FITC could be used to discriminate MDAMB231^{CXCR4+} from MDAMB231 cells.⁷⁵ In addition, Ac-TZ14011-FITC was able to identify CXCR4 positive tumor tissue in which the expression level was only 4.4-fold upregulated.⁹⁷

The receptor affinity of both Ac-TZ14011-Flu and Ac-TZ14011-Alexa488 ($\lambda_{\text{ex}} = 495 \text{ nm}$, $\lambda_{\text{em}} = 520 \text{ nm}$ for both compounds) is slightly lower than unlabeled Ac-TZ14011 (factor 3 and 1.5, respectively). Although these compounds are structurally very similar to Ac-TZ14011-FITC (Figure 3, Table 4), their affinity for the CXCR4 receptor seems to be higher.^{68,96} Moreover, Ac-TZ14011-Flu and Ac-TZ14011-Alexa488 possessed high specificity, since they did not bind to the closely related CXCR7 receptor, which was recently reported to also bind SDF-1.⁶³ Ac-TZ14011-Ahx-Flu and Ac-TZ14011-Ahx-TAMRA ($\lambda_{\text{ex}} = 543 \text{ nm}$, $\lambda_{\text{em}} =$

575 nm), which both contain an additional aminohexanoic acid (Ahx) spacer between the peptide and the label, show a binding affinity that is similar to Ac-TZ14011-Flu and Ac-TZ14011-Alexa488 (Table 4).^{68,96} Strangely, the binding affinity of Ac-TZ14011-Ahx-Alexa488 was significantly lower.^{68,96} Ac-TZ14011-Flu, Ac-TZ14011-Alexa488, Ac-TZ14011-Ahx-TAMRA and also Ac-TZ14011-Cy5 ($\lambda_{\text{ex}} = 650 \text{ nm}$, $\lambda_{\text{em}} = 670 \text{ nm}$) could visualize cells with fluorescence microscopy and flow cytometry.⁹⁸ Ac-TZ14011-Flu has also been successfully used in a bladder tumor model in mice.⁹⁹

Ac-TZ14011 has also been functionalized with a relatively large luminescent iridium complex (Ir-(Ac-TZ14011), Figure 3).⁷⁶ The dissociation constant (K_D) of this derivative is 84.4 nM which is in line with other labeled Ac-TZ14011 peptides (Table 4). Uniquely, the iridium complex ($\lambda_{\text{ex}} = 383 - 410 \text{ nm}$, $\lambda_{\text{em}} = 566 - 585 \text{ nm}$) was shown to have a luminescent lifetime of more than 200 ns; autofluorescence and organic fluorophores possess luminescence lifetimes shorter than 10 ns.⁷⁶ Based on this long lifetime, fluorescence lifetime imaging microscopy (FLIM) of CXCR4 expression on cells was performed.

For in vivo fluorescence imaging near-infrared (NIR) dyes are preferred, as lower background autofluorescence and better tissue penetration are observed using these dyes.¹⁰⁰ Ac-TZ14011 has been labeled with NIR dye IR783 ($\lambda_{\text{ex}} = 783 \text{ nm}$, $\lambda_{\text{em}} = 812 \text{ nm}$; Figure 3),^{62,98} which could be used for fluorescence guided surgery.⁶² Furthermore, Ac-TZ14011-IR783 can bind non-covalently to human serum albumin via the NIR dye. This self-assembled complex could be used to change the distribution profile of the peptide using an albumin-carrier.⁹⁸

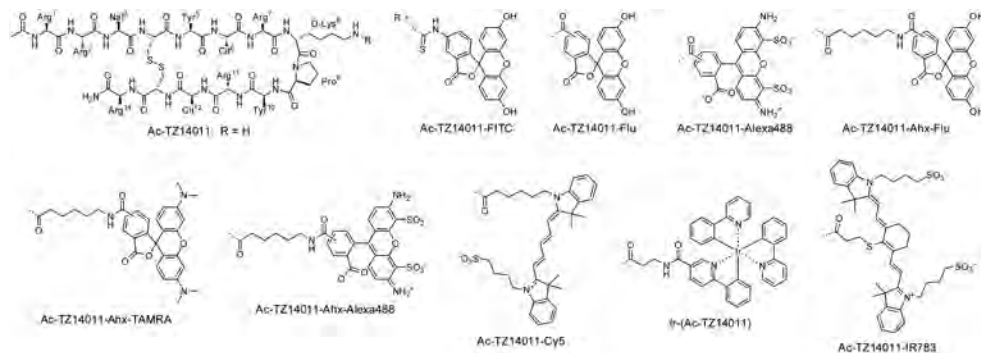


Figure 3. Monomeric fluorescent and phosphorescent T140 derivatives.

^{111}In -DTPA-Ac-TZ14011 is the first reported radiolabeled Ac-TZ14011 derivative (Figure 4).⁷¹ The indium-bound DTPA chelate reduced the CXCR4 binding affinity in a similar manner as the fluorescent dyes (Table 4).¹⁰¹ For single photon emission computed tomography/ computed tomography (SPECT/CT) imaging relatively low specific activities (0.20 MBq/ μg) were sufficient to visualize the tumor in a MIN-O transplantation model of ductal carcinoma in situ (DCIS) with only a four-fold overexpression of CXCR4 (Table 3).¹⁰¹ At 24 hrs post injection (p.i.) an increase in tumor uptake could be correlated to an increase in CXCR4 expression, which was not the case at one hr post injection. Distribution studies in the MIN-O tumor model and in a pancreatic tumor model at 1, 6 and 24 hrs post injection revealed a rapid clearance from the blood and a noticeable uptake and retention in the liver, kidneys and spleen (Table 5).^{71,101} Despite low CXCR4 expression in the liver, the accumulation appeared to be partly specific, since co-injection of a large excess of Ac-TZ14011 showed a marked decrease in uptake.⁷¹ Although the tumor accumulation was not very high, an adequate tumor-to-muscle (T/M) ratio was obtained at both 6 hrs post injection (4.43) and 24 hrs p.i. (7.17 ± 0.47) as the muscle uptake was low.^{71,101} The tumor accumulation in the low CXCR4-expressing 4T1 tumor model was significantly lower compared to accumulation in the MIN-O tumor model at 24 hrs p.i.¹⁰¹

An alternative radiotracer is ^{125}I -IB-Ac-TZ14011 (Figure 4). For this compound a ^{125}I -labeling procedure was developed using an 3-iodobenzoyl group, which was coupled to D-Lys⁸ of Ac-TZ14011.¹⁰² The distribution, which was only determined for non-tumor-bearing mice, showed a relatively fast clearance, mainly via the kidneys (Table 5). This large difference in the clearance profile is surprising given the relatively small difference in chemical structure with respect to ^{111}In -DTPA-Ac-TZ14011.

T140 has been labeled with ^{18}F by coupling 4- ^{18}F -fluorobenzoic acid (4- ^{18}F Bz) to the N-terminus of T140 (Figure 4).⁷⁰ This functionalization did not result in a reduction of binding affinity compared to the parental compound (see IC_{50} values in Table 4).⁸⁹ An effect that can possibly be explained by the fact that 4- ^{18}F Bz is small and can also provide additional hydrophobic interactions with the CXCR4 receptor. A potential disadvantage of ^{18}F labeling is that it is more laborious and time consuming than chelate-based labeling. Nonetheless, PET imaging was possible with 4- ^{18}F Bz-T140 (two hrs post injection), enabling tumor visualization despite high background signals (tumor-to-muscle ratio = 2.94; Table 5).⁷⁰ The authors suggested that the remarkable high blood uptake (14.3 percentage injected dose per gram (% ID/g)) was caused by non-CXCR4-mediated binding of 4- ^{18}F Bz-T140 to red blood cells. When ten μg cold 4-FBz-T140 was co-injected, both the

uptake in blood and the spleen were greatly reduced, leading to a maximal tumor-to-muscle (T/M) ratio of 21.6. A possible explanation for this behavior is that co-injection of unlabeled compound resulted in reduction of the specific activity in such a way that non-specific binding was avoided. This is underlined by the fact that red blood cell binding was not observed in studies wherein a low specific activity was used.^{71,101}

In an alternative attempt to reduce the red blood cell binding, Jacobson et al. replaced the 4-¹⁸FbZ group at the N-terminus with DOTA or NOTA (Figure 4).⁶⁹ The use of these larger DOTA and NOTA chelates resulted in steric hindrance when binding to CXCR4 and the chelates could not contribute to receptor binding via hydrophobic interactions. Accordingly, the affinity of DOTA-NFB and NOTA-NFB for CXCR4 was considerably reduced compared to 4-¹⁸FbZ-T140 (27- and 55-fold, respectively; Table 4). Both the radiolabeled versions ⁶⁴Cu-DOTA-NFB and ⁶⁴Cu-NOTA-NFB displayed very low binding to red blood cells and could be used for PET imaging, despite of their high specific activity of 12.21 - 14.8 MBq/μg. Regardless of the lower affinity, the tumor uptake of ⁶⁴Cu-DOTA-NFB and ⁶⁴Cu-NOTA-NFB was reported to be comparable to that of 4-¹⁸FbZ-T140 (Table 5). The blood and muscle uptake of ⁶⁴Cu-DOTA-NFB and ⁶⁴Cu-NOTA-NFB was lower than the uptake of 4-¹⁸FbZ-T140, yielding higher T/M ratios. Unfortunately, the uptake of ⁶⁴Cu-DOTA-NFB and ⁶⁴Cu-NOTA-NFB was again high in liver and kidney. Similar to what was observed with 4-¹⁸FbZ-T140, co-injection with cold tracer (meaning reduction of the specific activity) can possibly further improve the distribution.

Modification of the N-terminus of T140 with the 4-FBz group has also been used to increase the CXCR4 affinity of ¹¹¹In-DTPA-Ac-TZ14011. This radioactive indium-labeled compound, In-DTPA-4-FBz-T140, showed only a five-fold lower CXCR4 affinity than T140 (Table 4).¹⁰³ Unfortunately, no experiments with In-DTPA-4-FBz-T140 in mice have been reported up until now, making it difficult to estimate the effect of the 4-FBz modification *in vivo*.

Recently, a very similar agent, ⁶⁴Ga-DOTA-4-FBz-TN14003, was described (Figure 3).¹⁰⁴ A relatively high CXCR4 affinity and a high specific activity of maximal 11.6 MBq/μg were obtained (Table 4). The stability in human plasma of ⁶⁴Ga-DOTA-4-FBz-TN14003 is high; after 90 minutes 97% was still intact. *In vivo* experiments with this tracer have not yet been reported.

The T140 analog ⁶⁴Cu-T140-2D also includes the 4-FBz modification at the N-terminus in addition to two DOTA chelates on Lys⁷ and D-Lys⁸ (Figure 4).⁷² The IC₅₀ value of T140-2D was shown to be similar as that reported for T140 (Table 4). However, the IC₅₀ value of T140-2D was determined in the presence of ⁶⁴Cu-T140-2D and no IC₅₀ value of a reference

compound such as T140 was measured using the same assay. Therefore, the binding affinity of ^{64}Cu -T140-2D and T140 cannot be objectively compared. Based on previous results it seems likely that the two DOTA chelates will reduce the receptor affinity to some extent. Distribution studies with the ^{64}Cu -labeled derivative revealed red blood cell binding similar to 4- ^{18}F Bz-Ac-TZ14011 (Table 5). Again, co-injection of cold compound reduced the blood uptake, although less effectively than for 4- ^{18}F Bz-T140. The distribution of ^{64}Cu -T140-2D with co-injection of 5 mg of cold T140-2D still showed high liver, kidney and spleen uptake, similar to ^{111}In -DTPA-Ac-TZ14011. Reducing the specific activity by co-injection of 5 mg of cold T140-2D was also required for tumor visualization during PET imaging.

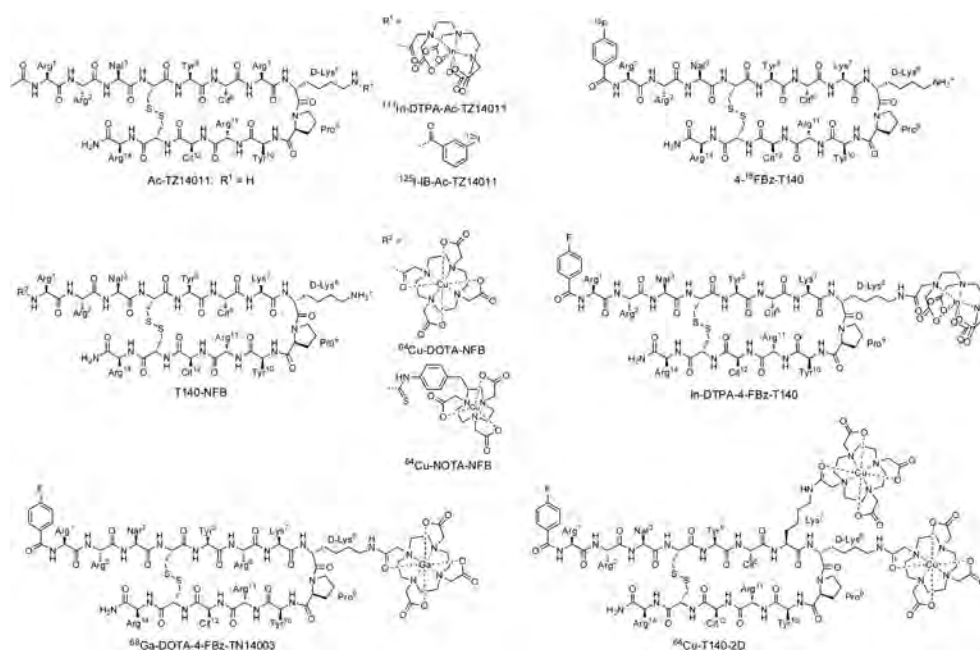


Figure 4. Monomeric radiolabeled T140 derivatives.

Ac-TZ14011 has also been labeled with a multifunctional single-attachment-point (MSAP) reagent,^{105,106} which consist out of a Cy5.5 like fluorophore and a DTPA chelate for indium binding (Figure 3).⁷⁵ This hybrid derivative, Ac-TZ14011-MSAP, had a similar affinity as the FITC and DTPA derivatives, again demonstrating that a relative large label such as MSAP does not hamper CXCR4 binding more than smaller labels (Table 4). The obtained T/M ratio was also similar to the ratio found with ^{111}In -DTPA-Ac-TZ14011 (4.55; Table 5).

reduce the negative influence of the MSAP label, probably by shielding the MSAP label (Figure 7B).⁷⁷ In distribution studies, the dimer and tetramer displayed significantly lower nonspecific muscle uptake compared to monomer, resulting in a higher T/M ratio for dimer (Ac-TZ14011)₂-MSAP-¹¹¹In (7.41) (Table 5). The T/M ratio of tetramer (Ac-TZ14011)₄-MSAP-¹¹¹In was lower than that of the dimer, due to lower tumor uptake.

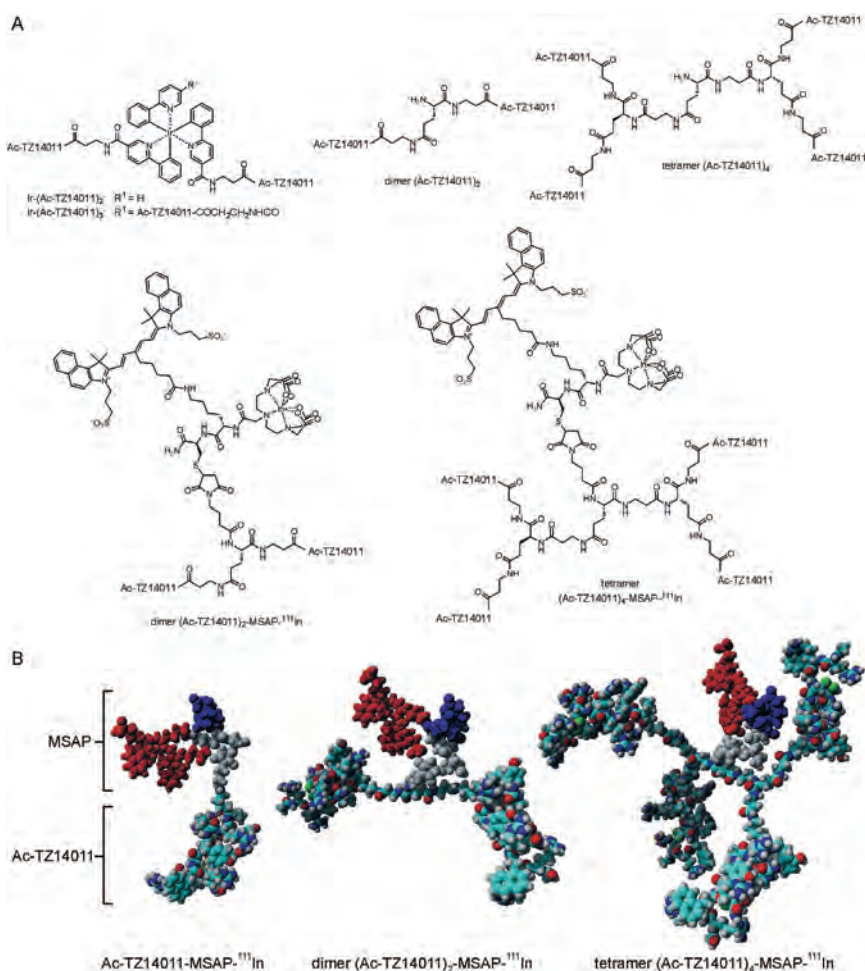


Figure 6. A) Multimeric T140 derivatives. B) Molecular models of the MSAP-labeled derivatives, illustrating the shielding of the MSAP label by the Ac-TZ14011 peptides.

Table 4. Receptor affinity and specificity of T140 derivatives

T140 derivative	IC ₅₀ (nM)	K _D (nM)	Specific activity (MBq/μg)	Imaging modality	Reference
T140	2.3 - 4	-	n/a	n/a	67,81
CVX15	0.6	1.1 - 46.7	n/a	n/a	84
Ac-TZ14011	5.2 ± 0.1	8.61 ± 1.42	n/a	n/a	68,75
Ac-TZ14011-FITC	-	204 ± 67	n/a	fluorescence	75
Ac-TZ14011-Flu	16 ± 0.8	-	n/a	fluorescence	68
Ac-TZ14011-Alexa488	8.1 ± 3.5	-	n/a	fluorescence	68
Ac-TZ14011-Ahx-Flu	26 ± 2.4	-	n/a	fluorescence	68
Ac-TZ14011-Ahx-TAMRA	14	-	n/a	fluorescence	96
Ac-TZ14011-Ahx-Alexa488	267 ± 19	-	n/a	fluorescence	68
Ac-TZ14011-Cy5	-	-	n/a	fluorescence	98
Ir-(Ac-TZ14011)	-	84.4 ± 13.7	n/a	phosphorescence	76
Ac-TZ14011-IR783	-	-	n/a	fluorescence	62,98
¹¹¹ In-DTPA-Ac-TZ14011	7.9	124 ± 24	0.37, 0.20	radioactivity	71,75
¹²⁵ I-B-Ac-TZ14011	-	-	1.7	radioactivity	102
4-18Fbz-T140	2.5	-	2.4	radioactivity	70
⁶⁴ Cu-DOTA-T140	68	-	12.21 - 14.8	radioactivity	69
⁶⁴ Cu-NOTA-T140	138	-	12.21 - 14.8	radioactivity	69
In-DTPA-4-FBz-T140	14 ± 1.0	-	-	radioactivity	103
⁶⁴ Ga-DOTA-4-FBz-T14003	1.99 ± 0.31	-	≤ 11.6	radioactivity	104
⁶⁴ Cu-T140-2D	2.47 ± 0.08	-	10.36 - 11.1	radioactivity	72
Ac-TZ14011-MSAP- ¹¹¹ In	-	186.9 ± 52.4	0.20	radioactivity and fluorescence	75,77
Ir-(Ac-TZ14011)2	-	254.4 ± 81.3	n/a	phosphorescence	76
Ir-(Ac-TZ14011)3	-	66.3 ± 28.0	n/a	phosphorescence	76
dimer (Ac-TZ14011)2	-	23.5 ± 2.43	n/a	n/a	77
tetramer (Ac-TZ14011)4	-	30.6 ± 4.84	n/a	n/a	77
dimer (Ac-TZ14011)2-MSAP- ¹¹¹ In	-	93.1 ± 10.1	0.20	radioactivity and fluorescence	77
tetramer (Ac-TZ14011)4-MSAP- ¹¹¹ In	-	80.5 ± 11.6	0.20	radioactivity and fluorescence	77

n/a = Not available

Table 5. Distribution of Tl40 derivatives

	¹¹¹ In-DTPA-Ac-TZ14011	¹¹¹ In-DTPA-Ac-TZ14011	¹²⁵ I-B-Ac-TZ14011	4- ¹⁸ Fbz-Tl40	4- ¹⁸ Fbz-Tl40 + 10 mg cold	⁶⁴ Cu-DOTA-Tl40	⁶⁴ Cu-NOTA-Tl40	⁶⁴ Cu-Tl40-2D + 5 mg cold	Ac-TZ14011-MSAP- ¹¹¹ In	dimer (Ac-TZ14011) ₂ -MSAP- ¹¹¹ In	tetramer (Ac-TZ14011) ₄ -MSAP- ¹¹¹ In
Time p. i. (h)	6	24	2	3	3	4	4	4	24	24	24
Blood	0.05 ± 0.01	0.02 ± 0.00	0.51 ± 0.118	14.3 ± 2.63	0.12 ± 0.04	0.34 ± 0.02	0.12 ± 0.01	0.85	0.14 ± 0.02	0.14 ± 0.03	0.11 ± 0.01
Brain	-	0.00 ± 0.00	0.022 ± 0.009	-	-	-	-	-	0.02 ± 0.00	0.03 ± 0.01	0.02 ± 0.00
Lungs	-	0.19 ± 0.01	0.168 ± 0.058	-	-	-	-	-	1.02 ± 0.13	2.13 ± 0.60	1.68 ± 0.31
Heart	-	0.08 ± 0.01	0.133 ± 0.034	-	-	-	-	-	0.89 ± 0.22	0.60 ± 0.12	0.43 ± 0.06
Liver	25.2 ± 2.0	5.53 ± 0.51	0.197 ± 0.066	1	18	23	25	25	22.46 ± 5.46	30.59 ± 5.45	22.43 ± 0.67
Kidneys	43.4 ± 6.3	24.82 ± 0.94	0.866 ± 0.352	2	60	21	40	40	7.50 ± 1.39	6.46 ± 1.36	4.37 ± 0.52
Spleen	7.57 ± 0.54	1.03 ± 0.11	0.073 ± 0.014	2	6.70 ± 0.86	4.59 ± 0.90	15	15	4.76 ± 1.23	7.01 ± 1.45	4.66 ± 0.46
Pancreas	0.05 ± 0.01	-	-	-	-	-	-	-	-	-	-
Stomach	-	0.08 ± 0.01	0.432 ± 0.15	-	-	-	-	-	0.81 ± 0.16	0.97 ± 0.52	1.09 ± 0.52
Intestines	-	0.16 ± 0.02	0.182 ± 0.371	3.5	1	1	2	2	1.85 ± 0.08	2.06 ± 0.26	1.56 ± 0.46
Bone	-	-	0.23 ± 0.054	0	0.5	-	-	-	-	-	-
Bone marrow	-	-	-	3	0.5	-	-	10	-	-	-
Thyroid	-	-	0.185 ± 0.031	-	-	-	-	-	-	-	-
Tumor	0.20 ± 0.03	-	-	2.3 ± 0.26	3.03 ± 0.31	4.98 ± 0.89	4.55 ± 0.66	4.12 ± 1.02	1.10 ± 0.60	0.57 ± 0.19	0.42 ± 0.10
Muscle	0.07 ± 0.00	0.03 ± 0.01	0.232 ± 0.046	0.72 ± 0.22	0.12 ± 0.06	0.2	0.1	0.3	0.31 ± 0.01	0.07 ± 0.03	0.08 ± 0.02
T/M ratio	4.43 ± 1.89	7.17 ± 0.47	-	2.94 ± 0.16	21.6 ± 7.14	19.32 ± 2.35	39.30 ± 2.26	12.56 ± 3.66	4.55 ± 0.68	7.41 ± 1.87	5.47 ± 0.50
Tumor model	AsPC-1	MIN-O	-	CHO-CXCR4	CHO-CXCR4	CHO-CXCR4	CHO-CXCR4	CHO-CXCR4	MIN-O	MIN-O	MIN-O
Reference	71	101	102	70	70	69	69	72	75	77	77

T/M ratio = tumor-to-muscle-ratio. P.i. = post injection

Discussion

For CXCR4 imaging luminescent and/or radioactive imaging labels have been used. Fluorescent labels are considered the best choice for *in vitro* evaluation, allowing e.g. microscopy and flow cytometric analysis. Additionally, fluorescence can be used for image guided surgery purposes. For *in vivo* imaging (SPECT, PET) and distribution studies radiolabels are the most desirable. Chelate-based radiolabeling is in general more convenient than e.g. ^{18}F and ^{125}I labeling, due to the shorter and more implementable labeling protocol. Hybrid labels based on fluorescence and radioactivity can be used for all applications mentioned above, which facilitates integration of the results from the various imaging techniques.⁷⁵

As described, a number of biological features of CXCR4 targeting are essential in the evaluation of a new imaging agent: the receptor affinity and specificity, high tumor and low background uptake and the cell line and tumor model. Based on these features, imaging agents of the T140 family were compared.

CXCR4 affinity and specificity

The receptor affinity and specificity of an imaging agent can be divided into two aspects: the potency of the parental compound and the (negative) influence of the imaging label. Both T140 and its derivative Ac-TZ14011 were shown to have a low nanomolar affinity for the CXCR4 receptor (Table 4).

Chemical modifications of T140 derivatives for imaging purposes generally reduce the affinity and specificity. Steric hindrance can be reduced to an acceptable level and nonspecific binding can be restrained by avoiding hydrophobic labels.

For labels attached to the D-Lys⁸ position there is no trend between the binding affinity and the size and hydrophobicity of the label (Table 4). Most likely this is due to the fact that the D-Lys⁸ functionalization yields a minimal amount of interactions between the label and the receptor (Figure 2). However, label-mediated nonspecific cell binding reduces the binding affinity to different degrees. Such nonspecific binding can partly be overcome by using multimerization approaches that shield the imaging label from the surrounding environment.⁷⁷ Variation in the experimental setup that is used in the different studies may be a major reason for the variation in the binding affinities reported for the different T140 derivatives.

Tumor and background accumulation

High tumor uptake and low retention in other organs are important for good tumor visualization and low toxicity. To reduce retention in non-tumorous tissue and the associated possible side effects, rapid renal clearance is generally preferred over slower

hepatic clearance. Radioactively labeled variants of Ac-TZ14011 are primarily cleared via the kidneys and in a lesser extent via the liver (Table 5). Rapid renal clearance of a compound decreases the (radioactivity-related) toxicity of a compound, as overall retention is reduced. Multimeric structures (Ac-TZ14011)₂ and (Ac-TZ14011)₄ are primarily cleared via the liver, which could be a result of the large size of the compounds.

Important to note is that CXCR4 is also present in the lymph nodes, spleen and bone marrow, which can result in background staining.¹⁰¹ A successful strategy to reduce the background staining of lymph nodes, spleen, bone marrow and red blood cells is the use of a low specific activity, whereby the excess of unlabeled compound is used to saturate CXCR4 in non-tumor tissue.^{71,101} With the addition of such background reductions, tumor accumulation of T140 derivatives has been proven to be CXCR4 specific. This was corroborated with low CXCR4-expressing tumors or blocking with high amounts of unlabeled compound.

The distribution and pharmacokinetics of T140 derivatives can be worsened or improved by imaging labels. Hydrophobic fluorescent dyes tend to cause more nonspecific uptake and result in slow clearance via the liver, whereas hydrophilic chelates reduce nonspecific uptake and promote fast renal clearance.

Cell lines and tumor models

The cell lines and tumor models used in the preclinical evaluation process have a large influence on the obtained results. To eliminate the variation caused by the use of different cell lines/tumor models, derivatives are best compared in an identical set-up.

Direct comparison of the reported tumor accumulation *in vivo* is nearly impossible, as high levels of tumor accumulation can be ascribed to the potency of the imaging agent and/or to the tumor model used. Comparative results, where the same imaging agent was used in different tumor models showed that uptake levels and T/M ratios were highest in the tumor models with the highest CXCR4 expression levels. Expectedly T/M ratios obtained in e.g. the transplantation-based MIN-O tumor model with a more clinically relevant CXCR4 expression level were clearly lower. This observation is in line with results reported by Cai et.al. who showed a linear correlation between tracer uptake and receptor expression.¹⁰⁷

A combination of high and low expressing models during the evaluation may result in a more optimal selection procedure for new imaging compounds. Where transfected models can be used for a black-and-white evaluation of the specificity of an imaging agent, models that more accurately represent the modest five-fold overexpression found in the clinical situation can best be used for evaluation of its potential clinical utility.

Conclusion

The T140 peptide family provides a number of interesting candidates for the visualization of CXCR4 expression using fluorescent-, radio-, and hybrid- imaging labels. Hereby the label and its placement on the parental peptide have a large influence on the affinity, specificity and distribution of the imaging agents. Important in investigations regarding the imaging potential of CXCR4 targeted imaging agents is the clinical challenge that such compounds are meant to help solve. We found that only in a very limited number of studies the biological evaluation had taken place using representative tumor models.

References

- 1 Kucia M, Jankowski K, Reza R, Wysoczynski M, Bandura L, Allendorf DJ, Zhang J, Ratajczak J, Ratajczak MZ. CXCR4-SDF-1 signalling, locomotion, chemotaxis and adhesion. *J Mol Histol.* 2004; 35: 233-245
- 2 Balkwill F. Cancer and the chemokine network. *Nat Rev Cancer.* 2004; 4: 540-550
- 3 Donzella GA, Schols D, Lin SW, Este JA, Nagashima KA, Maddon PJ, Allaway GP, Sakmar TP, Henson G, De Clercq E, Moore JP. AMD3100, a small molecule inhibitor of HIV-1 entry via the CXCR4 co-receptor. *Nat Med.* 1998; 4: 72-77
- 4 Tarasova NI, Stauber RH, Michejda CJ. Spontaneous and ligand-induced trafficking of CXC-chemokine receptor 4. *J Biol Chem.* 1998; 273: 15883-15886
- 5 Andreas K, Lubke C, Haupl T, Dehne T, Morawietz L, Ringe J, Kaps C, Sittlinger M. Key regulatory molecules of cartilage destruction in rheumatoid arthritis: an in vitro study. *Arthritis Res Ther.* 2008; 10: R9
- 6 Nanki T, Hayashida K, El-Gabalawy HS, Suson S, Shi K, Girschick HJ, Yavuz S, Lipsky PE. Stromal cell-derived factor 1-CXC chemokine receptor 4 interactions play a central role in CD4+ T cell accumulation in rheumatoid arthritis synovium. *J Immunol.* 2000; 165: 6590-6598
- 7 Nanki T, Takada K, Komano Y, Morio T, Kanegane H, Nakajima A, Lipsky PE, Miyasaka N. Chemokine receptor expression and functional effects of chemokines on B cells: implication in the pathogenesis of rheumatoid arthritis. *Arthritis Res Ther.* 2009; 11: R149
- 8 Balkwill F. The significance of cancer cell expression of the chemokine receptor CXCR4. *Semin Cancer Biol.* 2004; 14: 171-179
- 9 Akashi T, Koizumi K, Tsuneyama K, Saiki I, Takano Y, Fuse H. Chemokine receptor CXCR4 expression and prognosis in patients with metastatic prostate cancer. *Cancer Sci.* 2008; 99: 539-542
- 10 Holm NT, Byrnes K, Li BD, Turnage RH, Abreo F, Mathis JM, Chu QD. Elevated levels of chemokine receptor CXCR4 in HER-2 negative breast cancer specimens predict recurrence. *J Surg Res.* 2007; 141: 53-59
- 11 Lee HJ, Kim SW, Kim HY, Li S, Yun HJ, Song KS, Kim S, Jo DY. Chemokine receptor CXCR4 expression, function, and clinical implications in gastric cancer. *Int J Oncol.* 2009; 34: 473-480
- 12 Liu Y, Ji R, Li J, Gu Q, Zhao X, Sun T, Wang J, Du Q, Sun B. Correlation effect of EGFR and CXCR4 and CCR7 chemokine receptors in predicting breast cancer metastasis and prognosis. *J Exp Clin Cancer Res.* 2010; 29: 16

- 13 Marechal R, Demetter P, Nagy N, Berton A, Decaestecker C, Polus M, Closset J, Deviere J, Salmon I, Van Laethem JL. High expression of CXCR4 may predict poor survival in resected pancreatic adenocarcinoma. *Br J Cancer*. 2009; 100: 1444-1451
- 14 Otsuka S, Klimowicz AC, Kopciuk K, Petrillo SK, Konno M, Hao D, Muzik H, Stolte E, Boland W, Morris D, Magliocco AM, Bebb DG. CXCR4 overexpression is associated with poor outcome in females diagnosed with stage IV non-small cell lung cancer. *J Thorac Oncol*. 2011; 6: 1169-1178
- 15 Bai S, Wang D, Klein MJ, Siegal GP. Characterization of CXCR4 expression in chondrosarcoma of bone. *Arch Pathol Lab Med*. 2011; 135: 753-758
- 16 Wagner PL, Moo TA, Arora N, Liu YF, Zarnegar R, Scognamiglio T, Fahey TJ, 3rd. The chemokine receptors CXCR4 and CCR7 are associated with tumor size and pathologic indicators of tumor aggressiveness in papillary thyroid carcinoma. *Ann Surg Oncol*. 2008; 15: 2833-2841
- 17 Andre F, Xia W, Conforti R, Wei Y, Boulet T, Tomasic G, Spielmann M, Zoubir M, Berrada N, Arriagada R, Hortobagyi GN, Hung MC, Puztai L, Delaloge S, Michiels S, Cristofanilli M. CXCR4 expression in early breast cancer and risk of distant recurrence. *Oncologist*. 2009; 14: 1182-1188
- 18 Kang H, Watkins G, Douglas-Jones A, Mansel RE, Jiang WG. The elevated level of CXCR4 is correlated with nodal metastasis of human breast cancer. *Breast*. 2005; 14: 360-367
- 19 Cabioglu N, Sahin AA, Morandi P, Meric-Bernstam F, Islam R, Lin HY, Bucana CD, Gonzalez-Angulo AM, Hortobagyi GN, Cristofanilli M. Chemokine receptors in advanced breast cancer: differential expression in metastatic disease sites with diagnostic and therapeutic implications. *Ann Oncol*. 2009; 20: 1013-1019
- 20 Singh IP, Chauthe SK. Small molecule HIV entry inhibitors: Part I. Chemokine receptor antagonists: 2004 - 2010. *Expert Opin Ther Pat*. 2011; 21: 227-269
- 21 Patrussi L, Baldari CT. The CXCL12/CXCR4 axis as a therapeutic target in cancer and HIV-1 infection. *Curr Med Chem*. 2011; 18: 497-512
- 22 Choi WT, Duggineni S, Xu Y, Huang Z, An J. Drug Discovery Research Targeting the CXCR4 Chemokine Receptor 4 (CXCR4). *J Med Chem*. 2012; 55(3): 977-94
- 23 Burger JA, Stewart DJ, Wald O, Peled A. Potential of CXCR4 antagonists for the treatment of metastatic lung cancer. *Expert Rev Anticancer Ther*. 2011; 11: 621-630
- 24 Wong D, Korz W. Translating an antagonist of chemokine receptor CXCR4: from bench to bedside. *Clin Cancer Res*. 2008; 14: 7975-7980
- 25 Liang X. CXCR4, inhibitors and mechanisms of action. *Chem Biol Drug Des*. 2008; 72: 97-110

- 26 Woodard LE, Nimmagadda S. CXCR4-based imaging agents. *J Nucl Med.* 2011; 52: 1665-1669
- 27 Lee S, Xie J, Chen X. Peptides and peptide hormones for molecular imaging and disease diagnosis. *Chem Rev.* 2010; 110: 3087-3111
- 28 Pimlott SL, Sutherland A. Molecular tracers for the PET and SPECT imaging of disease. *Chem Soc Rev.* 2011; 40: 149-162
- 29 Correia JD, Paulo A, Raposinho PD, Santos I. Radiometallated peptides for molecular imaging and targeted therapy. *Dalton Trans.* 2011; 40: 6144-6167
- 30 Mankoff DA, Link JM, Linden HM, Sundararajan L, Krohn KA. Tumor receptor imaging. *J Nucl Med.* 2008; 49 Suppl 2: 149S-163S
- 31 Schottelius M, Wester HJ. Molecular imaging targeting peptide receptors. *Methods.* 2009; 48: 161-177
- 32 Lee S, Park K, Kim K, Choi K, Kwon IC. Activatable imaging probes with amplified fluorescent signals. *Chem Commun.* 2008: 4250-4260
- 33 Razgulin A, Ma N, Rao J. Strategies for in vivo imaging of enzyme activity: an overview and recent advances. *Chem Soc Rev.* 2011; 40: 4186-4216
- 34 de Jong M, Breeman WA, Kwekkeboom DJ, Valkema R, Krenning EP. Tumor imaging and therapy using radiolabeled somatostatin analogues. *Acc Chem Res.* 2009; 42: 873-880
- 35 Pepe G, Moncayo R, Bombardieri E, Chiti A. Somatostatin receptor SPECT. *Eur J Nucl Med Mol Imaging.* 2012; 39 Suppl 1: S41-S51
- 36 Schottelius M, Laufer B, Kessler H, Wester HJ. Ligands for mapping $\alpha_v\beta_3$ -integrin expression in vivo. *Acc Chem Res.* 2009; 42: 969-980
- 37 Beer AJ, Schwaiger M. Imaging of integrin $\alpha_v\beta_3$ expression. *Cancer Metastasis Rev.* 2008; 27: 631-644
- 38 Sancho V, Di Florio A, Moody TW, Jensen RT. Bombesin receptor-mediated imaging and cytotoxicity: review and current status. *Curr Drug Deliv.* 2011; 8: 79-134
- 39 Schroeder RP, van Weerden WM, Bangma C, Krenning EP, de Jong M. Peptide receptor imaging of prostate cancer with radiolabelled bombesin analogues. *Methods.* 2009; 48: 200-204
- 40 Schmid BC, Rudas M, Rezniczek GA, Leodolter S, Zeillinger R. CXCR4 is expressed in ductal carcinoma in situ of the breast and in atypical ductal hyperplasia. *Breast Cancer Res Treat.* 2004; 84: 247-250
- 41 Salvucci O, Bouchard A, Baccarelli A, Deschenes J, Sauter G, Simon R, Bianchi R, Basik M. The role of CXCR4 receptor expression in breast cancer: a large tissue microarray study. *Breast Cancer Res Treat.* 2006; 97: 275-283

- 42 Rubie C, Kollmar O, Frick VO, Wagner M, Brittner B, Graber S, Schilling MK. Differential CXC receptor expression in colorectal carcinomas. *Scand J Immunol.* 2008; 68: 635-644
- 43 Na IK, Scheibenbogen C, Adam C, Stroux A, Ghadjar P, Thiel E, Keilholz U, Coupland SE. Nuclear expression of CXCR4 in tumor cells of non-small cell lung cancer is correlated with lymph node metastasis. *Hum Pathol.* 2008; 39: 1751-1755
- 44 Wehler TC, Graf C, Biesterfeld S, Brenner W, Schadt J, Gockel I, Berger MR, Thuroff JW, Galle PR, Moehler M, Schimanski CC. Strong expression of chemokine receptor CXCR4 by renal cell carcinoma correlates with advanced disease. *J Oncol.* 2008; 2008: 626340
- 45 Woo SU, Bae JW, Kim CH, Lee JB, Koo BW. A significant correlation between nuclear CXCR4 expression and axillary lymph node metastasis in hormonal receptor negative breast cancer. *Ann Surg Oncol.* 2008; 15: 281-285
- 46 Chen G, Wang Z, Liu XY, Liu FY. High-level CXCR4 expression correlates with brain-specific metastasis of non-small cell lung cancer. *World J Surg.* 2011; 35: 56-61
- 47 Hassan S, Ferrario C, Saragovi U, Quenneville L, Gaboury L, Baccarelli A, Salvucci O, Basik M. The influence of tumor-host interactions in the stromal cell-derived factor-1/ CXCR4 ligand/receptor axis in determining metastatic risk in breast cancer. *Am J Pathol.* 2009; 175: 66-73
- 48 Ueda M, Shimada T, Goto Y, Tei K, Nakai S, Hisa Y, Kannagi R. Expression of CC-chemokine receptor 7 (CCR7) and CXC-chemokine receptor 4 (CXCR4) in head and neck squamous cell carcinoma. *Auris Nasus Larynx.* 2010; 37: 488-495
- 49 He X, Wei Q, Zhang X, Xiao J, Jin X, Zhu Y, Cui B, Ning G. Immunohistochemical expression of CXCR4 in thyroid carcinomas and thyroid benign lesions. *Pathol Res Pract.* 2010; 206: 712-715
- 50 Ying J, Xu Q, Zhang G, Liu B, Zhu L. The expression of CXCL12 and CXCR4 in gastric cancer and their correlation to lymph node metastasis. *Med Oncol.* 2012; 29(3): 1716-22.
- 51 Li T, Li H, Wang Y, Harvard C, Tan JL, Au A, Xu Z, Jablons DM, You L. The expression of CXCR4, CXCL12 and CXCR7 in malignant pleural mesothelioma. *J Pathol.* 2011; 223: 519-530
- 52 Wang L, Yang B, Yang Q, Qiao S, Wang Y, Sun Y. Strong expression of chemokine receptor CXCR4 by renal cell carcinoma cells correlates with metastasis. *Clin Exp Metastasis.* 2009; 26: 1049-1054
- 53 Blot E, Laberge-Le Couteux S, Jamali H, Cornic M, Guillemet C, Duval C, Hellot MF, Pille JY, Picquetot JM, Veyret C. CXCR4 membrane expression in node-negative breast cancer. *Breast J.* 2008; 14: 268-274
- 54 Cabioglu N, Gong Y, Islam R, Broglio KR, Sneige N, Sahin A, Gonzalez-Angulo AM, Morandi P, Bucana C, Hortobagyi GN, Cristofanilli M. Expression of growth factor and chemokine receptors: new insights in the biology of inflammatory breast cancer. *Ann Oncol.* 2007; 18: 1021-1029

-
- 55 Gockel I, Schimanski CC, Heinrich C, Wehler T, Frerichs K, Drescher D, von Langsdorff C, Domeyer M, Biesterfeld S, Galle PR, Junginger T, Moehler M. Expression of chemokine receptor CXCR4 in esophageal squamous cell and adenocarcinoma. *BMC Cancer*. 2006; 6: 290
 - 56 Stevenson CB, Ehtesham M, McMillan KM, Valadez JG, Edgeworth ML, Price RR, Abel TW, Mapara KY, Thompson RC. CXCR4 expression is elevated in glioblastoma multiforme and correlates with an increase in intensity and extent of peritumoral T2-weighted magnetic resonance imaging signal abnormalities. *Neurosurgery*. 2008; 63: 560-569; discussion 569-570
 - 57 Schrader AJ, Lechner O, Templin M, Dittmar KE, Machtens S, Mengel M, Probst-Kepper M, Franzke A, Wollensak T, Gatzlaff P, Atzpodien J, Buer J, Lauber J. CXCR4/CXCL12 expression and signalling in kidney cancer. *Br J Cancer*. 2002; 86: 1250-1256
 - 58 Wang SC, Lin JK, Wang HS, Yang SH, Li AF, Chang SC. Nuclear expression of CXCR4 is associated with advanced colorectal cancer. *Int J Colorectal Dis*. 2010; 25: 1185-1191
 - 59 D'Alterio C, Consales C, Polimeno M, Franco R, Cindolo L, Portella L, Cioffi M, Calemma R, Marra L, Claudio L, Perdona S, Pignata S, Facchini G, Carteni G, Longo N, Pucci L, Ottaiano A, Costantini S, Castello G, Scala S. Concomitant CXCR4 and CXCR7 expression predicts poor prognosis in renal cancer. *Curr Cancer Drug Targets*. 2010; 10: 772-781
 - 60 Muller A, Homey B, Soto H, Ge N, Catron D, Buchanan ME, McClanahan T, Murphy E, Yuan W, Wagner SN, Barrera JL, Mohar A, Verastegui E, Zlotnik A. Involvement of chemokine receptors in breast cancer metastasis. *Nature*. 2001; 410: 50-56
 - 61 Chu QD, Holm NT, Madumere P, Johnson LW, Abreo F, Li BD. Chemokine receptor CXCR4 overexpression predicts recurrence for hormone receptor-positive, node-negative breast cancer patients. *Surgery*. 2011; 149: 193-199
 - 62 Kuil J, Velders AH, van Leeuwen FWB. Multimodal tumor-targeting peptides functionalized with both a radio-and a fluorescent-label. *Bioconjugate Chem*. 2010; 21: 1709-1719
 - 63 Maksym RB, Tarnowski M, Grymula K, Tarnowska J, Wysoczynski M, Liu R, Czerny B, Ratajczak J, Kucia M, Ratajczak MZ. The role of stromal-derived factor-1 - CXCR7 axis in development and cancer. *Eur J Pharmacol*. 2009; 625: 31-40
 - 64 Lee S, Xie J, Chen X. Peptide-based probes for targeted molecular imaging. *Biochemistry*. 2010; 49: 1364-1376
 - 65 Furusato B, Mohamed A, Uhlen M, Rhim JS. CXCR4 and cancer. *Pathol Int*. 2010; 60: 497-505
 - 66 Kelland LR. Of mice and men: values and liabilities of the athymic nude mouse model in anticancer drug development. *Eur J Cancer*. 2004; 40: 827-836

- 67 Fujii N, Oishi S, Hiramatsu K, Araki T, Ueda S, Tamamura H, Otaka A, Kusano S, Terakubo S, Nakashima H, Broach JA, Trent JO, Wang ZX, Peiper SC. Molecular-size reduction of a potent CXCR4-chemokine antagonist using orthogonal combination of conformation- and sequence-based libraries. *Angew Chem Int Ed* 2003; 42: 3251-3253
- 68 Oishi S, Masuda R, Evans B, Ueda S, Goto Y, Ohno H, Hirasawa A, Tsujimoto G, Wang Z, Peiper SC, Naito T, Kodama E, Matsuoka M, Fujii N. Synthesis and application of fluorescein- and biotin-labeled molecular probes for the chemokine receptor CXCR4. *ChemBioChem*. 2008; 9: 1154-1158
- 69 Jacobson O, Weiss ID, Szajek LP, Niu G, Ma Y, Kiesewetter DO, Peled A, Eden HS, Farber JM, Chen X. Improvement of CXCR4 tracer specificity for PET imaging. *J Control Release*. 2012; 157: 216-223
- 70 Jacobson O, Weiss ID, Kiesewetter DO, Farber JM, Chen X. PET of tumor CXCR4 expression with 4-¹⁸F-T140. *J Nucl Med*. 2010; 51: 1796-1804
- 71 Hanaoka H, Mukai T, Tamamura H, Mori T, Ishino S, Ogawa K, Iida Y, Doi R, Fujii N, Saji H. Development of a ¹¹¹In-labeled peptide derivative targeting a chemokine receptor, CXCR4, for imaging tumors. *Nucl Med Biol*. 2006; 33: 489-494
- 72 Jacobson O, Weiss ID, Szajek LP, Niu G, Ma Y, Kiesewetter DO, Farber JM, Chen X. PET imaging of CXCR4 using copper-64 labeled peptide antagonist. *Theranostics*. 2011; 1: 251-262
- 73 De Silva RA, Peyre K, Pullambhatla M, Fox JJ, Pomper MG, Nimmagadda S. Imaging CXCR4 expression in human cancer xenografts: evaluation of monocyclam ⁶⁴Cu-AMD3465. *J Nucl Med*. 2011; 52: 986-993
- 74 Nimmagadda S, Pullambhatla M, Stone K, Green G, Bhujwala ZM, Pomper MG. Molecular imaging of CXCR4 receptor expression in human cancer xenografts with [⁶⁴Cu]AMD3100 positron emission tomography. *Cancer Res*. 2010; 70: 3935-3944
- 75 Kuil J, Buckle T, Yuan H, van den Berg NS, Oishi S, Fujii N, Josephson L, van Leeuwen FWB. Synthesis and evaluation of a bimodal CXCR4 antagonistic peptide. *Bioconjugate Chem*. 2011; 22: 859-864
- 76 Kuil J, Steunenbergh P, Chin PTK, Oldenburg J, Jalink K, Velders AH, van Leeuwen FWB. Peptide-functionalized luminescent iridium complexes for lifetime imaging of CXCR4 expression. *ChemBioChem*. 2011; 12: 1897-1903
- 77 Kuil J, Buckle T, Oldenburg J, Yuan H, Borowsky AD, Josephson L, van Leeuwen FWB. Hybrid peptide dendrimers for imaging of chemokine receptor 4 (CXCR4) expression. *Mol Pharm*. 2011; 8: 2444-2453

- 78 Nakamura T, Furunaka H, Miyata T, Tokunaga F, Muta T, Iwanaga S, Niwa M, Takao T, Shimonishi Y. Tachyplesin, a class of antimicrobial peptide from the hemocytes of the horseshoe crab (*Tachyplesus tridentatus*). Isolation and chemical structure. *J Biol Chem.* 1988; 263: 16709-16713
- 79 Miyata T, Tokunaga F, Yoneya T, Yoshikawa K, Iwanaga S, Niwa M, Takao T, Shimonishi Y. Antimicrobial peptides, isolated from horseshoe crab hemocytes, tachyplesin II, and polyphemusins I and II: chemical structures and biological activity. *J Biochem.* 1989; 106: 663-668
- 80 Masuda M, Nakashima H, Ueda T, Naba H, Ikoma R, Otaka A, Terakawa Y, Tamamura H, Ibuka T, Murakami T, Koyanagi Y, Waki M, Matsumoto A, Yamamoto N, Funakoshi S, Fujii N. A novel anti-HIV synthetic peptide, T-22 ([Tyr^{5,12},Lys⁷]-polyphemusin II). *Biochem Biophys Res Commun.* 1992; 189: 845-850
- 81 Tamamura H, Xu Y, Hattori T, Zhang X, Arakaki R, Kanbara K, Omagari A, Otaka A, Ibuka T, Yamamoto N, Nakashima H, Fujii N. A low-molecular-weight inhibitor against the chemokine receptor CXCR4: a strong anti-HIV peptide T140. *Biochem Biophys Res Commun.* 1998; 253: 877-882
- 82 Zhang WB, Navenot JM, Haribabu B, Tamamura H, Hiramatsu K, Omagari A, Pei G, Manfredi JP, Fujii N, Broach JR, Peiper SC. A point mutation that confers constitutive activity to CXCR4 reveals that T140 is an inverse agonist and that AMD3100 and ALX40-4C are weak partial agonists. *J Biol Chem.* 2002; 277: 24515-24521
- 83 Trent JO, Wang ZX, Murray JL, Shao W, Tamamura H, Fujii N, Peiper SC. Lipid bilayer simulations of CXCR4 with inverse agonists and weak partial agonists. *J Biol Chem.* 2003; 278: 47136-47144
- 84 Wu B, Chien EYT, Mol CD, Fenalti G, Liu W, Katritch V, Abagyan R, Brooun A, Wells P, Bi FC, Hamel DJ, Kuhn P, Handel TM, Cherezov V, Stevens RC. Structures of the CXCR4 chemokine GPCR with small-molecule and cyclic peptide antagonists. *Science.* 2010; 330: 1066-1071
- 85 Tamamura H, Omagari A, Oishi S, Kanamoto T, Yamamoto N, Peiper SC, Nakashima H, Otaka A, Fujii N. Pharmacophore identification of a specific CXCR4 inhibitor, T140, leads to development of effective anti-HIV agents with very high selectivity indexes. *Bioorg Med Chem Lett.* 2000; 10: 2633-2637
- 86 Tamamura H, Omagari A, Hiramatsu K, Gotoh K, Kanamoto T, Xu Y, Kodama E, Matsuoka M, Hattori T, Yamamoto N, Nakashima H, Otaka A, Fujii N. Development of specific CXCR4 inhibitors possessing high selectivity indexes as well as complete stability in serum based on an anti-HIV peptide T140. *Bioorg Med Chem Lett.* 2001; 11: 1897-1902

- 87 Tamamura H, Sugioka M, Odagaki Y, Omagari A, Kan Y, Oishi S, Nakashima H, Yamamoto N, Peiper SC, Hamanaka N, Otaka A, Fujii N. Conformational study of a highly specific CXCR4 inhibitor, T140, disclosing the close proximity of its intrinsic pharmacophores associated with strong anti-HIV activity. *Bioorg Med Chem Lett*. 2001; 11: 359-362
- 88 Tamamura H, Hiramatsu K, Kusano S, Terakubo S, Yamamoto N, Trent JO, Wang Z, Peiper SC, Nakashima H, Otaka A, Fujii N. Synthesis of potent CXCR4 inhibitors possessing low cytotoxicity and improved biostability based on T140 derivatives. *Org Biomol Chem*. 2003; 1: 3656-3662
- 89 Tamamura H, Hiramatsu K, Mizumoto M, Ueda S, Kusano S, Terakubo S, Akamatsu M, Yamamoto N, Trent JO, Wang Z, Peiper SC, Nakashima H, Otaka A, Fujii N. Enhancement of the T140-based pharmacophores leads to the development of more potent and bio-stable CXCR4 antagonists. *Org Biomol Chem*. 2003; 1: 3663-3669
- 90 Tamamura H, Hori A, Kanzaki N, Hiramatsu K, Mizumoto M, Nakashima H, Yamamoto N, Otaka A, Fujii N. T140 analogs as CXCR4 antagonists identified as anti-metastatic agents in the treatment of breast cancer. *FEBS Letters*. 2003; 550: 79-83
- 91 Liang Z, Wu T, Lou H, Yu X, Taichman RS, Lau SK, Nie S, Umbreit J, Shim H. Inhibition of breast cancer metastasis by selective synthetic polypeptide against CXCR4. *Cancer Res*. 2004; 64: 4302-4308
- 92 DeMarco SJ, Henze H, Lederer A, Moehle K, Mukherjee R, Romagnoli B, Robinson JA, Brianza F, Gombert FO, Lociuro S, Ludin C, Vrijbloed JW, Zumbunn J, Obrecht JP, Obrecht D, Brondani V, Hamy F, Klimkait T. Discovery of novel, highly potent and selective beta-hairpin mimetic CXCR4 inhibitors with excellent anti-HIV activity and pharmacokinetic profiles. *Bioorg Med Chem*. 2006; 14: 8396-8404
- 93 Tamamura H, Tsutsumi H, Masuno H, Mizokami S, Hiramatsu K, Wang Z, Trent JO, Nakashima H, Yamamoto N, Peiper SC, Fujii N. Development of a linear type of low molecular weight CXCR4 antagonists based on T140 analogs. *Org Biomol Chem*. 2006; 4: 2354-2357
- 94 Moncunill G, Armand-Ugon M, Clotet-Codina I, Pauls E, Ballana E, Llano A, Romagnoli B, Vrijbloed JW, Gombert FO, Clotet B, De Marco S, Este JA. Anti-HIV activity and resistance profile of the CXC chemokine receptor 4 antagonist POL3026. *Mol Pharmacol*. 2008; 73: 1264-1273
- 95 Narumi T, Ochiai C, Yoshimura K, Harada S, Tanaka T, Nomura W, Arai H, Ozaki T, Ohashi N, Matsushita S, Tamamura H. CD4 mimics targeting the HIV entry mechanism and their hybrid molecules with a CXCR4 antagonist. *Bioorg Med Chem Lett*. 2010; 20: 5853-5858

- 96 Nomura W, Tanabe Y, Tsutsumi H, Tanaka T, Ohba K, Yamamoto N, Tamamura H. Fluorophore labeling enables imaging and evaluation of specific CXCR4-ligand interaction at the cell membrane for fluorescence-based screening. *Bioconjugate Chem.* 2008; 19: 1917-1920
- 97 van den Berg NS, Buckle T, Kuil J, Wesseling J, van Leeuwen FWB. Direct fluorescent detection of CXCR4 using a targeted peptide antagonist. *Trans Oncol.* 2011; 4: 224-230
- 98 Bunschoten A, Buckle T, Kuil J, Luker GD, Luker KE, Nieweg OE, van Leeuwen FWB. Targeted non-covalent self-assembled nanoparticles based on human serum albumin. *Biomaterials.* 2012; 33: 867-875
- 99 Nishizawa K, Nishiyama H, Oishi S, Tanahara N, Kotani H, Mikami Y, Toda Y, Evans BJ, Peiper SC, Saito R, Watanabe J, Fujii N, Ogawa O. Fluorescent imaging of high-grade bladder cancer using a specific antagonist for chemokine receptor CXCR4. *Int J Cancer.* 2010; 127: 1180-1187
- 100 Kobayashi H, Ogawa M, Alford R, Choyke PL, Urano Y. New strategies for fluorescent probe design in medical diagnostic imaging. *Chem Rev.* 2010; 110: 2620-2640
- 101 Buckle T, van den Berg NS, Kuil J, Bunschoten A, Oldenburg J, Borowsky AD, Wesseling J, Masada R, Oishi S, Fujii N, van Leeuwen FWB. Non-invasive longitudinal imaging of tumor progression using an ¹¹¹Indium labeled CXCR4 peptide antagonist. *Am J Nucl Med Mol Imaging.* 2012; 2: 99-109
- 102 Han Y, Yin D, Zheng M, Zhou W, Lee Z, Zhan L, Ma Y, Wu M, Shi L, Wang N, Lee J, Wang C, Lee Z, Wang Y. Synthesis and preliminary evaluation of a novel ¹²⁵I-labeled T140 analog for quantitation of CXCR4 expression. *J Radioanal Nucl Chem.* 2010; 284: 279-286
- 103 Masuda R, Oishi S, Ohno H, Kimura H, Saji H, Fujii N. Concise site-specific synthesis of DTPA-peptide conjugates: Application to imaging probes for the chemokine receptor CXCR4. *Bioorg Med Chem.* 2011; 19: 3216-3220
- 104 Hennrich U, Seyler L, Schafer M, Bauder-Wust U, Eisenhut M, Semmler W, Bauerle T. Synthesis and in vitro evaluation of ⁶⁸Ga-DOTA-4-FBn-TN14003, a novel tracer for the imaging of CXCR4 expression. *Bioorg Med Chem.* 2012; 20: 1502-1510
- 105 Garanger E, Aikawa E, Reynolds F, Weissleder R, Josephson L. Simplified syntheses of complex multifunctional nanomaterials. *Chem Commun.* 2008: 4792-4794
- 106 Garanger E, Blois J, Hilderbrand SA, Shao F, Josephson L. Divergent oriented synthesis for the design of reagents for protein conjugation. *J Comb Chem.* 2010; 12: 57-64
- 107 Cai W, Chen K, He L, Cao Q, Koong A, Chen X. Quantitative PET of EGFR expression in xenograft-bearing mice using ⁶⁴Cu-labeled cetuximab, a chimeric anti-EGFR monoclonal antibody. *Eur J Nucl Med Mol Imaging.* 2007; 34: 850-858

Interventional Immunohistochemical detection molecular imaging, of CXCR4 expression in tumor tissue a hybrid approach using the fluorescent peptide antagonist Ac-TZ14011-FITC

Chapter 9

*Adapted from:
van den Berg NS#, Buckle T#, Kuil J, Wesseling J, van Leeuwen FWB.
Transl Oncol. 2011; 4(4): 234-40
authors contributed equally*

Abstract

Pathology is fundamental in the evaluation of tumor grade and stage, and in treatment planning of malignancies. Direct fluorescent labeling of the peptide Ac-TZ14011 with the fluorescent dye FITC, provides an alternative to conventional immunohistochemistry for the detection of CXCR4 in cells and tumor tissue. The use of Ac-TZ14011-FITC for staining of the chemokine receptor 4 (CXCR4) in human breast cancer cell lines MDAMB231 and MDAMB231^{CXCR4+} was evaluated during flow cytometric analysis. Staining specificity was validated via competition experiments and the efficacy of Ac-TZ14011-FITC was compared to commercially available antibodies. Confocal imaging revealed that CXCR4 staining was predominantly found on the cell membrane and/or in vesicles formed after endocytosis. Ac-TZ14011-FITC was able to differentiate MDAMB231 from MDAMB231^{CXCR4+} tumor cells and tumor tissue, proving its applicability in the detection of relatively small differences in levels of CXCR4 expression.

Introduction

Besides expression of the chemokine receptor 4 (CXCR4) in normal tissues, overexpression of CXCR4 has been reported for at least 23 types of cancer. A 5.5-fold upregulation of CXCR4 expression was found in breast cancer tissue¹⁻³ Overexpression of CXCR4, and/or its natural ligand stromal-derived factor 1 (SDF-1), has been correlated to worsened prognosis and disease-free survival.⁴⁻⁶ Due to its important role in the malignancy/metastasis of cancer, CXCR4 is considered a candidate biomarker for evaluating cancer progression and perhaps the selection/monitoring of treatment strategies.

Recently, a lot of effort has been focused on the development of CXCR4 specific antagonistic peptides.^{7,8} Small peptides, such as T140 and its derivative Ac-TZ14011, were selected based on their antagonistic properties towards the CXCR4 receptor and their potential for treatment.¹⁰ These and several other peptide derivatives have been used to reduce cell proliferation and migration in vitro and to cause inhibition of primary tumor growth and tumor metastasis in vivo.⁸⁻¹⁴ A useful property of the Ac-TZ14011 peptide is that it has one free lysine group situated at a significant distance from the pharmacophore allowing functionalization with a single diagnostic antenna. For example, an ¹¹¹Indium labeled DTPA-Ac-TZ14011 derivative has shown potential for use in non-invasive imaging of CXCR4 in vivo.^{14,15}

As CXCR4 is part of a family of membrane bound G protein-coupled receptors, staining of the cell surface membrane could be considered most representative. However, immunohistochemistry (IHC) on breast cancer tissue using antibodies directed against CXCR4 has shown staining of the cell surface membrane, the cytoplasm, and the nucleus of the cell.^{4-6,8,16-18} Such differences in localization and the natural role of CXCR4 may present actual changes in the localization of the receptor or may be caused by the staining techniques used. Another downside of using antibodies for IHC is that the agent used for detection will differ from the peptides used in vivo.

Ideally ex vivo validation is performed using an agent that accurately resembles the compound used for imaging. Nishizawa et al. have demonstrated the value of the fluorescein labeled T140 derivative TY14003 in the detection of high-grade bladder cancer.¹⁹ Hence we reasoned that a fluorescent derivative of Ac-TZ14011 (Ac-TZ14011-FITC) can also potentially be used for fluorescent IHC (FIHC) of breast tumor tissue.

In this Chapter Ac-TZ14011-FITC was used for FIHC to detect CXCR4 in MDAMB231 and MDAMB231^{CXCR4+} cells and tumor tissue. The efficacy of Ac-TZ14011-FITC in staining CXCR4 was compared to that of commercially available anti-CXCR4 antibodies.

Materials and Methods

Cell culture

Human breast cancer cell lines MDAMB231 and MDAMB231^{CXCR4+} were kindly provided by Olaf van Tellingen and Ed Roos (NKI-AvL, Amsterdam, The Netherlands), respectively. In the MDAMB231^{CXCR4+} cells CXCR4 expression was upregulated after culture under hypoxic conditions. Cells with high CXCR4 expression were selected using flow cytometry, resulting in the MDAMB231^{CXCR4+} cell line. MDAMB231 cells were used as control based on their basal CXCR4 expression. Both cell lines were maintained in Gibco's minimum essential medium (MEM) enriched with 10% fetal bovine serum, Penicillin, Streptomycin, L-glutamine, non-essential amino acids, sodium pyruvate, and MEM vitamins solution (all Life Technologies Inc.). Cells were kept under standard culture conditions.

Flow cytometry

Cell staining: determination of the specificity of Ac-TZ14011-FITC for CXCR4

Freshly cultured MDAMB231 or MDAMB231^{CXCR4+} cells were trypsinized, washed with 0.1% bovine serum albumin in phosphate buffered saline (0.1% BSA/PBS) and then incubated for one hr with monoclonal phycoerythrin (PE) labeled anti-CXCR4 antibody (12G5-PE (1:5) or 2B11-PE (1:100); BD Biosciences) or with Ac-TZ14011-FITC (1:200; for the preparation of Ac-TZ14011-FITC see the Annex of Chapter 9). Cells were labeled on ice or at room temperature (RT). Following incubation, cells were washed with 0.1% BSA/PBS and five min prior to analysis, propidium iodide (PI; 1:10,000; BD Biosciences) was added to distinguish live and dead cells.

For fixed cell conditions, cells were trypsinized, washed with 0.1% BSA/PBS, and fixed with formalin overnight, again washed with 0.1% BSA/PBS and incubated for one hr with 12G5-PE, 2B11-PE or Ac-TZ14011-FITC on ice, followed by washing with 0.1% BSA/PBS.

Peptides and antibodies were diluted in 0.1% BSA/PBS in all flow cytometry experiments. Non-antibody/peptide incubated cells served as controls.

Cell-staining: SDF-1 and Ac-TZ14011 competition experiment

One hr prior to the start of the experiment, MDAMB231 or MDAMB231^{CXCR4+} cells were given fresh culture medium. Following trypsinization, 6.0×10^6 cells/mL were incubated for one hr on ice with 12G5-PE and SDF-1 (Peprotech via Bio Connect; [8.87

nM]), Ac-TZ14011-FITC and SDF-1 ([0.67 μ M]) or Ac-TZ12011-FITC and unlabeled Ac-TZ14011 ([0.67 μ M] and [6.70 μ M], respectively). Cells were washed with 0.1% BSA/PBS. PI was added before cells were analyzed.

Cell-staining: SDF-1 block experiment

One hr prior to the start of the experiment, MDAMB231 or MDAMB231^{CXCR4+} cells were given fresh culture medium. After trypsinization, 2.0×10^6 cells/mL were incubated for 90 min at 37°C with 1.5 μ g SDF-1 in culture medium. SDF-1 was removed by centrifugation (five min, 1200 rpm, 4°C), and cells were resuspended at 6.0×10^6 cells/mL before incubation on ice for one hr with 12G5-PE or Ac-TZ14011-FITC. Hereafter, cells were washed with 0.1% BSA/PBS, PI was added and cells were analyzed.

Flow cytometry settings

After staining, cells were analyzed using a Beckton Dickinson FACScalibur device (BD Biosciences) equipped with Cell Quest Pro software (BD Biosciences). FITC fluorescence was detected in the FL1 channel (excitation 488 nm; emission filter 585/42 nm). PE fluorescence was detected in the FL2 channel (excitation 488 nm; emission filter 530/30 nm). PI was detected in the FL3 channel (excitation 488 nm; emission filter > 670 nm).

Mean fluorescence signal intensity ratio's (MFIRs) were calculated by dividing the mean fluorescent signal intensity of the antibody or peptide incubated condition by the mean fluorescent signal intensity of the control condition. To determine statistical significance between the different cell lines (Table 1) or the different incubation conditions (Table 2 and 3), a standard T-test was performed. All experiments were performed at least in triplicate.

Generation mouse tumor models

Prior to injection *in vivo*, cells were washed three times with Hank's buffered salt solution (HBSS; Life Technologies) and resuspended in HBSS to a final concentration of 50.0×10^6 cells/mL and kept on ice.

Six to eight week old female Balb/c nude mice were anaesthetized with a mixture of hypnorm (Vetapharma), dormicum (Roche Diagnostics GmbH) and water suitable for injection (1:1:2; 5 μ L/gr intraperitoneal). 1.0×10^6 MDAMB231 or MDAMB231^{CXCR4+} cells were injected into the left inguinal mammary fat pad. As CXCR4 expression in the lymph nodes is intrinsically high, the left inguinal lymph node was cleared before injection of the

tumor cells, hereby creating a low background niche at the site of injection. Six to eight weeks following transplantation, mice were sacrificed and primary tumors (~ 4 cm³) were taken out (n = 20). Hereafter, fresh tumor tissue could be directly stained and analyzed or formalin-fixed and paraffin-embedded prior to staining (IHC and fluorescence IHC (FIHC)).

All animal experiments were performed in accordance with Dutch animal welfare regulations and approved by the local ethics committee.

Immunohistochemistry

Four micron formalin-fixed paraffin-embedded MDAMB231 or MDAMB231^{CXCR4+} tumor tissue sections were deparaffinized. Sections were heated for 30 min at 95°C in citrate buffer (pH 6) to retrieve antigenic activity, followed by 30 min cooling at RT. For antigen retrieval, slides were incubated for 30 min with protein kinase or 20 min with trypsin at 37°C or heated for 30 min at 95°C in TRIS/EDTA (pH 9) followed by 30 min cooling at room temperature (RT). Slides were rinsed with PBS and incubated overnight at 4°C with an monoclonal anti-CXCR4-antibody (clone 2B11 (1:100) (n= 5 - 10) or clone 12G5 (1:100) (n = 3); BD Biosciences). After washing, slides were incubated for one hr at RT with the secondary antibody, goat-anti-rat (sc-2041; 1:100; Santa Cruz Technology) or with goat-anti-mouse (E0433; 1:500; DAKO) for clone 2B11 and 12G5, respectively. Negative controls were only incubated with the secondary antibody. Hereafter slides were washed, incubated for 30 min with horseradish-peroxidase-labeled StreptAvidin-Biotin Complex (HRP-sABC; 1:200; DAKO), developed with 3,3'-diamobenzidine tetrahydrochloride (DAB; Sigma-Aldrich) and slightly counterstained with haematoxylin (Sigma-Aldrich). Images were taken with a color CCD microscope system (Axiovert S100 with AxioCam HRc, Carl Zeiss) and analyzed using AxioVision (Carl Zeiss).

Confocal imaging

Fluorescent immunohistochemistry of formalin-fixed paraffin-embedded tumor tissue

Following deparaffinization, antigen retrieval incubation and three PBS washes (as described in the IHC section), slides were incubated for one hr at RT with Ac-TZ14011-FITC (1:200) (n = 3). Slides were washed with PBS, counterstained with 4',6-diamidine-2'-phenylindole dihydrochloride (DAPI; 1:1000; Roche Diagnostics GmbH) and washed thoroughly. Negative controls were only incubated with DAPI. Slides were mounted with Vectashields mounting medium for fluorescence to preserve the fluorescent signal (Vector Laboratories Inc.).

In vitro immunofluorescence

24 - 48 Hrs prior to the start of the experiment, 1.0×10^5 MDAMB231 and MDAMB231^{CXCR4+} cells were seeded onto coverslips (\varnothing 24 mm; Karl Hecht GmbH&Co). When 80% confluency was reached, cells were washed with PBS and incubated with Ac-TZ14011-FITC (1:200) for one hr on ice or at RT and washed again with ice cold PBS. Cells were kept on ice until analysis. For evaluation of internalization, images were taken at $t = 0, 15, 30$ and 60 min.

For fixed cell conditions, cells were fixed with formalin overnight, washed with PBS and then incubated for one hr on ice with Ac-TZ14011-FITC. Confocal images were taken after washing with ice cold PBS. Non-peptide incubated slides served as negative control.

Ex vivo fluorescent tumor tissue imaging

MDAMB231 or MDAMB231^{CXCR4+} tumor-bearing mice were sacrificed, and excised tumor tissue was formalin-fixed for 24 hrs ($n = 3$). Tissue slices were incubated for one hr with Ac-TZ14011-FITC (1:200) followed by washing with PBS and incubation with DAPI (1:1000) for 10 min and again thoroughly washed with ice cold PBS.

Ex vivo detection after intravenous administration of Ac-TZ14011-FITC

MDAMB231 or MDAMB231^{CXCR4+} tumor-bearing mice were intravenously injected with 50 μ g Ac-TZ14011-FITC ($n = 3$). 24 hrs after injection, mice were sacrificed, tumors were excised and kept on ice in PBS. Thin slices were cut, washed with ice-cold PBS and incubated for ten min with DAPI and again thoroughly washed before images were taken. Furthermore, excised tissue was formalin-fixed on ice for three hrs, cut into thin slices and washed with ice cold PBS and incubated with DAPI before imaging. Controls were only incubated with DAPI.

Confocal microscope properties

Confocal images were taken on a Leica TCS-SP2-AOBS Live confocal microscope (Leica Microsystems; magnification 400x / 630x) and a Leica TCS-NT confocal microscope (Leica Microsystems; magnification 630x). DAPI was excited at 405 nm and emission was detected between 409 - 468 nm. FITC was excited at 488 nm and emission was detected between 510 - 585 nm. Leica Confocal Software was used to analyze the images.

Results

A FITC labeled antagonistic CXCR4 peptide, Ac-TZ14011-FITC, was investigated for use in the direct fluorescence-based visualization of CXCR4 expression levels in MDAMB231 and MDAMB231^{CXCR4+} cells and tumors derived thereof.

Determination of the specificity of Ac-TZ14011-FITC for CXCR4

The specificity of Ac-TZ14011-FITC for CXCR4 was validated using flow cytometric analysis. The MFIR of MDAMB231^{CXCR4+} (high level of CXCR4 expression) was 2.4-fold higher ($p = 0.0003$) compared to MDAMB231 cells (low level of CXCR4 expression) when live cells were incubated on ice with Ac-TZ14011-FITC (Table 1). However, after incubation at RT, only a 1.7-fold higher signal intensity could be detected ($p = 0.04$; Table 1). PE labeled anti-CXCR4 antibody clones 12G5 or 2B11 (referred to as 12G5-PE or 2B11-PE, respectively) were used as a reference. After incubation with 12G5-PE a 4.4-fold higher MFIR could be detected in MDAMB231^{CXCR4+} cells compared to MDAMB231 cells (Table 1; $P = 0.01$). Incubation at RT resulted in a 7.5-fold higher MFIR ($P = 0.0012$). For 2B11-PE the measured difference in MFIR was only 1.3-fold ($P = 0.003$) and 1.2-fold ($P = 0.0035$) higher when incubated on ice or at RT.

When formalin-fixed cells were stained with Ac-TZ14011-FITC, signal intensities and thereby the MFIRs increased for both MDAMB231 (MFIR = 25.788 ± 1.575) and MDAMB231^{CXCR4+} (MFIR = 62.357 ± 7.920) cells. However, the ratio between the two remained identical to that in live cells incubated on ice, namely 2.4 ($P < 0.0001$). Significant differences could no longer be detected when formalin-fixed MDAMB231 and MDAMB231^{CXCR4+} cells were incubated with 12G5-PE (MFIRs 7.380 ± 3.573 and 11.046 ± 2.143 ; $P = 0.22$) or 2B11-PE (MFIRs 18.814 ± 6.636 and 13.378 ± 3.267 ; $P = 0.29$; Table 1).

Ac-TZ14011 competition experiment

When cells were co-incubated with a 100-fold excessive amount of unlabeled Ac-TZ14011 and Ac-TZ14011-FITC, the MFIR of MDAMB231^{CXCR4+} cells decreased with 57% ($P = 0.0041$; Table 2) indicating a higher affinity for Ac-TZ14011. The latter is in line with the slight decrease in affinity seen after functionalization of Ac-TZ14011 with other fluorophores.⁸

Table 1. CXCR4 related fluorescence intensity measured in MDAMB231 and MDAMB231^{CXCR4+} cells incubated at different conditions.

	Cell type		Signal intensity Difference MDAMB231/ MDAMB231 ^{CXCR4+}
	MDAMB231	MDAMB231 ^{CXCR4+}	
	MFIR \pm SD	MFIR \pm SD	
12G5-PE			
Live cells; on ice	1.116 \pm 0.054	4.920 \pm 1.463	4.4*
Live cells; RT	1.160 \pm 0.108	8.747 \pm 1.245	7.5**
Fixed cells; on ice	7.380 \pm 3.573	11.046 \pm 2.143	1.5
2B11-PE			
Live cells; on ice	1.179 \pm 0.072	1.487 \pm 0.051	1.3**
Live cells; RT	1.206 \pm 0.047	1.435 \pm 0.042	1.2**
Fixed cells; on ice	18.814 \pm 6.636	13.378 \pm 3.267	0.7
Ac-TZ14011-FITC			
Live cells; on ice	2.337 \pm 0.341	5.505 \pm 0.900	2.4**
Live cells; RT	2.970 \pm 0.289	4.941 \pm 0.487	1.7*
Fixed cells; on ice	25.788 \pm 1.575	62.357 \pm 7.920	2.4**

For significance: MDAMB231 MFIRs were compared to MDAMB231^{CXCR4+} MFIRs; *P = < 0.05; **P = < 0.005; MFIR = mean fluorescent intensity ratio; SD = standard deviation; RT = room temperature; n = 3 - 6.

SDF-1 competition experiment

In further competition experiments a corresponding amount of SDF-1 was added to occupy the CXCR4 receptors, hereby preventing binding of Ac-TZ14011-FITC to the receptor. In the presence of Ac-TZ14011-FITC and SDF-1, a decrease of 33% was seen in the MFIR in MDAMB231^{CXCR4+} cells compared to cells who were incubated with Ac-TZ14011-FITC alone (P = 0.002). Co-incubation of 12G5-PE and SDF-1 resulted in an 8% decrease in the MFIR in MDAMB231^{CXCR4+} cells (P = 0.13). No significant change in MFIR was seen in MDAMB231 cells (Table 2).

Table 2. Competition of antagonistic Ac-TZ14011-FITC with SDF-1 and Ac-TZ14011 for the CXCR4 receptor.

	Cell type			
	MDAMB231		MDAMB231CXCR4+	
	MFIR \pm SD	%	MFIR \pm SD	%
12G5-PE	1.134 \pm 0.033		2.186 \pm 0.048	
SDF-1 + 12G5-PE	1.174 \pm 0.009	+ 3	2.015 \pm 0.080	- 8
Ac-TZ14011-FITC	1.900 \pm 0.049		6.905 \pm 0.174	
SDF-1 + Ac-TZ14011-FITC	2.010 \pm 0.044	+ 6	4.643 \pm 0.339	- 33**
Ac-TZ14011 + Ac-TZ14011-FITC	2.266 \pm 0.095	+ 19*	2.985 \pm 0.291	- 57**

For significance: 12G5-PE/Ac-TZ14011-FITC MFIRs were compared to MFIRs of SDF-1/unlabeled Ac-TZ14011 + 12G5-PE/Ac-TZ14011-FITC incubated conditions; *P = < 0.05; **P = < 0.005; % = Percentage change in fluorescent signal intensity; MFIR = mean fluorescence intensity ratio; SD = standard deviation; n = 3.

SDF-1 block experiment

The CXCR4 receptor internalizes upon binding of SDF-1 resulting in clearance from the membrane.^{27,30} To study this effect, MDAMB231^{CXCR4+} cells were preincubated for 1.5 hrs with SDF-1 at 37°C. After removal of the excess SDF-1 in solution, cells were incubated with 12G5-PE or Ac-TZ14011-FITC for one hr on ice to determine the amount of available membranous CXCR4. As can be seen in Table 3, preincubation of MDAMB231^{CXCR4+} cells with SDF-1 followed by incubation with Ac-TZ14011-FITC resulted in a 29% decrease in MFIR compared to incubation with Ac-TZ14011-FITC alone (P = 0.0037). The MFIR decreased with 14% after preincubation with SDF-1 followed by 12G5-PE incubation (P = 0.0043). Possibly this indicates that a significant number of the available CXCR4-receptors internalized after binding SDF-1, hereby preventing binding of Ac-TZ14011-FITC and 12G5-PE.

Table 3: blocking of CXCR4 with SDF-1

	Cell type	
	MDAMB231CXCR4+	
	MFIR \pm SD	%
12G5-PE	1.485 \pm 0.018	
SDF-1 + 12G5-PE	1.274 \pm 0.033	- 14**
Ac-TZ14011-FITC	5.184 \pm 0.144	
SDF-1 + Ac-TZ14011-FITC	3.699 \pm 0.034	- 29**

For significance: 12G5-PE/Ac-TZ14011-FITC MFIRs were compared to MFIRs of SDF-1 + 12G5-PE/Ac-TZ14011-FITC incubated conditions; *P = < 0.05; **P = < 0.005; % = Percentage change in fluorescent signal intensity; MFIR = mean fluorescence intensity ratio; SD = standard deviation; n = 3.

Ac-TZ14011-FITC distribution in cultured tumor cells

Cellular localization of the CXCR4 receptor was evaluated using confocal imaging. As Figure 1A shows, only a faint membranous staining could be detected on MDAMB231 cells (i), whereas the degree of membranous staining in MDAMB231^{CXCR4+} cells was much higher (ii). Longitudinal imaging (t = 0 – 60 min; Figure 1C) revealed progressive internalization of the fluorescence signal into the cell. Here endocytosis resulted in internalization of Ac-TZ14011-FITC in vesicle like structures visible in the cytoplasm.

Incubation of formalin-fixed cells with Ac-TZ14011-FITC yielded an entirely different staining pattern. Ac-TZ14011-FITC, was found throughout the entire cell, in both MDAMB231 (Figure 1Bi) and MDAMB231^{CXCR4+} (Figure 1Bii) cells. However, the staining of MDAMB231^{CXCR4+} cells was more intense than that of MDAMB231 cells, which is in line with the higher MFIR seen with flow cytometric analysis of cells under fixed conditions (Table 1).

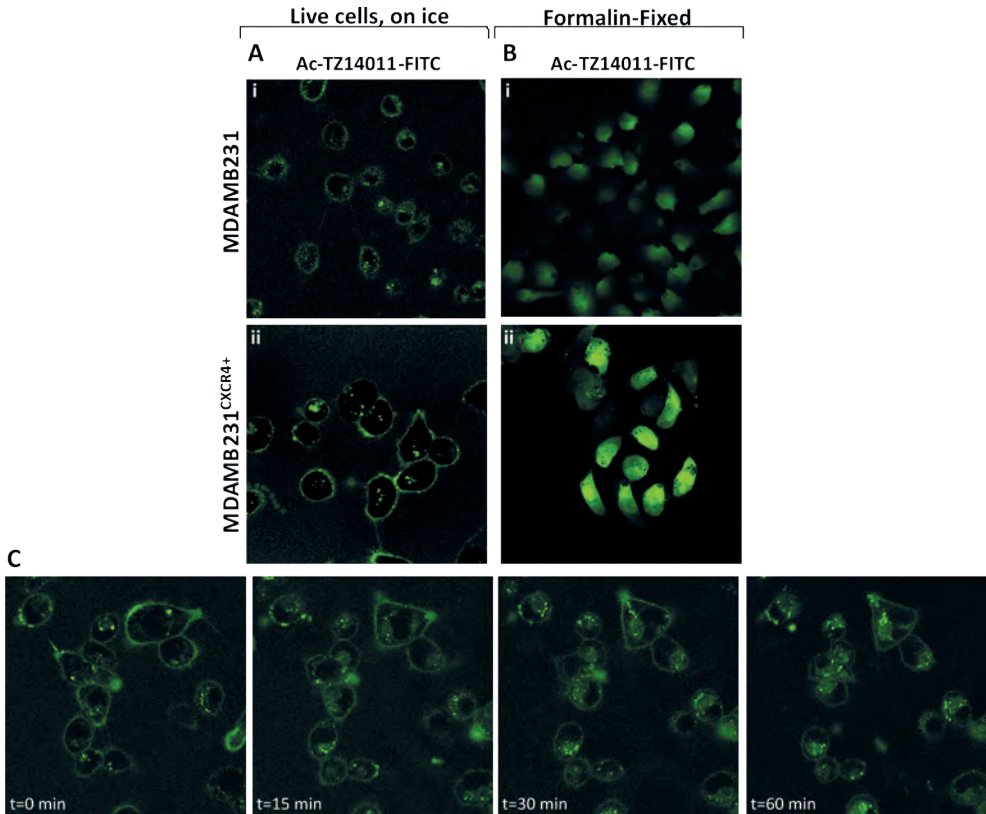


Figure 1. Ac-TZ14011-FITC distribution in live and formalin-fixed MDAMB231 and MDAMB231^{CXCR4+} tumor cells. A) Live MDAMB231 and MDAMB231^{CXCR4+} cells were incubated with Ac-TZ12011-FITC for one hr on ice. B) Formalin-fixed cells were incubated for one hr with Ac-TZ12011-FITC on ice. C) MDAMB231^{CXCR4+} cells were incubated for one hr with Ac-TZ12011-FITC on ice, and confocal images were taken (t = 0 min). Over time, Ac-TZ12011-FITC-CXCR4 receptor complexes internalized via vesicles (t = 15 - 60 min). Magnification 630x.

(F)IHC

Standard IHC was performed on formaline-fixed paraffin-embedded tissue to determine the CXCR4 expression level in tumor tissue. Using the 12G5 antibody, only a minor degree of staining could be detected in the MDAMB231 tumor tissue. MDAMB231^{CXCR4} tumor tissue however, stained brownish all over but no clear cytoplasmic or membranous staining could be discriminated. Control tumor tissue (only incubated with secondary antibody) showed a similar staining pattern (data not shown). Therefore these results were deemed non-specific. Use of different antigen retrieval methods did not result in

visualization of specific staining of the tissue (data not shown). Incubation of MDAMB231^{CXCR4} tissue with the 2B11 antibody resulted in strongly positively stained regions. In these regions, both membranous and cytoplasmic staining could be detected (Figure 2Bii). In comparison, little to no staining was detected on MDAMB231 tumor tissue (Figure 2Bi). The negative control slides showed no non-specific staining.

Incubation with Ac-TZ14011-FITC was initially also performed on formalin-fixed paraffin-embedded tumor tissue. MDAMB231 tumor tissue showed strong non-specific staining in the nuclear membrane, nucleoli and connective tissue (Figure 2Ci). MDAMB231^{CXCR4+} tumor tissue slides showed a somewhat different staining profile with predominantly cytoplasmic and membranous staining (Figure 2Cii).

When tumor tissue was not paraffin embedded, but only formalin-fixed for 24 hrs, incubation with Ac-TZ14011-FITC resulted in more intense staining of MDAMB231^{CXCR4+} tumor tissue (Figure 2Dii) compared to MDAMB231 tumor tissue (Figure 2Di). This result is in line with the difference in staining observed with 2B11 (Figure 2Bi and ii). However, as can be seen in Figure 2Di and ii, staining was detected throughout the entire cell and staining was not confined to the membrane and cytoplasm. This staining pattern in fixed tissue was highly similar to that observed in fixed cells (Figure 1Bi and ii).

FIHC of tumor tissue after intravenous administration of Ac-TZ14011-FITC in mice

Alternatively to ex vivo incubation of tissue, Ac-TZ14011-FITC can also be used for in vivo tumor staining (Figure 3). After intravenous administration, MDAMB231^{CXCR4+} tumor tissue slices showed positive staining for CXCR4 (Figure 3Bii). In MDAMB231 tumor tissue (Figure 3Bi) hardly any CXCR4 staining was observed.

Formalin fixation of Ac-TZ14011-FITC preincubated tissue predominantly revealed cytoplasmic staining for CXCR4 in MDAMB231^{CXCR4+} tumor tissue slices (Figure 3Cii) where MDAMB231 tumor tissue again stained weakly positive (Figure 3Ci). Importantly, the background signal found on formalin-fixed tumor tissue slices was relatively low (data not shown).

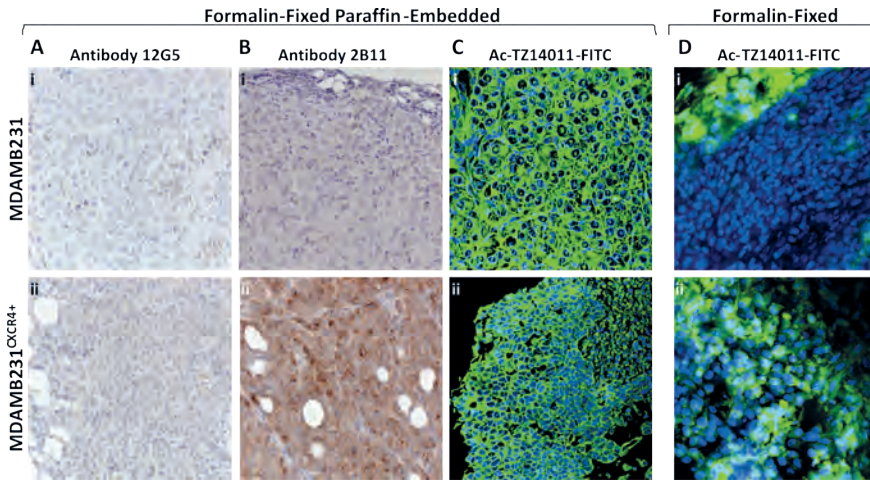


Figure 2. Predominant cytoplasmic CXCR4 expression on formalin-fixed paraffin-embedded and freshly isolated, formalin-fixed, breast cancer tissue. A) Formalin-fixed paraffin-embedded slides were incubated with the primary anti-CXCR4-antibody clone 12G5, B) primary anti-CXCR4-antibody clone 2B11 (Magnification 400x, n = 5 - 10); or C) incubated with Ac-TZ12011-FITC. Magnification 630x, n = 3 D) Freshly isolated, formalin-fixed tumor tissue incubated with Ac-TZ12011-FITC showed a different staining pattern. Magnification 630x, n = 3

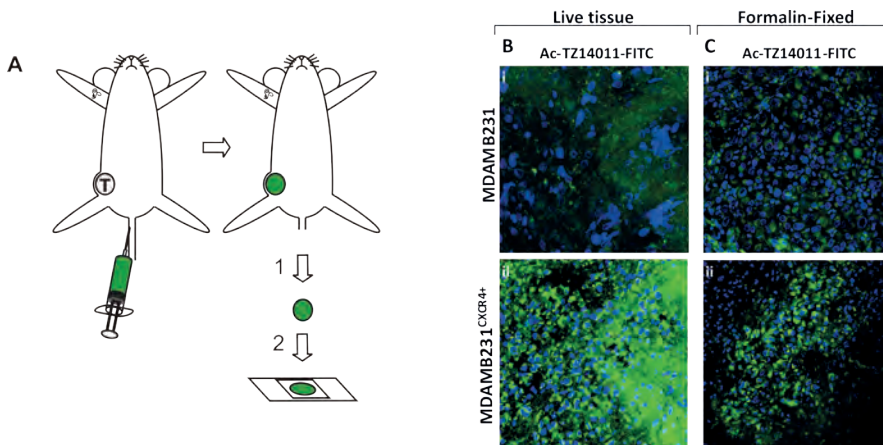


Figure 3. Predominantly cytoplasmic CXCR4 expression in in vivo Ac-TZ12011-FITC incubated MDAMB231^{CXCRA+} tumor tissue. A) Schematic overview of the principle of intravenously Ac-TZ14011-FITC incubation: 1. Mice were sacrificed and the tumor was isolated 24 hrs after 50 µg Ac-TZ14011-FITC was intravenously injected; 2. Tumors were cut into thin slices and placed on a coverslip. Hereafter confocal images were taken. B) Confocal images of live tumor tissue. Magnification 630x. Staining in controls was less profound (data not shown). C) Freshly isolated tumor tissue was formalin-fixed and imaged. Magnification 400x. Controls showed no staining (data not shown).

Discussion

Pathology, or rather IHC, is considered the golden standard in the assessment of tumor tissue. In this Chapter the potential of the fluorescent peptide Ac-TZ14011-FITC for evaluation of CXCR4 expression was evaluated. Other than conventional antibody based IHC procedures, this fluorescent derivative of Ac-TZ14011 may in the future be used to visualize exactly the same features at FIHC as can be detected with non-invasive SPECT imaging using the radioactive derivative ^{111}In -DTPA-Ac-TZ14011.

CXCR4 overexpressing cell lines rather than CXCR4 transfected cell lines

The CXCR4 negative and positive cell lines used show a small (factor 2.4 - 7.5) difference in CXCR4 expression levels (Table 1). Clearly, this minor difference makes it more difficult to differentiate between these two cell lines using FIHC. This is especially so because the MDAM231 cell line cannot be considered completely CXCR4 negative, but has a low or basal CXCR4 expression. CXCR4 transfected and/or down regulated cell lines would make the differences much clearer. However, we reasoned that differences in clinical breast tumor samples would also be marginal, as an up regulation factor of 5.5 has been reported.¹

Due to this similarity in overexpression, we consider the difference between our MDAM231 cell lines more representative for the clinical situation and thus this experimental set-up may better predict the potential clinical value of the approach.

Selectivity of Ac-TZ14011-FITC for CXCR4

Ac-TZ14011-FITC was able to discriminate between MDAMB231 and MDAM231^{CXCR4+} cells (Table 1). Selectivity of Ac-TZ14011-FITC was further evaluated via competition with the natural ligand for CXCR4, SDF-1. Both competition and blocking experiments showed a reduction in binding of Ac-TZ14011-FITC (Table 2 and 3). From these results it can be concluded that SDF-1 has a higher affinity for CXCR4 than Ac-TZ14011-FITC, which is in accordance with results found by Nomura et al.²⁰ For the antibody 12G5-PE, no significant reduction in uptake during a competition experiment with SDF-1 was seen, suggesting both can simultaneously interact with CXCR4.

Cellular localization of CXCR4

Using different antibodies, positive staining of the cell membrane, the cytoplasm and even the nucleus has been reported.^{4-6,16,17,21-23} However, as previously mentioned by Fischer et al.²² and Kryczek et al.,²³ nuclear localization would not be compatible with CXCR4 being a membrane receptor and its function in cancer cell migration and homing. Hence membranous staining is considered most representative. Identical to results published by Nomura et al.²⁰ and Zhang et al.²⁴ we found that Ac-TZ14011-FITC predominantly bound to CXCR4 on the cell membrane (Figure 1A) when live cells were incubated with Ac-TZ14011-FITC. Furthermore, membrane Ac-TZ14011-FITC-CXCR4 complexes internalized into the cell in cytoplasmic vesicles over time (Figure 1C).^{20,25} Distribution of Ac-TZ14011-FITC throughout the entire cell was only observed when fixed cells or tissues were incubated. These results suggest fixation may influence the distribution of the agent used for staining.

Viable vs. fixed material

Confocal images helped resolve questions about the difference in signal intensity seen with flow cytometry between live and fixed cells (Figure 1 and Table 1). The distribution of Ac-TZ14011-FITC in fixed cells, wherein the whole cell was stained, was completely different from the distribution observed in viable cells. Formalin slightly permeabilizes the cell membranes, which might induce cellular and nuclear uptake of Ac-TZ14011-FITC. Although the fixed cells were positively stained all over, the staining intensity of MDAMB231^{CXCR4+} cells was more intense than seen in MDAMB231 cells, which is in accordance with the results obtained with flow cytometry (Table 1). Fixation artifacts may also be of influence on the distribution patterns of Ac-TZ14011-FITC observed at IHC. The latter may thus not accurately represent the CXCR4 expression patterns in viable tissue.

In addition to fixation, paraffinization also had a negative influence on the peptide-based staining (Figure 2). A clear differentiation could, however, be made on only formalin-fixed tissue (Figure 2D).

Antibodies vs. peptides

Anti-CXCR4 antibody clones 12G5 and 2B11 were used as reference in both flow cytometric analysis and IHC. These antibodies differ in the type of CXCR4 that they recognize; where antibody 12G5 recognizes human origin CXCR4, antibody 2B11 is

directed against murine CXCR4. With flow cytometric analysis using viable cells, antibody 12G5-PE was able to nicely distinguish MDAMB231 from MDAMB231^{CXCR4+} cells, while antibody 2B11-PE did not perform as well (Table 1). However, when the cells were fixed, the antibodies were unable to distinguish the two cell lines based on their CXCR4 expression levels. Surprisingly, in IHC an opposite effect was observed; anti-murine 2B11 antibody gave specific staining on the human-originated MDA tumors while anti-human 12G5 antibody did not (Figure 2Ai and ii). This observation underlines that antibodies are not always interchangeable between different detection viz. flow cytometric analysis and IHC, whereas Ac-TZ14011-FITC peptide can be used in both cases.

To overcome the need to use different antibodies for different applications (e.g. flow cytometric analysis and IHC staining), Ac-TZ14011-FITC can be used. This peptide showed corresponding results in studies on cells and tumor tissue (Table 1 and Figures 1B and 2D). Clearly this will be most beneficial for evaluation of the more 'experimental' biomarkers such as CXCR4. Multispectral FIHC could even allow simultaneous detection of multiple biomarkers at once.

The main advantage of using peptides for IHC visualization of CXCR4 is that it makes it easier to directly correlate IHC stainings to imaging findings obtained with e.g. the ¹¹¹In-DTPA-Ac-TZ14011 analogue. Such a combination of differently labeled derivatives of the same peptide sequence would improve the integration of in vitro and in vivo diagnostics. A similar approach may be achieved using a combination of e.g. ¹²⁵I-12G5 and 12G5-PE.²⁵ However, use of antibody takes away the advantages small molecules such as peptides have.

Signal intensity differences obtained in flow cytometry varied between 12G5-PE and Ac-TZ14011-FITC (Table 1). While the latter showed significant differences under all the conditions studied, 12G5-PE showed larger differences between the live conditions studied in MDAMB231 and MDAMB231^{CXCR4+} cells. This result suggests that with Ac-TZ14011-FITC there is somewhat more nonspecific cellular uptake than with 12G5-PE.

Ex vivo visualization of CXCR4 expression in tumor tissue

During ex vivo (F)IHC, the peptide/antibody has access to the whole tumor tissue slide and, therefore, is able to stain all CXCR4 present. Intravenously administrated Ac-TZ14011-FITC (Figure 3) predominantly has access to the blood supplied areas of the tumor and will only provide a specific signal after binding to membranous CXCR4 (Figure 1C and 3B), resulting in a more local staining.

Intravenous administration of Ac-TZ14011-FITC

To overcome the fixation artifacts seen in fixed cells and tumor tissue, and to study CXCR4 expression of the tumor tissue in its most natural environment, Ac-TZ14011-FITC was intravenously administered to tumor-bearing mice (Figure 3A). Analysis of the freshly isolated tissue before or after fixation, revealed stronger staining of the cytoplasm of MDAMB231^{CXCR4+} tumor tissue as compared to MDAMB231 tumor tissue (Figure 3B and C). In line with the results obtained with viable tumor cells at RT (Figure 1C) the staining in the tumor cells was intracellularly localized after the incubation period. Furthermore, the intravenous administration of Ac-TZ14011-FITC visualized the staining efficacy that may be predictive for the molecular imaging agent ¹¹¹In-DTPA-Ac-TZ14011. This illustrates how the Ac-TZ14011 peptide (and perhaps many others), in combination with different diagnostic antennae, can in the future be used to directly correlate in vivo findings with ex vivo staining.

Conclusion

The present study illustrates the value of Ac-TZ14011-FITC to identify tumor cells with slight levels of CXCR4 overexpression in both FIHC and flow cytometric applications. Where results with antibodies rely on employment of different antibodies for different applications, Ac-TZ14011-FITC is applicable in vitro, in vivo and even ex vivo, broadening the applicability of the peptide.

References

- 1 Kang H, Watkins G, Douglas-Jones A, Mansel RE, Jiang WG. The elevated level of CXCR4 is correlated with nodal metastasis of human breast cancer. *The Breast*. 2005; 14: 360-367
- 2 Balkwill F. The significance of cancer cell expression of the chemokine receptor CXCR4. *Semin Cancer Biol*. 2004; 14: 171-179
- 3 Kulbe H, Levinson NR, Balkwill F, Wilson JL. The chemokine network in cancer – Much more than directing cell movement. *Int J Dev Biol*. 2004; 48: 489-496
- 4 Kato M, Kitayama J, Kazama S, Nagawa H. Expression pattern of CXC chemokine receptor-4 is correlated with lymph node metastasis in human invasive ductal carcinoma. *Breast Cancer Res*. 2003; 5: R144-150
- 5 Mirisola V, Zuccarino A, Bachmeier BE, Sormani MP, Falter J, Nerlich A, Pfeffer U. CXCL12/SDF1 expression by breast cancers is an independent prognostic marker of disease-free and overall survival. *Eur J Cancer*. 2009; 45: 2579-2587
- 6 Kang H, Watkins G, Parr C, Douglas-Jones A, Mansel RE, Jiang WG. Stromal cell derived factor-1: Its influence on invasiveness and migration of breast cancer cells in vitro, and its association with prognosis and survival in human breast cancer. *Breast Cancer Res*. 2005; 7: R402-410
- 7 Huang X, Shen J, Cui M, Shen L, Luo X, Pei G, Jiang H, Chen K. Molecular Dynamics simulations on SDF-1a: Binding with CXCR4 receptor. *Biophys J*. 2003; 84: 171-184
- 8 Kuil J, Buckle T, van Leeuwen FWB. Imaging agents for the chemokine receptor 4 (CXCR4). *Chem Soc Rev* 2012; 41(5): 5239-5261
- 9 Trent JO, Wang Z, Murray JL, Shao W, Tamamura H, Fujii N and Peiper SC. Lipid bilayer simulations of CXCR4 with inverse agonists and weak partial agonists. *J Biol Chem*. 2003; 278: 47136-47144
- 10 Zhang W, Navenot JM, Haribabu B, Tamamura H, Hiramatsu K, Omagari A, Pei G, Manfredi JP, Fujii N, Broach JR, Peiper SC. A point mutation that confers constitutive activity to CXCR4 reveals that T140 is an inverse agonist and that AMD3100 and ALX40-4C are weak partial agonists. *J Biol Chem*. 2002; 277: 24515-24521
- 11 Tamamura H, Omagari A, Oishi S, Kanamoto T, Yamamoto N, Peiper SC, Nakashima H, Otake A, Fujii N. Pharmacophore identification of a specific CXCR4 inhibitor, T140, leads to development of effective anti-HIV agents with very high selectivity indexes. *Bioorg Med Chem Lett*. 2000; 10: 2633-2637
- 12 Liang Z, Wu T, Lou H, Yu X, Taichman RS, Lau SK, Nie S, Umbreit J, Shim H. Inhibition of breast cancer metastasis by selective synthetic polypeptide against CXCR4. *Cancer Res*. 2004; 64: 4302-4308

- 13 Huang EH, Singh B, Cristofanilli M, Gelovani J, Wei C, Vincent L, Cook KR, Lucci A. A CXCR4 antagonist CTCE-9908 inhibits primary tumor growth and metastasis of breast cancer. *J Surg Res.* 2009; 155: 231-236
- 14 Hanaoka H, Mukai T, Tamamura H, Mori T, Ishino S, Ogawa K, Iida Y, Doi R, Fujii N, Saji H. Development of ¹¹¹In-labeled peptide derivative targeting a chemokine receptor, CXCR4, for imaging tumors. *Nucl Med Biology.* 2006; 33: 489-494
- 15 Kuil J, Velders AH, van Leeuwen FWB. Multimodal tumor-targeting peptides functionalized with both a radio- and a fluorescent label. *Bioconjugate Chem.* 2010; 21: 1707-1719
- 16 Woo SU, Bae JW, Kim CW, Lee JL, Koo BW. A significant correlation between nuclear CXCR4 expression and axillary lymph node metastasis in hormonal receptor negative breast cancer. *Ann Surg Oncol.* 2008; 15: 281-285
- 17 Andre F, Xia W, Conforti R, Wei Y, Boulet T, Tomasic G, Spielmann M, Zoubir M, Berrada N, Arriagada R, Hortobagyi GN, Hung M-C, Puzstai L, Delaloge S, Michiels S, Cristofanilli M. CXCR4 expression in early breast cancer and risk of distant recurrence. *The Oncologist.* 2009; 14: 1182-1188
- 18 Li YM, Pan Y, Wei Y, Cheng X, Zhou BP, Tan M, Zhou X, Xia W, Hortobagyi GN, Yu D, Hung M-C. Upregulation of CXCR4 is essential for HER2-mediated tumor metastasis. *Cancer Cell.* 2004; 6: 459-469
- 19 Nishizawa K, Nishiyama H, Oishi S, Tanahara N, Kotani H, Mikami Y, Toda Y, Evans BJ, Peiper SC, Saito R, Watanabe J, Fujii N, Ogawa O. Fluorescent imaging of high-grade bladder cancer using a specific antagonist for chemokine receptor CXCR4. *Int. J. Cancer.* 2009; 127: 1180-1187
- 20 Nomura W, Tanabe Y, Tsutsumi H, Tanaka T, Ohba K, Yamamoto N, Tamamura H. Fluorophore labeling enables imaging and evaluation of specific CXCR4-ligand interaction at the cell membrane for fluorescence-based screening. *Bioconjugate Chem.* 2008; 19: 1917-1920
- 21 Arya M, Ahmed H, Silhi N, Williamson M, Patel HRH. Clinical importance and therapeutic implications of the pivotal CXCL12-CXCR4 (chemokine ligand-receptor) interaction in cancer cell migration. *Tumor Biol.* 2007; 28: 123-131
- 22 Fischer T, Nagel F, Jacobs S, Stumm R, Schultz S. Reassessment of CXCR4 chemokine receptor expression in human normal and neoplastic tissues using the novel rabbit monoclonal antibody UMB-2. *PLoS One.* 2008; 3: e4069
- 23 Kryczek I, Wei S, Keller E, Liu R, Zou W. Stromal-derived factor (SDF-1/CXCL12) and human tumor pathogenesis. *Am J Phys Cell Phys.* 2007; 292: C987-995

- 24 Zhang Y, Foudi A, Geay JF, Berthebaud M, Buet D, Jarrier P, Jalil A, Vainchenker W, Louache F. Intracellular localization and constitutive endocytosis of CXCR4 in human CD34⁺ hematopoietic progenitor cells. *Stem Cells* 2004; 22: 1015-1029
- 25 Nimmagadda S, Pullambhatla M, Pomper MG. Immunoimaging of CXCR4 expression in brain tumor xenografts using SPECT/CT. *J Nucl Med.* 2009; 7: 1124-1130

Appendix Chapter 9

Synthesis Ac-TZ14011-FITC

The antagonistic CXCR4 peptide, Ac-TZ14011, was synthesized as described previously.¹ Fluorescein isothiocyanate isomer I (FITC; 2.32 mg, 5.95 μmol) in 500 μL of dimethyl sulfoxide was added to the antagonistic CXCR4 peptide (11.1 mg, 3.96 μmol) in 1 mL of 0.1 M NaHCO_3 (Merck) and 2 mL of CH_3CN (Acros, Belgium). The mixture was stirred overnight at room temperature (RT), solvents were evaporated and the product was purified by preparative HPLC using a Waters HPLC system with a UV detector operating at 230 nm and a Waters Atlantis C18 10 μm column using a gradient of 0.05% trifluoroacetic acid (TFA; Sigma-Aldrich) in $\text{H}_2\text{O}/\text{CH}_3\text{CN}$ 9:1 to 0.05% TFA in $\text{H}_2\text{O}/\text{CH}_3\text{CN}$ 1:4 in 40 min. A yellow fluffy solid (4.3 mg, 35%) was obtained after lyophilization of the pooled fractions and characterized by MALDI-TOF-MS.

The fluorescein labeled CXCR4 peptide antagonist will be reverted to as Ac-TZ14011-FITC. All experiments were performed in the absence of light when fluorescent labels were used.

References

- 1 Nomura W, Tanabe Y, Tsutsumi H, Tanaka T, Ohba K, Yamamoto N, Tamamura H. Fluorophore labeling enables imaging and evaluation of specific CXCR4-ligand interaction at the cell membrane for fluorescence-bases screening. *Bioconjugate Chem.* 2008; 19: 1917-1920
-

Interventional Non-invasive longitudinal imaging molecular imaging, of tumor progression using an ¹¹¹Indium a hybrid approach labeled CXCR4 peptide antagonist

Chapter 10

Adapted from:

*Buckle T, van den Berg NS, Kuil J, Bunschoten A, Oldenburg J, Borowsky AD,
Wesseling J, Masada R, Oishi S, Fujii N, van Leeuwen FWB.
Am J Nucl Med Mol Imaging 2012; 2(1): 99-109*

Abstract

CXCR4 targeted (molecular) imaging approaches may have diagnostic value in the detection of premalignant lesions such as ductal carcinoma in situ (DCIS). To this end, the indium labeled CXCR4 peptide antagonist, ^{111}In -DTPA-Ac-TZ14011, was used to detect CXCR4 in a mammary intraepithelial neoplastic outgrowth (MIN-O) mouse tumor model that resembles human DCIS. MIN-O lesion development was longitudinally monitored using single photon emission tomography/computed tomography (SPET/CT). Tracer uptake was compared to uptake in low CXCR4 expressing 4T1 control lesions. Expression of CXCR4 was validated using immunohistochemistry (IHC) and flow cytometric analysis. The uptake of ^{111}In -DTPA-Ac-TZ14011 was related to tumor angiogenesis using ^{111}In -c[RGDfK]-DTPA. Twenty-four hrs after tracer injection, MIN-O lesions could be discriminated from the low CXCR4 expressing control tumor lesions, while the degree of angiogenesis (based on the $\alpha_v\beta_3$ integrin expression) was similar in both tumor types. The uptake of ^{111}In -DTPA-Ac-TZ14011 in early stage MIN-O lesions was significantly lower than in larger intermediate and late stage lesions, 2.5-fold ($P = 0.03$) and 7-fold ($P = 0.002$), respectively. In concordance, intermediate and late stage lesions showed a higher degree of membranous CXCR4 staining at IHC and flow cytometric analysis. These results show that ^{111}In -DTPA-Ac-TZ14011 can be used to monitor the level of CXCR4 expression in MIN-O lesions longitudinally.

Introduction

A possible clinical application of the chemokine receptor 4 (CXCR4) as an imaging target is the visualization of breast cancer lesions such as ductal carcinoma in situ (DCIS). Salvucci et al. reported that 69% of the DCIS lesions evaluated in their patient study was CXCR4 positive at immunohistochemistry (IHC),¹ whereas Schmid et al. reported a 92% positivity rate.² Non-invasive visualization of DCIS is clinically challenging; X-ray mammography and contrast enhanced magnetic resonance imaging (MRI) does not always accurately detect DCIS lesions.³⁻⁵ Hence, CXCR4 targeting imaging agents are expected to help improve clinical diagnostics.

The well described mammary intraepithelial neoplastic outgrowth (MIN-O) model, a mouse tumor model resembling human DCIS^{6,7} has been previously used in imaging studies.⁸ In this model, preinvasive lesions progress to invasive lesions.^{9,10} Progression is consistent over time, and conveniently, lesions that have progressed to the invasive phenotype become palpable. Differences in tumor cell differentiation, gene expression, and metabolism associated with progression have been reported and these features correspond to similar features in human DCIS progression.

The preclinical MIN-O model and a low CXCR4 expressing 4T1 tumor model were used to evaluate the ability of the CXCR4 targeting peptide antagonist ¹¹¹In-DTPA-Ac-TZ14011. Here the challenge was to longitudinally monitor the progression of the tumor lesions via the level of CXCR4 expression. Imaging results were compared to immunohistochemical and flow cytometric analysis of the tumor tissue. Furthermore, ¹¹¹In-DTPA-c[RGDfK] was used to determine the influence of angiogenesis on the uptake of ¹¹¹In-DTPA-Ac-TZ14011 in both tumor models.

Materials and methods

In vivo mouse model

For generation of the MIN-O tumor lesions FVB mice (n = 20; 3 - 4 weeks of age) were used. Before transplantation (and imaging), mice were anaesthetized using a hypnorm (VetaPharma Ltd)/dormicum (Midazolam; Roche)/water solution (1:1:2; 5µL/g i.p.). Via a small incision, the inguinal lymph node was excised where after a piece of preinvasive MIN-O tissue (line 8w-B)¹⁰ was placed into the remaining tissue of the fourth mammary gland. Approximately three weeks after transplantation, lesions were deemed suitable for further experiments.

Control experiments were performed using orthotopic transplantation of 0.25×10^5 4T1 tumor cells into the mammary tissue of Balb/c nude mice ($n = 20$; 6-8 weeks of age). 4T1 cells were cultured under standard conditions in MEM medium containing MEM vitamins, L-glutamin, non-essential amino acids, natrium/pyruvate and penicillin/streptomycin solution (all BD Biosciences). Before transplantation, cells were trypsinized and washed with HBSS (BD Biosciences). Transplantation of cells was carried out under identical conditions as placement of the MIN-O segments. All animal experiments were performed in accordance with Dutch welfare regulations and after approval was obtained by the local ethics committee.

Synthesis and radiolabeling

DTPA-Ac-TZ14011 (Figure 1A) was synthesized as previously described by Hanaoka et al.⁸ Synthesis of DTPA-c[RGDfK] is described the Appendix of this Chapter.

Imaging using single photon emission computed tomography/computed tomography (SPECT/CT)

Mice were injected intravenously with $50 \mu\text{g}$ ^{111}In -DTPA-Ac-TZ14011 (10 MBq) or with $25 \mu\text{g}$ ^{111}In -DTPA-c[RGDfK] (10 MBq). SPECT/CT scans were conducted as described previously¹¹ on a preclinical SPECT/CT scanner (Nanospect; Bioscan) at one hr and 24 hrs post injection. After acquisition, the CT data was reconstructed using a cone-beam filtered back projection. SPECT data was reconstructed using HiSPECT software (Scvis GmbH). In a region of interest including only the tumor, the percentage of the injected dose (%ID) was calculated using the following formula: ((MBq measured in tissue/injected dose) $\times 100\%$). MIN-O and 4T1 tumor lesions within the same size range were compared. Signal intensities were analyzed using the InVivoScope postprocessing software (Bioscan, Inc.).¹¹ CT images were used to perform size measurements on the tumor. The formula for ellipsoid shapes: $3/4 \pi \times (1/2a) \times (1/2b) \times (1/2c)$, was used to calculate tumor volume.

Tumor stages were differentiated by size and histology. Size limits for the different stages were based on values reported by Abbey et al.⁷ and correlations between tumor volume and immunohistochemistry using our own data. Tumor lesions $< 100 \text{ mm}^3$ were deemed as early stage, lesions between 100 and 400 mm^3 were deemed as intermediate stage, and $> 400 \text{ mm}^3$ as late stage lesions. In the mice that were longitudinally followed, only the %ID could be determined, as the weight of the tumor was unknown. Moreover, the density of the lesions differs between stages and tumor lesions. Corrections based on tumor volume were therefore considered inaccurate.

Tracer distribution

After the final SPECT/CT scan mice were sacrificed. Organs and tumor lesions were excised and weighed to determine the percentage of the injected dose per gram (%ID/g). The amount of radioactivity present in the tissue was counted using a gamma counter (Wizard 3" 1480 automatic gamma counter, Perkin Elmer; 245 keV; 60 sec). The percentage of the injected dose (%ID/g) was calculated as follows: ((MBq measured in tissue/ injected dose) x100 %) / (weight of tissue). Statistics were conducted using a standard T-test.

Immunohistochemistry (IHC)

Formalin-fixed paraffin-embedded MIN-O or 4T1 tumor tissue sections were stained according to the protocol previously described with a monoclonal anti-CXCR4 antibody (Rat-anti-CXCR4 clone 2B11 1:100; BD Biosciences).¹² Slides were assessed by a consultant breast pathologist and scored as positive or negative for membranous and cytoplasmic CXCR4 staining. Images were taken with a color CCD microscope system (Axiovert S100 with AxioCamHRc, Carl Zeiss) at a 25x or 40x magnification.

The percentage of cytoplasmic and/or membranous staining was determined per slide by dividing the amount of stained cells in a specific area by the total amount of cells in that area and multiplying this by 100%. Per tumor type/stage 5 different tumor slides were assessed. Per slide, 5 different areas were evaluated (magnification 40x). The ratio between staining in the MIN-O and 4T1 tumor lesions was determined by dividing the percentage of membranous staining in the MIN-O tumor lesions by the percentage of membranous staining in the 4T1 tumor lesions. Increase in membranous staining in the different MIN-O tumor stages was determined by dividing the percentage of staining in the intermediate or late stage MIN-O tumor lesions by the percentage of staining of the early stage MIN-O tumor lesions.

For the MIN-O model, early, intermediate, and late stage tumor lesions were assessed. For the 4T1 tumor model, only large tumor lesions (corresponding in size with late stage MIN-O lesions) were assessed as CXCR4 expression levels between different stages of 4T1 lesions did not differ. Statistics were performed using a standard T-test.

Flow cytometry

Tumor-bearing mice were sacrificed, tumor lesions were excised and single cell suspensions were made. All stages of MIN-O lesions were assessed. Again, for the 4T1 tumor model, only late stage tumor lesions were used.

500,000 cells per measuring condition were washed with 0.1% bovine serum albumin in phosphate buffered saline (0.1% BSA/PBS) and incubated for one hr on ice with monoclonal phycoerythrin (PE) labeled anti-CXCR4 antibody 2B11 (2B11-PE; 1:100; BD Biosciences) to determine their CXCR4 expression levels. After incubation, cells were washed with 0.1% BSA/PBS and propidium iodide (PI; 1:10000; BD Biosciences) was added five min prior to analysis.

For evaluation of the amount of lymphocytes within the CXCR4 positive population in the tumor cell suspensions, cells were co-incubated for one hr with the 2B11-PE antibody and an Alexa-Fluor-700 (AF700) labeled anti-CD45 antibody (CD45-AF700 clone 30 F11; 1:200; eBioscience). The percentage of CXCR4 positive lymphocytes was determined by dividing the CD45 positive population within the CXCR4 positive population by the total amount cells and multiplying this by 100%.

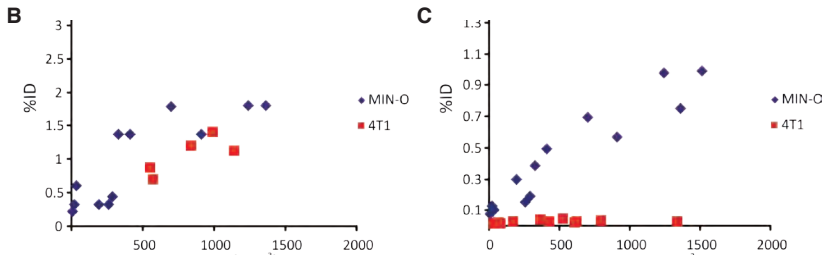
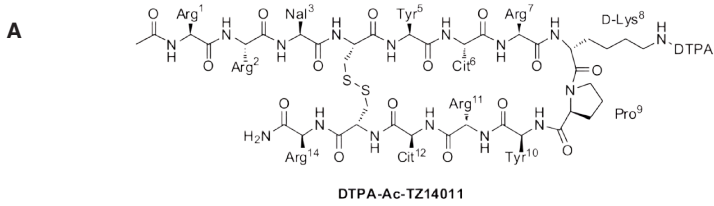
Antibodies were diluted in 0.1% BSA/PBS in all flow cytometric experiments. Non-antibody incubated cells served as controls. After staining, cells were analyzed using a Beckton Dickinson FACScalibur device equipped with Cell Quest Pro software (BD Biosciences). PE fluorescence was detected in the FL2 channel (excitation 488 nm; emission filter 530/30 nm). PI and AF700 were detected in the FL3 channel (excitation 488 nm; emission filter > 670 nm).

Mean fluorescence signal intensity ratio's (MFIRs) were calculated as followed: (mean fluorescence signal intensity antibody incubated condition)/(mean fluorescence signal intensity control (no antibody)). Increase in signal in the different MIN-O tumor stages was determined by dividing the MFIR obtained in the intermediate or late stage MIN-O tumor lesions by the MFIR of the early stage MIN-O tumor lesions.

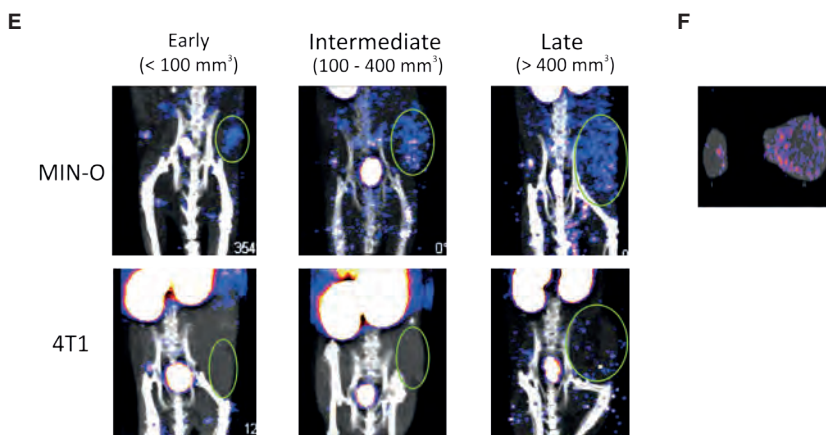
Results

To evaluate the potential of ^{111}In -DTPA-Ac-TZ14011 to visualize tumor lesions via their CXCR4 expression, a group of animals was scanned longitudinally (Figure 1). SPECT/CT scans were made when tumor lesions were < 100 mm³ (early stage), 100 - 400 mm³ (intermediate stage) and > 400 mm³ (late stage) in size.

Figure 1. Longitudinal SPECT/CT imaging of ^{111}In -DTPA-Ac-TZ14011. A) Chemical structure of DTPA-Ac-TZ14011. Uptake of ^{111}In -DTPA-Ac-TZ14011 in the tumor lesions measured at B) one hr and C) 24 hrs after injection was set out against the tumor volume. D) Uptake in tumor lesions within the same size range was compared. E) SPECT/CT images (MIP) of MIN-O and 4T1 tumor lesions at 24 hrs after injection. F) Ex vivo tracer distribution in a 4T1 (i) and MIN-O (ii) tumor lesion after SPECT/CT imaging. Significance between uptake values was determined using a standard T-test. ns = not significant, P-values < 0.02 for comparison with late stage MIN-O lesions were noted as ** and P-values < 0.002 as ***. nd = not determined.

**D**

	%ID in tumor			
	MIN-O 1hr	4T1 1hr	MIN-O 24hr	4T1 24hr
Early stage (< 100 mm ³)	0.38 ± 0.20 **	n.d.	0.10 ± 0.003 ***	0.014 ± 0.004
Intermediate stage (100 - 400 mm ³)	0.62 ± 0.51 **	n.d.	0.25 ± 0.11 ***	0.030 ± 0.008
Late stage (> 400 mm ³)	1.62 ± 0.72	1.06 ± 0.28 ns	0.74 ± 0.21	0.030 ± 0.009 ***



As the time between injection of an imaging agent and time point of imaging can influence the imaging outcome, the optimal incubation time of $^{111}\text{In-DTPA-Ac-TZ14011}$ was determined. This was done by comparing the tumor uptake at two different time points post injection. At one hr post injection MIN-O tumor lesions could be detected but differences between CXCR4 positive (MIN-O) and control (4T1) tumor lesions were not apparent (Figure 1B). Uptake in late stage MIN-O lesions seemed to be higher than the uptake (%ID) in 4T1 tumor lesions at one hr post injection, however, this difference was not significant (Figure 1D). At 24 hrs post injection uptake in the tumor lesions had overall decreased, but at this time point the differences between the MIN-O and 4T1 lesions were highly significant (Figure 1C and D). More importantly, uptake in 4T1 tumor lesions was low in tumor lesions of all sizes (between 0.014 ± 0.004 %ID to 0.030 ± 0.009 %ID), whereas the uptake in MIN-O lesions increased with lesion size (Figure 1D). Uptake increased from $0.10 \pm 0.03\%$ of the injected dose in early stage lesions to $0.25 \pm 0.11\%$ in intermediate stage and $0.74 \pm 0.21\%$ in late stage MIN-O lesions. Uptake levels in MIN-O tumor lesions larger than 10 mm^3 exceeded uptake levels found in 4T1 tumor lesions with a size range up to 1338 mm^3 . Figure 1E shows SPECT/CT images of the lesions during the different stages of tumor progression of both 4T1 and MIN-O tumor lesions. After the final SPECT/CT scan in the longitudinal series, the distribution and quantitative tumor uptake (%ID/g) was determined. In late stage MIN-O tumor lesions (0.27 ± 0.06) uptake was higher compared to uptake in 4T1 lesions of comparable size (0.14 ± 0.02 ; $P = 0.05$). The tumor-to-muscle ratio was 1.5-fold higher in the late stage MIN-O tumor lesions; 7.17 ± 0.47 compared to 4.75 ± 0.90 in 4T1 tumor lesions ($P = 0.01$). Ex vivo SPECT/CT imaging shows the distribution throughout the tumor in the two tumor types (Figure 1F).

Distribution studies at 24 hrs post injection revealed that $^{111}\text{In-DTPA-Ac-TZ14011}$ was predominantly cleared via the kidneys, and to a lesser extent via the liver (Table 1). Hanaoka et al. previously reported on the distribution of $^{111}\text{In-DTPA-Ac-TZ14011}$ which also included a blocking study using unbound peptide.⁸ Here the distribution was evaluated using a different peptide dose but overall, we found that the distribution profile was comparable.

Table 1. Distribution of $^{111}\text{In-DTPA-Ac-TZ14011}$.

Tissue	$^{111}\text{In-DTPA-Ac-TZ14011}$ %ID/g
Blood	0.02 ± 0.00
Brain	0.00 ± 0.00
Lungs	0.19 ± 0.01
Heart	0.08 ± 0.01
Liver	5.53 ± 0.51
Kidneys	24.82 ± 0.94
Spleen	1.03 ± 0.11
Stomach	0.08 ± 0.01
Intestines	0.16 ± 0.02
Muscle	0.03 ± 0.01
Mammary fatpad	0.05 ± 0.02
Axillary lymph nodes	1.33 ± 0.81

Mice were sacrificed 24 hrs after injection of $^{111}\text{In-DTPA-Ac-TZ14011}$. Tissues were excised and radioactivity in the tissues was determined using a gamma counter. %ID/g was calculated using the following formula: ((MBq measured in tissue/ injected dose)* 100%)/weight tissue.

To validate that the tumor uptake of $^{111}\text{In-DTPA-Ac-TZ14011}$ could be correlated to CXCR4 expression, the level of CXCR4 expression in the different tumor tissues was evaluated by IHC. Slices of MIN-O and 4T1 tumor tissue were stained using the 2B11 anti-CXCR4 antibody and cytoplasmic and membranous CXCR4 staining was analyzed. In MIN-O lesions, staining patterns varied between different areas in the tumor, showing clear CXCR4 positive and negative areas (Figure 2A). Further evaluation demonstrated that in MIN-O lesions, CXCR4 staining was located in the cytoplasm and on the membrane of the tumor cells. 4T1 and early stage MIN-O lesions showed predominantly cytoplasmic staining and only sporadic membranous staining. Membranous staining was more evident in the larger intermediate stage MIN-O lesions and most apparent in the largest MIN-O lesions investigated (Figure 2).

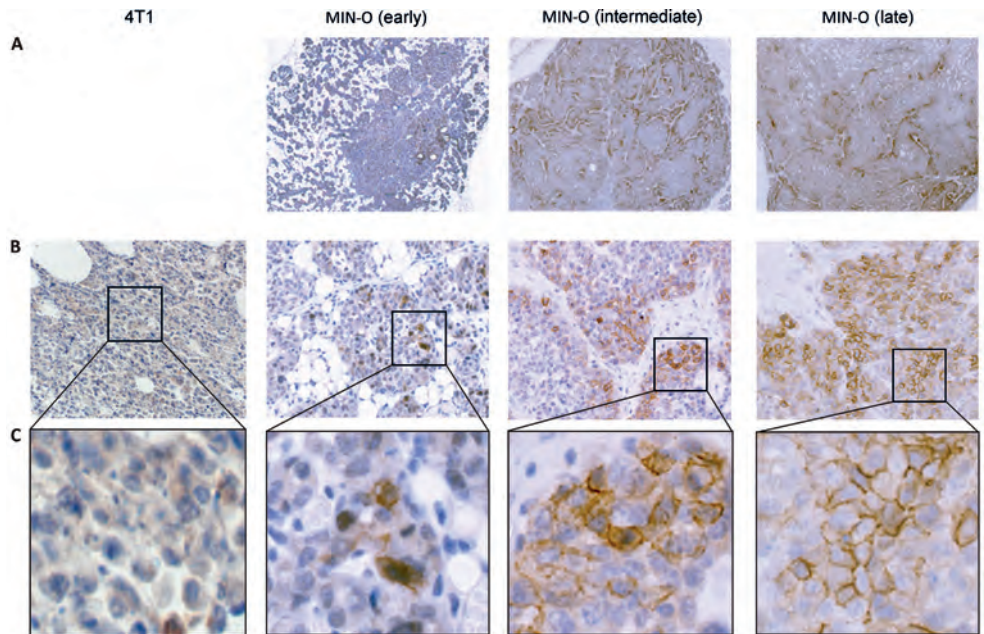


Figure 2. Immunohistochemistry: CXCR4 staining in 4T1 and MIN-O tumor tissue. A) Distribution pattern of the CXCR4 staining of the different MIN-O tumor stages. B) At a 25x magnification, in 4T1 tumor tissue only cytoplasmatic staining can be seen. In MIN-O tumor tissue, next to cytoplasmatic staining, an increasing level of membranous staining is observed. C) Membranous staining at 40x magnification.

This visual observation was further underlined by quantitative analysis of the stained tissue slides. In Table 2, the percentage of CXCR4 staining determined by IHC in the different MIN-O stages and in the 4T1 control tumor lesions is shown. No significant difference in cytoplasmic staining was observed between the different tumor lesions, but differences in percentages of membranous staining were apparent.

While membranous staining in 4T1 and early stage MIN-O lesions was almost identical ($3.8 \pm 1.9\%$ and $4.1 \pm 2.3\%$), the percentage of membranous staining increased 3.3-fold in intermediate and 5.1-fold in late stage MIN-O lesions compared to the early stage MIN-O lesions. As only one representative slide per tumor was evaluated, this contributed to the relatively high SD in the quantitative analysis of the staining percentages (Table 2).

Table 2. Quantitative analysis of CXCR4 staining.

Tumor type	% Cytoplasmic staining	% Membranous staining
MIN-O Early stage (< 100 mm ³)	81.1 ± 10.6	4.1 ± 2.3 ***
MIN-O Intermediate stage (100 – 400 mm ³)	84.8 ± 8.6	13.5 ± 5.8 **
MIN-O Late stage (> 400 mm ³)	90.6 ± 3.3	21.0 ± 8.0
4T1 Late stage (> 400 mm ³)	92.2 ± 3.0	3.8 ± 1.9 ***

Tumor cells were counted under 40x magnification (n = 5 per tumor type). Percentage cytoplasmic and membranous staining was calculated by dividing the amount of stained cells in an area by the total amount of cells counted in that area and multiplying this by 100%. P-values < 0.05 for comparison with late stage MIN-O lesions were noted as ** and P-values < 0.01 as ***.

Table 3. Flow cytometric analysis CXCR4 and the percentage of lymphocytes in 4T1 and MIN-O tumor cells.

Tumor type	MFIR CXCR4	% lymphocytes
MIN-O Early stage (< 100mm ³)	2.25 ± 0.17	0.43 ± 0.002
MIN-O Intermediate stage (100 - 400mm ³)	4.32 ± 0.02	2.07 ± 0.001
MIN-O Late stage (> 400mm ³)	5.36 ± 1.80	3.48 ± 0.004
4T1 Late stage (> 400mm ³)	1.70 ± 1.07	3.39 ± 0.002

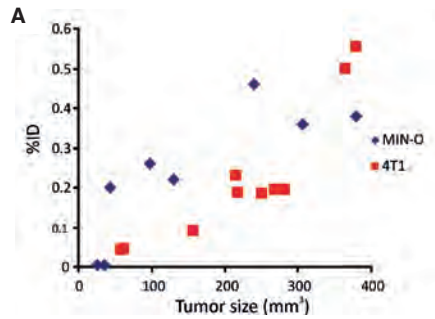
Tumor cell suspensions were incubated with 2B11-PE. The fluorescence signal in CXCR4 positive cells was measured (n = 3 per tumor type) and mean fluorescence intensity ratios (MFIR) were determined. The percentage of lymphocytes within the CXCR4 positive population was determined after co-incubation with 2B11-PE and an AF700 labeled anti-CD45 antibody.

Further evaluation of the membranous CXCR4 expression in the tumor lesions was conducted using flow cytometric analysis. Viable tumor cells were incubated with a PE-labeled version of the anti-CXCR4 antibody that was used for IHC. By performing the labeling on ice, the metabolic activity of the cells is slowed down preventing endocytosis, enabling visualization of only the cell-membrane-receptor-bound signal. Therefore, the level of fluorescence that could be detected in the tumor cell suspensions provided a measure of the membranous CXCR4 expression. Similar to results obtained with IHC (Table 2), a clear difference between the level of CXCR4 expression in the 4T1 and MIN-O tumor lesions was found (Table 3). MFIRs in the MIN-O tumor cells increased with progression of the lesions. The MFIR in intermediate and late stage MIN-O tumor cells was

respectively 1.9-fold and 2.4-fold higher than the MFIR in early stage MIN-O tumor cells. In all stages of MIN-O tumor progression, a higher level of fluorescence was detected than in the 4T1 tumor cells used in these experiments.

As can be seen in Table 1, tracer uptake was relatively high in the spleen and axillary lymph nodes. Both organs are part of the immune system and are known to harbor large amounts of CXCR4 positive lymphocytes.¹⁴ The presence of such CXCR4 positive lymphocytes in the tumor lesions can be of influence on uptake levels of ¹¹¹In-DTPA-Ac-TZ14011. For this reason, the level of lymphocytes present within the CXCR4 positive tumor cell population was evaluated. Flow cytometric analysis was done after co-incubation of an AF700 labeled anti-CD45 antibody and the PE-labeled anti-CXCR4 antibody (Table 3). The percentage of lymphocytes present in MIN-O tumor tissue increased with tumor stage; in early stage tumor cells only 0.43% of the cells in the tumor were CD45 positive, increasing to 2.07% in intermediate and 3.48% in late stage MIN-O tumor lesions. However, the presence of lymphocytes in late stage 4T1 tumor tissue (3.39%) was comparable to late stage MIN-O tumor tissue. Pathological analysis of tumor slices also revealed low amounts (\approx 2%) of lymphocytes in the tumor tissue. It is therefore not likely that uptake levels of ¹¹¹In-DTPA-Ac-TZ14011 in the MIN-O and 4T1 tumor lesions were influenced by the presence of lymphocytes in the tumor.

To further specify that the uptake of ¹¹¹In-DTPA-Ac-TZ14011 in the tumor lesions is related to the level of CXCR4 expression in the tumor cells, factors such as the effect of angiogenesis (based on $\alpha_v\beta_3$ integrin expression) had to be evaluated. Therefore, the uptake of ¹¹¹In-c[RGDfK]-DTPA was studied in both tumor models. The RGD peptide c[RGDfK], binds to $\alpha_v\beta_3$ integrin, of which expression is linked to angiogenesis.¹⁵ Uptake of ¹¹¹In-c[RGDfK]-DTPA in MIN-O and in 4T1 lesions increased with increasing lesion size, but no significant difference in uptake between the models was observed (Figure 3). Unlike SPECT/CT imaging with ¹¹¹In-DTPA-Ac-TZ14011, lesions were only followed until they reached 400 mm³. The necrotic areas in larger 4T1 tumor lesions resulted in unreliable uptake values for ¹¹¹In-c[RGDfK]-DTPA.



B

Tumor type	%ID
MIN-O Early stage (< 100 mm ³)	0.12 ± 0.13
MIN-O Intermediate stage (100 – 400 mm ³)	0.34 ± 0.10
MIN-O Late stage (> 400 mm ³)	0.09 ± 0.09
4T1 Late stage (> 400 mm ³)	0.30 ± 0.17

Figure 3. Longitudinal SPECT/CT imaging of ¹¹¹In-c[RGDfK]-DTPA. A) Tumor uptake of ¹¹¹In-c[RGDfK] was longitudinally monitored at 24 hrs after injection. B) Uptake in tumor lesions of tumor lesions within the same size range were compared.

Discussion

The potential of ¹¹¹In-DTPA-Ac-TZ14011 to longitudinally monitor CXCR4 expression was studied in a MIN-O mouse tumor model resembling human DCIS. The present study has demonstrated that a CXCR4 targeting imaging approach can be used to monitor lesion progression from small early stage lesions to larger intermediate and late stage lesions via the CXCR4 expression of a lesion.

Rather than using subcutaneous xenograft based models wherein transfected (human) cell lines with extremely high CXCR4 expression rates,¹⁶ small early stage MIN-O mouse tumor segments were transplanted orthotopically into the mammary fatpad. This transplantation-based model may resemble human lesion progression more accurately than that of a (CXCR4 transfected) xenograft model. Moreover, in the MIN-O model the CXCR4 expression is in line with the 5-fold overexpression reported in human tumor samples.¹ The difference between lesions with high and low expression levels of CXCR4 will possibly be more black-and-white when transfected cell lines are used, but the CXCR4 expression in these (mostly) homogeneous tumor lesions is likely to have less similarity with the human situation. In

the murine MIN-O model lesions with a modest CXCR4 expression level could be accurately detected; a 5.4-fold increase in uptake compared to surrounding mammary tissue was found. This allowed differentiation from the cell line based 4T1 control tumor tissues. Also important, CXCR4 expression in MIN-O lesions is heterogeneous. Ex vivo SPECT/CT imaging showed a patchy staining pattern in the tumor (Figure 1F) and IHC revealed clear positive and negative areas (Figure 2A) in the MIN-O tumor tissue. This heterogeneous presence of CXCR4 is in line with what is seen in breast cancer patient biopsies.²

Initial SPECT/CT measurements were performed using a lower dose of the imaging agent (10 μg ; data not shown). Unfortunately, tumor lesions could not be visualized clearly. Increasing the dose to 50 μg led to a lower specific activity but also to a better visualization of the tumor. This is in line with results reported by Jacobsen et al. who showed that tumor uptake increased after co-injection of 50 μg unlabeled peptide.¹³ In antibody-based imaging this phenomenon is well studied. Here an increase in dose was shown to improve tumor penetration and to decrease background staining.¹⁷⁻¹⁹ Imaging using SPECT/CT revealed that an ¹¹¹In-DTPA-Ac-TZ14011 signal could already be detected in MIN-O lesions as small as 10 mm³ and tumor uptake levels in lesions beyond 10 mm³ exceeded the uptake in 4T1 control tumor lesions. These findings illustrate the potential of CXCR4 imaging for visualization of small tumor lesions. Obviously, ducts in the human mammary gland are not as closely packed as in the mouse model. Hence the value of these findings in a clinical setting still requires further investigation. Our preclinical findings, however, indicate that the signal detected in MIN-O lesions is 7.2-fold higher than the signal found in the muscle and 5.4-fold as high as the signal found in the opposite mammary fat pad.

Compared to human clinical trials the MIN-O mouse model of DCIS progression simplifies these experiments. Nevertheless, in our opinion, the imaging data combined with the reported detection of CXCR4 in human DCIS examples^{1,2} warrants further investigation towards using CXCR4 targeting imaging agents to detect DCIS via its CXCR4 expression levels. An important step herein will be the further ex vivo assessment of CXCR4 expression levels in existing human DCIS samples and their surrounding stroma and mammary gland tissue.

In the MIN-O tumor model, uptake levels of ¹¹¹In-DTPA-Ac-TZ14011 increased with progression of lesion size, which is identical to results shown with ¹⁸F-FDG PET.⁷ However, accumulation of the metabolic tracer ¹⁸F-FDG in the 4T1 control tumor lesions has also been reported.²⁰ Clearly, the uptake of targeted imaging agents in the tumor needs to be directly related to the level of receptor expression. Unfortunately, such as perfusion may also influence the uptake of an imaging agent. An increase in the amount of new blood vessels

can increase perfusion of a tumor lesion resulting in higher uptake of an imaging agent. Evidently this can obscure the interpretation of the imaging data. Evidence that the uptake of ^{111}In -DTPA-Ac-TZ14011 is not governed by the degree of tumor angiogenesis is provided by the SPECT/CT experiments, as data obtained with ^{111}In -DTPA-c[RGDFK] shows a comparable uptake in both tumor types. This result, combined with the absence of membranous staining in the control tumor lesions and the increase in membranous staining in intermediate and late stage MIN-O tumor lesions seen with IHC and flow cytometry (Figure 2, Table 2 and 3), underlines that the uptake of the ^{111}In -DTPA-Ac-TZ14011 in the MIN-O lesions is driven by the presence of the CXCR4 receptor on the membrane of the cell.

Next to presence of the target, we found that the specificity of the signal in the tumor lesions (Figure 2) was greatly influenced by the time between injection and the SPECT measurements. Other than the data reported by De Silva et al.²¹ and Nimmagadda et. al,²² who showed that the best results were obtained at 90 min after injection of [^{64}Cu]AMD3465 and [^{64}Cu]AMD3100, with ^{111}In -DTPA-Ac-TZ14011 no discrimination could be made between MIN-O and control tumor lesions at one hr after injection (Figure 1). A differentiation could only be clearly made at 24 hrs after injection. This suggests a high level of non-specific uptake of ^{111}In -DTPA-Ac-TZ14011 at earlier time points. Hanaoka et al. previously evaluated the distribution of ^{111}In -DTPA-Ac-TZ14011 in a CXCR4 positive tumor model for pancreatic cancer at various time points.⁸ They showed that tumor uptake was highest at one hr post injection, but that non-specific background was significantly decreased after 24 hrs. Reasoning that at earlier time points (e.g. one hr and six hrs) the possibility of presence of unbound compound in the tumor exists, which could decrease the overall visibility of the tumor. The best imaging time point for this specific tracer was considered to be 24 hrs post injection. This time span is still significantly shorter than the reported antibody based CXCR4 imaging approaches, which require a 48 hrs incubation time.¹⁶ A 24 hrs incubation time, however, limits imaging studies to the use of longer living isotopes such as ^{111}In and ^{89}Zr .

Conclusion

IHC and flow cytometry validate that ^{111}In -DTPA-Ac-TZ14011 based imaging of CXCR4 receptor expression enabled longitudinal monitoring of the tumor lesion progression in a mouse model resembling human DCIS. Presence of CXCR4 positive lymphocytes and tumor-angiogenesis were shown to have little effect on the uptake of ^{111}In -DTPA-Ac-TZ14011 in the tumor.

References

- 1 Salvucci O, Bouchard A, Baccarelli A, Deschênes J, Sauter G, Simon R, Bianchi R, Basik M. The role of CXCR4 receptor expression in breast cancer: a large tissue microarray study. *Breast Cancer Res Treat.* 2006; 97: 275-283
- 2 Schmid BC, Rudas M, Resniczek GA, Leodolter S, Zeillinger R. CXCR4 is expressed in ductal carcinoma in situ of the breast and in atypical ductal hyperplasia. *Breast Cancer Res Treat.* 2004; 84: 247-250
- 3 Leonard GD, Swain SM. Ductal carcinoma in situ, complexities and challenges. *JNCI.* 2004; 96: 906-920
- 4 Irvine T, Fentiman IS. Biology and treatment of ductal carcinoma in situ. *Expert Rev Anticancer Ther.* 2007; 7: 135-145
- 5 Virnig BA, Tuttle TM, Shanliyan T, Kane RL. Ductal carcinoma in situ of the breast: a systematic review of incidence, treatment, and outcomes. *J Natl Cancer Inst.* 2010; 102: 170-178
- 6 Maglione JE, McGoldrick ET, Young LJT, Namba R, Gregg JP, Liu L, Moghanaki D, Ellies LG, Borowsky AD, Cardiff RD, MacLeod CL. Polyomavirus middle T-induced mammary intraepithelial neoplasia outgrowths: single origin, divergent evolution, and multiple outcomes. *Mol Cancer Ther.* 2004; 3: 941-953
- 7 Abbey CK, Borowski AD, McGoldrick, Gregg JP, Maglione JE, Cardiff RD, Cherry SR. In vivo positron-emission tomography imaging of progression and transformation in a mouse model of mammary neoplasia. *Proc Natl Ac Sci.* 2004; 101: 11438-11443
- 8 Hanaoka H, Mukai T, Tamamura H, Mori T, Ishino S, Ogawa K, Iida Y, Doi R, Fujii N, Saji H. Development of a ¹¹¹In-labeled peptide derivative targeting a chemokine receptor, CXCR4, for imaging tumors. *Nucl Med Biol.* 2006; 33: 489-493
- 9 Namba R, Young LJT, Maglione JE, McGoldrick ET, Liu S, Wurz GT, DeGregorio, Borowsky AD, MacLeod CL, Cardiff RD, Gregg JP. Selective estrogen receptor modulators inhibit growth and progression of premalignant lesions in a mouse model of ductal carcinoma in situ. *Breast Cancer Res.* 2005; 7: R881-889
- 10 Namba R, Maglione JE, Davis R, Baron CA, Liu S, Carmack CE, Young LJT, Borowsky AD, Cardiff RD, Gregg JP. Heterogeneity of mammary lesions represent molecular differences. *BMC Cancer.* 2006; 6: 1-19
- 11 van Leeuwen FWB, Buckle T, Batteau L, Pool B, Sinaasappel M, Jonkers J, Gilhuijs KGA. Potential value of color-coded dynamic breast-specific gamma-imaging; comparing ^{99m}Tc-(V)-DMSA, ^{99m}Tc-MIBI, and ^{99m}Tc-HDP in a mouse mammary model. *Appl Rad Isotopes.* 2010; 21: 355101

- 12 van den Berg NS, Buckle T, Kuil J, Wesseling J, van Leeuwen FWB. Immunohistochemical detection of the CXCR4-expression in tumor tissue using the fluorescent peptide antagonist Ac-TZ14011-FITC. *Transl Oncol.* 2011; 4: 224-230
- 13 Jacobsen O, Weiss ID, Kiesewetter DO, Farber JM, Chen X. PET of tumor CXCR4 expression with 4-¹⁸F-T140. *J Nucl Med.* 2010; 51: 1796-1804
- 14 Nie Y, Waite J, Brewer F, Sunshine M-J, Littman DR, Zou Y-R. The role of CXCR4 in maintaining peripheral B cell compartments and humoral immunity. *J Exp Med.* 2004; 9: 1145-1156
- 15 Beer AJ, Schwaiger M. Imaging of integrin alphavbeta3 expression. *Cancer Metastasis Rev.* 2008; 27: 631-644
- 16 Nimmagadda S, Pullambhatla M, Pomper MG. Immuno imaging of CXCR4 expression in brain tumor xenografts using SPECT/CT. *J Nucl Med.* 2009; 50: 1124-1130
- 17 Thurber GM, Weissleder R. Quantitating antibody uptake in vivo: Conditional dependence on antigen expression levels. *Mol Imaging Biol.* 2011; 12: 623-632¹⁸
- 18 Thurber GM, Schmidt MM, Wittrup KD. Antibody tumor penetration: Transport opposed by systemic and antigen-mediated clearance. *Adv Drug Del Rev.* 2008; 60: 1421-1434
- 19 Sharkey RM, Karacay H, Cardillo TM, Chang C-H, McBride WJ, Rossi EA, Horak ID, Goldenberg DM. Improving the delivery of radionuclides for imaging and therapy of cancer using pretargeting methods. *Clin Cancer Res.* 2005; 11: 7109s-7121s
- 19 Cao Q, Cai W, Niu G, He L, Chen X. Multimodality imaging of IL-18-binding protein-Fc therapy of experimental lung metastasis. *Clin Cancer Res.* 2008; 14(19): 6137-6145
- 20 De Silva R.A., Peyre K, Pullambhatla M, Fox JJ, Pomper MG, Nimmagadda S. Imaging CXCR4 expression in human cancer xenografts: evaluation of monocyclam ⁶⁴Cu-AMD3465. *J Nucl Med.* 2011; 52(6): 986-993
- 21 Nimmagadda S, Pullambhatla M, Stone K, Green G, Bhujwala ZM, Pomper MG. Molecular Imaging of CXCR4 receptor expression in human cancer xenografts with [⁶⁴Cu]AMD3100 positron emission tomography. *Cancer Res.* 2010; 70: 3935-3944

Appendix Chapter 10

Ac-TZ14011

Ac-TZ14011 was synthesized according to previously described procedures.¹

DTPA-Ac-TZ14011

DTPA-Ac-TZ14011 was synthesized according to previously described procedures.¹

For imaging of one mouse, 50 μg of the DTPA- Ac-TZ14011 peptide antagonist was dissolved in 80 mL 0.1 M acetic acid after which 20 μL $^{111}\text{In Cl}_3$ (10 MBq; Covidien-Mallinkrodt) was added. After 30 min incubation, labeling was validated using thin layer chromatography. In all cases, labeling efficacy was > 99%. Before injection, 1 mL of saline was added.

Synthesis and radiolabeling DTPA-c[RGDfK]

The RGD peptide, c[RGDfK], binds to the $\alpha_v\beta_3$ integrin receptor, of which expression has been linked to angiogenesis.² c[RGDfK] was synthesized by Fmoc/tBu-SPPS on a trityl resin. The protected peptide was cleaved from the resin and cyclized head-to-tail with BOP/HOBt. After purification by silica column chromatography, the remaining protecting groups were removed and the product was purified by RP-HPLC.

DTPA-c[RGDfK] was synthesized by reacting the in situ formed succinimidyl ester of DTPA(tBu)₄ with c[RGDfK]. The protecting groups were removed with TFA/TIS/water and the product was purified by RP-HPLC. For imaging of one mouse, 25 mg of DTPA-c[RGDfK] was dissolved in 50 mL 0.1M acetic acid and 25 mL InCl₃ (10 MBq) was added. After 30 min incubation, labeling was validated using thin layer chromatography. In all cases, labeling efficacy was > 99%. Before injection, 100 mL of saline was added.

References

- 1 Hanaoka H, Mukai T, Tamamura H, Mori T, Ishino S, Ogawa K, Iida Y, Doi R, Fujii N, Saji H. Development of a ^{111}In -labeled peptide derivative targeting a chemokine receptor, CXCR4, for imaging tumors. *Nucl Med Biol* 2006; 33: 489-494
 - 2 Beer AJ, Schwaiger M. Imaging of integrin alphavbeta3 expression. *Cancer Metastasis Rev.* 2008; 27: 631-644
-

Interventional molecular imaging, of a hybrid CXCR4 antagonistic peptide a hybrid approach

Synthesis and evaluation

Chapter 11

Adapted from:

Kuil J#, Buckle T#, Yuan H, van den Berg NS, Oishi S, Fujii N, Josephson L, van Leeuwen FWB.

Bioconjugate Chem. 2011; 22(5): 859-64

authors contributed equally

Abstract

Conjugation of a hybrid imaging label to the CXCR4 targeting Ac-TZ14011 peptide results in an imaging agent that can be detected using multiple imaging modalities. To examine the influence of such a hybrid label on the CXCR4 specificity and targeting affinity, Ac-TZ14011 was labeled with a multifunctional single attachment point (MSAP) reagent containing a DTPA chelate and a fluorescent dye. Although the affinity of Ac-TZ14011-MSAP was slightly lower than that of the unlabeled peptide, flow cytometry and confocal microscopy showed that the hybrid peptide was specifically bound to the receptor. Furthermore, Ac-TZ14011-MSAP was able to discriminate between MDAMB231 and MDAMB231^{CXCR4+} cells. Here the CXCR4 targeting antibody 12G5-PE, was used as a reference. In vivo, Ac-TZ14011-MSAP could be used for pre- and intraoperative tumor visualization using SPECT and fluorescence imaging.

Introduction

For molecular imaging of cancer-related biomarkers several modalities are in use, including single photon emission computed tomography (SPECT), positron emission tomography (PET), magnetic resonance imaging (MRI) and fluorescence imaging.¹ Each modality has its own strengths and weaknesses and therefore often a combination of modalities is needed during the clinical trajectory.²⁻⁵ To ensure detectability using multiple modalities an imaging agent needs to contain at least two different diagnostic labels. The combination of radiolabels for SPECT or PET and fluorescent labels in particular has potential in peptide-based molecular imaging.⁴ This combination benefits from the high sensitivity of nuclear imaging and the high spatial resolution of fluorescence imaging.⁵

Hybrid imaging agents were shown to be of added value in surgical guidance by combining pre- and intraoperative imaging.⁶⁻⁸ In this setting surgical planning is based on the radioactive signal and optical surgical guidance is achieved via the fluorescent component. This application can be expanded to tumor targeting peptides for visualization of tumor tissue.⁴

For evaluation of chemokine receptor 4 (CXCR4) expression levels, several CXCR4 antagonistic peptides have been developed.^{9,10} The binding of dye- and chelate-labeled Ac-TZ14011 peptides to CXCR4 has already been validated *in vitro* and *in vivo*;^{4,11-13} the specificity of Ac-TZ14011 for CXCR4 has been underlined by the fact that a scrambled peptide and a peptide with inversed stereocenters could not label CXCR4 expressing cells.¹⁴ However, a hybrid derivative of this CXCR4-targeting peptide has not yet been reported.

In this Chapter, the conjugation of a hybrid multifunctional single attachment point (MSAP) reagent^{15,16} to Ac-TZ14011 is described. Using the hybrid imaging agent Ac-TZ14011-MSAP *in vitro* validation studies were performed to examine the influence of the MSAP label on the specificity and receptor affinity. Furthermore, initial *in vivo* experiments are described.

Materials and Methods

General

All chemicals were obtained from commercial sources and used without further purification. Preparation of compounds, recording of absorption and emission spectra and radiolabeling of the peptides are described in the Appendix of this Chapter.

In vitro experiments

Cell culture

Human breast cancer cell lines MDAMB231 and MDAMB231^{CXCR4+} were kindly provided by Olaf van Tellingen and Ed Roos (both NKI-AvL, Amsterdam, The Netherlands), respectively. In the MDAMB231^{CXCR4+} cells CXCR4 expression was upregulated after culture under hypoxic conditions. Cells with high CXCR4 expression were selected using flow cytometry, resulting in the MDAMB231^{CXCR4+} cell line. MDAMB231 cells were used as control based on their basal CXCR4 expression. Both cell lines were maintained in Gibco's minimum essential medium (MEM) enriched with 10% fetal bovine serum, Penicillin/Streptomycin, L-glutamine, non-essential amino acids, sodium pyruvate and MEM vitamins solution (all Life Technologies Inc.). Cells were kept under standard culture conditions.

Flow cytometry analysis of MDAMB231 and MDAMB231^{CXCR4+} cell binding

Freshly cultured MDAMB231 or MDAMB231^{CXCR4+} cells were trypsinized, aliquoted in portions of 300.000 cells, centrifuged (1200 rpm, five min, 4°C) and decanted. 6.4 nM of monoclonal phycoerythrin (PE) labeled anti-CXCR4 antibody (CD184 12G5-PE (12.5 µg/mL), BD Biosciences) or 1 µM of Ac-TZ14011-MSAP or Ac-TZ14011-MSAP-In in 50 µL of 0.1% bovine serum albumin (BSA) in phosphate buffered saline (PBS) was added to the cells. After one hr of incubation at 4°C, the cells were washed (twice) with 300 µL of 0.1% BSA in PBS, resuspended in 300 µL of 0.1% BSA in PBS and fluorescence was measured using a CyAn ADP flow cytometer (DakoCytomation) at APC-Cy7 settings (635 nm laser and 750 nm long pass filter). Live cells were gated on Forward Scatter, Side Scatter and Pulse Width and approximately 20.000 viable cells were analyzed. All experiments were performed in triplicate.

Determination of dissociation constants

MDAMB231^{CXCR4+} cells were trypsinized and aliquoted in portions of 300.000 cells. For saturation binding experiments different concentrations of Ac-TZ14011-MSAP or Ac-TZ14011-MSAP-In, in a range of 0 – 1000 nM, were added. For competition experiments different concentrations (0 – 10,000 nM) of Ac-TZ14011, Ac-TZ14011-DTPA or Ac-TZ14011-FITC in the presence of 250 nM of Ac-TZ14011-MSAP were added. Cells were incubated for one hr at 4°C. The cells were washed twice with 300 µL of 0.1% BSA in PBS, resuspended in

300 μL of 0.1% BSA in PBS and fluorescence was measured using a CyAn ADP flow cytometer (DakoCytomation) at APC-Cy7 settings. Live cells were gated on Forward Scatter, Side Scatter and Pulse Width and approximately 20,000 viable cells were analyzed. All experiments were performed in duplicate.

The normalized geometric means were fitted with equations in the GraphPad Prism 5 software. The K_D values of Ac-TZ14011-MSAP and Ac-TZ14011-MSAP-In were calculated using the 'Binding – Saturation, One site – Total' nonlinear regression equation (Eq. 1). The K_D values of Ac-TZ14011, Ac-TZ14011-DTPA and Ac-TZ14011-FITC were calculated using the 'Binding – Competitive, One site – Fit K_i ' nonlinear regression equation (Eq. 2 and 3).

$$y = \frac{B_{\max} * x}{K_D + x} + NS * x + \text{Background} \quad (\text{Eq. 1})$$

y	= normalized fluorescence
B_{\max}	= maximum specific binding in the units of the y axis
x	= concentration of Ac-TZ14011-MSAP or Ac-TZ14011-MSAP-In in nM
K_D	= equilibrium dissociation constant of Ac-TZ14011-MSAP or Ac-TZ14011-MSAP-In in nM
NS	= slope of nonspecific binding
Background	= amount of normalized fluorescence with no added compound

$$\log IC_{50} = \log(10^{\log K_D} * (1 + \frac{[Ac - TZ14011 - MSAP]}{K_{D, Ac - TZ14011 - MSAP}})) \quad (\text{Eq. 2})$$

$$y = \text{Bottom} + \frac{\text{Top} - \text{Bottom}}{1 + 10^{(x - \log IC_{50})}} \quad (\text{Eq. 3})$$

IC_{50}	= concentration of competitor that results in binding half-way between Bottom and Top
K_D	= equilibrium dissociation constant of the competitor in nM
[Ac-TZ14011-MSAP]	= concentration of Ac-TZ14011-MSAP (250 nM)
$K_{D, Ac-TZ14011-MSAP}$	= dissociation constant of Ac-TZ14011-MSAP (186.9 nM)
y	= normalized fluorescence
Bottom and Top	= plateaus in the units of the y-axis

Confocal microscopy

MDAMB231^{CXCR4+} cells were seeded onto coverslips (Ø 24mm; Karl Hecht GmbH & Co) and incubated overnight. The cells were washed with PBS and incubated with 1 µM of Ac-TZ14011-MSAP for one hr at 4°C and washed again with ice cold PBS. Confocal microscopy images were taken at 37°C on a Leica TCS-SP2-AOBS Live confocal microscope (Leica Microsystems Heidelberg GmbH).

In vivo experiments

In vivo model

For generation of the CXCR4 positive mouse tumor lesions, FVB mice (n = 3; 3 - 4 weeks of age) were used. Before transplantation (and imaging), mice were anaesthetized using a hypnorm (VetaPharma Ltd)/dormicum (Midazolam; Roche)/water solution (1:1:2; 5 µL/g i.p.). Via a small incision, the inguinal lymph node was excised where after a piece of preinvasive 8w-B MIN-O tissue was placed into the remaining tissue of the fourth mammary gland.⁶⁻⁸ Approximately six weeks after transplantation, lesions were deemed suitable for further experiments. Control experiments were performed using orthotopic transplantation of 0.25 x 10⁵ 4T1 mouse tumor cells into the mammary tissue of Balb/c nude mice (n = 3; 6 - 8 weeks of age). Cells were cultured under standard conditions in MEM medium containing MEM vitamins, L-glutamine, non-essential amino acids, sodium pyruvate and Penicillin/Streptomycin solution (all BD Biosciences). Before transplantation, cells were trypsinized and washed with HBSS (BD Biosciences). Transplantation of cells was carried out under identical conditions as placement of the MIN-O segments. All animal experiments were performed in accordance with Dutch welfare regulations and approved by the local ethics committee.

Single photon emission computed tomography/ computed tomography (SPECT/CT)

24 Hrs after intravenously injection of 50 µg of ¹¹¹In-labeled Ac-TZ14011-MSAP (10 MBq), the mice were placed in a temperature controlled (37 °C) animal holder (Equipment Veterinaire MINERVE) before performing a SPECT/CT scan on the nanoSPECT/CT (Bioscan Inc.) The region of interest incorporating the whole mouse was selected, based on a (sagittal) tomographic planning X-ray image followed by a helical 3D CT. Hereafter, a sequential total body SPECT scan of the same field of view was performed. Following

acquisition, the data was reconstructed with HiSPECT software (Scivis GmbH). The SPECT and CT data sets were automatically co-registered. The images were analyzed using the InVivoScope post processing software (Bioscan Inc.).

Fluorescence imaging

After SPECT/CT, the mice were sacrificed. In vivo fluorescence imaging was conducted on a preclinical fluorescence scanner (IVIS 200; Xenogen Corp.) using Living Imaging Acquisition and Analysis software (Xenogen Corp.). Images were acquired with standard Cy5.5 (excitation 615 - 665 nm and emission 695 - 770 nm) settings.

Distribution studies

After fluorescence imaging, tissues were excised. Tissues were weighed and the amount of radioactivity present in the tissues was counted using a Perkin Elmer 1480 Wizard 3" automatic gamma counter (245 keV; 60 sec). Counts per minute were converted into MBq and corrected for decay. The percentage of the injected dose per gram of tissue (%ID/g) was calculated as followed: $((\text{MBq measured in tissue} / \text{injected dose}) * 100\%) / \text{weight of tissue}$.

Results

The hybrid peptide derivative was generated using a MSAP reagent, which contains a DTPA and a CyAL-5.5_p fluorochrome reporter and a reactive NHS ester.¹⁵⁻¹⁷ Via the active NHS ester the MSAP reagent was selectively coupled to the D-Lys⁸ amine functionality on Ac-TZ14011 (Figure 3C, Appendix Scheme A1). To study the possible influence of chelation of a metal ion in the DTPA moiety, a portion of Ac-TZ14011-MSAP was coordinated to (non-radioactive) indium, yielding Ac-TZ14011-MSAP-In (Appendix Scheme A1).

The absorption spectra of Ac-TZ14011-MSAP and Ac-TZ14011-MSAP-In were shown to be analogous and the emission spectra were also very similar (Figure 1). For both compounds the absorption maximum was found at 680 nm and the emission maximum at 704 nm. Moreover, binding of indium in the DTPA chelate did not reduce the fluorescent intensity.

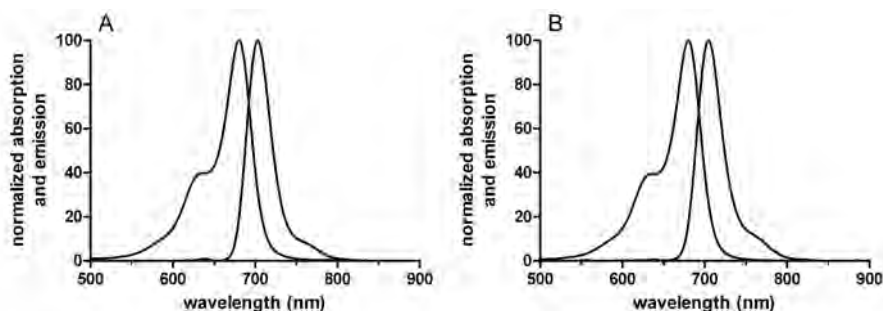


Figure 1. Absorption and emission spectra of compounds A) Ac-TZ14011-MSAP and B) Ac-TZ14011-MSAP-In.

The ability of Ac-TZ14011-MSAP and Ac-TZ14011-MSAP-In to discriminate between basal and CXCR4 overexpressing tumor cells was quantitatively examined with flow cytometry. As a reference the commercially available phycoerythrin (PE) labeled anti-CXCR4 antibody CD184, clone 12G5 (12G5-PE), was used. Incubation with the antibody revealed a 4.4-fold upregulation of CXCR4 in the higher CXCR4 expressing cells, MDAMB231^{CXCR4+}, compared to the basal cell line MDAMB231 (Table 1). The ratio between the fluorescence signals found for Ac-TZ14011-MSAP was a factor 4.1, which nicely corresponds to the ratio obtained with the antibody (Figure 1, Table 1). This indicates that the antibody and the peptide are both suited to detect CXCR4.

Where the ratio between the fluorescence signals was similar to that of the antibody, the mean fluorescence intensity ratios (MFIRs) obtained with Ac-TZ14011-MSAP were approximately 10 times higher (Table 1). This difference might be caused by the fact that the concentration used for the antibody was significantly lower than that of the peptides, 6.4 nM and 1 μ M, respectively. Moreover, due to the lower autofluorescence at the flow cytometer settings used for the MSAP peptides, the voltage of the photomultiplier detector could be set higher when the MSAP peptides were measured, compared to the PE-labeled antibody.

Table 1. Quantitative analysis of cellular uptake of MDAMB231 and MDAMB231^{CXCR4+} cells using a CXCR4 antibody, Ac-TZ14011-MSAP and Ac-TZ14011-MSAP-In.

compound	MFIR \pm SD MDAMB231	MFIR \pm SD MDAMB231 ^{CXCR4+}	MFIR ratio
12G5-PE antibody	1.116 \pm 0.054	4.920 \pm 1.46	4.4
Ac-TZ14011-MSAP	10.94 \pm 1.62	45.27 \pm 2.19	4.1
Ac-TZ14011-MSAP-In	18.24 \pm 1.93	56.67 \pm 2.84	3.1

MFIR = mean fluorescence intensity ratio

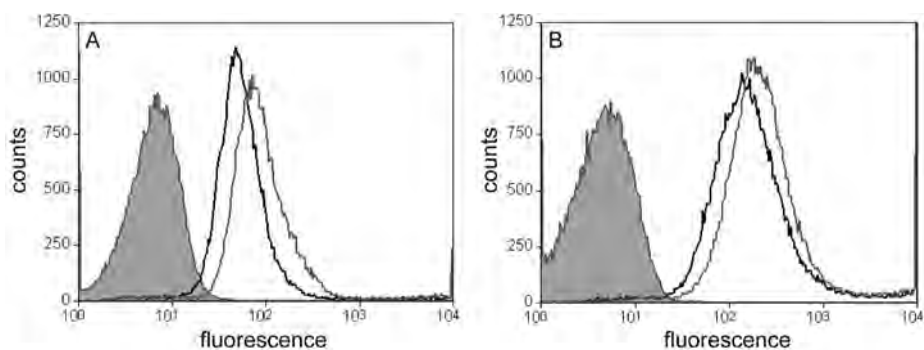


Figure 2. Flow cytometry analysis of the peptides Ac-TZ14011-MSAP and Ac-TZ14011-MSAP-In using A) MDAMB231 cells or B) MDAMB231^{CXCR4+} cells. Both graphs show untreated cells (trace filled with grey), 1 μ M of Ac-TZ14011-MSAP (black trace) and 1 μ M of Ac-TZ14011-MSAP-In (grey trace).

Incubation of the cells with Ac-TZ14011-MSAP-In resulted in a slightly lower ratio between fluorescence intensities in high and low CXCR4 expressing cells, namely 3.1 compared to 4.1 for Ac-TZ14011-MSAP (Table 1). Since the MFIR in the MDAMB231 cells was increased after incubation with Ac-TZ14011-MSAP-In compared to Ac-TZ14011-MSAP and the antibody (Table 1), it is plausible that incubation with Ac-TZ14011-MSAP-In results in increased nonspecific binding (Figure 2).

Incubation of MDAMB231^{CXCR4+} cells with different concentrations of Ac-TZ14011-MSAP yielded a binding curve that appears to exist out of two components (Figure 3A). The nonlinear component of the binding curve can be ascribed to specific receptor binding and the linear component to nonspecific cell binding. By using this binding model, direct determination of the nonspecific binding was not required. The similarity in the CXCR4-receptor affinities of Ac-TZ14011-MSAP and Ac-TZ14011-MSAP-In (Table 2) indicates that indium binding does not affect the interaction between the peptide and CXCR4.

Table 2. Dissociation constants (K_D) of the constructs.

Construct	K_D (nM)
Ac-TZ14011-unlabeled	8.61 ± 1.42
Ac-TZ14011-MSAP	186.9 ± 52.4
Ac-TZ14011-MSAP-In	177.1 ± 37.2
Ac-TZ14011-DTPA	124.4 ± 23.9
Ac-TZ14011-FITC	203.5 ± 67.1
TR14010 (scrambled peptide)	> 5000

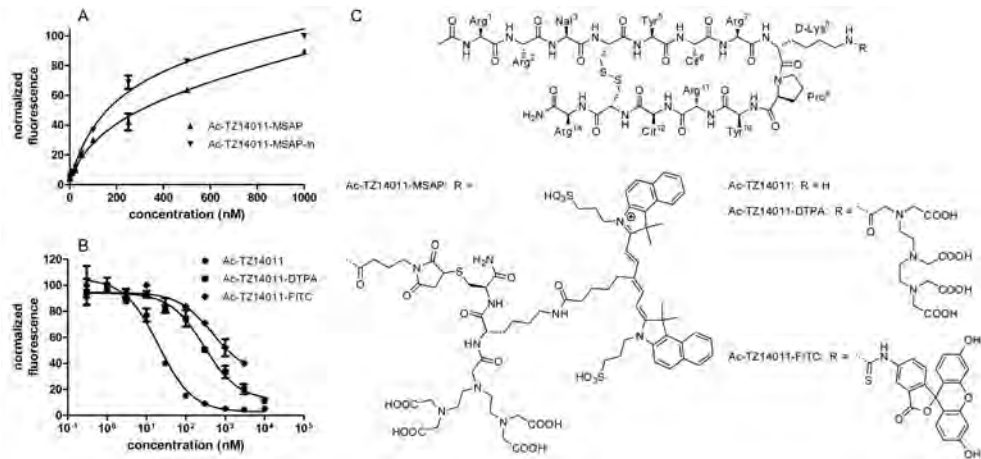


Figure 3. A) Determination of affinity of constructs Ac-TZ14011-MSAP and Ac-TZ14011-MSAP-In with saturation binding experiments. B) Competition experiments with three other Ac-TZ14011 peptides in the presence of 250 nM of Ac-TZ14011-MSAP. C) Structures of the peptides used for competition experiments.

To compare the receptor affinity of Ac-TZ14011-MSAP and Ac-TZ14011-MSAP-In with the other peptide derivatives, different amounts of Ac-TZ14011, Ac-TZ14011-DTPA or Ac-TZ14011-FITC were added in the presence of 250 nM of Ac-TZ14011-MSAP (Figure 3B and 3C). All three peptide derivatives could compete with Ac-TZ14011-MSAP for CXCR4 binding, confirming the specificity of Ac-TZ14011-MSAP. The K_D values, obtained by fitting the inhibition curves with a competition model, of the monolabeled peptides Ac-TZ14011-DTPA and Ac-TZ14011-FITC were in the order of the K_D values of Ac-TZ14011-MSAP and Ac-TZ14011-MSAP-In (Table 1). In line with previous reports, the scrambled peptide TR14010 did not show significant binding; $K_D > 5000$ nM (Table 2).¹⁹

The cellular distribution of Ac-TZ14011-MSAP was evaluated to see if binding to CXCR4 on the cell membrane did occur. Confocal microscopy imaging performed at 4°C revealed clear staining of the cell membrane of MDAMB231^{CXCR4+} cells after incubation with Ac-TZ14011-MSAP (Figure 4). During imaging at 37°C minor staining in vesicular structures was detected, which is common for internalizing membrane receptors.

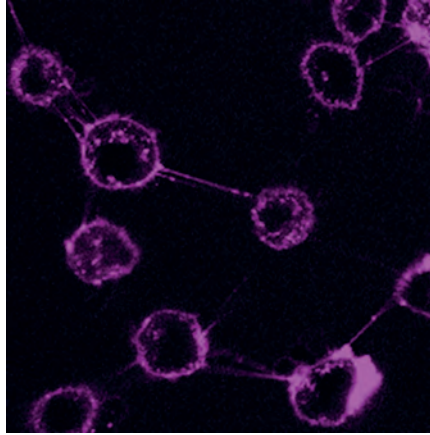


Figure 4. Confocal microscopy of Ac-TZ14011-MSAP using MDAMB231^{CXCR4+} cells.

As the CXCR4 expression in MDAMB231CXCR4⁺ cells decreases to basal levels in vivo, mice with CXCR4 positive 'spontaneous' MIN-O tumors were used. Low CXCR4 expressing 4T1 tumor lesions served as control. Tumor-bearing mice were injected with ¹¹¹In-labeled Ac-TZ14011-MSAP 24 hrs prior to the SPECT/CT and fluorescence imaging (Figure 5). MIN-O tumor lesions could be accurately detected with both modalities. The obtained tumor-to-muscle ratio was significantly higher in MIN-O tumor lesions compared to 4T1 tumor lesions; 4.55 ± 0.68 vs. 1.20 ± 0.12 ($P < 0.01$). This indicates that Ac-TZ14011-MSAP can be used to discriminate CXCR4 positive from CXCR4 negative tumors in vivo.

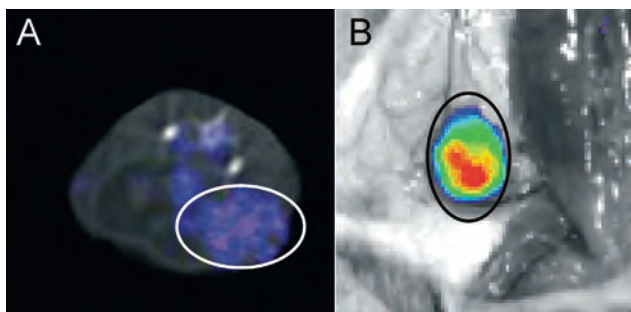


Figure 5. A) SPECT/CT (axial) of a MIN-O tumor-bearing mouse. B) Fluorescence image of an intersected MIN-O tumor-bearing mouse.

Discussion

Conjugation of a hybrid imaging label to a peptide results in an imaging agent that can be detected using multiple imaging modalities. Unfortunately, conjugation of such a label can have a negative influence on the affinity of the targeting moiety.⁴ This was also seen after conjugation of the MSAP reagent to Ac-TZ14011 as the receptor affinity of the unlabeled peptide was approximately 20-fold higher than for the labeled derivatives (Table 2). Since the affinity of Ac-TZ14011-MSAP-In remains in the nanomolar range, this decrease is not likely to be an obstruction for using Ac-TZ14011-MSAP-In in molecular imaging applications.²⁰ Furthermore, comparison between the receptor affinities of differently labeled derivatives of Ac-TZ14011 illustrated that the hybrid MSAP label does not hamper receptor binding more than the smaller FITC and DTPA labels do.

The uptake ratio obtained with Ac-TZ14011-MSAP-In in the MDAMB231^{CXCR4+} and MDAMB231 cells was somewhat lower compared to Ac-TZ14011-MSAP, namely 3.1 and 4.1, respectively (Table 1). This effect can be caused by an increase in nonspecific binding of Ac-TZ14011-MSAP-In (Figure 2). Such an increase in nonspecific binding is most likely a charge related effect; the DTPA chelate in Ac-TZ14011-MSAP is mainly -2 charged and indium bound DTPA in Ac-TZ14011-MSAP has a charge of -1,^{21,22} increasing hydrophobicity of the label. In general, labels with increased hydrophobicity drive (nonspecific) cellular uptake.⁴

Molecular modeling studies showed that D-Lys⁸ in T140 (the parental compound of Ac-TZ14011) does not interact with CXCR4.²³ Furthermore, the crystal structure of CVX15, which is similar to T140, bound to CXCR4 also showed no crucial interactions in this area.²⁴ However, we found that D-Lys⁸ functionalization in Ac-TZ14011 still influenced the binding affinity. This influence might be explained by evaluation of the possible different effects of peptide modification on (CXCR4) receptor binding. A modification on the peptide: i) can directly change a receptor interaction (e.g. a hydrogen bond), ii) can change the 3D structure of the peptide, and/or iii) can hinder the pharmacophore to bind properly to the receptor via steric hindrance.²⁵ Here, the third effect is most likely the cause of the decrease in affinity.

A logical chemical modification to reduce the steric hindrance would be the incorporation of a larger spacer between the imaging label and the pharmacophore. Although it has been shown that incorporation of a 6-aminocaproic acid spacer does not yield a higher affinity,²⁶ it is possible that longer spacers will be more effective.

Conclusion

In this Chapter, the first hybrid CXCR4 antagonistic peptide, containing a Cy5.5-like dye and a DTPA chelate is described. Despite functionalization with a relatively large hybrid label Ac-TZ14011-MSAP retained its specificity and nanomolar CXCR4-affinity *in vitro*. Moreover, indium binding to the chelate did not affect the fluorescence properties. The initial *in vivo* studies showed that Ac-TZ14011-MSAP was able to discriminate between CXCR4 positive and negative tumors.

References

- 1 Mather S. Molecular imaging with bioconjugates in mouse models of cancer. *Bioconjugate Chem.* 2009; 20: 631-643
- 2 Jennings LE, Long, NJ. 'Two is better than one'-probes for dual-modality molecular imaging. *Chem Commun.* 2009 28; (24): 3511-24
- 3 Louie A. Multimodality imaging probes: design and challenges. *Chem Rev.* 2010; 110: 3146-3195
- 4 Kuil J, Velders AH, van Leeuwen FWB. Multimodal tumor-targeting peptides functionalized with both a radio-and a fluorescent-label. *Bioconjugate Chem.* 2010; 21: 1709-1719
- 5 Culver J, Akers W, Achilefu S. Multimodality molecular imaging with combined optical and SPECT/PET modalities. *J Nucl Med.* 2008; 49: 169-172
- 6 Buckle T, Chin PTK, van den Berg NS, Loo CE, Koops W, Gilhuijs KG, van Leeuwen FWB. Tumor bracketing and safety margin estimation using multimodal marker seeds: a proof of concept. *J Biomed Opt.* 2010; 15: 056021
- 7 Buckle T, van Leeuwen AC, Chin PTK, Janssen H, Muller SH, Jonkers J, van Leeuwen FWB. A self-assembled multimodal complex for combined pre- and intraoperative imaging of the sentinel lymph node. *Nanotechnology.* 2010; 21: 355101
- 8 Van der Poel HG, Buckle T, Brouwer OR, Valdés Olmos RA, van Leeuwen FWB. Intraoperative laparoscopic fluorescence guidance to the sentinel lymph node in prostate cancer patients; clinical proof of concept of an integrated functional imaging approach using a multimodal tracer. *Eur. Urol.* 2011; 60: 826-33
- 9 Tamamura H, Omagari A, Hiramatsu K, Gotoh K, Kanamoto T, Xu Y, Kodama E, Matsuoka M, Hattori T, Yamamoto N, Nakashima H, Otaka A, Fujii N. Development of specific CXCR4 inhibitors possessing high selectivity indexes as well as complete stability in serum based on an anti-HIV peptide T140. *Bioorg. Med. Chem. Lett.* 2001; 11: 1897-1902
- 10 Tamamura H, Hiramatsu K, Kusano S, Terakubo S, Yamamoto N, Trent JO, Wang Z, Peiper SC, Nakashima H, Otaka A, Fujii N. Synthesis of potent CXCR4 inhibitors possessing low cytotoxicity and improved biostability based on T140 derivatives. *Org. Biomol. Chem.* 2003; 1: 3656-3662
- 11 Nomura W, Tanabe Y, Tsutsumi H, Tanaka T, Ohba K, Yamamoto N, Tamamura H. Fluorophore labeling enables imaging and evaluation of specific CXCR4-ligand interaction at the cell membrane for fluorescence-based screening. *Bioconjugate Chem.* 2008; 19: 1917-1920

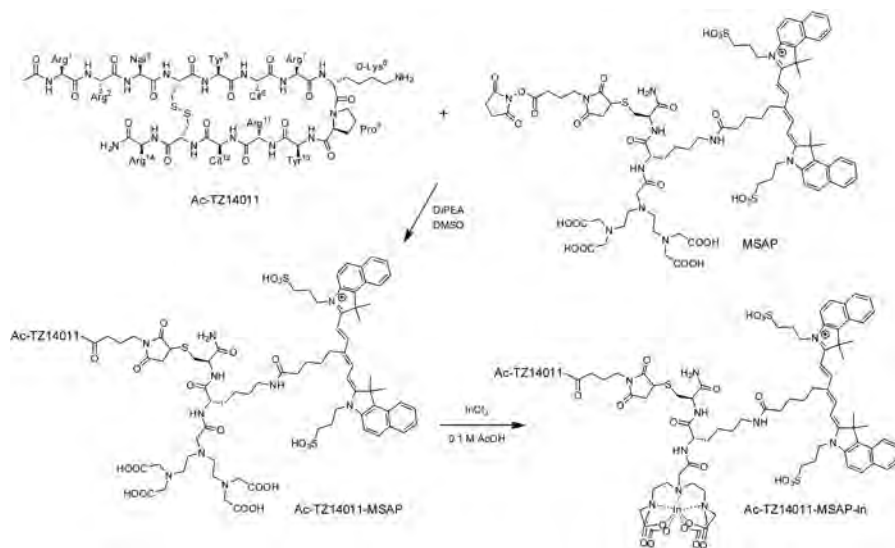
- 12 Oishi S, Masuda R, Evans B, Ueda S, Goto Y, Ohno H, Hirasawa A, Tsujimoto G, Wang Z, Peiper SC, Naito T, Kodama E, Matsuoka M, Fujii N. Synthesis and application of fluorescein- and biotin-labeled molecular probes for the chemokine receptor CXCR4. *ChemBioChem*. 2008; 9: 1154-1158
- 13 Hanaoka H, Mukai T, Tamamura H, Mori T, Ishino S, Ogawa K, Iida Y, Doi R, Fujii N, Saji H. Development of a ¹¹¹In-labeled peptide derivative targeting a chemokine receptor, CXCR4, for imaging tumors. *Nucl. Med. Biol.* 2006; 33: 489-494
- 14 Nishizawa K, Nishiyama H, Oishi S, Tanahara N, Kotani H, Mikami Y, Toda Y, Evans BJ, Peiper SC, Saito R, Watanabe J, Fujii N, Ogawa O. Fluorescent imaging of high-grade bladder cancer using a specific antagonist for chemokine receptor CXCR4. *Int. J. Cancer*. 2010; 127: 1180-1187
- 15 Garanger E, Aikawa E, Reynolds F, Weissleder R, Josephson L. Simplified syntheses of complex multifunctional nanomaterials. *Chem. Commun.* 2008; 4792-4794
- 16 Garanger E, Blois J, Hilderbrand SA, Shao F, Josephson L. Divergent oriented synthesis for the design of reagents for protein conjugation. *J. Comb. Chem.* 2010; 12: 57-64
- 17 Furusato B, Mohamed A, Uhlen M, Rhim JS. CXCR4 and cancer. *Pathol. Int.* 2010; 60: 497-505
- 18 Bhandari D, Robia SL, Marchese A. The E3 ubiquitin ligase atrophin interacting protein 4 binds directly to the chemokine receptor CXCR4 via a novel WW domain-mediated interaction. *Mol. Biol. Cell.* 2009; 20: 1324-1339
- 19 Nishizawa K, Nishiyama H, Oishi S, Tanahara N, Kotani H, Mikami Y, Toda Y, Evans BJ, Peiper SC, Saito R, Watanabe J, Fujii N, Ogawa O. Fluorescent imaging of high-grade bladder cancer using a specific antagonist for chemokine receptor CXCR4. *Int. J. Cancer*. 2010; 127: 1180-1187
- 20 Schottelius M, Wester HJ. Molecular imaging targeting peptide receptors. *Methods*. 2009; 48: 161-177
- 21 Moulin C, Amekraz B, Steiner V, Plancque G, Ansoberlo E. Speciation studies on DTPA using the complementary nature of electrospray ionization mass spectrometry and time-resolved laser-induced fluorescence. *Appl. Spectrosc.* 2003; 57: 1151-1161
- 22 Maecke HR, Riesen A, Ritter W. The molecular structure of indium-DTPA. *J. Nucl. Med.* 1989; 30: 1235-1239
- 23 Balkwill F. The significance of cancer cell expression of the chemokine receptor CXCR4. *Semin. Cancer Biol.* 2004; 14: 171-179

- 24 Wu B, Chien EYT, Mol CD, Fenalti G, Liu W, Katritch V, Abagyan R, Brooun A, Wells P, Bi FC, Hamel DJ, Kuhn P, Handel TM, Cherezov V, Stevens RC. Structures of the CXCR4 chemokine GPCR with small-molecule and cyclic peptide antagonists. *Science*. 2010; 330: 1066-1071
- 25 Trent JO, Wang ZX, Murray JL, Shao W, Tamamura H, Fujii N, Peiper SC. Lipid bilayer simulations of CXCR4 with inverse agonists and weak partial agonists. *J. Biol. Chem.* 2003; 278: 47136-47144
- 26 Oishi S, Masuda R, Evans B, Ueda S, Goto Y, Ohno H, Hirasawa A, Tsujimoto G, Wang Z, Peiper SC, Naito T, Kodama E, Matsuoka M, Fujii N. Synthesis and application of fluorescein- and biotin-labeled molecular probes for the chemokine receptor CXCR4. *ChemBioChem*. 2008; 9: 1154-1158

Appendix Chapter 11

General

All chemicals were obtained from commercial sources and used without further purification. The reactions were monitored by thin layer chromatography (TLC).



Scheme A1. Conjugation of the MSAP label to Ac-TZ14011 and subsequent indium labeling.

Ac-TZ14011

Ac-TZ14011 was synthesized according to described procedures.¹

CyAL-5.5b

CyAL-5.5_b (Figure A1) was synthesized according to previously described procedures.²

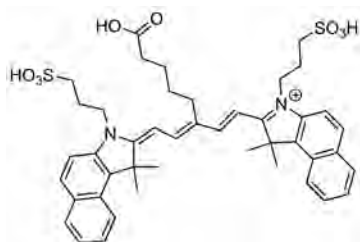


Figure A1. Chemical structure of CyAL-5.5_b.

MSAP reagent

The multifunctional single attachment point (MSAP) reagent was synthesized based on previously described procedures.^{3,4}

Ac-TZ14011 (8.4 mg, 3.0 μmol) and the MSAP reagent (3.4 mg, 2.0 μmol) were dissolved in 2 mL of DMSO. DiPEA (7.0 μL , 40 μmol) was added and the mixture was stirred overnight at room temperature, after which the mixture was purified by preparative HPLC using a Waters HPLC system with a UV detector operating at 230 nm and a Waters Atlantis C18 10 μm (250 \times 19 mm) column. A gradient of 0.05% TFA in $\text{H}_2\text{O}/\text{CH}_3\text{CN}$ 9:1 to 0.05% TFA in $\text{H}_2\text{O}/\text{CH}_3\text{CN}$ 1:4 40 minutes was used. The product was obtained as a blue fluffy solid (3.9 mg, 45%) after pooling of the appropriate fractions and lyophilization. MS (MALDI-TOF): $[\text{M}+\text{H}]^+$ calculated 3676.677, found 3676.256.

For the chemical structure of Ac-TZ14011-MSAP, see Scheme A1

Radiolabeling of Ac-TZ14011-MSAP

Ac-TZ14011-MSAP was dissolved in 0.1 M of acetic acid (50 $\mu\text{g}/100 \mu\text{L}$) and InCl_3 (10 MBq/50 μg of Ac-TZ14011-MSAP; Covidien-Mallinkrodt) was added. After 30 min of incubation, labeling was validated with thin layer chromatography (TLC) using 74 mM of sodium citrate (pH 5) as an eluent and a VCS-201 TLC scanner (Veenstra Instruments). In all cases, labeling efficacy was >99%. Before injection, saline (1:1) was added.

Ac-TZ14011-MSAP-In

A solution of Ac-TZ14011-MSAP with a concentration of 160 μM in 0.1 M AcOH was prepared. Half of this solution was diluted (1:1 v/v) with 0.1 M of AcOH to yield a stock solution of 80 μM of Ac-TZ14011-MSAP. The other half was added to the same amount of 160 μM of InCl_3 in AcOH, incubated for 30 min, yielding a stock solution of 80 μM of Ac-TZ14011-MSAP-In.

Ac-TZ14011-DTPA

Ac-TZ14011-DTPA was synthesized according to previously described procedures.¹

References

- 1 Hanaoka H, Mukai T, Tamamura H, Mori T, Ishino S, Ogawa K, Iida Y, Doi R, Fujii N, Saji H. Development of an ^{111}In -labeled peptide derivative targeting a chemokine receptor, CXCR4, for imaging tumors. *Nucl Med Biol.* 2006; 33: 489-494
 - 2 Shao F, Yuan H, Josephson L, Weissleder R, Hilderbrand SA. Facile synthesis of mono-functional pentamethine carbocyanine fluoreophores. *Pigments.* 2011; 90: 119-122
 - 3 Garanger E, Aikawa E, Reynolds F, Weissleder R, Josephson L. Simplified synthesis of complex multifunctional nanomaterials. *Chem Commun.* 2008; 4792-4794
 - 4 Garanger E, Blios J, Hilderbrand SA, Shao F, Josephson L. Divergent oriented synthesis for the design of reagents for protein conjugation. *J Comb Chem.* 2010; 12: 57-64
 - 5 Nishizawa K, Nishiyama H, Oishi S, Tanahara N, Kotani H, Mikami Y, Toda Y, Evamns BJ, Peiper SC, Saito R, Watanabe J, Fujii N, Ogawa O. Fluorescent imaging of high-grade bladder cancer using a specific antagonist for chemokine receptor CXCR4. *Int J Cancer.* 2010; 127: 1180-1187
-

Interventional

Hybrid peptide dendrimers for imaging
molecular imaging,
of chemokine receptor 4 (CXCR4) expression
a hybrid approach

Chapter 12

Adapted from:

Kuil J, Buckle T, Oldenburg J, Yuan H, Borowsky AD, Josephson L, van Leeuwen FWB.

Mol Pharm. 2011; 8(6): 2444-53

Abstract

Conjugation of a hybrid MSAP label was shown to have a negative influence on the affinity of the CXCR4 targeting peptide Ac-TZ14011. To investigate if multimerization, e.g. increasing the amount of targeting peptides per molecule, could be used to minimize the influence of the MSAP label on the binding affinity of Ac-TZ14011, mono-, di- and tetrameric Ac-TZ14011-containing dendrimers were prepared and functionalized with a MSAP label. Confocal microscopy revealed membranous staining of MDAMB231^{CXCR4+} cells after incubation with the dendrimers at 4°C, consistent with the localization of CXCR4. Unlabeled, the CXCR4 affinity of the dimer and tetramer was somewhat lower than the affinity of the monomer. However, when labeled with the hybrid label the CXCR4 affinity of the dimer and tetramer increased compared to the monomer. Distribution studies revealed that the presence of additional peptides in the dimer and tetramer reduced nonspecific muscle uptake. Thus, multimerization of the Ac-TZ14011 peptide reduced the negative influence of the hybrid label on the receptor affinity and the biodistribution.

Introduction

The development of hybrid imaging agents is attaining a significant interest in the field of molecular imaging as hybrid imaging agents can be used in more than one imaging modality.¹⁻⁶ Each modality has its own strengths and weaknesses, and therefore, a combination of modalities is often used in the clinic. In principle, hybrid imaging agents can also be used for postoperative pathology and assessment for the effectiveness of chemo- and/or immunotherapy.

Several receptor targeting peptides (e.g. RGD, octreotate, bombesin and Ac-TZ14011) have been functionalized with labels that combine radioactivity and fluorescence.^{1,7} Such labels are often as large as the tumor targeting peptide. Therefore, this hybrid labeling technology can have a significant (negative) influence on the receptor binding and the biodistribution. Especially the dye-driven, nonspecific uptake by organs and tissues is a substantial concern.¹ We reasoned that use of multimeric peptide dendrimers, consisting of multiple peptides (e.g. 4) and one hybrid label, can possibly reduce the influence of the label.¹ Multimerization is a well known strategy in order to enhance the receptor affinity and specificity for a targeting moiety.⁸⁻¹⁴ By increasing the amount of peptides with respect to the label, the label can be shielded from the biological environment.¹

The strategy of peptide multimerization has already been successfully applied with radiolabels and fluorescent labels.¹⁵⁻¹⁹ However, only nano-sized multimeric peptides have been prepared with both a radiolabel and a fluorescent label.^{20,21} Despite the fact that nanoparticles can generally benefit from the enhanced permeability and retention (EPR) effect,²² these specific 'large' nanoparticles suffer from high nonspecific (liver) uptake and are not able to extravasate from blood vessels into the tumor.^{20,21} Surprisingly, small hybrid peptide dendrimers, which generally have a better biodistribution, have never been reported. Here, the first hybrid Ac-TZ14011-containing dimeric and tetrameric dendrimers for targeting the chemokine receptor 4 (CXCR4) are described.

Materials and Methods

Cell culture

The human breast cancer cell line MDAMB231^{CXCR4+} was kindly provided by Ed Roos (NKI-AvL, Amsterdam, The Netherlands). In the MDAMB231^{CXCR4+} cells CXCR4 expression was upregulated after culture under hypoxic conditions. Cells with high CXCR4 expression

were selected using flow cytometry, resulting in the MDAMB231^{CXCR4+} cell line. Cells were maintained in Gibco's minimum essential medium (MEM) enriched with 10% fetal bovine serum, Penicillin/Streptomycin, L-glutamine, non-essential amino acids, sodium pyruvate and MEM vitamins solution (all Life Technologies Inc.). Cells were kept under standard culture conditions.

Confocal microscopy

MDAMB231^{CXCR4+} cells were seeded onto coverslips (Ø 24mm; Karl Hecht GmbH & Co) and incubated overnight. The cells were washed with medium and incubated with 1 µM of compound in medium for one hr at 4°C and washed again with ice cold phosphate buffered saline (PBS). Confocal microscopy images were taken at 37°C on a Leica TCS-SP2-AOBS Live confocal microscope (Leica Microsystems Heidelberg GmbH).

Determination of dissociation constants by flow cytometry

MDAMB231^{CXCR4+} cells were trypsinized and aliquoted in portions of 300000 cells. For saturation binding experiments different concentrations of (Ac-TZ14011)₂-MSAP or (Ac-TZ14011)₄-MSAP ranging between 0 - 1000 nM in 50 µL of 0.1% bovine serum albumin (BSA) in PBS were added. For competition experiments different concentrations (0 -100,000 nM) of (Ac-TZ14011)₂ or (Ac-TZ14011)₄ in the presence of 250 nM of Ac-TZ14011-MSAP in 50 µL of 0.1% BSA in PBS were added. Cells were incubated for one hr at 4°C. The cells were washed (two times) with 300 µL of 0.1% BSA in PBS, resuspended in 300 µL of 0.1% BSA in PBS and fluorescence was measured using a CyAn ADP flow cytometer (DakoCytomation) with APC-Cy7 settings (635 nm laser and 750 nm long pass filter). Live cells were gated on Forward Scatter, Side Scatter and Pulse Width and 20000 viable cells were analyzed. All experiments were performed in duplicate.

The normalized geometric means were fitted with equations in the GraphPad Prism 5 software. The K_D values of (Ac-TZ14011)₂-MSAP and (Ac-TZ14011)₄-MSAP were calculated using the 'Binding – Saturation, One site – Total' nonlinear regression equation (Eq. 1). The K_D values of (Ac-TZ14011)₂ and (Ac-TZ14011)₄ were calculated using the 'Binding - Competitive, One site – Fit K_i' ' nonlinear regression equation (Eq. 2 and 3). The K_D values of Ac-TZ14011-MSAP (186.9 nM) and Ac-TZ14011 (8.61 nM) have previously been reported.¹⁰

$$y = \frac{B_{\max} * x}{K_D + x} + NS * x + Background \quad (\text{Eq. 1})$$

y	= normalized fluorescence
B_{\max}	= maximum specific binding in the units of the y axis
x	= concentration of Ac-TZ14011-MSAP or Ac-TZ14011-MSAP-In in nM
K_D	= equilibrium dissociation constant of Ac-TZ14011-MSAP or Ac-TZ14011-MSAP-In in nM
NS	= slope of nonspecific binding
Background	= amount of normalized fluorescence with no added compound

$$\log IC_{50} = \log(10^{\log K_D} * (1 + \frac{[Ac - TZ14011 - MSAP]}{K_{D, Ac - TZ14011 - MSAP}})) \quad (\text{Eq. 2})$$

$$y = Bottom + \frac{Top - Bottom}{1 + 10^{(x - \log IC_{50})}} \quad (\text{Eq. 3})$$

IC_{50}	= concentration of competitor that results in binding half-way between Bottom and Top
K_D	= equilibrium dissociation constant of the competitor in nM
[Ac-TZ14011-MSAP]	= concentration of Ac-TZ14011-MSAP (250 nM)
$K_{D, Ac-TZ14011-MSAP}$	= dissociation constant of Ac-TZ14011-MSAP (186.9 nM)
y	= normalized fluorescence
Bottom and Top	= plateaus in the units of the y-axis

Cell viability analysis

Cell viability, based on the percentage of gated cells, was assessed using the flow cytometry data obtained from the saturation binding and competition experiments. For compounds Ac-TZ14011-MSAP, (Ac-TZ14011)₂-MSAP and (Ac-TZ14011)₄-MSAP the percentage of gated cells when no compound was added was defined as 100% and the percentage of gated cells for the different concentrations of Ac-TZ14011-MSAP, (Ac-TZ14011)₂-MSAP and (Ac-TZ14011)₄-MSAP was calculated with respect to this. For compounds Ac-TZ14011, (Ac-TZ14011)₂ and (Ac-TZ14011)₄ the percentage of gated cells when only 250 nM of Ac-TZ14011-MSAP was added was defined as 100% and the percentage of gated cells for the different concentrations of Ac-TZ14011, (Ac-TZ14011)₂, (Ac-TZ14011)₄ was calculated in accordance.

In vivo model

For generation of the CXCR4-positive mouse tumor lesions, FVB mice (n = 3 for each compound; 3 - 4 weeks of age) were used. Before MIN-O lesion segment transplantation (and imaging), mice were anaesthetized using a hypnorm (VetaPharma Ltd)/dormicum (Midazolam; Roche)/water solution (1:1:2; 5 µL/g i.p.). Via a small incision, the inguinal lymph node was excised, whereafter a piece of preinvasive 8w-B MIN-O tissue was placed into the remaining tissue of the 4th mammary gland.²³⁻²⁵ Approximately 6-8 weeks after transplantation, lesions were deemed suitable for further experiments (0.8 - 1 cm in diameter). All animal experiments were performed in accordance with Dutch welfare regulations and approved by the local ethics committee.

Radiolabeling

Compounds Ac-TZ14011-MSAP, (Ac-TZ14011)₂-MSAP and (Ac-TZ14011)₄-MSAP were dissolved in 0.1 M of acetic acid (50 µg/100 µL) and InCl₃ (10 MBq/50 µg of compound; Covidien-Mallinkrodt) was added. After 30 min of incubation, the labeling was validated with TLC using 74 mM of sodium citrate (pH 5) as an eluent and a VCS-201 TLC scanner (Veenstra Instruments). In all cases, labeling efficacy was >99%. Before injection, the solution was diluted (1:1) with saline (0.90% w/v of NaCl in water).

Single photon emission computed tomography/computed tomography (SPECT/CT)

24 Hrs after intravenously injection of 50 µg of ¹¹¹In-labeled compound (10 MBq), the mice were placed in a temperature controlled (37°C) animal holder (Equipment Veterinaire MINERVE) before performing a SPECT/CT scan on the nanoSPECT/CT (Bioscan Inc.). The region of interest (ROI) incorporating the whole body was selected based on a (sagittal) tomographic planning X-ray image followed by a helical 3D CT. After ROI selection, a sequential total body SPECT scan of the same field of view was performed. After acquisition, the data was reconstructed with HiSPECT software (Scivis GmbH). The SPECT and CT data sets were automatically co-registered. The images were analyzed using the InVivoScope post processing software (Bioscan Inc.).

Distribution

After SPECT/CT imaging, tissues were excised and weighed. The amount of radioactivity present in the tissues was counted using a Perkin Elmer 1480 Wizard 3^o automatic gamma counter (245 keV; 60 sec). Counts per minute were converted into MBq

and corrected for decay. The percentage of the injected dose per gram of tissue (%ID/g) was calculated as followed: ((MBq measured in tissue/ injected dose) *100%)/weight of tissue. P values were calculated using an unpaired t test (GraphPad).

Results

Design and synthesis

In order to minimize the negative influence of the hybrid MSAP label on the receptor affinity of the CXCR4 targeting peptide Ac-TZ14011, dimeric and tetrameric dendrimers were prepared, where the MSAP label was placed in the core of the dendrimer (Figure 1). Additional β -alanine spacers were incorporated to ensure that the peptide epitopes would not hinder the CXCR4 binding of the other peptides. The design of the multimeric compounds was verified by inserting the respective models of Figure 1 into the crystal structure of CXCR4 using the modeling program Yasara.²⁶ The modeling data suggested that the spacers were long enough to avoid steric hindrance (see the Appendix of this Chapter). The synthesis of the dendrimers is outlined in the Appendix of this Chapter (Scheme A1).

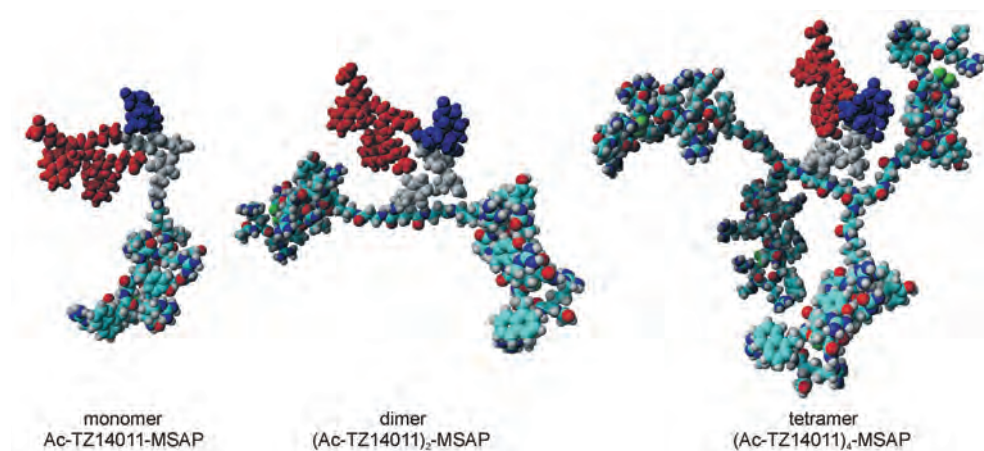


Figure 1. Molecular models of the mono-, di- and tetrameric Ac-TZ14011 dendrimers with the MSAP label. For clarity, the MSAP label is not colored by element: the CyAL-5.5₆ fluorophore is displayed in red, the indium-bound DTPA chelate in blue and the spacer in grey. In the dimer and, especially, in the tetramer a smaller percentage of the whole molecule comprises the MSAP label.

In vitro evaluation

The CXCR4 receptor affinity of the unlabeled constructs was determined using a previously reported cell-based competition assay, where the unlabeled peptides compete with monomer Ac-TZ14011-MSAP for binding to the CXCR4 receptor on MDAMB231^{CXCR4+} cells (Figure 2A).⁷ The dissociation constant (K_D) of the monomer Ac-TZ14011 has previously been reported to be 8.61 nM (Table 1).⁷ The receptor affinity of both dimer (Ac-TZ14011)₂ and tetramer (Ac-TZ14011)₄ was found to be somewhat lower; 23.5 nM and 30.6 nM, respectively. A multivalency effect based on e.g. bivalent binding or statistical rebinding was not observed, but rather a slight decrease in affinity (Table 1).

Table 1. Dissociation constants (K_D) of the Ac-TZ14011 derivatives.

	Unlabeled derivatives		MSAP-labeled derivatives	
	compound	K_D (nM)	compound	K_D (nM)
monomers	Ac-TZ14011	8.61 ± 1.42	Ac-TZ14011-MSAP	186.9 ± 52.4
dimers	(Ac-TZ14011) ₂	23.5 ± 2.43	(Ac-TZ14011) ₂ -MSAP	93.1 ± 10.1
tetramers	(Ac-TZ14011) ₄	30.6 ± 4.84	(Ac-TZ14011) ₄ -MSAP	80.5 ± 11.6

The receptor affinity of the MSAP-labeled constructs Ac-TZ14011-MSAP, (Ac-TZ14011)₂-MSAP and (Ac-TZ14011)₄-MSAP was determined using saturation binding experiments (Figure 2B). The affinity of the monomer Ac-TZ14011-MSAP amounts to 186.9 nM.⁷ Interestingly, the dimer (Ac-TZ14011)₂-MSAP had a two-fold higher affinity (93.1 nM). This clear effect is in contrast with the trend found for the unlabeled peptide derivatives; the unlabeled dimer (Ac-TZ14011)₂ had an almost three-fold decrease in affinity compared to the monomer Ac-TZ14011 (Table 1). For the tetramer (Ac-TZ14011)₄-MSAP (K_D = 80.5 nM) the improvement with respect to dimer (Ac-TZ14011)₂-MSAP was minimal. However, the saturation binding curve showed that the nonspecific cell binding was considerably reduced for the tetramer (Ac-TZ14011)₄-MSAP, i.e. the linear part of the curve is less steep than that Ac-TZ14011-MSAP (Figure 2B and Eq 1). This suggests that the peptides in the tetramer indeed shield the MSAP label from nonspecific cell membrane binding, as was designed.

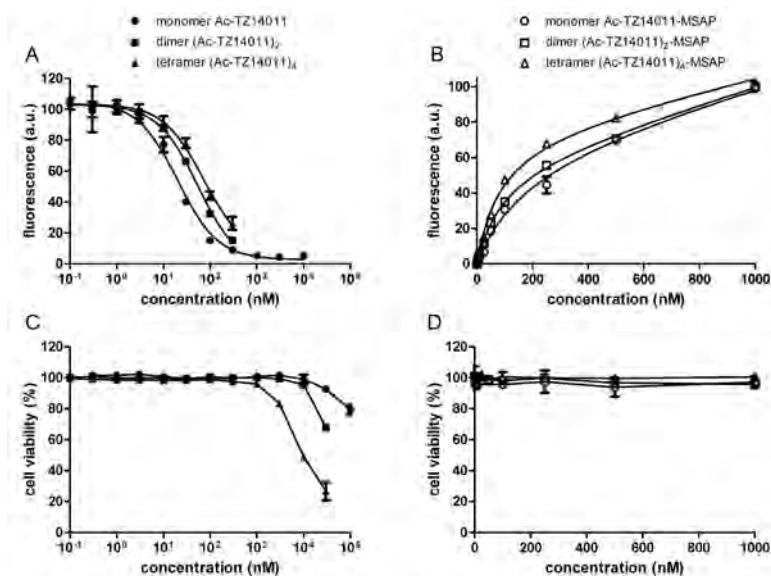


Figure 2. A) Competition experiments of Ac-TZ14011, (Ac-TZ14011)₂ and (Ac-TZ14011)₄ in the presence of 250 nM of Ac-TZ14011-MSAP. B) Saturation binding experiments of Ac-TZ14011-MSAP, (Ac-TZ14011)₂-MSAP and (Ac-TZ14011)₄-MSAP. C and D) Cell viability of MDAMB231^{CXCR4+} cells in the presence of different concentrations of Ac-TZ14011, (Ac-TZ14011)₂ and (Ac-TZ14011)₄. C) and Ac-TZ14011-MSAP, (Ac-TZ14011)₂-MSAP and D) (Ac-TZ14011)₄-MSAP. For all graphs the bars represent average \pm SD.

Next to the CXCR4 affinity studies with flow cytometry, the cellular distribution of Ac-TZ14011-MSAP, (Ac-TZ14011)₂-MSAP and (Ac-TZ14011)₄-MSAP was evaluated using confocal microscopy. MDAMB231^{CXCR4+} cells were incubated with 1 μ M of compound for one hr at 4°C, to minimize active internalization. All three peptide conjugates displayed membranous staining (Figure 3), which is in accordance with the location of the CXCR4 receptor.^{7,27-29} Also a small amount of internalization Ac-TZ14011-MSAP, (Ac-TZ14011)₂-MSAP and (Ac-TZ14011)₄-MSAP observed. This internalization was most likely caused by the fact that the confocal imaging was performed at 37°C, resulting in some receptor mediated endocytosis during the image acquisition. As a negative control, cells were incubated with the MSAP label alone, as the latter showed almost no staining (Figure 3D). Hence the cell membrane staining pattern of compounds Ac-TZ14011-MSAP, (Ac-TZ14011)₂-MSAP and (Ac-TZ14011)₄-MSAP is driven by the targeting peptide moieties and is not caused by nonspecific binding of the MSAP label.

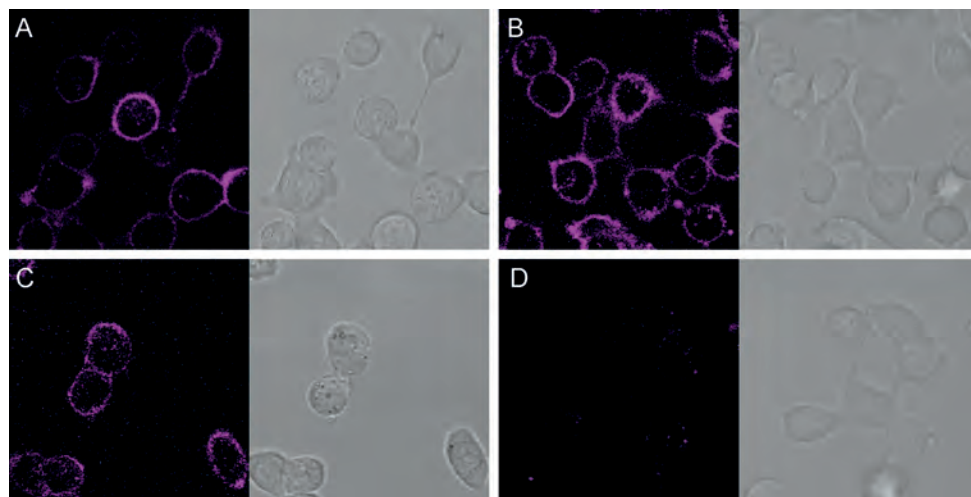


Figure 3. Confocal microscopy and transmission images of the hybrid peptide conjugates on MDAMB231^{CXCR4+} cells. A) 1 μM of monomer Ac-TZ14011-MSAP; B) 1 μM of dimer (Ac-TZ14011)₂-MSAP; C) 1 μM of tetramer (Ac-TZ14011)₄-MSAP; D) 1 μM of MSAP label.

The effect of the monomers Ac-TZ14011 and Ac-TZ1401-MSAP, dimers (Ac-TZ14011)₂ and (Ac-TZ14011)₂-MSAP and tetramers (Ac-TZ14011)₄ and (Ac-TZ14011)₄-MSAP on the cell viability during the K_D determination was measured (Figure 2C-D); reduced cell viability may increase nonspecific binding and/or uptake. None of the six compounds influenced cell viability up to concentrations of 1 μM . The tetramer (Ac-TZ14011)₄ displayed toxic effects ($IC_{50} = 13.0 \mu\text{M} \pm 0.29$) at lower concentrations compared to the dimer (Ac-TZ14011)₂ ($IC_{50} = 88.9 \mu\text{M} \pm 8.77$) and the monomer Ac-TZ14011 ($IC_{50} = 1912 \mu\text{M} \pm 285$) (Figure 2C).

In vivo evaluation

In vivo imaging studies were performed to evaluate the tumor targeting ability of Ac-TZ14011-MSAP, (Ac-TZ14011)₂-MSAP and (Ac-TZ14011)₄-MSAP at 24 hrs after injection of ¹¹¹In-labeled compounds (Figure 4).

All three compounds enabled visualization of the tumor lesions. Biodistribution of the dendrimers was compared to the distribution of Ac-TZ14011-DTPA, containing only a DTPA chelate as an imaging label.³⁰ As a negative control, the MSAP label was used without further functionalization (reactive group was neutralized).

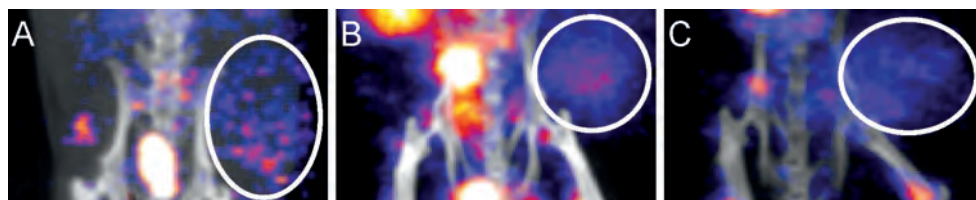


Figure 4. SPECT/CT of A) monomer Ac-TZ14011-MSAP, B) dimer (Ac-TZ14011)₂-MSAP and C) tetramer (Ac-TZ14011)₄-MSAP.

Table 2. Distribution of ¹¹¹In-labeled Ac-TZ14011-DTPA, MSAP label, monomer Ac-TZ14011-MSAP, dimer (Ac-TZ14011)₂-MSAP and tetramer (Ac-TZ14011)₄-MSAP in MIN-O tumor bearing mice at 24 hrs post injecting.

Uptake (%ID/g)					
tissue	Ac-TZ14011-DTPA	MSAP	monomer Ac-TZ14011-MSAP	dimer (Ac-TZ14011) ₂ -MSAP	tetramer (Ac-TZ14011) ₄ -MSAP
Blood	0.01 ± 0.00	0.32 ± 0.09**	0.14 ± 0.02***	0.14 ± 0.03**	0.11 ± 0.01***
Brain	0.00 ± 0.00	0.03 ± 0.01	0.02 ± 0.00	0.03 ± 0.01	0.02 ± 0.00
Lungs	0.13 ± 0.02	0.65 ± 0.18**	1.02 ± 0.13***	2.13 ± 0.60**	1.68 ± 0.31**
Heart	0.05 ± 0.00	0.64 ± 0.12**	0.89 ± 0.22**	0.60 ± 0.12**	0.43 ± 0.06***
Liver	5.08 ± 0.52	5.76 ± 1.11	22.46 ± 5.46**	30.59 ± 5.45**	22.43 ± 0.67***
Kidneys	27.07 ± 0.74	6.49 ± 2.99***	7.50 ± 1.39***	6.46 ± 1.36***	4.37 ± 0.52***
Spleen	1.14 ± 0.32	0.93 ± 0.13	4.76 ± 1.23**	7.01 ± 1.45**	4.66 ± 0.46***
Stomach	0.06 ± 0.01	0.81 ± 0.45*	0.81 ± 0.16**	0.97 ± 0.52*	1.09 ± 0.52*
Intestines	0.10 ± 0.01	1.02 ± 0.31**	1.85 ± 0.08***	2.06 ± 0.26***	1.56 ± 0.46**
Tumor	0.19 ± 0.03	n.d.	1.10 ± 0.60	0.57 ± 0.19*	0.42 ± 0.10*
Muscle (paw)	0.03 ± 0.00	0.22 ± 0.06**	0.31 ± 0.01***	0.07 ± 0.03	0.08 ± 0.02*

The significance with respect to ¹¹¹In-labeled Ac-TZ14011-DTPA is indicated by the asterisks (* = P < 0.05, ** = P < 0.01, *** = P < 0.001). N.d. = not determined.

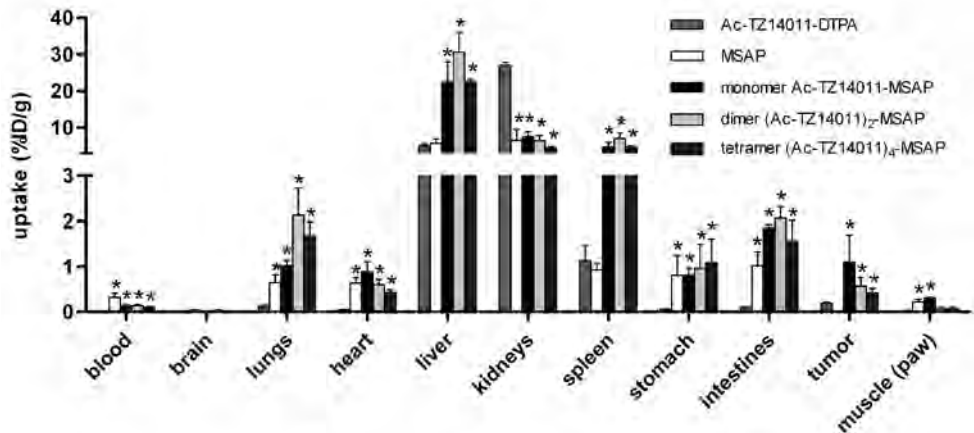


Figure 5. Distribution of ^{111}In -labeled Ac-TZ14011-DTPA, MSAP label, monomer Ac-TZ14011-MSAP, dimer (Ac-TZ14011)₂-MSAP and tetramer (Ac-TZ14011)₄-MSAP in MIN-O tumor-bearing mice at 24 hrs post injection. Significant differences ($P < 0.05$) with respect to ^{111}In -labeled Ac-TZ14011-DTPA are indicated by the asterisks. (* = $P < 0.05$).

Injection of the monomer Ac-TZ14011-MSAP resulted in an increase in liver and intestinal uptake and a reduction in kidney uptake compared to the reference Ac-TZ14011-DTPA, suggesting a change in the clearance route (Table 2, Figure 5). Tumor uptake of the monomer Ac-TZ14011-MSAP was more than five times higher than for Ac-TZ14011-DTPA. However, this increase was accompanied with higher nonspecific uptake in the lungs, heart, spleen, stomach, intestines and muscles, most likely caused by interactions with the relative hydrophobic CyAL-5.5_b fluorophore. Overall, this resulted in a lower tumor-to-muscle ratio compared to Ac-TZ14011-DTPA, 4.55 vs. 6.67, respectively (Table 3). The dimer (Ac-TZ14011)₂-MSAP had a similar uptake profile as the monomer (Table 2, Figure 5). However, the muscle uptake was significantly lower than that of the monomeric MSAP peptide ($P < 0.0001$). The tumor and heart uptake was lower than that of monomer Ac-TZ14011-MSAP, although this difference was not significant. The decrease of the uptake in the muscle and heart was larger than in the tumor, resulting in an improved tumor-to-muscle ratio of 7.41 (Table 3). This improvement was again not significant, as the standard deviation found for (Ac-TZ14011)₂-MSAP was rather high.

The same trend was seen for the tetramer (Ac-TZ14011)₄-MSAP (Table 2, Figure 5). The uptake in the tumor and in the heart was slightly lower than that of dimer (Ac-TZ14011)₂-MSAP, while uptake in muscle was not reduced further for the tetramer (Ac-TZ14011)₄-MSAP. As a consequence, the tumor-to-muscle ratio of the tetramer was lower than that of the dimer (5.47 vs. 7.41, respectively; Table 3).

Table 3. Tumor-to-muscle ratios derived from the biodistribution studies.

Compound	Tumor-to-muscle ratio	Relative ratio compared to compound Ac-TZ14011-DTPA
Ac-TZ14011-DTPA	6.67 ± 0.66	1
monomer Ac-TZ14011-MSAP	4.55 ± 0.68*	0.68
dimer (Ac-TZ14011) ₂ -MSAP	7.41 ± 1.87	1.11
tetramer (Ac-TZ14011) ₄ -MSAP	5.47 ± 0.50	0.82

* P < 0.05 for the comparison of compound Ac-TZ14011-MSAP with Ac-TZ14011-DTPA.

Discussion

The main goal of this study was to minimize the negative influence of the hybrid MSAP label on receptor binding and nonspecific binding *in vivo* by using multimeric structures.

It is challenging to design relatively small dendrimers that can position peptide-binding epitopes correctly for simultaneous binding to multiple G-protein coupled receptors (GPCRs). Previously reported iridium complexes outfitted with one, two or three Ac-TZ14011 peptides did not display a considerable multivalency effect.²⁷ Moreover, Tanaka et al. have shown that bivalent pentapeptidic CXCR4 ligands with spacers larger than 4.5 nm (15 proline residues) only display a modest increase in affinity of maximal 3.2-fold due to multivalent interactions.³¹ These findings are not uncommon for peptides binding to GPCRs, as multimeric octreotides also do not bind in a multivalent manner to the somatostatin GPCR.^{49,50}

However, the relatively short spacers that were used during the synthesis of the dimer (Ac-TZ14011)₂-MSAP and the tetramer (Ac-TZ14011)₄-MSAP did enable the shielding of the MSAP label from the biological environment by the peptides (Figure 1). As a consequence, the different peptide moieties on the dendrimers will not be able to bind multiple CXCR4 receptors simultaneously. Most likely this requires larger spacers of 5.5 – 6.5 nm.³¹ However, our design can increase the binding affinity via statistical rebinding,⁸⁻¹⁰ which is caused by an overall slower off-rate of the multimeric compound due to the close proximity of other CXCR4-binding peptide epitopes. As such, the bound peptide can be replaced by another peptide when released from the binding site.

The affinity of (Ac-TZ14011)₂-MSAP and (Ac-TZ14011)₄-MSAP was approximately two-fold higher compared to the affinity of the monomer. The increase in affinity of the

tetramer with respect to the dimer was minimal, but the saturation binding curve showed that the nonspecific cell binding was considerably reduced for the tetramer, i.e. the linear part of the curve was less steep than that of the monomer (Figure 2B). Combined this suggests that addition of a peptide moiety reduces the negative influence of the MSAP label on the receptor affinity and that the peptides in the tetramer indeed increase the shielding of the MSAP label.

The increasing multimeric character of the Ac-TZ14011 peptide seemed to lead to more cytotoxicity. Increasing the positive charge from +6 in the monomeric Ac-TZ14011-MSAP, to +11 in the dimeric (Ac-TZ14011)₂-MSAP and +21 in the tetrameric (Ac-TZ14011)₄-MSAP may result in charge-driven (nonspecific) membranous binding and cause cytotoxicity, similar to that reported for positively charged PAMAM dendrimers.^{27,34}

In vivo, an increase in nonspecific binding and a reduction in tumor-to-muscle ratio is a common effect when using monomeric hybrid labeled peptides.¹ This is most likely caused by the relative large size of the (hybrid) imaging label. Addition of a peptide moiety in (Ac-TZ14011)₂-MSAP clearly reduced nonspecific muscle uptake of monomer Ac-TZ14011-MSAP compared to Ac-TZ14011-DTPA. While the uptake profile of both the monomer Ac-TZ14011-MSAP and the dimer (Ac-TZ14011)₂-MSAP were similar (Table 2 and Figure 5), the muscle uptake was significantly lower than that of the monomeric MSAP peptide ($P < 0.001$). Lower uptake levels in the muscle and heart resulted in an improved tumor-to-muscle ratio for the dimer (Ac-TZ14011)₂-MSAP (Table 3). Unfortunately, this improvement was not significant, as the standard deviation was rather high (Table 3).

Nonspecific uptake of tetramer (Ac-TZ14011)₄-MSAP in organs such as the lungs, heart and liver was slightly lower compared to the dimer (Ac-TZ14011)₂-MSAP. The two additional peptides decreased the MSAP label driven nonspecific uptake even further and increased overall clearance from the body. Faster clearance is generally accompanied with reduced blood concentrations, and therefore, reduced the amount of compound available for receptor binding in the tumor. This effect appeared to have overruled the higher CXCR4 affinity of tetramer (Ac-TZ14011)₄-MSAP compared to dimer (Ac-TZ14011)₂-MSAP resulting in a slightly reduced uptake in the tumor.

Based on the in vitro experiments the dimer (Ac-TZ14011)₂-MSAP provides the most promising imaging agent as it practically has the same high affinity for CXCR4 as the tetramer (Ac-TZ14011)₄-MSAP, has considerable less influence on the cell viability and is easier to prepare than the tetravalent derivative (Ac-TZ14011)₄-MSAP.

From the results of the in vivo studies a comparable conclusion can be drawn as the

additional peptide in dimer (Ac-TZ14011)₂-MSAP reduced the negative influence of the hybrid MSAP label in monomer (Ac-TZ14011)-MSAP, yielding a tumor-to-muscle ratio higher than that of monomer (Ac-TZ14011)-MSAP, and even than Ac-TZ14011-DTPA. The addition of two more peptides, as in tetramer (Ac-TZ14011)₄-MSAP, however, did not result in a further improvement of the tumor-to-muscle ratio.

Conclusion

Multimerization resulted in reduction of the nonspecific binding caused by the hybrid label. The dimer, however, has less influence on the cell viability and the tumor-to-muscle ratio of the dimer is higher. Thus, dimer (Ac-TZ14011)₂-MSAP is the most promising CXCR4 imaging probe.

The concept of multimerization of hybrid peptides can also be applied to other targeting peptides. It seems that the use of highly positively charged peptides and highly hydrophobic peptides should be avoided to suppress the cytotoxicity and the nonspecific cell and tissue binding.

References

- 1 Kuil J, Velders AH, van Leeuwen FWB. Multimodal tumor-targeting peptides functionalized with both a radio- and a fluorescent-label. *Bioconjugate Chem.* 2010; 21: 1709-1719
- 2 Louie A. Multimodality imaging probes: design and challenges. *Chem Rev.* 2010; 110: 3146-3195
- 3 Thorp-Greenwood FL, Coogan MP. Multimodal radio- (PET/SPECT) and fluorescence imaging agents based on metallo-radioisotopes: current applications and prospects for development of new agents. *Dalton Trans.* 2011; 40: 6129-6143
- 4 Culver J, Akers W, Achilefu S. Multimodality molecular imaging with combined optical and SPECT/PET modalities. *J Nucl Med.* 2008; 49: 169-172
- 5 Lee S, Chen X. Dual-modality probes for in vivo molecular imaging. *Mol Imaging.* 2009; 8: 87-100
- 6 Buckle T, Chin PTK, van Leeuwen FWB. (Non-targeted) radioactive/fluorescent nanoparticles and their potential in combined pre- and intraoperative imaging during sentinel lymph node resection. *Nanotechnology.* 2010; 21: 482001
- 7 Kuil J, Buckle T, Yuan H, van den Berg NS, Oishi S, Fujii N, Josephson L, van Leeuwen FWB. Synthesis and evaluation of a bimodal CXCR4 antagonistic peptide. *Bioconjugate Chem.* 2011; 22: 859-864
- 8 Kiessling LL, Gestwicki JE, Strong LE. Synthetic multivalent ligands as probes of signal transduction. *Angew Chem Int Ed.* 2006; 45: 2348-2368
- 9 Pieters RJ. Maximising multivalency effects in protein-carbohydrate interactions. *Org Biomol Chem.* 2009; 7: 2013-2025
- 10 Kuil J, Branderhorst HM, Pieters RJ, de Mol NJ, Liskamp RMJ. ITAM-derived phosphopeptide-containing dendrimers as multivalent ligands for Syk tandem SH2 domain. *Org Biomol Chem.* 2009; 7: 4088-4094
- 11 Mammen M, Choi SK, Whitesides GM. Polyvalent interactions in biological systems: implications for design and use of multivalent ligands and inhibitors. *Angew Chem Int Ed.* 1998; 37: 2754-2794
- 12 Lundquist JJ, Toone EJ. The cluster glycoside effect. *Chem Rev.* 2002; 102: 555-578
- 13 Kitov PI, Bundle DR. On the nature of the multivalency effect: a thermodynamic model. *J Am Chem Soc.* 2003; 125: 16271-16284
- 14 Reczek JJ, Kennedy AA, Halbert BT, Urbach AR. Multivalent recognition of peptides by modular self-assembled receptors. *J Am Chem Soc.* 2009; 131: 2408-2415

- 15 Cheng Z, Wu Y, Xiong Z, Gambhir SS, Chen X. Near-infrared fluorescent RGD peptides for optical imaging of integrin $\alpha_v\beta_3$ expression in living mice. *Bioconjugate Chem.* 2005; 16: 1433-1441
- 16 Liu, S., Radiolabeled cyclic RGD peptides as integrin $\alpha_v\beta_3$ -targeted radiotracers: maximizing binding affinity via bivalency. *Bioconjugate Chem.* 2009; 20: 2199-2213
- 17 Almutairi A, Rossin R, Shokeen M, Hagooley A, Ananth A, Capoccia B, Guillaudeau S, Abendschein D, Anderson CJ, Welch MJ, Frechet JM. Biodegradable dendritic positron-emitting nanoprobe for the noninvasive imaging of angiogenesis. *Proc Natl Acad Sci USA.* 2009; 106: 685-690
- 18 Galibert M, Sancey L, Renaudet O, Coll JL, Dumy P, Boturyn D. Application of click-click chemistry to the synthesis of new multivalent RGD conjugates. *Org Biomol Chem.* 2010; 8: 5133-5138
- 19 Abiraj K, Jaccard H, Kretschmar M, Helm L, Maecke HR. Novel DOTA-based prochelator for divalent peptide vectorization: synthesis of dimeric bombesin analogues for multimodality tumor imaging and therapy. *Chem Commun.* 2008; 3248-3250
- 20 Cai W, Chen K, Li ZB, Gambhir SS, Chen X. Dual-function probe for PET and near-infrared fluorescence imaging of tumor vasculature. *J Nucl Med.* 2007; 48: 1862-1870
- 21 Boswell CA, Eck PK, Regino CA, Bernardo M, Wong KJ, Milenic DE, Choyke PL, Brechbiel MW. Synthesis, characterization, and biological evaluation of integrin $\alpha_v\beta_3$ -targeted PAMAM dendrimers. *Mol Pharm.* 2008; 5: 527-539
- 22 Iyer AK, Khaled G, Fang J, Maeda H. Exploiting the enhanced permeability and retention effect for tumor targeting. *Drug Discov Today.* 2006; 11: 812-818
- 23 Maglione JE, McGoldrick ET, Young LJ, Namba R, Gregg JP, Liu L, Moghanaki D, Ellies LG, Borowsky AD, Cardiff RD, MacLeod CL. Polyomavirus middle T-induced mammary intraepithelial neoplasia outgrowths: single origin, divergent evolution, and multiple outcomes. *Mol. Cancer Ther.* 2004; 3: 941-953
- 24 Namba R, Young LJ, Maglione JE, McGoldrick ET, Liu S, Wurz GT, DeGregorio MW, Borowsky AD, MacLeod CL, Cardiff RD, Gregg JP. Selective estrogen receptor modulators inhibit growth and progression of premalignant lesions in a mouse model of ductal carcinoma in situ. *Breast Cancer Res.* 2005; 7: R881-889
- 25 Namba R, Young LJ, Abbey CK, Kim L, Damonte P, Borowsky AD, Qi J, Tepper CG, MacLeod CL, Cardiff RD, Gregg JP. Rapamycin inhibits growth of premalignant and malignant mammary lesions in a mouse model of ductal carcinoma in situ. *Clin Cancer Res.* 2006; 12: 2613-2621

- 26 Wu B, Chien EYT, Mol CD, Fenalti G, Liu W, Katritch V, Abagyan R, Brooun A, Wells P, Bi FC, Hamel DJ, Kuhn P, Handel TM, Cherezov V, Stevens RC. Structures of the CXCR4 chemokine GPCR with small-molecule and cyclic peptide antagonists. *Science*. 2010; 330: 1066-1071
- 27 Kuil J, Steunenberg P, Chin PTK, Oldenburg J, Jalink K, Velders AH, van Leeuwen FWB. Peptide-functionalized luminescent iridium complexes for lifetime imaging of CXCR4 expression. *ChemBioChem*. 2011; 12: 1897-1903
- 28 Nomura W, Tanabe Y, Tsutsumi H, Tanaka T, Ohba K, Yamamoto N, Tamamura H. Fluorophore labeling enables imaging and evaluation of specific CXCR4-ligand interaction at the cell membrane for fluorescence-based screening. *Bioconjugate Chem*. 2008; 19: 1917-1920
- 29 Oishi S, Masuda R, Evans B, Ueda S, Goto Y, Ohno H, Hirasawa A, Tsujimoto G, Wang Z, Peiper SC, Naito T, Kodama E, Matsuoka M, Fujii N. Synthesis and application of fluorescein- and biotin-labeled molecular probes for the chemokine receptor CXCR4. *ChemBioChem*. 2008; 9: 1154-1158
- 30 Hanaoka H, Mukai T, Tamamura H, Mori T, Ishino S, Ogawa K, Iida Y, Doi R, Fujii N, Saji H. Development of a ¹¹¹In-labeled peptide derivative targeting a chemokine receptor, CXCR4, for imaging tumors. *Nucl Med Biol*. 2006; 33: 489-494
- 31 Tanaka T, Nomura W, Narumi T, Masuda A, Tamamura H. Bivalent ligands of CXCR4 with rigid linkers for elucidation of the dimerization state in cells. *J Am Chem Soc*. 2010; 132: 15899-15901
- 32 Yim CB, Boerman OC, de Visser M, de Jong M, Dechesne AC, Rijkers DTS, Liskamp RMJ. Versatile conjugation of octreotide to dendrimers by cycloaddition ("click") chemistry to yield high-affinity multivalent cyclic peptide dendrimers. *Bioconjugate Chem*. 2009; 20: 1323-1331
- 33 Yim CB, Dijkgraaf I, Merckx R, Versluis C, Eek A, Mulder GE, Rijkers DTS, Boerman OC, Liskamp RMJ. Synthesis of DOTA-conjugated multimeric [Tyr³]octreotide peptides via a combination of Cu(I)-catalyzed "click" cycloaddition and thio acid/sulfonyl azide "sulfo-click" amidation and their in vivo evaluation. *J Med Chem*. 2010; 53: 3944-3953
- 34 Albertazzi L, Serresi M, Albanese A, Beltram F. Dendrimer internalization and intracellular trafficking in living cells. *Mol Pharm*. 2010; 7: 680-688

Appendix Chapter 12

General

All chemicals were obtained from commercial sources and used without further purification. The reactions were monitored by thin layer chromatography (TLC). NMR spectra were taken using a Bruker Ultrashield 300 spectrometer (300 MHz ^1H NMR, 75 MHz ^{13}C NMR) and the chemical shifts are given in ppm (δ) relative to tetramethylsilane (TMS). Abbreviations used include singlet (s), doublet (d), doublet of doublets (dd) and unresolved multiplet (m). MS (ESI) spectra were measured on a Waters LCTTM Orthogonal Acceleration Time of Flight Mass Spectrometer equipped with a Waters 2795 Separation Module (Alliance HT) and a Waters 2996 Photodiode Array Detector (190 - 750 nm). HPLC was performed on a Waters HPLC system using a 1525EF pump and a 2489 UV detector. For preparative HPLC a Dr. Maisch GmbH Reprosil-Pur 120 C18-AQ 10 μm (250 x 20 mm) column was used and a gradient of 0.1% TFA in $\text{H}_2\text{O}/\text{CH}_3\text{CN}$ 9:1 to 0.1% TFA in $\text{H}_2\text{O}/\text{CH}_3\text{CN}$ 1:9 in 40 min (12 mL/min) was employed. For analytical HPLC a Dr. Maisch GmbH Reprosil-Pur C18-AQ 5 μm (250 x 4.6 mm) column was used and a gradient of 0.1% TFA in $\text{H}_2\text{O}/\text{CH}_3\text{CN}$ 95:5 to 0.1% TFA in $\text{H}_2\text{O}/\text{CH}_3\text{CN}$ 5:95 in 20 min (1 mL/min) was employed.

MSAP reagent

The multifunctional single attachment point (MSAP) reagent was synthesized based on previously described procedures.¹

Ac-TZ14011 was synthesized according to previously described procedures.²

Ac-TZ14011-MSAP

Ac-TZ14011-MSAP was synthesized according to previously described procedures.¹ For use in confocal imaging, the active NHS ester of the MSAP label was hydrolyzed prior to the incubation: 150 μg of MSAP was dissolved in 29 μL of EtOH, 262 μL of H_2O and 2.5 μL of 4 M NaOH. After one hr stirring at 20°C, 3 μL of AcOH was added to neutralize the solution. This stock solution was further diluted in medium.

Ac-TZ14011-DTPA

Ac-TZ14011-DTPA (Figure A1) was synthesized according to previously described procedures.²

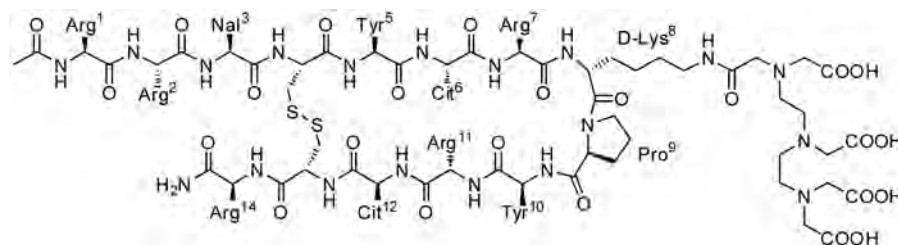


Figure A1. Structure of Ac-TZ14011-DTPA

Boc-Glu(β -Ala-OH)- β -Ala-OH

Boc-Glu-OH (9.10 g, 36.8 mmol), β -alanine methyl ester hydrochloride (14.0 g, 100 mmol) and N-hydroxysuccinimide (8.60 g, 75 mmol) were dissolved in 500 mL of DMF. DiPEA (17.4 mL, 100 mmol) was added and the solution was cooled to 0°C. DCC (15.5 g, 75 mmol) was added and the mixture was stirred overnight at 20°C. DMF was evaporated and H₂O was added. The aqueous phase was extracted with EtOAc (three times). The combined organic phases were washed with 0.1 M Na₂CO₃ (three times), 5% citric acid (three times) and brine, dried with MgSO₄, filtered and concentrated affording 9.8 g (23.5 mmol, 64%) of Boc-Glu(β -Ala-OMe)- β -Ala-OMe. The product was used without further purification.

Boc-Glu(β -Ala-OMe)- β -Ala-OMe (1.47 g, 10 mmol) was dissolved in 105 mL of dioxane and 37.5 mL of MeOH. 7.5 mL of 4 M NaOH (30 mmol) was added and the solution was stirred for one hr at 20°C. The volatiles were evaporated and H₂O was added. The aqueous phase was washed with EtOAc (two times), acidified with citric acid and extracted with EtOAc (five times). The combined organic phases were washed with 5% citric acid and brine, dried with MgSO₄, filtered and concentrated. The product was purified by silica gel column chromatography (1% AcOH in CH₂Cl₂/MeOH 93:7) yielding 2.79 g (72%) of a Boc-Glu(β -Ala-OH)- β -Ala-OH as a white solid. ¹H NMR (DMSO-d₆, 300 MHz) δ = 1.37 (s, 9H, 3

CH₃), 2.03-2.07 (m, 2H, Glu β CH₂), 2.33-2.39 (m, 4H, Glu δ CH₂ and CH₂COOH), 2.62 (d, 2H, CH₂COOH), 3.18-3.28 (m, 4H, 2 CH₂CH₂COOH), 3.82 (dd, 1H, Glu α CH), 6.79 (d, 1H, NH Boc), 7.79-7.86 (m, 2H, 2 β-Ala NH). ¹³C NMR (DMSO-d₆, 75 MHz) δ = 28.0 (Glu β CH₂), 28.1 (3 CH₃), 31.2 (Glu δ CH₂), 33.8, 33.9, 34.7, 34.7 (4 β-Ala CH₂), 71.8 (Glu α CH), 78.0 (Boc C), 155.1 (Boc CO), 171.2, 171.6 (2 amide CONH), 172.8 (2 COOH).

Boc-protected dimer (Ac-TZ14011)₂

Boc-Glu(β-Ala-OH)-β-Ala-OH (1.95 mg, 5 μmol), Ac-TZ14011 (35 mg, 12.5 μmol) and BOP (5.53 mg, 12.5 μmol) were dissolved in 2 mL of DMSO. DiPEA (17 μL, 100 μmol) was added and the mixture was stirred overnight at 20°C, after which the mixture was purified by preparative HPLC. The product was obtained as a white fluffy solid (16.5 mg, 58%) after pooling of the appropriate fractions and lyophilization. MS (ESI): [M+3H]³⁺ calculated 1522.78, found 1522.45; [M+4H]⁴⁺ calculated 1142.34, found 1142.06; [M+5H]⁵⁺ calculated 914.07, found 914.08; [M+6H]⁶⁺ calculated 761.89, found 761.71.

Dimer (Ac-TZ14011)₂

Boc-protected dimer (Ac-TZ14011)₂ (4.68 mg, 0.844 μmol) was dissolved in H₂O (100 μL) and TFA (2 mL) and the solution was stirred for three hrs at 20°C. TFA was evaporated and the product was lyophilized from CH₃CN/H₂O yielding the product in quantitative yield as a white fluffy solid. MS (ESI): [M+4H]⁴⁺ calculated 1117.32, found 1117.56; [M+5H]⁵⁺ calculated 894.06, found 894.25; [M+6H]⁶⁺ calculated 745.22, found 745.39; [M+7H]⁷⁺ calculated 638.90, found 639.06.

Dimer (Ac-TZ14011)₂-MSAP

Dimer (Ac-TZ14011)₂ (2.27 mg, 0.397 μmol) and MSAP (1.34 mg, 0.793 μmol) were dissolved in 800 μL of DMSO. DiPEA (2.6 μL, 15 μmol) was added and the solution was stirred overnight at 20°C, after which the mixture was purified by preparative HPLC. The product was obtained as a blue fluffy solid (1.97 mg, 69%) after pooling of the appropriate fractions and lyophilization. MS (ESI): [M+6H]⁶⁺ calculated 1006.82, found 1006.67; [M+7H]⁷⁺ calculated 863.13, found 863.19; [M+8H]⁸⁺ calculated 755.36, found 755.30.

Boc-protected tetramer (Ac-TZ14011)₄

Boc-protected dimer (Ac-TZ14011)₂ (11.42 mg, 1.46 μmol) was dissolved in H₂O (200

μL) and TFA (2.8 mL) and the solution was stirred for 3 hrs at 20 °C. TFA was evaporated and the residue was dissolved in 1 mL of DMSO. DiPEA (5 μL , 29 μmol), Boc-Glu(β -Ala-OH)- β -Ala-OH (0.19 mg, 0.50 μmol) and BOP (0.66 mg, 1.5 μmol) were added and the solution was stirred overnight at 20°C, after which the mixture was purified by preparative HPLC. The product was obtained as a white fluffy solid (2.61 mg, 45%) after pooling of the appropriate fractions and lyophilization. MS (ESI): $[\text{M}+8\text{H}]^{8+}$ calculated 1161.47, found 1161.76; $[\text{M}+9\text{H}]^{9+}$ calculated 1032.53, found 1032.73; $[\text{M}+10\text{H}]^{10+}$ calculated 929.37, found 929.87; $[\text{M}+11\text{H}]^{11+}$ calculated 844.98, found 845.05; $[\text{M}+12\text{H}]^{12+}$ calculated 774.65, found 774.64.

Tetramer (Ac-TZ14011)₂

Boc-protected tetramer (Ac-TZ14011)₄ (2.61 mg, 0.23 μmol) was dissolved in H₂O (100 μL) and TFA (2 mL) and the solution was stirred for three hrs at 20°C. TFA was evaporated and the product was lyophilized from CH₃CN/H₂O yielding the product in quantitative yield as a white fluffy solid. MS (ESI): $[\text{M}+9\text{H}]^{9+}$ calculated 1021.41, found 1021.63; $[\text{M}+10\text{H}]^{10+}$ calculated 919.37, found 919.50; $[\text{M}+11\text{H}]^{11+}$ calculated 835.88, found 836.00.

Tetramer (Ac-TZ14011)₄-MSAP

Tetramer (Ac-TZ14011)₄ (2.08 mg, 0.18 μmol) and MSAP (0.51 mg, 0.30 μmol) were dissolved in 1 mL of DMSO. DiPEA (10 μL , 57 μmol) was added and the solution was stirred overnight at 20°C, after which the mixture was purified by preparative HPLC. The product was obtained as a blue fluffy solid (0.97 mg, 50%) after pooling of the appropriate fractions and lyophilization. MS (ESI): $[\text{M}+19\text{H}]^{19+}$ calculated 567.40, found 568.95; $[\text{M}+33\text{H}]^{33+}$ calculated 327.08, found 327.86; $[\text{M}+34\text{H}]^{34+}$ calculated 317.49, found 316.91.

Molecular modeling

The structures of MSAP label (the succinimidyl group was omitted), dimer Glu(β -Ala-OH)- β -Ala-OH and tetramer Glu(β -Ala-Glu(β -Ala-OH)- β -Ala-OH)- β -Ala-Glu(β -Ala-OH)- β -Ala-OH were minimized in Chem3D Pro 12.0 using the MM2 force field (minimum RMS gradient = 0.100) and PDB files of these minimized structures were made. The PDB file of CXCR4 complexed with the Ac-TZ14011 analog CVX15 (PDB entry code 3OE0) was loaded in YASARA (<http://www.yasara.org>).³ CXCR4 was deleted and the CVX15 peptide was modified to Ac-TZ14011 (Gln⁶ \rightarrow Cit⁶; Lys⁷ \rightarrow Arg⁷; D-Pro⁸ \rightarrow D-Lys⁸; Gly¹⁵ and D-Pro¹⁶ \rightarrow deleted). Ac-TZ14011 was minimized in YASARA: a simulation cell, in which each axis was

extended 5.0 Å from the molecule, was defined. The Amber99 forcefield was used and the temperature control was step-10 annealing, starting from 298 K and at every 10 simulation steps the velocity of all atoms was reduced to 90%. The simulation was stopped after 10 000 fs, when the atoms almost did not move anymore. A PDB file was made of the minimized Ac-TZ14011 peptide.

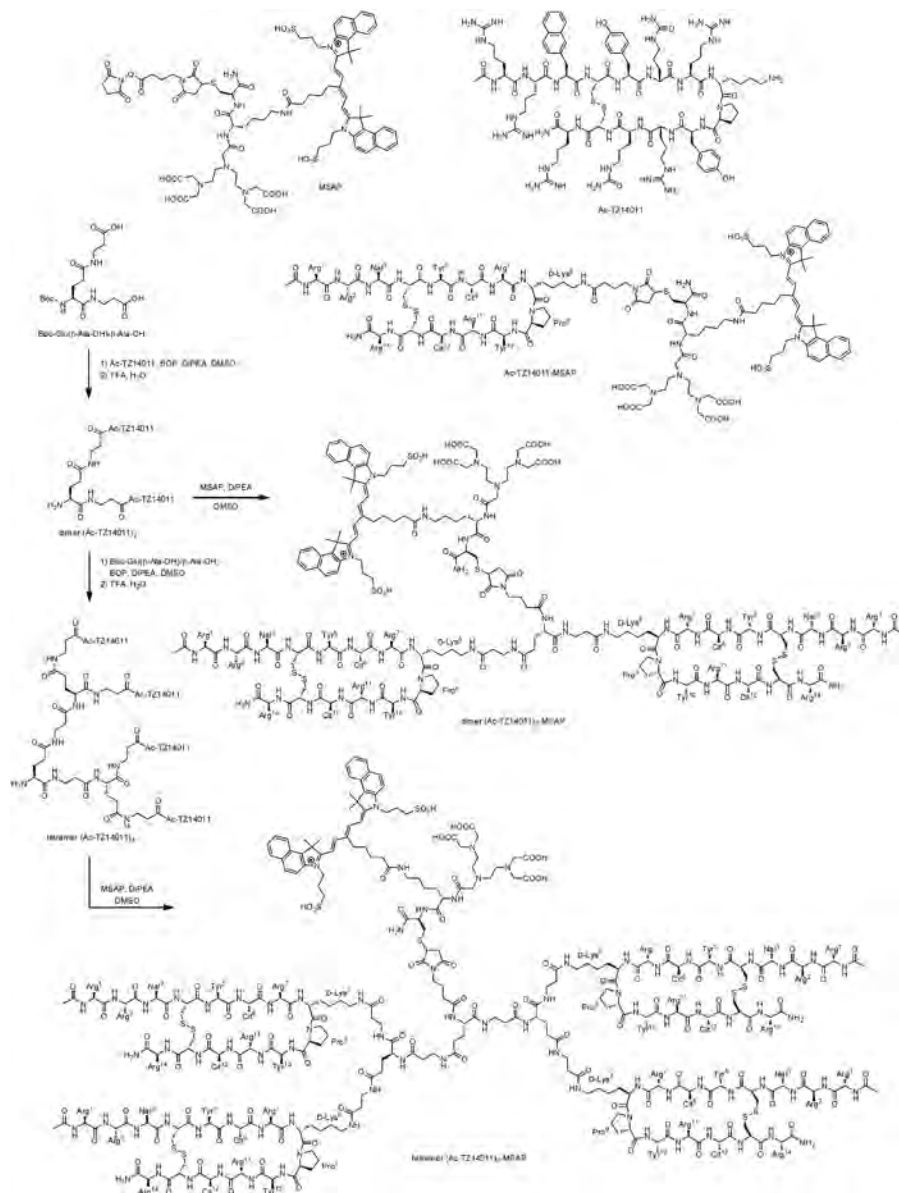
For the monomer Ac-TZ14011-MSAP the PDB files of the minimized Ac-TZ14011 and MSAP label were loaded and the MSAP label was properly placed with respect to the amine of D-Lys8 and a peptide bond was created, yielding a model of monomer Ac-TZ14011-MSAP.

For the dimer (Ac-TZ14011)₂-MSAP the PDB files of the minimized Ac-TZ14011 (four times), dimer Glu(β-Ala-OH)-β-Ala-OH and MSAP label were loaded and the molecules were properly placed with respect to each other and peptide bonds were created, yielding a model of dimer (Ac-TZ14011)₂-MSAP.

For the tetramer (Ac-TZ14011)₄-MSAP the PDB files of the minimized Ac-TZ14011 (four times), tetramer Glu(β-Ala-Glu(β-Ala-OH)-β-Ala-OH)-β-Ala-Glu(β-Ala-OH)-β-Ala-OH and MSAP label were loaded and the molecules were properly placed with respect to each other and peptide bonds were created, yielding a model of tetramer (Ac-TZ14011)₄-MSAP.

For the models of Ac-TZ14011-MSAP, (Ac-TZ14011)₂-MSAP and (Ac-TZ14011)₄-MSAP binding to CXCR4 (see Figure A2), the PDB files of CXCR4 with the CVX15 peptide (PDB entry code 3OE0) and of Ac-TZ14011-MSAP, (Ac-TZ14011)₂-MSAP or (Ac-TZ14011)₄-MSAP were loaded. An Ac-TZ14011 peptide in Ac-TZ14011-MSAP, (Ac-TZ14011)₂-MSAP or (Ac-TZ14011)₄-MSAP was overlaid onto CVX15 and CVX15 was deleted, yielding models of Ac-TZ14011-MSAP, (Ac-TZ14011)₂-MSAP and (Ac-TZ14011)₄-MSAP binding to CXCR4.

To estimate the size of Ac-TZ14011-MSAP, (Ac-TZ14011)₂-MSAP and (Ac-TZ14011)₄-MSAP, the largest distances between two atoms in the models were established. The sizes were 27.5 Å, 48.5 Å and 71.2 Å for Ac-TZ14011-MSAP, (Ac-TZ14011)₂-MSAP and (Ac-TZ14011)₄-MSAP, respectively.



Scheme A1. Synthesis of dimer (Ac-TZ14011)₂, dimer (Ac-TZ14011)₂-MSAP, tetramer (Ac-TZ14011)₄ and tetramer (Ac-TZ14011)₄-MSAP and the structures of MSAP reagent, Ac-TZ14011 and monomer Ac-TZ14011-MSAP.

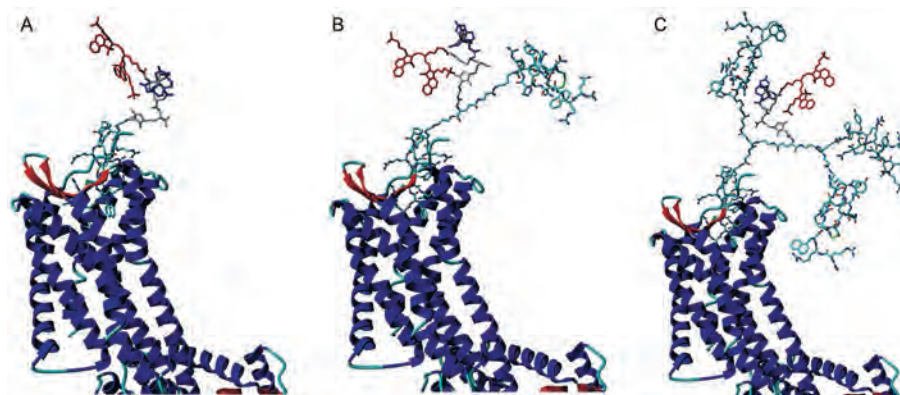


Figure A2. Molecular models of the Ac-TZ14011-MSAP derivatives binding to CXCR4. A) CXCR4 is shown in ribbon representation and monomer Ac-TZ14011-MSAP, B) dimer (Ac-TZ14011)₂-MSAP and C) tetramer (Ac-TZ14011)₄-MSAP as stick models, which is colored by element. For clarity, the MSAP label is not colored by element: the CyAL-5.5₆ fluorophore is displayed in red, the indium-bound DTPA chelate in blue and the spacer in grey.

References

- 1 Kuil J, Buckle T, Yuan H, van den Berg NS, Oishi S, Fujii N, Josephson L, van Leeuwen FWB. Synthesis and evaluation of a bimodal CXCR4 antagonistic peptide. *Bioconjugate Chem.* 2011; 22: 859-864
 - 2 Hanaoka H, Mukai T, Tamamura H, Mori T, Ishino S, Ogawa K, Iida Y, Doi R, Fujii N, Saji H. Development of a ¹¹¹In-labeled peptide derivative targeting a chemokine receptor, CXCR4, for imaging tumors. *Nucl Med Biol.* 2006; 33: 489-494
 - 3 Wu B, Chien EY, Mol CD, Fenalti G, Liu W, Katritch V, Abagyan R, Brooun A, Wells P, Bi FC, Hamel DJ, Kuhn P, Handel TM, Cherezov V, Stevens RC. Structures of the CXCR4 chemokine GPCR with small-molecule and cyclic peptide antagonists. *Science.* 2010; 330(6007): 1066-1071
-

Interventional

Integrating target validation with in vivo
molecular imaging,
and ex vivo imaging of mouse tumor
a hybrid approach
lesions resembling human DCIS using

a single hybrid imaging agent

Chapter 13

*Buckle T, Kuil J, van den Berg NS, Bunschoten A, Lamb HJ, Yuan H,
Josephson L, Jonkers J, Borowsky AD, van Leeuwen FWB.*

Submitted

Abstract

Screening of biomarker expression levels in tumor biopsy samples provides not only an assessment of prognostic and predictive factors, but may also be used for the selection of biomarker specific imaging strategies. To assess the feasibility of using a biopsy specimen for a personalized selection of an imaging approach, the chemokine receptor 4 (CXCR4) was used as a reference biomarker. A hybrid CXCR4 targeting peptide (MSAP-Ac-TZ14011) containing a fluorescent dye and a chelate for radioactive labeling, was used to directly compare initial flow cytometry based target validation in fresh tumor tissue to in vivo single photon emission computed tomography (SPECT) imaging and in vivo and ex vivo fluorescence imaging. Flow cytometric analysis of mouse tumor derived cell suspensions enabled discrimination between 4T1 control tumor lesions with low CXCR4 expression levels and CXCR4 positive early, intermediate and late stage MIN-O lesions; CXCR4^{basal}, CXCR4⁺ and CXCR4⁺⁺ cell populations could be accurately discriminated. Mean fluorescent intensity ratios between MIN-O and 4T1 tissue found with flow cytometry were comparable to ratios obtained with in vivo SPECT/CT and fluorescence imaging, ex vivo fluorescence evaluation and standard immunohistochemistry. This Chapter demonstrates that the hybrid nature of a targeting imaging agent like MSAP-Ac-TZ14011 enables integration of target selection, in vivo imaging and ex vivo validation using a single imaging agent. The use of biopsy tissue for biomarker screening can readily be expanded to other targeting hybrid imaging agents and can possibly help increase the clinical applicability of tumor specific imaging approaches.

Introduction

Screening of biomarker expression levels in breast cancer biopsy samples using immunohistochemistry (IHC) is a routine procedure that provides an assessment of prognostic and predictive factors such as histological grade, subtype and hormone receptor and human epidermal growth factor receptor 2 (Her2/neu) status.^{1,2} The molecular insights derived from these biopsy samples can be used for decision-making in (personalized) treatment planning. For example, estrogen receptor (ER) and/or the Her2/neu status in biopsy samples predicts a response to trastuzumab when added to standard adjuvant chemotherapy.³⁻⁵ Additionally, staining of biopsy tissue for less established biomarkers such as the chemokine receptor 4 (CXCR4) has been shown to correlate with aggressiveness/invasiveness and metastatic potential in breast cancer.⁶⁻⁸

The current standard of care in (preoperative) non-invasive imaging of breast cancer is implementation of contrast enhanced MRI and ¹⁸F-FDG PET. Both modalities are widely implemented in the detection of cancer and many other diseases as they rely on differences in perfusion/vascular leakiness (MRI) and metabolism/glucose uptake (PET) between diseased and normal tissue. For more specific visualization of e.g. tumor tissue, at present, numerous alternative imaging agents are being developed for direct targeting of all kinds of biomarkers expressed on the cell membrane.

Expression patterns of such biomarkers tend to be heterogeneous and vary between patients and tumor subtypes, which could also imply the need for more than one targeting compound for accurate imaging-based assessment of a specific tumor lesion. However, realistically, one cannot perform consecutive biomarker screening studies in a single patient. Similar to their use in treatment selection, individual biomarker expression patterns may also be exploited for specific imaging strategies, as was shown by Dijkers et al. who performed non-invasive positron emission tomography (PET) imaging of Her2/neu positive lesions in patients with metastatic breast cancer.⁹

Identification of a biomarker or rather a diagnostic target during the different logistical steps in clinical management viz. IHC of biopsy tissue, (preoperative) imaging, intraoperative surgical guidance and pathological evaluation of excision margins, are all commonly performed using different methods and different (targeting) compounds. This variation may lead to a discrepancy in findings; in an ideal situation, target selection and further follow-up are conducted using one and the same imaging agent. This should yield more interchangeable and complementary results during the whole logistical process of cancer management (Figure 1). As such a smart screening method for an imaging approach or a combination thereof is required.

A tailored selection process that identifies the best diagnostic target will be instrumental for the successful application of biomarker specific imaging agents. With this in mind we reasoned that a biopsy specimen can potentially be used for the selection of a specific imaging approach.

To demonstrate the feasibility of the integrating biopsy in fresh breast tumor tissue with in vivo imaging, the chemokine receptor 4 (CXCR4) was used as a reference biomarker. In a recent critical review, in which we evaluated CXCR4 targeting imaging agents based on their affinity, specificity and biodistribution, the T140 peptide derivative Ac-TZ14011 was shown to be one of the best targeting moieties for fluorescence imaging of CXCR4 expression levels.¹⁰ Different imaging labels on the peptide Ac-TZ14011 can aid the specific visualization of CXCR4 expressing tumor cells with: i) fluorescence IHC (FITC labeled version), ii) flow cytometric analysis (FITC labeled version), iii) SPECT/CT (¹¹¹In-DTPA labeled version) and iv) in vivo fluorescence imaging (near-infrared labeled version).¹¹⁻¹³ The synthetic development of a hybrid version of this targeting peptide (MSAP-Ac-TZ14011), which contains both a fluorescent label and a chelate for radioactive labeling, enabled integration of in vitro affinity evaluations and in vivo imaging methods.^{14,15}

In this study the concept of using a biopsy specimen for a personalized selection of the most optimal targeting imaging approach was evaluated using MSAP-Ac-TZ14011. The fluorescent label was used to assess the membranous CXCR4 expression pattern in fresh tumor segments obtained from tumor-bearing mice, while after radioactive labeling with ¹¹¹indium, the imaging agent was suitable for in vivo SPECT/CT imaging. The initial screening results obtained with flow cytometry (Figure 1A) were directly correlated to in vivo imaging results (SPECT/CT and fluorescence imaging; Figure 1B), and microscopic ex vivo analysis (fluorescence confocal microscopy; Figure 1C); hereby comprising all steps in clinical cancer management.

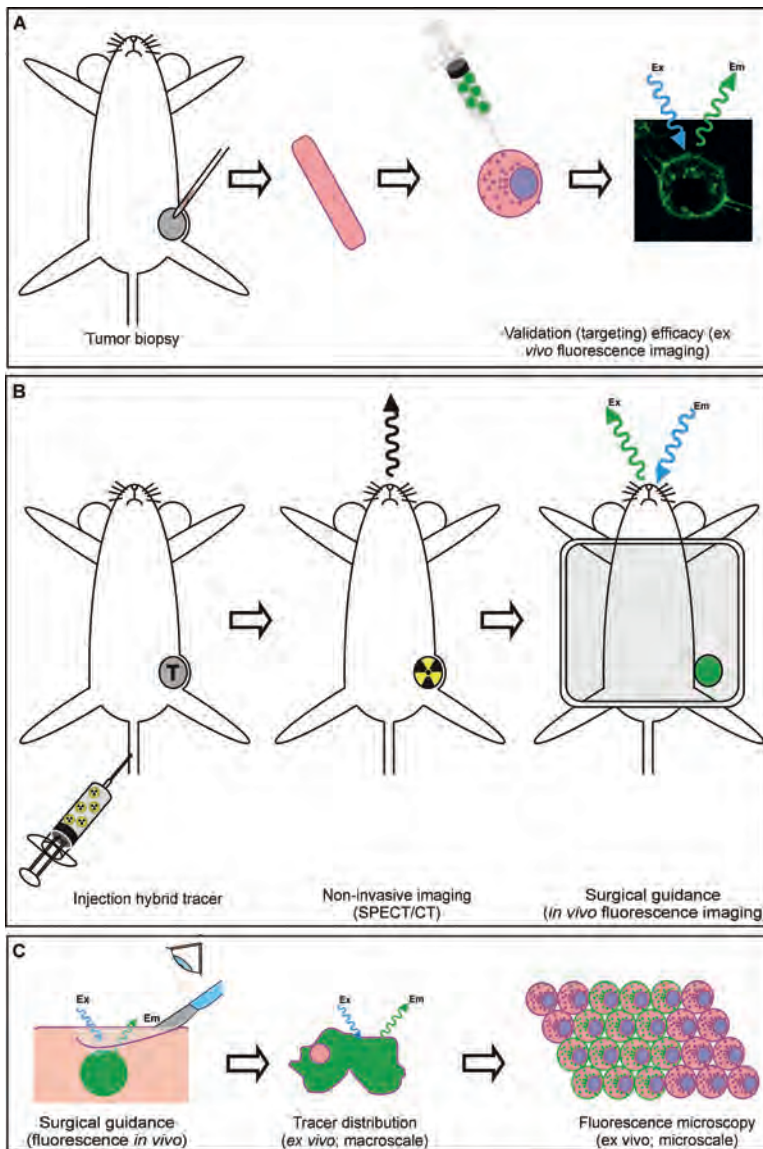


Figure 1. Schematic representation of the integrated logistics made possible by using a targeting hybrid imaging agent. A) Analysis of tumor biopsy samples using the fluorescent beacon of the imaging agent using flow cytometry. B) Non-invasive tumor visualization using SPECT/CT after radiolabeling of the hybrid agent. Fluorescence imaging enables intraoperative surgical guidance. C) Ex vivo evaluation of tracer distribution using fluorescence imaging and -microscopy after excision of the tumor.

Materials and Methods

Synthesis and radiolabeling of MSAP-Ac-TZ14011

MSAP-Ac-TZ14011 (Figure 2) was synthesized and radiolabeled according to previously described procedures.¹⁵

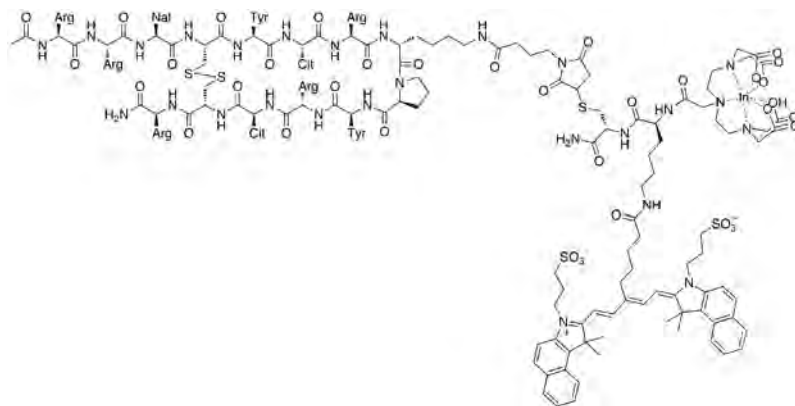


Figure 2. Structure of MSAP-Ac-TZ14011

In vivo model

As a CXCR4 positive tumor model, the orthotopic MIN-O transplantation model resembling human ductal carcinoma in situ was used.^{16,17} In this model, preinvasive lesions progress into invasive lesions with increasing membranous CXCR4 expression.¹² Tumor lesions were staged according to previously reported criteria; based on CT-based size measurements and discrimination was made between early stage (< 100 mm³), intermediate stage (100 - 400 mm³), and late stage (> 400 mm³) lesions.¹²

Cell line based 4T1 tumor lesion served as control. In these control tumors, CXCR4 expression is constantly low during tumor progression and therefore no discrimination between stages was applied.¹² 4T1 cells (from American Type Culture Collection, ATCC) were a kind gift of dr. O. van Tellingen (NKI-AvL, Amsterdam, The Netherlands).

All tumor lesions were generated as reported previously.¹² Animal experiments were performed in accordance with Dutch welfare regulations and were approved by the ethics committee of the Netherlands Cancer Institute under references 08021 B19 and 08021 B21. Implantation of tumor tissue or cells and in vivo imaging were performed under hypnorm/dormicum/water (1:1:2; 5 µL/g i.p.) anesthesia. All efforts were made to minimize suffering.

Fresh tumor tissue analysis

From fresh tumor specimens (MIN-O: n = 6 per stage; 4T1: n = 6) single cell suspensions were made by cutting the tumor into small pieces with a scalpel and suspending them using a 18G, 21G and a 25G needle, respectively. The cell suspension was incubated for five min with an ER-lysis buffer (0.31 M NH_4Cl , 0.02 M KHCO_3 , 0.5 M EDTA in 2 L H_2O ; pH 7.4) to remove red blood cells. 300,000 cells per measuring condition were washed with 0.1% bovine serum albumin in phosphate buffered saline (0.1% BSA/PBS) and incubated for one hr at 4°C under dark conditions with MSAP-Ac-TZ14011 (1:200 from a stock of 1 mg/mL) or with the monoclonal phycoerythrin (PE) labeled anti-CXCR4 antibody 2B11 (2B11-PE; 1:100; BD Biosciences). For evaluation of the overlap in staining between MSAP-Ac-TZ14011 and 2B11-PE, cells were co-incubated with MSAP-Ac-TZ14011 and 2B11-PE.

Following incubation cells were washed with 0.1% BSA/PBS and propidium iodide (PI; 1:10,000; BD Biosciences) was added to allow the selection of viable cells. Antibodies were diluted in 0.1% BSA/PBS in all flow cytometric experiments. Non-peptide/antibody incubated cells served as controls. Cells were analyzed (approximately 20,000 events per sample) using a CyAn ADP flowcytometer (DakoCytomation) equipped with Summit v4.3 software (DakoCytomation). PE fluorescence was detected after excitation at 488 nm. Emission was collected at 575/25 nm. PI was detected after excitation at 488 nm and emission was collected at 613/20 nm. The CyAL-5.5_b dye on the MSAP label was excited at 635 nm and emission was collected at 665/20 nm. Cell viability was comparable between samples.

For evaluation of CXCR4 staining, stained populations were divided into CXCR4⁻ (CXCR4 negative cells), CXCR4^{basal} (basal/low expression of CXCR4), CXCR4⁺ and CXCR4⁺⁺, based on the measured cell surface associated fluorescence; populations were discriminated based on differences in the mean fluorescence of that specific population. Mean fluorescence intensity ratios (MFIRs) were calculated by dividing the mean fluorescent intensity of all cells stained by MSAP-Ac-TZ14011 by the mean fluorescence intensity of the non-incubated control. The ratio between the MIN-O and 4T1 tumor lesion was determined by dividing the MFIR of the various MIN-O tumor lesions by MFIR of the 4T1 tumor lesion. The ratio between the CXCR4^{basal} and the CXCR4⁺ and CXCR4⁺⁺ populations was determined by calculating the MFIR between the CXCR4⁺ or CXCR4⁺⁺ and the CXCR4^{basal} population. This resulted in a semi quantitative evaluation of the level of overexpression.

To evaluate the amount of lymphocytes in the CXCR4 positive population in the tumor cell suspension, cells were co-incubated with MSAP-Ac-TZ14011 and the PE-labeled

anti-CD45 antibody (CD45-PE; 1:200; eBioscience). The percentage of CXCR4 positive lymphocytes was determined by dividing the CD45 positive (CD45⁺) population within the whole CXCR4 positive population by the total amount of counted cells and multiplied by 100%. Statistics were performed using a standard T-test.

Confocal imaging of fresh tumor slices

For direct ex vivo evaluation of CXCR4 staining, 4T1 (n = 3) and late stage MIN-O (n = 3) tumor-bearing mice were sacrificed and the tumor was removed. Next, the tumor was cut into thin tissue slices which were then incubated with MSAP-Ac-TZ14011 (1:200 in MEM medium) for one hr at 4°C under dark conditions.

For comparison, 4T1 (n = 3) and late stage MIN-O (n = 3) tumor-bearing mice were intravenously injected with 50 µg MSAP-Ac-TZ14011. 24 Hrs after injection, mice were sacrificed where after the tumor was removed and cut into thin slices.

Before analysis using the Leica TCS SPII AOBS confocal microscope (Leica Microsystems), slices were incubated with DAPI, washed thoroughly with PBS and placed on 24 mm ø glass coverslips. Non-incubated tumor slices were used as negative control. Images were acquired at 37°C following excitation at 633 nm at 10x and 63x magnification. Emission was collected from 650 - 725 nm. DAPI was excited at 405 nm and emission was collected from 409 - 468 nm. Images were analysed using Leica Confocal Software (Leica Microsystems).

Immunohistochemistry (IHC)

Formalin-fixed paraffin-embedded MIN-O or 4T1 tumor tissue sections were stained according to the protocol previously reported by van den Berg et al.¹¹ with a monoclonal anti-CXCR4 antibody (rat-anti-CXCR4 clone 2B11 1:100; BD Biosciences). Images were obtained at 40x magnification. Membranous staining was assessed as previously reported.¹² The ratio between the MIN-O and 4T1 tumor lesions was determined by dividing the percentage of membranous staining in the MIN-O tumor lesions by the percentage of membranous staining in the 4T1 tumor lesions. Statistics were performed using a standard T-test.

In vivo imaging

Mice (n = 5 for intermediate stage MIN-O (100 - 400 mm³) lesions and n = 5 for late stage 4T1 tumor lesion (< 400 mm³)) were injected intravenously with 50 µg ¹¹¹In-MSAP-Ac-TZ14011 (10 MBq). SPECT/CT scans were conducted on a preclinical SPECT/CT scanner

(Nanospect; Bioscan) 24 hrs post injection. After acquisition, the CT data was reconstructed using a cone-beam filtered back projection and SPECT data were reconstructed iteratively with HiSPECT software (Scvis GmbH). Signal intensities were analyzed using the InVivoScope post-processing software (Bioscan Inc.). For further details, see van Leeuwen et al.¹⁸ After SPECT/CT imaging, mice were sacrificed. Tumor-to-muscle ratios (T/M) were determined after measurement of radioactivity as previously reported.¹²

In vivo fluorescence imaging was conducted on the IVIS 200 camera (Xenogen Corp.) using Living Imaging Acquisition and Analysis software (Xenogen Corp.). Images were acquired with standard Cy5.5 (excitation 615 - 665 nm and emission 695 - 770 nm) settings. Fluorescent content was measured in photons/sec/cm².

Results

To set up an analytical method that can be applied for screening of fresh biopsy specimens, cell suspensions of freshly obtained tumor segments were prepared. After incubation of the tumor derived cell suspensions with MSAP-Ac-TZ14011, flow cytometric analysis revealed differences in fluorescent intensity levels between the samples.

Table 1. Evaluation of CXCR4 expression with flow cytometric analysis and IHC.

	MFIR CXCR4 ⁺ and CXCR4 ⁺⁺ population	Ratio MFIR MIN-O/4T1	Ratio membranous staining MIN-O/4T1
MIN-O early stage	165.5 ± 13.8	1.8	1.1
MIN-O intermediate stage	329.6 ± 33.6	3.6	3.5
MIN-O Late stage	367.9 ± 22.4	4.0	5.5
4T1	91.5 ± 14.4	-	-

For MIN-O tumor tissue, six biopsy samples per stage were evaluated. Also, six 4T1 biopsy samples were assessed. All samples were evaluated in triplicate. MFIR: mean fluorescence intensity ratio. Ratio of membranous staining calculated from data reported in ¹⁵.

CXCR4 expression levels in MIN-O and 4T1 tumor lesions

In the MIN-O tumor lesions MFIR of all stained cells increased from 165.5 ± 13.8 in early stage to 367.9 ± 22.4 in late stage MIN-O lesions (for MFIR values see Table 1). Overall, the MFIR found in the MIN-O lesions was 3-fold (range 1.8 - 4) higher than in the 4T1 tumor

lesions (MFIR 91.5 ± 14.4 ; $P < 0.001$; Table 1). This result is comparable to the ratios found between MIN-O and 4T1 control tumor lesions after flow cytometric assessment using the anti-CXCR4 antibody 2B11-PE.¹² Comparable ratios were also found when comparing ratios found with MSAP-Ac-TZ14011 based flow cytometry (Table 1) to quantified membranous staining (IHC) in MIN-O and 4T1 tumor lesions.

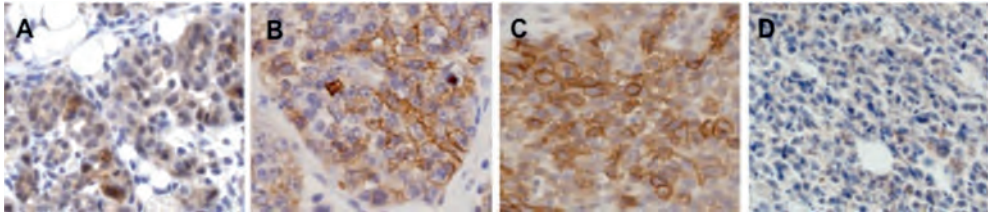


Figure 3. CXCR4 staining using immunohistochemistry. Membranous staining of fixed tumor tissue slices after incubation with the anti-CXCR4 antibody 2B11 in A) early, B) intermediate, C) late stage MIN-O tumor lesions and D) 4T1 control tumors (40x magnification).

Identification of individual cell populations

IHC revealed increasing but heterogeneous membranous staining for CXCR4 in the MIN-O lesions (Table 1, Figure 3). Flow cytometric analysis enabled identification of different CXCR4 expressing cell populations after incubation with MSAP-AcTZ14011 (Figure 4). As incubation occurred at 4°C, these populations were differentiated based on the cell membrane associated binding of the imaging agent. Figure 4A shows that besides a low percentage of CXCR4 negative cells (CXCR4⁻ mean 13.2 ± 2.6), three distinct populations were evident; CXCR4^{basal} (mean 58.9 ± 3.7), CXCR4⁺ (mean 367.3 ± 47.0) and CXCR4⁺⁺ (mean 2197.4 ± 413.3).

The different cell populations were found in the MIN-O lesions as well as in the 4T1 tumor specimens. The increase in fluorescence intensity between the different populations was determined by calculating the MFIR between the CXCR4^{basal} and the CXCR4⁺ or CXCR4⁺⁺ population. This resulted in a 7.8 ± 1.2 -fold higher ratio in the CXCR4⁺ and a 47.0 ± 10.4 -fold higher ratio in the CXCR4⁺⁺ population compared to the CXCR4^{basal} population. Carlisle et al. reported comparable differences in fluorescent intensities when comparing several cell lines with different levels of CXCR4 expression.¹⁹ As such it appears that different CXCR4 positive cell populations exist within a tumor.

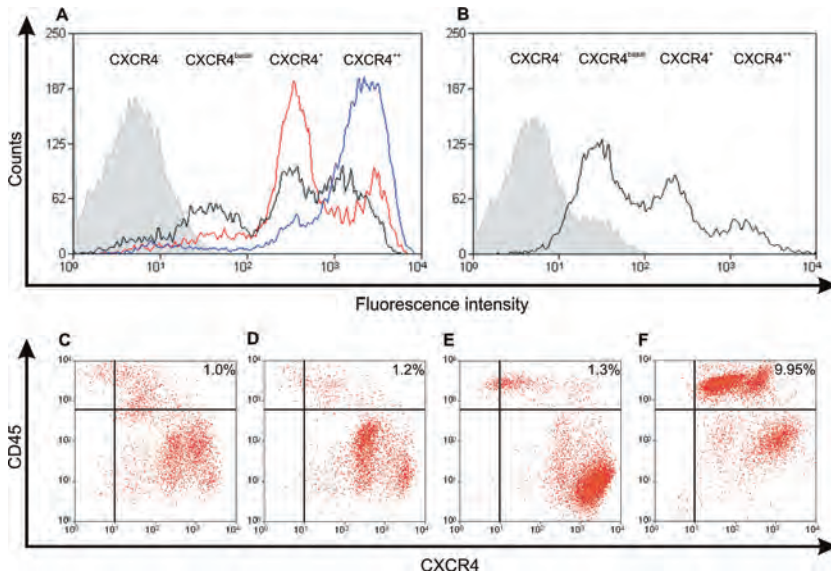


Figure 4. Fluorescence based fresh tumor biopsy analysis after incubation with MSAP-Ac-TZ14011. A) CXCR4 staining pattern in early (black), intermediate (red) and late stage (blue) MIN-O biopsy samples. B) CXCR4 staining pattern in 4T1 biopsy samples. Non-incubated control samples are depicted in grey. C - F) Analysis of CD45 expression in CXCR4 positive cells in early, intermediate and late stage MIN-O tumor lesions and 4T1 tumor lesions.

Further analysis of the results obtained with flow cytometry revealed that the percentage of CXCR4^{basal} cells was highest in the 4T1 tumor samples and that in the MIN-O lesions this percentage of cells decreased during lesion progression (Table 2). The percentage of strongly CXCR4 positive (CXCR4⁺ and CXCR4⁺⁺) cells increased from $68.6 \pm 1.5\%$ in early stage MIN-O lesions to $86.6 \pm 0.9\%$ and $93.0 \pm 0.7\%$ in intermediate and late stage MIN-O lesions, respectively (Table 2). Furthermore, the percentage of strongly CXCR4 positive cells was significantly higher in all stages of MIN-O progression compared to the percentage found in the control 4T1 tumor lesions ($44.6 \pm 6.0\%$; $P < 0.001$).

In the MIN-O lesions the percentage CXCR4⁺ and CXCR4⁺⁺ cells varied during tumor progression (Figure 4A). In the early stage MIN-O lesions $38.4 \pm 2.3\%$ of the cells was CXCR4⁺ and $30.3 \pm 2.0\%$ of the cells was CXCR4⁺⁺. Intermediate stage lesions showed a similar expression pattern, but the percentage of CXCR4⁺ cells increased to $53.5 \pm 2.8\%$, whereas in late stage lesions the percentage of CXCR4⁺ cells had decreased to $12.9 \pm 1.0\%$. A 2.5-fold (range 2.4 - 2.6) increase in CXCR4⁺⁺ cells could be seen in the late stage lesions when compared to the intermediate and early stage lesions ($80.0 \pm 1.4\%$ vs. $33.1 \pm 3.2\%$ and $30.3 \pm 2.0\%$, respectively) (Table 2).

Table 2. Staining percentages of populations with different CXCR4 expression.

	% CXCR4 ⁻	% CXCR4 ^{basal}	% CXCR4 ⁺	% CXCR4 ⁺⁺	% CXCR4 ⁺⁺⁺
MIN-O Early stage	6.9 ± 0.8	25.9 ± 0.8	38.4 ± 2.3	30.3 ± 2.0	68.6 ± 1.5
MIN-O Intermediate stage	2.9 ± 0.3	11.4 ± 0.7	53.5 ± 2.8	33.1 ± 3.2	86.6 ± 0.9
MIN-O Late stage	3.0 ± 0.5	4.7 ± 0.5	12.9 ± 1.0	80.0 ± 1.4	93.0 ± 0.7
4T1	1.2 ± 0.4	56.1 ± 5.3	27.0 ± 2.3	18.3 ± 4.3	44.6 ± 6.0

Identification of the amount of CXCR4 expressing lymphocytes

CXCR4 is not only expressed by tumor cells, but can also be expressed by native immune cells such as lymphocytes.²⁰ As the latter can also be present in tumor lesions,¹² a control staining for lymphocytes to exclude over- or underestimation of the amount of CXCR4 positive tumor cells is required. Co-incubation with both MSAP-Ac-TZ14011 and an anti-CD45 antibody were used to determine the amount of lymphocytes (CD45⁺) that were CXCR4 positive. Flow cytometric analysis revealed that the percentage of CD45⁺ lymphocytes was highest in the 4T1 tumor cell suspensions (9.95%). On the contrary, in the MIN-O lesions, the amount of CD45⁺ lymphocytes was very low, and only increased slightly from 1.0% in early stage to 1.2% in intermediate and 1.3% in late stage lesions.

Co-staining could be used to specify which CXCR4 positive populations contained the CD45⁺ cells (Figure 4C - F) by differentiating between the different CXCR4 expressing cell populations (x-axis) and the CD45 expression of the cells (y-axis). In the MIN-O lesions concomitant staining between CXCR4 and CD45 was mainly seen in the CXCR4^{basal} population (Figure 4C - E) whereas in the 4T1 controls CD45⁺ cells were predominantly present in the CXCR4^{basal} and CXCR4⁺ populations (Figure 4F). Although clearly detectable, the percentages of CD45⁺ cells found in the different MIN-O and 4T1 tumor tissue samples are not likely to influence the CXCR4 based discrimination between the MIN-O and the 4T1 tumor lesions.

Fluorescence IHC of CXCR4 expression

Similar to Ac-TZ14011-FITC,¹⁰ MSAP-Ac-TZ14011 could also be used during fluorescence IHC applications. Confocal microscopy at 37°C after ex vivo incubation (at 4°C of fresh tumor slices revealed both membranous and cytoplasmic staining throughout the late stage MIN-O tumor lesion (Figure 5A I and 5A II). In the 4T1 control lesions hardly any fluorescent staining could be observed under the same conditions (Figure 6).

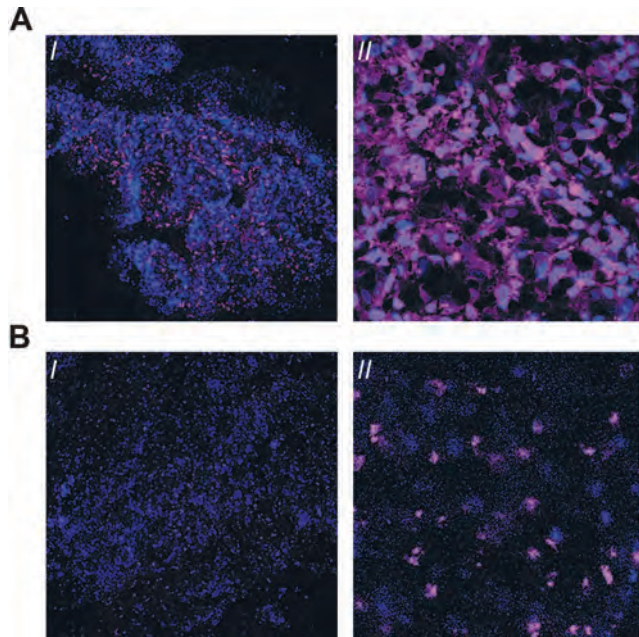


Figure 5. Evaluation of freshly isolated MIN-O tumor slices after A) ex vivo incubation with MSAP-Ac-TZ14011 and B) after intravenous injection of MSAP-Ac-TZ14011 24 hrs prior to evaluation of the tissue. I: 10x magnification. II) 63x magnification. Signal emitted by MSAP-Ac-TZ14011 is depicted in magenta and DAPI (blue) was used to visualize the cell nucleus.

In vivo SPECT/CT and fluorescence imaging

Flow cytometric and fluorescence IHC data combined allowed an accurate differentiation between predominantly CXCR4-basal 4T1 tumors and CXCR4 positive MIN-O lesions. In vivo, MIN-O lesions characterized as mainly CXCR4⁺/CXCR4⁺⁺ at initial screening (see above) could be accurately identified with SPECT/CT imaging after intravenous injection of ¹¹¹In labeled MSAP-Ac-TZ14011 (¹¹¹In-MSAP-Ac-TZ14011). The 4T1 tumor lesions showed no tracer accumulation at the same imaging settings (Figure 6A).

Evaluation of the ¹¹¹In-MSAP-Ac-TZ14011 uptake levels in the tumor lesions (%ID/g) resulted in a T/M ratio that was 3.8-fold higher in the late stage MIN-O lesions (4.55 ± 0.67) as compared to the 4T1 lesions (1.20 ± 0.12). Biodistribution for both models was conform previously reported results.¹⁵ Quantification of the fluorescent signal intensities in these tumor lesions revealed results comparable to the radioactivity measurements. The signal intensity was 4.2-fold higher in the late stage MIN-O lesions compared to the 4T1 tumor lesions ($1.09 \times 10^9 \pm 1.7 \times 10^8$ vs. $2.5 \times 10^8 \pm 3.8 \times 10^7$ photons/sec/cm² respectively)

(Figure 6B). This 4-fold difference seen with both SPECT/CT and fluorescence imaging was in accordance with the differences found in membranous CXCR4 expression (Table 1).

Ex vivo assessment of tracer distribution

Ex vivo fluorescent assessment of the tracer distribution in fresh tumor tissue segments following the systemic injection of MSAP-Ac-TZ14011 (24 hrs prior to tumor excision) predominantly revealed accumulation of the imaging agent in the cytoplasm of MIN-O lesions (Figure 5A I and II and Figure 6D), something that was not seen in the 4T1 controls (Figure 6D). This cytoplasmic staining is in line with the internalization of CXCR4 receptors over time at 37°C.¹⁰

Differences in staining patterns were observed after direct (ex vivo) incubation of tumor tissue samples with MSAP-Ac-TZ14011 (Figure 5A) compared to systemic tracer administration (Figure 4B). Whereas direct, ex vivo, incubation of the tumor tissue will probably enable visualization of 'all' CXCR4 positive cells present, systemic administration will most certainly only stain cells that could be reached by the tracer via the vascular network.

Evaluation of the $\alpha_v\beta_3$ -integrin expression in late stage MIN-O lesions and 4T1 tumor lesions previously revealed that the degree of angiogenesis in both MIN-O and 4T1 tumor lesions is similar.¹² The lesions are overall well perfused, but some regions contained more and larger blood vessels than others. This heterogeneity in the vascular physiology will likely be of influence on the distribution of the tracer throughout the tumor.

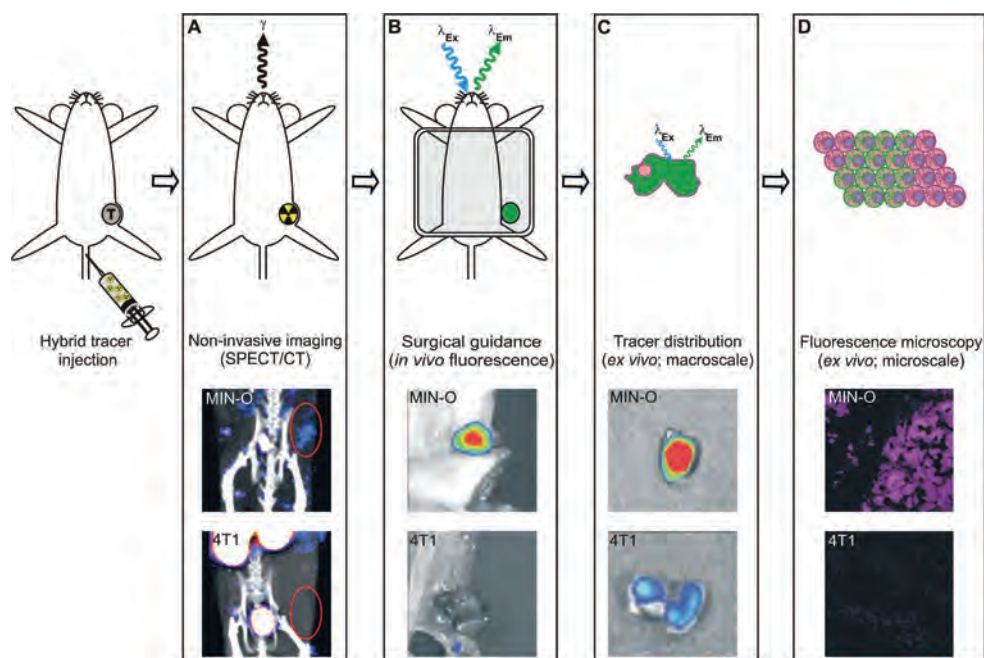


Figure 6. Non-invasive imaging. A) SPECT/CT imaging after intravenous injection of ^{111}In -MSAP-Ac-TZ14011. B) in vivo and C) ex vivo fluorescence imaging. D) fluorescence microscopy (10x magnification). Intermediate stage MIN-O: top images. Late stage 4T1: bottom images.

Discussion

Imaging applications using hybrid tracers are rapidly emerging²¹⁻²⁴ and have already been successfully applied in clinical studies facilitating integrated pre- and intraoperative imaging of sentinel nodes.²⁵⁻²⁸ By adding a receptor targeting moiety, the utility of hybrid imaging agents can be expanded to pre-imaging screening of biomarker expression levels and subsequent (imaging) target selection.

In a previous comparison of currently available imaging agents for CXCR4, Ac-TZ14011 showed great potential in fluorescence imaging and hybrid imaging applications.¹⁰ Ac-TZ14011 was shown to bind selectively to CXCR4 and could be used to visualize CXCR4 positive tumor lesions in vivo.^{11,12,14,15,29} It must be noted that MSAP-Ac-TZ14011 derivatives are the only hybrid imaging agents available for CXCR4 targeting.¹⁰ For in vivo imaging experiments with this tracer the use of a relatively low specific activity was shown to be beneficial for tumor visualization.¹⁰ In a recent review on imaging agents for CXCR4 we have demonstrated that tumor models, which more accurately represent

the modest five-fold overexpression found in the clinical situation, such as the MIN-O model used in this study, better represent the clinically found CXCR4 expression levels in tumors.¹⁰ As a result the *in vivo* SPECT/CT images obtained in this study (Figure 6) provide less of a black-and-white discrimination between CXCR4 positive tumors and their background, than can be obtained using transfected tumor cells with extremely high levels of CXCR4 expression.¹⁰

The hybrid nature of the CXCR4 targeting imaging agent MSAP-Ac-TZ14011 has allowed us to successfully demonstrate the concept of integrating target selection in fresh (biopsy) tumor tissue with *in vivo* imaging and microscopic validation (Figure 1), all using a single imaging agent.

Similar to the *in vitro* evaluation of fluorescently labeled imaging agents,^{14,15} flow cytometry could be used to analyze the level of CXCR4 expression in the tumor cell suspensions. In this application incubation with MSAP-Ac-TZ14011 allowed effective discrimination between MIN-O (stages) and 4T1 tumor lesions using the fluorescent label present in the targeting hybrid imaging agent (Figure 4 and Table 2). These findings were further confirmed with IHC (Table 2), *in vivo* SPECT/CT (using the radiolabel) and fluorescence imaging (Figure 6); the ratio between the late stage MIN-O and similarly sized 4T1 control lesions was comparable with all visualization methods.

Flow cytometry is already being used in a clinical setting for applications such as diagnosis of leukemia and lymphoma³⁰⁻³³ and dependent on the analyzer used, flow cytometry enables assessment of up to 15 cell surface parameters in one sample.³² Even the small early stage tumors (< 100 mm³), which are comparable in size with human biopsy samples, contain sufficient cells for characterization of multiple samples. In this study co-incubation of MSAP-Ac-TZ14011 and an anti-CD45 antibody showed that at least two markers could be simultaneously evaluated in fresh tumor specimens and that the presence of native immune cells in the tumor tissue could be assessed. For future applications in cancer management it will be possible to set up such screens using a number of biomarker targeting imaging agents simultaneously. By labeling each agent with a different fluorescent dye a tailored selection of the most prominently available receptor proteins suitable for imaging can be made. The method of staining and the fact that perfusion is essential for good visualization *in vivo* should, however, be taken into account when comparing flow cytometry/IHC to *in vivo* imaging results.

We have previously demonstrated that CXCR4 expression in MIN-O lesions is heterogeneous and that the degree of membranous staining of CXCR4 at IHC increases with lesion progression.¹² This increase in membranous staining was in concordance with

the increase in uptake of ^{111}In -Ac-TZ14011 during MIN-O lesion progression.¹² With IHC only total staining percentages can be obtained, whereas flow cytometry can also be used for the accurate evaluation of cell populations with different expression levels within one tumor sample (Table 1).¹⁹ As fluorescence intensities vary with varying receptor expression on the cells, the (semi-quantitative) signal intensity levels can be directly, linked to receptor CXCR4 expression levels.³⁴ Flow cytometric analysis after incubation of the tumor cell suspensions with MSAP-Ac-TZ14011 underlined that CXCR4 positivity increased during the progression of MIN-O lesions. An increase in the percentage of CXCR4⁺ cells seemed to mark the transition into intermediate stage lesions. Concurrently, invasive late stage lesions mainly contained CXCR4⁺⁺ cells, which is in line with the clinically reported higher expression of CXCR4 in more invasive types of breast cancer.⁶

One can envision that besides the ability to select the most appropriate targeting imaging procedure, the level of overexpression of a biomarker that is associated with e.g. malignancy of a tumor,^{8,36,36} may also influence clinical decision-making. For example, CXCR4 expression is linked to a higher tendency to metastasize and higher levels of CXCR4 expression have been found in (distant) metastasis compared to the primary tumor.³⁵ It has also been proposed that CXCR4 expression levels can be used to select subsets of tumor lesion that show a more aggressive biological behavior.³⁷ Furthermore, Chu et al. previously proposed that CXCR4 expression levels allow for the identification of subsets of patients who are at risk of developing recurrent disease, even within patient groups with an initial good prognosis.³⁶

The orthotopic MIN-O transplantation model used in this study serves as an ideal model for the evaluation of tumor progression into an invasive phenotype.^{17,38} As MIN-O strains that metastasize have also been described,¹⁶ it will be interesting to investigate what the influence of the presence of CXCR4⁺⁺ cells will be on metastatic ability of metastatic MIN-O tumor models.¹⁶

The main goal of this study was to evaluate the concept of using biopsy tissue specimens for a personalized selection of the most optimal targeted imaging approach. Obviously, the concept described above is not limited to the targeting of CXCR4. A hybrid version of any imaging agent targeting a biomarker of choice can potentially be used. Possibly, also a cocktail of imaging agents can be used for the simultaneous assessment of several markers at once. Use of different fluorescent dyes and/or radioactive isotopes will then enable discrimination between biomarkers. In this way, the screening and in vivo imaging data can still be used for accurate staging of the tumor lesions. The latter will not be possible when identically labeled imaging agents are used.

Conclusion

Hybrid imaging agents can be applied during the different steps encountered in the clinical management of cancer. Comparable quantitative results have been obtained during target selection in biopsy tissue (flow cytometry), in vivo imaging (SPECT/CT and fluorescence imaging) and during pathological validation (ex vivo microscopy) of the surgically excised tissue (ex vivo microscopic analysis). Incubation with MSAP-Ac-TZ14011 enabled accurate staging of MIN-O lesion progression via the CXCR4 expression pattern of the lesions. Although only CXCR4 was used in this proof of concept study, this approach can readily be expanded to other targeting hybrid imaging agents and will help increase the clinical applicability of tumor specific imaging approaches.

References

- 1 Allred DC. Issues and updates: evaluating estrogen receptor-alpha, progesterone receptor, and HER2 in breast cancer. *Modern Pathology*. 2010; 23 Suppl 2: S52-59
- 2 Leong AS, Zhuang Z. The changing role of pathology in breast cancer diagnosis and treatment. *Pathobiology*. 2011; 78(2): 99-114
- 3 Pritchard KI, Shepherd LE, O'Malley FP, Andrulis IL, Tu D, Bramwell VH, Levine MN; National Cancer Institute of Canada Clinical Trials Group. HER2 and responsiveness of breast cancer to adjuvant chemotherapy. *New Eng J Med*. 2006; 354(20): 2103-2111
- 4 Penault-Llorca F, Cayre A, Bouchet Mishellany F, Amat S, Feillel V, Le Bouedec G, Ferrière JP, De Latour M, Chollet P. Induction chemotherapy for breast carcinoma: predictive markers and relation with outcome. *Int J Oncol*. 2003; 22(6): 1319-1325
- 5 International Breast Cancer Study Group (IBSG), Endocrine responsiveness and tailoring adjuvant therapy for postmenopausal lymph node-negative breast cancer: A randomized trial. *J Natl Cancer Inst*. 2002; 94(14): 1054-1065
- 6 Salvucci O, Bouchard A, Baccarelli A, Deschênes J, Sauter G, Simon R, Bianchi R, Basik M. The role of CXCR4 receptor expression in breast cancer: a large tissue microarray study. *Breast Cancer Res Treat*. 2006; 97(3): 275-283
- 7 Müller A, Homey B, Soto H, Ge N, Catron D, Buchanan ME, McClanahan T, Murphy E, Yuan W, Wagner SN, Barrera JL, Mohar A, Verástegui E, Zlotnik A. Involvement of chemokine receptors in breast cancer metastasis. *Nature*. 2001; 410(6824): 50-56
- 8 Kang H, Watkins G, Douglas-Jones A, Mansel RE, Jiang WG. The elevated level of CXCR4 is correlated with nodal metastasis of human breast cancer. *Breast*. 2005; 14(5): 360-367
- 9 Dijkers EC, Oude Munnink TH, Kosterink JG, Brouwers AH, Jager PL, de Jong JR, van Dongen GA, Schröder CP, Lub-de Hooge MN, de Vries EG. Biodistribution of ⁸⁹Zr-trastuzumab and PET imaging of HER2-positive lesions in patients with metastatic breast cancer. *Clin Pharm Ther*. 2010; 87(5): 586-592
- 10 Kuil J, Buckle T, van Leeuwen FWB. Imaging agents for the chemokine receptor 4 (CXCR4). *Chem Soc Rev*. 2012; 41(15): 5239-5261
- 11 van den Berg NS, Buckle T, Kuil J, Wesseling J, van Leeuwen FWB. Immunohistochemical detection of the CXCR4 expression in tumor tissue using the fluorescent peptide antagonist Ac-TZ14011-FITC. *Transl Oncol*. 2011; 4(4): 234-240

- 12 Buckle T, van den Berg NS, Kuil J, Bunschoten A, Oldenburg J, Borowsky AD, Wesseling J, Masada R, Oishi S, Fujii N, van Leeuwen FWB. Non-invasive longitudinal imaging of tumor progression using an 111-Indium labeled CXCR4 peptide antagonist. *Am J Nucl Med Mol Imaging*. 2012; 2(1): 99-109
- 13 Bunschoten A, Buckle T, Kuil J, Luker GD, Luker KE, Nieweg OE, van Leeuwen FWB. Targeted non-covalent self-assembled nanoparticles based on human serum albumin. *Biomaterials*. 2012; 33(3): 867-875
- 14 Kuil J, Buckle T, Oldenburg J, Yuan H, Borowsky AD, Josephson L, van Leeuwen FWB. Hybrid Peptide dendrimers for imaging of chemokine receptor 4 (CXCR4) expression. *Mol Pharm*. 2011; 8(6): 2444-2453
- 15 Kuil J, Buckle T, Yuan H, van den Berg NS, Oishi S, Fujii N, Josephson L, van Leeuwen FWB. Synthesis and evaluation of a bimodal CXCR4 antagonistic peptide. *Bioconjug Chem*. 2011; 22(5): 859-864
- 16 Namba R, Young LJ, Abbey CK, Kim L, Damonte P, Borowsky AD, Qi J, Tepper CG, MacLeod CL, Cardiff RD, Gregg JP. Rapamycin inhibits growth of premalignant and malignant mammary lesions in a mouse model of ductal carcinoma in situ. *Clin Cancer Res*. 2006; 12(8): 2613-2621
- 17 Namba R, Young LJ, Maglione JE, McGoldrick ET, Liu S, Wurz GT, DeGregorio MW, Borowsky AD, MacLeod CL, Cardiff RD, Gregg JP. Selective estrogen receptor modulators inhibit growth and progression of premalignant lesions in a mouse model of ductal carcinoma in situ. *Breast Cancer Res*. 2005; 7(6): R881-889
- 18 van Leeuwen AC, Buckle T, Bendle G, Vermeeren L, Valdés-Olmos R, van de Poel HG, van Leeuwen FWB. Tracer-cocktail injections for combined pre- and intraoperative multimodal imaging of lymph nodes in a spontaneous mouse prostate tumor model. *J Biomed Opt*. 2011; 16(1): 016004
- 19 Carlisle AJ, Lyttle CA, Carlisle RY, Maris JM. CXCR4 expression heterogeneity in neuroblastoma cells due to ligand-independent regulation. *Molecular Cancer*. 2009;8:126
- 20 Balkwill F. The significance of cancer cell expression of the chemokine receptor CXCR4. *Semin Cancer Biol*. 2004; 14(3): 171-179
- 21 Kuil J, Velders AH, van Leeuwen FWB. Multimodal tumor-targeting peptides functionalized with both a radio- and a fluorescent label. *Bioconjugate Chem*. 2010; 21(10): 1709-1719

- 22 Azhdarinia A, Ghosh P, Ghosh S, Wilganowski N, Sevick-Muraca EM. Dual-Labeling Strategies for Nuclear and Fluorescence Molecular Imaging: A Review and Analysis. *Mol. Imaging Biol.* 2012; 14(3): 261-276
- 23 Banerjee SR, Pullambhatla M, Byun Y, Nimmagadda S, Foss CA, Green G, Fox JJ, Lupold SE, Mease RC, Pomper MG. Sequential SPECT and optical imaging of experimental models of prostate cancer with a dual modality inhibitor of the prostate-specific membrane antigen. *Angewandte Chemie.* 2011; 50(39): 9167-9170
- 24 Sampath L, Kwon S, Ke S, Wang W, Schiff R, Mawad ME, Sevick-Muraca EM. Dual-labeled trastuzumab-based imaging agent for the detection of human epidermal growth factor receptor 2 overexpression in breast cancer. *J Nucl Med.* 2007; 48(9): 1501-1510
- 25 van der Poel HG, Buckle T, Brouwer OR, Valdés-Olmos RA, van Leeuwen FWB. Intraoperative laparoscopic fluorescence guidance to the sentinel lymph node in prostate cancer patients: clinical proof of concept of an integrated functional imaging approach using a multimodal tracer. *Eur Urol.* 2011; 60(4): 826-833
- 26 Brouwer OR, Klop WM, Buckle T, Vermeeren L, van den Brekel MW, Balm AJ, Nieweg OE, Valdés-Olmos RA, van Leeuwen FWB. Feasibility of Sentinel Node Biopsy in Head and Neck Melanoma Using a Hybrid Radioactive and Fluorescent Tracer. *Ann Surg Oncol.* 2012 Jun; 19(6): 1988-1994
- 27 van den Berg NS, Brouwer OR, Klop WM, Karakullukcu B, Zuur CL, Tan IB, Balm AJ, van den Brekel MW, Valdés-Olmos RA, van Leeuwen FWB. Concomitant radio- and fluorescence-guided sentinel lymph node biopsy of the oral cavity using ICG-(99m) Tc-nanocolloid. *Eur J Med Mol Imaging.* 2012 Jul; 39(7): 1128-1136
- 28 Brouwer OR, Buckle T, Vermeeren L, Klop WM, Balm AJ, van der Poel HG, van Rhijn BW, Horenblas S, Nieweg OE, van Leeuwen FWB, Valdés-Olmos RA. Comparing the hybrid fluorescent-radioactive tracer indocyanine green-99mTc-nanocolloid with 99mTc-nanocolloid for sentinel node identification: A validation study using lymphoscintigraphy and SPECT/CT. *J Nucl Med.* 2012; 53: 1-7
- 29 Hanaoka H, Mukai T, Tamamura H, Mori T, Ishino S, Ogawa K, Iida Y, Doi R, Fujii N, Saji H. Development of a ¹¹¹In-labeled peptide derivative targeting a chemokine receptor, CXCR4, for imaging tumors. *Nucl Med Biol.* 2006; 33: 489-494
- 30 Estey EH. Acute myeloid leukemia: update on diagnosis, risk stratification, and management. *Am J Haematol.* 2012; 87(1): 89-99

- 31 Zare H, Bashashati A, Kridel R, Aghaeepour N, Haffari G, Connors JM, Gascoyne RD, Gupta A, Brinkman RR, Weng AP. Automated analysis of multidimensional flow cytometry data improves diagnostic accuracy between mantle cell lymphoma and small lymphocytic lymphoma. *Am J Clin Pathol.* 2012; 137(1): 75-85
- 32 Nolan GP. Flow cytometry in the post fluorescence era. *Best practice & research. Clin Haematol.* 2011; 24(4): 505-508
- 33 Taly V, Pekin D, El Abed A, Laurant-Puig P. Detecting biomarkers with microdroplet technology. *Trends Mol Med.* 2012; 18(7): 405-416
- 34 Yura H, Ishihara M, Kanatani Y, Takase B, Hattori H, Suzuki S, Kawakami M, Matsui T. Interaction study between synthetic glycoconjugate ligands and endocytic receptors using flow cytometry. *J Biochem.* 2006; 139(4): 637-643
- 35 Hassan S, Ferrario C, Saragovi U, Quenneville L, Gaboury L, Baccarelli A, Salvucci O, Bask M. The influence of tumor-host interactions in the stromal cell-derived factor-1/ CXCR4 ligand/receptor axis in determining metastatic risk in breast cancer. *Am J Pathol.* 2009; 175(1): 66-73
- 36 Chu QD, Holm NT, Madumere P, Johnson LW, Abreo F, Li BD. Chemokine receptor CXCR4 overexpression predicts recurrence for hormone receptor-positive, node-negative breast cancer patients. *Surgery.* 2011; 149(2): 193-199
- 37 Holm NT, Byrnes K, Li BD, Turnage RH, Abreo F, Mathis JM, Chu QD. Elevated levels of chemokine receptor CXCR4 in HER-2 negative breast cancer specimens predict recurrence. *J Surg Res.* 2007; 141(1): 53-59
- 38 Abbey CK, Borowsky AD, McGoldrick ET, Gregg JP, Maglione JE, Cardiff RD, Cherry SR. In vivo positron-emission tomography imaging of progression and transformation in a mouse model of mammary neoplasia. *Proc Natl Ac Sci USA.* 2004; 101(31): 11438-11443

**Interventional
Future perspectives
molecular imaging,
a hybrid approach**

Chapter 14

The initial clinical implementation of the hybrid surgical guidance concept for SLN biopsy procedures was a step in the right direction to achieve clinical benefit from intraoperative fluorescence imaging. Nevertheless, the widespread development of surgical fluorescence camera's and the development and clinical implementation of new imaging agents are essential for further improvement of surgical efficacy. Current efforts that focus on fine-tuning of the clinical utility of the developed technology include: i) visualization of tumor induced angiogenesis using hybrid targeting imaging agents, ii) tumor bracketing and margin estimation, and iii) image navigation. All may facilitate a broader implementation of the hybrid surgical guidance concept, and as such, open doors for new (hybrid) imaging applications.

Visualization of tumor induced angiogenesis using hybrid targeting imaging agents

The CXCR4-based hybrid imaging approach can be further expanded by including a different targeting moiety. In recent years, numerous tumor targeting imaging agents have been developed, but besides MSAP-Ac-TZ14011 only hybrid agents that target the human epidermal growth factor receptor 2 (HER2) or prostate specific membrane antigen (PSMA) have been described for use in surgical guidance. Where biomarkers like HER2 and PSMA are only expressed in a specific type of cancer, e.g. respectively in breast and prostate cancer, overexpression of $\alpha\beta3$ integrin is involved in the more common event of (tumor-induced) angiogenesis. Therefore $\alpha\beta3$ integrin would be a more widely applicable candidate for the specific visualization of tumor tissue. Using a hybrid arginine-glycine-aspartate (RGD) derivative (^{111}In -MSAP-RGD) that targets $\alpha\beta3$ integrin, we have shown the potential of this biomarker in targeted hybrid imaging applications. Both the primary tumor and distant metastases could be preoperatively detected with single photon computed tomography/computed tomography (SPECT/CT).¹ Intraoperatively, the primary tumor and metastases could be detected with fluorescence imaging (Figure 1). As $\alpha\beta3$ integrin is expressed in angiogenic regions of the tumor, this targeting strategy is optimal for improving tumor margin delineation, which might possibly aid the surgical excision of a lesion.

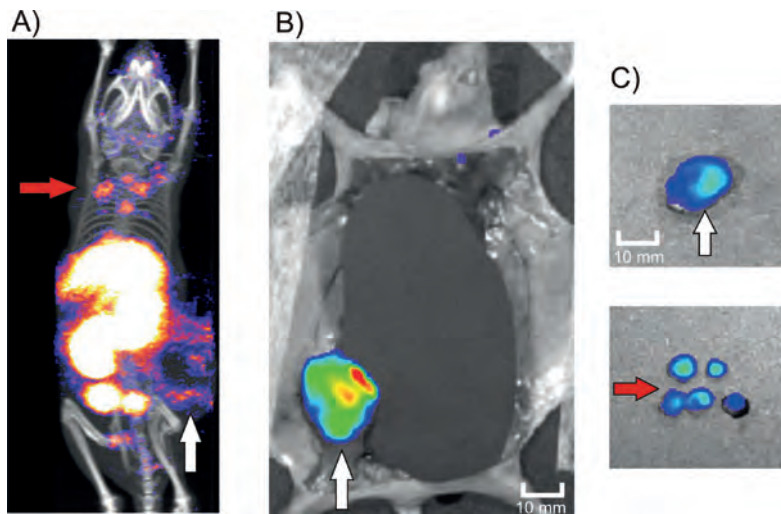


Figure 1. Surgical guidance toward the margins of the primary tumor and distant metastases. A) SPECT/CT image depicting both the rim around the primary tumor and distant metastases in the neck area. B) Fluorescence imaging depicting the margins of the primary tumor. Note that the organs are shielded. C) Ex vivo fluorescence imaging of the tumor and metastases.

Tumor bracketing and margin estimation

Clinically, tumor lesions can be marked before surgical removal, e.g. in breast cancer, and are preferably excised with a surgical safety margin of 0.5 – 1.0 cm to prevent the need for re-excisions. Hybrid marker seeds may extend the use of current tumor marking approaches, as they can be used to aid in the visualization of these surgical safety margins. We have shown that hybrid marker seeds are applicable during the entire pre-, intra- and postoperative trajectory (Figure 2).² The different properties of hybrid marker seeds can be used for image guided seed placement, verification of the placement accuracy, fluorescence guided excision with the appropriate safety margin and ex vivo verification of original specimen orientation. Via inclusion of a cocktail of contrast agents, all these properties could be incorporated into a single marker that can be detected with e.g. fluorescence imaging, X-ray, ultrasound (US), positron emission tomography (PET), and or SPECT.

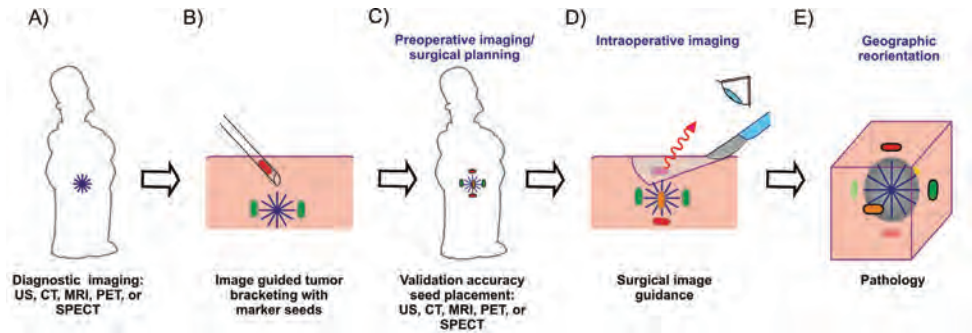


Figure 2. Schematic representation of the combined pre-, intra- and postoperative imaging paradigm that can be achieved with hybrid marker seeds. A) Diagnostic imaging procedure. B) Image-guided placement of tumor bracketing with marker seeds. C) Preoperative validation of the accuracy of marker placement. D) Intraoperative optical detection of the markers. E) Geographical (re)orientation of the excised tissue section at pathology.

Phantom experiments with hybrid markers showed their potential in margin estimation.² Use of a dual emissive fluorescent dye (InP/ZnS quantum dots)³ provided the unique opportunity to intraoperatively estimate the depth at which the seed was placed in the tissue.² By using particles with different visible colors, the original geographic orientation of the excised tissue could be determined. Where the dual emissive dye could be used to estimate marker depth using two emissions, the same can be achieved by using two standard fluorescent dyes with different levels of tissue penetration in a single marker.⁴ More rapid approval for a clinical use of this concept is probably most easily obtained using already clinically applied contrast media like the fluorescent dyes FITC and ICG.

Image navigation

Even when fluorescence imaging is combined with preoperative surgical planning based on SPECT/CT and intraoperative gamma ray detection, surgical orientation of e.g. SLNs can still be difficult. More accurate navigation toward the areas of interest could therefore help optimize surgical guidance.

Other than real time US, CT and or MRI guidance, surgical navigation based on a preoperative data set is traditionally performed during rigid procedures in the brain and orthopedics. In soft, non-rigid, areas movements occurring during the intervention may significantly impair the navigation accuracy. Although this approach remains highly challenging, hybrid imaging agents may help overcome this shortcoming of the navigation process. The fluorescence signal, which is not able to penetrate through more than one

cm of tissue, provides a real-time optical read-out for the navigation accuracy. While the technology is likely to remain limited to more rigid areas such as the pelvic area, this expansion with navigation may have major impact in the field of surgical guidance.

Initial pilot experiments show that navigation of a fluorescence laparoscope based on 3D SPECT/CT images is feasible and may improve intraoperative localization of areas that were defined to be of interest on SPECT/CT (Figure 3).⁵

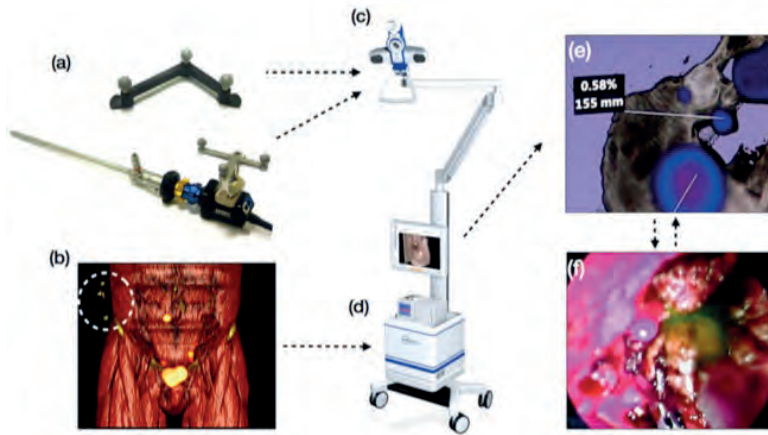


Figure 3. Hybrid imaging approach. A) The set-up includes two different input systems: the reference targets are placed on the patient and fluorescence endoscope. B) The preoperative SPECT/CT images are acquired with a fixed reference target placed on a rigid structure on the patient/phantom (white circle). C) An optimal tracking system (OTS) determines the pose of the reference targets. D,E) The preoperative SPECT/CT and the poses determined by the OTS are processed by the data-processing unit to a virtual view of the SPECT/CT images from the perspective of the endoscope. F) Navigation of the tracked fluorescence endoscopes toward the target identified on SPECT/CT results in real-time gradual visualization of the fluorescent signal on a second display, thus providing confirmation of the navigation accuracy.

Obviously, implementation of the hybrid surgical guidance concept is not limited to the field of oncology. For instance, the hybrid concept can possibly also be applied in visualization of critical structures such as nerves where specific targeting agents can be used in sparing the structures during surgical excisions or in the assessment of the presence of functional damage.

References

- 1 Bunschoten A#, Buckle T#, Visser N, Yuan H, Josephson L, Vahrmeijer AL, van Leeuwen FWB. Multimodal interventional molecular imaging of tumor margins and distant metastases using the $\alpha\beta3$ -integrin expression. *ChemBioChem*. 2012; 13(7): 1039-1045 (# authors contributed equally)
- 2 Buckle T, Chin PT, van den Berg NS, Loo CE, Koops W, Gilhuijs KG, van Leeuwen FWB. Tumor bracketing and safety margin estimation using multimodal marker seeds: a proof of concept. *J Biomed Opt*. 2010; 15(5): 056021
- 3 Chin PT, Buckle T, Aguirre de Miguel A, Meskers SC, Janssen RA, van Leeuwen FWB. Dual-emissive quantum dots for multispectral intraoperative fluorescence imaging. *Biomaterials*. 2010; 31(26): 6823-6832
- 4 Chin PTK, Beekman AC, Buckle T, Josephson L, van Leeuwen FWB. Multispectral visualization of surgical safety margins using fluorescent marker seeds. *Am J Nucl Med Mol Imaging*. 2012; 2(2): 151-162
- 5 Brouwer OR, Buckle T, Bunschoten A, Kuil J, Wendler T, Vahrmeijer AL, Valdés-Olmos RA, van der Poel HG, van Leeuwen FWB. Image navigation as a means to improve the accuracy of fluorescence guided surgery: fine tuning (hybrid) image guided surgery. *Phys Med Biol*. 2012; 57: 3123 -3136

Interventional molecular imaging, a hybrid approach

Summary

Chapter 15

In this thesis the use of (hybrid) imaging agents in combined pre- and intraoperative detection of the sentinel lymph node (SLN) and during evaluation of the chemokine receptor 4 (CXCR4) expression levels were discussed. A summary is provided below.

Part I: Hybrid guidance for sentinel lymph node biopsy

SLN biopsy presents physicians with the opportunity to detect early metastatic disease. Radiocolloids such as ^{99m}Tc -nanocolloid are currently used to preoperatively identify SLNs and to provide acoustic gamma probe guidance during their resection. To enable optical guidance, additional dyes are commonly injected during surgery. In **Chapter 2 to 7** new surgical guidance methods that integrate preoperative SLN identification with intraoperative optical detection were discussed.

Chapter 2

Non-targeted hybrid nanoparticles represent a relatively unexploited area of chemical/nanotechnological development. In the field of nanotechnology the SLN biopsy procedure is appealing, as diagnostics of the SLN provide a clear clinical precedent where nano-sized molecules (10 – 100 nm) are preferred. Nano-sized particles induce sufficient retention in the SLN, after which the fluorescent dyes and radiolabels attached to these particles can be detected in the lymph node. A good example is the hybrid radiocolloid ICG- ^{99m}Tc -nanocolloid, which is formed after the mixing the clinically applied components ^{99m}Tc -nanocolloid and the fluorescent dye indocyanine green (ICG).

Chapter 3

In an orthotopic mouse model for metastatic breast cancer the dynamics of ^{99m}Tc -nanocolloid, ICG and ICG- ^{99m}Tc -nanocolloid were studied. It was shown that in mice the drainage and retention pattern of both the parental and the hybrid radiocolloids were highly similar, while free ICG was rapidly cleared.

Chapter 4

The potential of combined pre- and intraoperative imaging using ICG- ^{99m}Tc -nanocolloid was further evaluated in a spontaneous mouse prostate tumor model. To provide a more translational tracer formulation, in this study a cocktail-solution of imaging agents was used. The stability of the hybrid radiocolloid was found to be higher than that

of the non-colloidal ICG-^{99m}Tc-human serum albumin complex. Furthermore, in this Chapter the first (ex vivo) patient data were presented.

Results from the two preclinical studies (**Chapter 3 and 4**) revealed that in mice the hybrid approach helped improve fluorescence based guidance and enabled both accurate surgical planning and intraoperative detection, based on a single injection.

Chapter 5

In a reproducibility study in 25 patients with melanoma in the head and neck region, the trunk, or with penile carcinoma, a clinical comparison between lymphoscintigraphic drainage patterns of the European gold standard ^{99m}Tc-nanocolloid and the hybrid imaging agent ICG-^{99m}Tc-nanocolloid was made. Similar to the preclinical situation, this study revealed identical drainage patterns.

Chapter 6

The added value of ICG-^{99m}Tc-nanocolloid during laparoscopic procedures was shown in eleven patients who underwent a robot-assisted laparoscopic prostatectomy and lymph node dissection. Preoperatively, SLNs could be identified with lymphoscintigraphy and with single photon emission computed tomography combined with computed tomography (SPECT/CT). The hybrid nature of the imaging agent enabled intraoperative SLN identification via fluorescence imaging. During surgery, radioguidance and fluorescence detection proved to be complementary; Fluorescence particularly improved surgical guidance in areas with a high radioactive background signal such as the injection site, whereas radioguidance was found to supplement the limiting tissue penetration of the fluorescence signal.

Chapter 7

An additional benefit of ICG-^{99m}Tc-nanocolloid is that the optical component can also be exploited in ex vivo applications. Ex vivo fluorescence imaging was used to determine the location of ICG-^{99m}Tc-nanocolloid injection deposits in embedded prostate samples. It was found that the location of the deposits of the imaging agent correlates with the lymphatic drainage pattern as seen preoperatively on lymphoscintigraphy. From these results it could be concluded that the location of intraprostatic deposition of the imaging agent influenced the lymphatic drainage pattern, and as such, the SLN procedure as a whole.

Part II: CXCR4 targeting applications

For specific visualization of tumor cells, imaging agents that target a biomarker expressed on a tumor cell are of value. The biomarker CXCR4 is overexpressed in many types of cancer and is an emerging target in the field of molecular imaging and therapeutics. Preclinical evaluation of differently labeled Ac-TZ14011 peptide based CXCR4 targeting imaging agents, including hybrid derivatives, were discussed in **Chapter 8 to 13**.

Chapter 8

During evaluation of a targeting imaging agent, both the preclinical set-up and the receptor affinity of the imaging agent are of influence on the obtained results. Transfected cell lines with (very) high levels of CXCR4 expression can best be used for the initial evaluation of an imaging agent. When binding to the receptor has been verified, models with a level of overexpression that is more comparable to the five-fold overexpression found in the clinical situation should be used for further evaluation. The CXCR4 receptor affinity of Ac-TZ14011 peptide derivatives can be influenced by the addition of an imaging label. While these charge and/or size related alterations slightly decrease the affinity for the receptor, it still remains in the nanomolar range and thus sufficient for in vivo use.

Chapter 9

Functionalization of Ac-TZ14011 with the fluorescent dye FITC enabled evaluation of CXCR4 expression levels and receptor localization in vitro in breast cancer cells. CXCR4 staining was predominantly found on the membrane of the cell and/or in vesicles formed after endocytosis. Ac-TZ14011-FITC enabled discrimination between cells with only a four-fold difference in CXCR4 expression. Furthermore, the efficacy of Ac-TZ14011-FITC was comparable to commercially available anti-CXCR4-antibodies.

Chapter 10

An indium labeled version of the Ac-TZ14011 peptide (^{111}In -DTPA-Ac-TZ14011) could be used to evaluate CXCR4 expression levels in a MIN-O mouse tumor model that resembles human ductal carcinoma in situ. Longitudinal assessment of CXCR4 expression during lesions development enabled discrimination between early preinvasive tumor lesions, intermediate and late stage invasive MIN-O tumor lesions. In the MIN-O lesions membranous CXCR4 expression was heterogeneous and receptor expression levels increased during lesion progression.

Chapter 11

Addition of a multifunctional single attachment point reagent (MSAP) that contains both a DTPA chelate and a fluorescent dye resulted in a hybrid version of Ac-TZ14011 (MSAP-Ac-TZ14011). Functionalization of Ac-TZ14011 with the MSAP label resulted in a lower affinity for the CXCR4 receptor compared to the unlabeled peptide. However, the affinity was similar to that found after functionalization with either the FITC or DTPA label, and allowed for visualization of CXCR4 in both the pre- and intraoperative setting.

Chapter 12

Multimerization could be used to minimize the negative influence of the MSAP label on the binding affinity of Ac-TZ14011. Unlabeled, the CXCR4 affinity of the dimer and tetramer was somewhat lower than the affinity of the monomer. When labeled with the hybrid label the CXCR4 affinity of the dimer and tetramer increased. Distribution studies revealed that the presence of additional peptides reduced non-specific uptake.

Chapter 13

The hybrid imaging concept was further extended by using the fluorescent beacon on MSAP-Ac-TZ14011 to study the presence of the CXCR4 receptor in fresh tumor tissue biopsy specimens. Flow cytometric analysis of these tumor specimens revealed different CXCR4 positive populations and could be used to accurately stage the progression of MIN-O lesions. These findings were shown to accurately predict visualization of tumor tissue using imaging methods such as SPECT/CT and fluorescence imaging. Furthermore, the fluorescent signature could be used to validate the CXCR4 staining in tumor samples *ex vivo*. As such, the hybrid nature of MSAP-Ac-TZ14011 enabled integration of biomarker screening, *in vivo* and *ex vivo* validation of tumor tissue using a single agent.

Chapter 14 (Future perspectives)

Further development of fluorescence camera's and development and clinical implementation of new imaging agents are essential for improvement of surgical accuracy. Current efforts have been focused on fine-tuning of the utility of the hybrid surgical guidance concept described in this thesis.

The biomarker specific hybrid approach can also be applied for other biomarkers, for instance $\alpha\beta3$ integrin. ^{111}In -MSAP-RGD, which binds to $\alpha\beta3$ integrin can be used to visualize tumor margins and metastases.

(Breast) tumors can be marked with marker seeds to improve localization during surgery. Hybrid marker seeds can be used to expand the currently applied marking approach. The fluorescent features can be used for estimation of surgical safety margins.

Even when fluorescence is combined with preoperative imaging and intraoperative detection of gamma rays, surgical identification of deeply situated SLNs can still be difficult. Pilot experiments have shown that navigation of a fluorescence laparoscope based on 3D SPECT/CT images is feasible and can possibly be used to further optimize surgical guidance.

Conclusion

The results described in this thesis demonstrate the potential of hybrid imaging agents in the translation of preoperative findings to the operating room. The hybrid concept was shown to be of additional value during clinical SLN biopsy procedures and during the visualization of tumor cells in a preclinical setting. Current expansions of this exciting research field are expected to further increase the applicability of hybrid imaging agents.

**Interventional
molecular imaging,
a hybrid approach**

**Dutch summary
Nederlandse samenvatting**

Chapter 16

In dit proefschrift is het gebruik van (hybride) contrastmiddelen voor gecombineerde pre- en intra-operatieve detectie van de schildwachtklier (sentinel lymph node; SLN), en voor evaluatie van het expressie niveau van de chemokine receptor 4 (CXCR4) in tumor weefsel besproken. Een samenvatting vindt u hieronder.

Deel I: Hybride geleiding van de SLN biopsie

Een biopsie van de SLN maakt vroege detectie van gemetastaseerde ziekte in het lymfesysteem mogelijk. Radioactief gelabelde nanodeeltjes, zoals technetium gelabelde albumine aggregaten (^{99m}Tc -nanocolloïd), worden momenteel gebruikt voor het preoperatief identificeren van de SLN. Tijdens de interventie kan dit radioactieve signaal gebruikt worden voor akoestische geleiding met behulp van een gamma stralen detector. Voor optische chirurgische geleiding worden veelal extra kleurstoffen geïnjecteerd tijdens de ingreep. Gebruik van deze kleurstoffen resulteert echter veelal niet tot verbeterde detectie van de SLN. Nieuwe chirurgische geleidingsmethoden die preoperatieve identificatie van de SLN integreren met intra-operatieve optische detectie zijn besproken in **Hoofdstuk 2 t/m 7**.

Hoofdstuk 2

Ontwikkeling van niet biomarker gerichte hybride nanodeeltjes vormt een relatief nieuwe tak van onderzoek binnen de chemie/nanotechnologie. Binnen dit onderzoeksveld vormt de SLN biopsie een aantrekkelijke toepassing, aangezien er tijdens de diagnostiek van de SLN een duidelijke voorkeur is voor deeltjes met het formaat van 10-100 nm. Dit formaat zorgt voor voldoende retentie in de SLN, waardoor de (fluorescente) kleurstoffen en radiolabels die gekoppeld zijn aan dit deeltje ook in de lymfeklier kunnen worden gedetecteerd. Een goed voorbeeld hiervan is het hybride ICG- ^{99m}Tc -nanocolloïd, dat bestaat uit een complex van het reeds klinisch toegepaste radioactief gelabelde humaan serum albumine complex nanocolloïd en de fluorescente kleurstof Indocyanine groen (ICG).

Hoofdstuk 3

De dynamiek van ^{99m}Tc -nanocolloïd, ICG, en ICG- ^{99m}Tc -nanocolloïd is bestudeerd in een orthotoop muismodel voor metastaserende borstkanker. Deze studie toont aan dat de drainage en het retentie patroon van beide radiocolloïden in muizen vergelijkbaar zijn, terwijl vrij ICG snel geklaard wordt.

Hoofdstuk 4

De potentie van gecombineerde pre- en intra-operatieve beeldvorming met behulp van het hybride ICG-^{99m}Tc-nanocolloïd is verder geëvalueerd in een spontaan muis model voor prostaatkanker. Gebruik van een mengsel van de fluorescente kleurstof en het radiocolloïd zorgde voor een meer translationele formulering van het contrastmiddel. De stabiliteit van het hybride radiocolloïd bleek groter te zijn dan de stabiliteit van een niet-colloïdaal ICG-^{99m}Tc-humaan serum albumine complex. In dit hoofdstuk werden bovendien de eerste (ex vivo) resultaten in patiënten gepresenteerd.

De resultaten van de twee preklinische studies (**Hoofdstuk 3 en 4**) laten zien dat de hybride aanpak bijdraagt aan de verbetering van de op fluorescentie gebaseerde intra-operatieve geleiding. Tevens kon gecombineerde chirurgische planning en intra-operatieve detectie bewerkstelligd worden op basis van een enkele injectie met ICG-^{99m}Tc-nanocolloïd.

Hoofdstuk 5

In een reproduceerbaarheidsstudie waarin 25 patiënten met een melanoom in het hoofd-halsgebied, de romp, of met peniscarcinoom zijn geïnculdeerd, werd een klinische vergelijking gemaakt tussen de lymfatische drainage patronen van de Europese gouden standaard ^{99m}Tc-nanocolloïd en ICG-^{99m}Tc-nanocolloïd. Vergelijkbaar met de resultaten van de preklinische situatie, werden identieke drainage patronen gevonden voor beide contrastmiddelen.

Hoofdstuk 6

De toegevoegde waarde van ICG-^{99m}Tc-nanocolloïd tijdens laparoscopische procedures werd aangetoond in elf patiënten waarbij een robot geassisteerde laparoscopische prostatectomie werd uitgevoerd, in combinatie met een lymfeklier dissectie. Pre-operatief kon de SLN worden geïdentificeerd aan de hand van de verkregen lymfoscintigrammen en de SPECT/CT beelden, terwijl het hybride karakter van het contrastmiddel intra-operatieve optische identificatie van de SLN mogelijk maakte door middel van fluorescentie beeldvorming. Tijdens de ingreep bleken detectie van het radioactieve en fluorescentie signaal complementair; Fluorescentie verbeterde de chirurgische geleiding in gebieden met een hoog radioactief achtergrond signaal, zoals rond de plaats van injectie. Radiogeleiding werd gebruikt als aanvulling op de beperkte weefselpenetratie van het fluorescentie signaal.

Hoofdstuk 7

Een additionele eigenschap van ICG-^{99m}Tc-nanocolloïd is dat de optische component gebruikt kan worden voor de ex vivo evaluatie van de locatie van het ICG-^{99m}Tc-nanocolloïd injectie depot. Door met fluorescentie beeldvorming de locatie van de injectie deposito's in ingebedde prostaat monsters te bepalen, en deze direct te linken aan het lymfedrainage patroon zoals preoperatief gezien op lymfoscintigrafie, kon een correlatie tussen beiden worden aangetoond. Uit de resultaten van deze studie kon worden geconcludeerd dat de plaatsing van de injectie in de prostaat het lymfedrainage patroon beïnvloedt, en als zodanig van invloed is op de SLN biopsie procedure als geheel.

Deel II: Chemokine recetor 4 (CXCR4) gerichte toepassingen

Voor de visualisatie van tumorcellen moet men gebruik maken van beeldvormende technieken die een specifieke biomarker op een tumorcel zichtbaar maakt. CXCR4 is een biomarker die tot over-expressie wordt gebracht in verschillende soorten kanker en is een opkomend target binnen de moleculaire beeldvorming een target voor therapie. De pre-klinische evaluatie van verschillend gelabelde contrastmiddelen gericht tegen CXCR4, gebaseerd op het aan CXCR4 bindende peptide Ac-TZ14011, zijn besproken in **hoofdstuk 8 t/m 13**.

Hoofdstuk 8

Bij de beoordeling van een (hybride) biomarker specifiek contrastmiddel zijn zowel de pre-klinische set-up als de affiniteit van de probe voor de receptor van invloed op de verkregen resultaten. Getransfecteerde cellijnen met zeer hoge CXCR4 expressie niveaus kunnen gebruikt worden voor de initiële evaluatie van een contrastmiddel. Tumor modellen met een over-expressie niveau dat beter vergelijkbaar is met de viervoudige over-expressie die gevonden is in de klinische situatie, kunnen het beste gebruikt worden om de klinische relevantie van contrastmiddelen voor CXCR4 te bestuderen.

De affiniteit van Ac-TZ14011 peptide derivaten voor CXCR4 kan worden beïnvloed door de toevoeging van een fluorescent label of een radio label. Toevoeging van een label veroorzaakt een afname in affiniteit voor de receptor. De affiniteit blijft echter in alle gevallen voldoende voor gebruik in vivo.

Hoofdstuk 9

Door functionalisatie van Ac-TZ14011 met de fluorescente kleurstof FITC konden in vitro, in borstkanker cellen, CXCR4 receptor expressie niveaus en de lokalisatie van de receptor geëvalueerd worden. CXCR4 bleek voornamelijk aanwezig te zijn op het celmembraan en/of in endosomen/lysosomen in het cytoplasma na het optreden van endocytose. Met Ac-TZ14011-FITC konden cellen met slechts een viervoudige overexpressie van CXCR4 worden onderscheiden van normale tumorcellen. Bovendien bleek de aankleuring na incubatie met Ac-TZ14011-FITC vergelijkbaar met de aankleuring die verkregen wordt na incubatie met commercieel verkrijgbare anti-CXCR4-antilichamen.

Hoofdstuk 10

Een indium gelabelde variant van het Ac-TZ14011 peptide (^{111}In -DTPA-Ac-TZ14011) maakte evaluatie van CXCR4 expressie niveaus mogelijk in het MIN-O muis tumor model dat vergelijking vertoont met humaan ductaal carcinoom in situ. Op basis van de CXCR4 expressie kon onderscheid worden gemaakt tussen een (pre-invasief) vroeg, overgangs- en een (invasief) laat stadium in de progressie van MIN-O tumorlaesies. De membraneuze CXCR4 expressie bleek heterogeen verdeeld over de tumor en de receptor expressie nam toe gedurende de progressie van de MIN-O laesies.

Hoofdstuk 11

Toevoeging van een groep die zowel het chelaat DTPA als een fluorescerende kleurstof bevat (multifunctional single attachment point reagent; MSAP) leidde tot de vorming van een hybride versie van Ac-TZ14011 (Ac-TZ14011-MSAP). Deze functionalisatie resulteerde in een lagere affiniteit voor de CXCR4 receptor in vergelijking met het niet-gelabelde Ac-TZ14011 peptide. De affiniteit van het hybride contrastmiddel was echter vergelijkbaar met de affiniteit die verkregen was na toevoeging van zowel het FITC- of het DTPA-label aan Ac-TZ14011. Met het MSAP-label was het mogelijk om CXCR4 positieve tumoren te visualiseren in zowel de pre- als intra-operatieve setting.

Hoofdstuk 12

Multimerisatie kan worden gebruikt om de negatieve invloed van het MSAP-label op de bindingsaffiniteit van Ac-TZ14011 te minimaliseren. Terwijl de affiniteit voor CXCR4 van een ongelabelde dimeer en tetrameer iets lager was dan de affiniteit van de ongelabelde

monomeer, werd een vermindering van de specifieke binding gezien voor de MSAP gelabelde dimeer en tetrameer in vergelijking met de MSAP-gelabelde monomeer. De dimeer bleek minder invloed op de levensvatbaarheid van de cellen te hebben en zorgde voor een hogere ratio tussen opname in tumor- en spierweefsel.

Hoofdstuk 13

Het concept van hybride beeldvorming kon verder worden uitgebreid door het fluorescente label van MSAP-Ac-TZ14011 te gebruiken voor het bestuderen van de aanwezigheid van CXCR4 receptoren in vers MIN-O biopsie weefsel. Met behulp van flow cytometrische analyse konden verschillende CXCR4 positieve celpopulaties worden aangetoond, wat een nauwkeurige stadiëring van de laesies mogelijk maakte. Deze bevindingen werden gebruikt om nauwkeurig te voorspellen of in vivo visualisatie van tumor weefsel met behulp van beeldvormende technieken zoals SPECT/CT en fluorescentie detectie haalbaar was. Bovendien kon het fluorescente label ook ex vivo worden gebruikt om de CXCR4 gerelateerde aankleuring in tumormonsters bevestigen. Als zodanig bleek het hybride karakter van MSAP-Ac-TZ14011 geschikt voor integratie van biomarker screening, in vivo beeldvorming en ex vivo validatie van tumor weefsel met behulp van een enkel contrastmiddel.

Hoofdstuk 14 (toekomst visie)

Verdere ontwikkeling van fluorescentie camera's en ontwikkeling en klinische implementatie van nieuwe contrastmiddelen zullen essentieel zijn voor de verdere verbetering van de accuraatheid van een chirurgische ingreep. Momenteel wordt er op verschillende manieren geprobeerd om het in dit proefschrift beschreven hybride concept verder te optimaliseren en/of uit te breiden.

De biomarker specifieke hybride imaging aanpak kan ook worden toegepast voor andere biomarkers, bijvoorbeeld $\alpha_v\beta_3$ integrine. Via deze benadering kunnen met ^{111}In -MSAP-RGD, welke gericht is tegen $\alpha_v\beta_3$ integrine, zowel tumor marges als metastasen zichtbaar gemaakt worden.

(Borst) tumoren kunnen worden gemerkt met bv. markeringszaadjes om chirurgische lokalisatie te vergemakkelijken. Hybride markeringszaadjes kunnen worden gebruikt voor het uitbreiden van de huidige markeringsmethodes en de fluorescentie eigenschappen kunnen worden gebruikt voor het inschatten van de chirurgische veiligheidsmarges.

Zelfs wanneer fluorescentie gecombineerd wordt met pre-operatieve beeldvorming en intra-operatieve detectie van gamma stralen, kan de chirurgische identificatie van bijvoorbeeld diepliggende SLNs nog steeds moeilijk zijn. Pilot experimenten hebben laten zien dat, op 3D SPECT/CT gebaseerde, navigatie van een fluorescentie laparoscopie haalbaar is en mogelijk de chirurgische geleiding verder kan optimaliseren.

Conclusie

De resultaten beschreven in dit proefschrift laten het potentieel zien van hybride contrastmiddelen in de translatie van preoperative bevindingen naar de operatiekamer. Het hybride concept bleek van aanvullende waarde tijdens klinische SLN-biopsie procedures. Hiernaast is dit hybride concept preklinisch ook al succesvol toegepast voor de specifieke visualisatie van tumor cellen.

Interventional molecular imaging, a hybrid approach

List of publications

- 1 Kuil J, **Buckle T**, van Leeuwen FWB. Imaging agents for the chemokine receptor 4 (CXCR4). *Chem Soc Rev.* 2012 7; 41(15): 5239-5261
- 2 **Buckle T**, Brouwer OR, Valdés-Olmos RA, van der Poel HG, van Leeuwen FWB. Relation between intraprostatic tracer deposits and sentinel lymph node mapping in prostate cancer patients. *J Nucl Med.* 2012; 53: 1026-1033
- 3 Brouwer OR, **Buckle T**, Vermeeren L, Klop WMC, Balm AJM, van der Poel HG, van Rhijn BW, Horenblas S, Nieweg OE, van Leeuwen FWB, Valdés-Olmos RA. Comparing the Hybrid Fluorescent-Radioactive Tracer Indocyanine Green-99mTc-Nanocolloid with 99mTc-Nanocolloid for Sentinel Node Identification: A Validation Study Using Lymphoscintigraphy and SPECT/CT. *J Nucl Med.* 2012; 53: 1034-1040
- 4 Brouwer OR, **Buckle T**, Bunschoten A, Kuil J, Wendler T, Vahrmeijer AL, Valdés-Olmos RA, van der Poel HG, van Leeuwen FWB. Image navigation as a means to improve the accuracy of fluorescence guided surgery: fine tuning (hybrid) image guided surgery. *Phys Med Biol.* 2012; 57: 3123
- 5 Brouwer OR, Klop MWC, **Buckle T**, van den Brekel MWM, Balm FJM, Nieweg OE, Valdés-Olmos RA, van Leeuwen FWB. Feasibility of sentinel node biopsy in head and neck melanoma using a hybrid radioactive and fluorescent tracer. *Ann Surg Oncol.* 2012; 19(6): 1988-1994
- 6 Bunschoten A#, **Buckle T**#, Visser N, Yuan H, Josephson L, Vahrmeijer AL, van Leeuwen FWB. Multimodal interventional molecular imaging of tumor margins and distant metastases using the $\alpha_v\beta_3$ -integrin expression. *ChemBioChem.* 2012; 13(7): 1039-1045 (# authors contributed equally)
- 7 **Buckle T**, van den Berg NS, Kuil J, Bunschoten A, Oldenburg J, Borowsky AD, Wesseling J, Masada R, Oishi S, Fujii N, van Leeuwen FWB. In vivo imaging of CXCR4 in breast cancer using an ^{111}In labeled peptide antagonist. *Am J Nucl Med Mol Imaging.* 2012; 2(1): 99-109
- 8 Steunenbergh P, Ruggi A, van den Berg NS, Kuil J, **Buckle T**, van Leeuwen FWB, Velders AH. Synthesis, cellular uptake and localization of luminescent amino-acid functionalized tris(phenylpyridine)iridium(III) complexes. *Inorg Chem.* 2012; 51: 2105-2114
- 9 Chin PTK, Beekman CA, **Buckle T**, Josephson L, van Leeuwen FWB. Multispectral visualization of surgical safety-margins using multimodal marker seeds. *Am J Nucl Med Mol Imaging.* 2012; 2(2): 151-162

- 10 Bunschoten A, **Buckle T**, Kuil J, Luker GD, Luker KE, Nieweg OE, van Leeuwen FWB. Targeted non-covalent self-assembled nanoparticles based on human serum albumin. *Biomaterials*. 2012; 33(3): 867-875
- 11 de Vries NA, **Buckle T**, Zhao J, Beijnen JH, Schellens JH, van Tellingen O. Restricted brain penetration of the tyrosine kinase inhibitor erlotinib due to the drug transporters P-gp and BCRP. *Invest New Drugs*. 2012; 30(2): 443-449
- 12 van der Poel HG, Brouwer OR, van den Berg NS, **Buckle T**, van Leeuwen FWB. Reply to K. Polom, D. Murawa, W. Polom's Letter to the Editor re: Henk G. van der Poel, Tessa Buckle, Oscar R. Brouwer, Renato A. Valdés-Olmos, Fijs W.B. van Leeuwen. Intraoperative Laparoscopic Fluorescence Guidance to the Sentinel Lymph Node in Prostate Cancer Patients: Clinical Proof of Concept of an Integrated Functional Imaging Approach Using a Multimodal Tracer. *Eur Urol*. 2011; 60: 826-833
- 13 Kuil J, **Buckle T**, Oldenburg J, Yuan H, Borowsky AD, Josephson L, van Leeuwen FWB. Hybrid Peptide dendrimers for imaging of chemokine receptor 4 (CXCR4) expression. *Mol Pharm*. 2011; 8(6): 2444-2453
- 14 van den Berg NS#, **Buckle T**#, Kuil J, Wesseling J, van Leeuwen FWB. Immunohistochemical detection of the CXCR4 expression in tumor tissue using the fluorescent peptide antagonist Ac-TZ14011-FITC. *Transl Oncol*. 2011; 4(4): 234-240 (#authors contributed equally)
- 15 Kuil J#, **Buckle T**#, Yuan H, van den Berg NS, Oishi S, Fujii N, Josephson L, van Leeuwen FWB. Synthesis and evaluation of a bimodal CXCR4 antagonistic peptide. *Bioconjug Chem*. 2011; 22(5): 859-864. (# authors contributed equally)
- 16 van der Poel HG, **Buckle T**, Brouwer OR, Valdés Olmos RA, van Leeuwen FWB. Intraoperative laparoscopic fluorescence guidance to the sentinel lymph node in prostate cancer patients: clinical proof of concept of an integrated functional imaging approach using a multimodal tracer. *Eur Urol*. 2011; 60(4): 826-833
- 17 van Leeuwen AC#, **Buckle T**#, Bendle G, Vermeeren L, Valdés-Olmos RA, van de Poel HG, van Leeuwen FWB. Tracer-cocktail injections for combined pre- and intraoperative multimodal imaging of lymph nodes in a spontaneous mouse prostate tumor model. *J Biomed Opt*. 2011; 16(1): 016004. (# authors contributed equally)
- 18 Beekman CAC#, **Buckle T**#, van Leeuwen AC, Valdés-Olmos RA, Verheij M, Rottenberg S, van Leeuwen FWB. Questioning the value of (99m)Tc-HYNIC-annexin V based response monitoring after docetaxel treatment in a mouse model for hereditary breast cancer. *Appl Radiat Isot*. 2011; 69(4): 656-62. (# authors contributed equally)

- 19 **Buckle T**, Chin PT, van Leeuwen FWB. (Non-targeted) radioactive/fluorescent nanoparticles and their potential in combined pre- and intraoperative imaging during sentinel lymph node resection. *Nanotechnology*. 2010; 21(48): 482001
- 20 **Buckle T**, Chin PT, van den Berg NS, Loo CE, Koops W, Gilhuijs KG, van Leeuwen FWB. Tumor bracketing and safety margin estimation using multimodal marker seeds: a proof of concept. *J Biomed Opt*. 2010; 15(5): 056021
- 21 **Buckle T**, van Leeuwen AC, Chin PT, Janssen H, Muller SH, Jonkers J, van Leeuwen FWB. A self-assembled multimodal complex for combined pre- and intraoperative imaging of the sentinel lymph node. *Nanotechnology*. 2010; 21(35): 355101
- 22 van Leeuwen FWB, **Buckle T**, Batteau L, Pool B, Sinaasappel M, Jonkers J, Gilhuijs KG. Potential value of color-coded dynamic breast-specific gamma-imaging; comparing (99m)Tc-(V)-DMSA, (99m)Tc-MIBI, and (99m)Tc-HDP in a mouse mammary tumor model. *Appl Radiat Isot*. 2010; 68(12): 2117-2124
- 23 Chin PT, **Buckle T**, Aguirre de Miguel A, Meskers SC, Janssen RA, van Leeuwen FWB. Dual-emissive quantum dots for multispectral intraoperative fluorescence imaging. *Biomaterials*. 2010; 31(26): 6823-6832
- 24 de Vries NA, Bruggeman SW, Hulsman D, de Vries HI, Zevenhoven J, **Buckle T**, Hamans BC, Leenders WP, Beijnen JH, van Lohuizen M, Berns AJ, van Tellingen O. Rapid and robust transgenic high-grade glioma mouse models for therapy intervention studies. *Clin Cancer Res*. 2010; 16(13): 3431-3441
- 25 Oostendorp RL, **Buckle T**, Lambert G, Garrigue JS, Beijnen JH, Schellens JH, van Tellingen O. Paclitaxel in self-micro emulsifying formulations: oral bioavailability study in mice. *Invest New Drugs*. 2011; 29(5): 768-776
- 26 **Buckle T**, van Leeuwen FWB. Validation of intratracheal instillation of lung tumour cells in mice using single photon emission computed tomography/computed tomography imaging. *Lab Anim*. 2010; 44(1): 40-45
- 27 Beumer JH, Franke NE, Tolboom R, **Buckle T**, Rosing H, Lopez-Lazaro L, Schellens JH, Beijnen JH, van Tellingen O. Disposition and toxicity of trabectedin (ET-743) in wild-type and *mdr1* gene (P-gp) knock-out mice. *Invest New Drugs*. 2010; 28(2): 145-155
- 28 van Leeuwen FWB, **Buckle T**, Kersbergen A, Rottenberg S, Gilhuijs KG. Noninvasive functional imaging of P-glycoprotein-mediated doxorubicin resistance in a mouse model of hereditary breast cancer to predict response, and assign P-gp inhibitor sensitivity. *Eur J Nucl Med Mol Imaging*. 2009; 36(3): 406-412

-
- 29 Niers TM, Brüggemann LW, Klerk CP, Muller FJ, **Buckle T**, Reitsma PH, Richel DJ, Spek CA, Van Tellingen O, Van Noorden CJ. Differential effects of anticoagulants on tumor development of mouse cancer cell lines B16, K1735 and CT26 in lung. *Clin Exp Metastasis*. 2009; 26(3): 171-178
 - 30 Marchetti S, de Vries NA, **Buckle T**, Bolijn MJ, van Eijndhoven MA, Beijnen JH, Mazzanti R, van Tellingen O, Schellens JH. Effect of the ATP-binding cassette drug transporters ABCB1, ABCG2, and ABCC2 on erlotinib hydrochloride (Tarceva) disposition in in vitro and in vivo pharmacokinetic studies employing Bcrp1-/-/Mdr1a/1b-/- (triple-knockout) and wild-type mice. *Mol Cancer Ther*. 2008; 7(8): 2280-2287
 - 31 Oostendorp RL, **Buckle T**, Beijnen JH, van Tellingen O, Schellens JH. The effect of P-gp (Mdr1a/1b), BCRP (Bcrp1) and P-gp/BCRP inhibitors on the in vivo absorption, distribution, metabolism and excretion of imatinib. *Invest New Drugs*. 2009; 27(1): 31-40
 - 32 de Vries NA, Zhao J, Kroon E, **Buckle T**, Beijnen JH, van Tellingen O. P-glycoprotein and breast cancer resistance protein: two dominant transporters working together in limiting the brain penetration of topotecan. *Clin Cancer Res*. 2007; 13(21): 6440-6449
 - 33 Klerk CP, Overmeer RM, Niers TM, Versteeg HH, Richel DJ, **Buckle T**, Van Noorden CJ, van Tellingen O. Validity of bioluminescence measurements for noninvasive in vivo imaging of tumor load in small animals. *Biotechniques*. 2007; 43(1 Suppl): 7-13, 30
 - 34 Bruggeman SW, Hulsman D, Tanger E, **Buckle T**, Blom M, Zevenhoven J, van Tellingen O, van Lohuizen M. Bmi1 controls tumor development in an Ink4a/Arf-independent manner in a mouse model for glioma. *Cancer Cell*. 2007; 12(4): 328-341
 - 35 de Vries NA, Ouwehand M, **Buckle T**, Beijnen JH, van Tellingen O. Determination of topotecan in human and mouse plasma and in mouse tissue homogenates by reversed-phase high-performance liquid chromatography. *Biomed Chromatogr*. 2007; 21(11): 1191-1200
 - 36 Kemper EM, Leenders W, Küsters B, Lyons S, **Buckle T**, Heerschap A, Boogerd W, Beijnen JH, van Tellingen O. Development of luciferase tagged brain tumour models in mice for chemotherapy intervention studies. *Eur J Cancer*. 2006; 42(18): 3294-3303
 - 37 Beumer JH, **Buckle T**, Ouwehand M, Franke NE, Lopez-Lazaro L, Schellens JH, Beijnen JH, van Tellingen O. Trabectedin (ET-743, Yondelis) is a substrate for P-glycoprotein, but only high expression of P-glycoprotein confers the multidrug resistance phenotype. *Invest New Drugs*. 2007; 25(1): 1-7

- 38 Press RR, **Buckle T**, Beijnen JH, van Tellingen O. The effect of P-glycoprotein and cytochrome P450 3a on the oral bioavailability of vinorelbine in mice. *Cancer Chemother Pharmacol.* 2006; 57(6): 819-825
- 39 van Tellingen O, Bardelmeijer HA, **Buckle T**, Ouwehand M, Beijnen JH, Schellens JH. Cannulation of the jugular vein in mice. *Lab Anim.* 2005; 39(1): 130
- 40 van Tellingen O, **Buckle T**, Jonker JW, van der Valk MA, Beijnen JH. P-glycoprotein and Mrp1 collectively protect the bone marrow from vincristine-induced toxicity in vivo. *Br J Cancer.* 2003; 89(9): 1776-1782
- 41 Bardelmeijer HA, **Buckle T**, Ouwehand M, Beijnen JH, Schellens JH, van Tellingen O. Cannulation of the jugular vein in mice: a method for serial withdrawal of blood samples. *Lab Anim.* 2003; 37(3): 181-187
- 42 Bardelmeijer HA, Ouwehand M, **Buckle T**, Huisman MT, Schellens JH, Beijnen JH, van Tellingen O. Low systemic exposure of oral docetaxel in mice resulting from extensive first-pass metabolism is boosted by ritonavir. *Cancer Res.* 2002; 62(21): 6158-6164

**Interventional
Curriculum Vitae
molecular imaging,
a hybrid approach**



Tessa Buckle werd geboren op 9 januari 1979 te Utrecht. Na het behalen van haar HAVO diploma in 1996 aan het Cals College in Nieuwegein startte zij de bachelor opleiding Life Sciences (specialisatie zoölogie) van de Hogere Laboratorium Opleiding (HLO) aan de Hogeschool van Utrecht. Hier behaalde ze in 2001 haar diploma.

Tussen 2001 en 2008 was ze werkzaam bij de Farmacokinetiek groep van Dr. Olaf van Tellingen op de afdeling Klinische Chemie van het Nederlands Kanker Instituut - Antoni van Leeuwenhoek ziekenhuis (NKI-AvL). In deze groep werkte ze onder andere aan het ontwikkelen van bioluminescente tumor cellijnen, microchirurgische technieken en preklinische (tumor-)modellen. Deze heeft zij vervolgens toegepast in farmacologische studies voor de evaluatie van (nieuwe) kanker medicijnen en therapeutische interventies voor de behandeling van kanker.

In 2008 maakte zij de overstap naar het molecular imaging onderzoeksveld. Hiervoor verhuisde ze naar de afdelingen Radiologie en Nucleaire Geneeskunde binnen het NKI-AvL, waar ze hielp bij het opzetten van de Interventional Molecular Imaging groep van Dr. Fijs van Leeuwen. Tevens vervulde zij een belangrijke rol tijdens de opstartfase van de Mouse Cancer Clinic op het NKI-AvL, waarvan zij later coördinator werd. In deze periode deed zij uitgebreide ervaring op met verscheidene imaging modaliteiten zoals bioluminescentie, fluorescentie, CT, ultrasound, SPECT, PET en MRI. Nauwe samenwerking met de kliniek leidde tot de ontwikkeling van een hybride contrastmiddel voor beeldgeleide chirurgie, die na preklinische validatie nu klinisch worden toegepast voor de visualisatie van schildwachtklieren. Hiernaast was, en is, ze betrokken bij de ontwikkeling en preklinische validatie van (nieuwe) getargete contrastmiddelen voor de visualisatie van tumorweefsel.

In 2011 maakte zij, samen met de Interventional Molecular Imaging groep, de overstap van het NKI-AvL naar de afdeling Radiologie van het Leids Universitair Medisch Centrum (LUMC) in Leiden. Na haar promotie zal ze binnen deze groep verder werken aan het ontwikkelen van nieuwe contrastmiddelen en de preklinische validatie hiervan, waarbij de focus steeds zal liggen op de klinische translatie van deze nieuwe contrastmiddelen.

**Interventional
molecular imaging,
a hybrid approach**

**Acknowledgements
Dankwoord**

Dit proefschrift dient voor mij als afsluiting van een geweldige periode op het NKI en een nieuw begin op het LUMC. Een mooie gelegenheid om iedereen te bedanken die mij hierbij geholpen heeft!
Dus bij deze!!

In het bijzonder:

Mijn promotoren, Professor Bloem en Professor van de Velde,
voor het geven van deze kans.

Fijs van Leeuwen, mijn co-promotor en zeer gewaardeerde baas. Voor de assertiviteits training(en) en de onvoorwaardelijke steun en het vertrouwen.

Mijn mede groepsleden, Joeri, Anton, Patrick, Nynke, Mark, Oscar, Danny, Renato, Thomas, Daphne en Sharon voor alle input en gezelligheid!
"Mijn" studenten, Anne, Wouter, Nynke, Véronique en Joppe,
voor jullie hulp en tomeloze inzet.

All my co-authors, for your feedback, assistance and support. Greatly appreciated!

Alle collega's van de Radiologie en Nucleaire Geneeskunde van het NKI,
o.a. voor het maken van alle spuitjes en de scans 'tussendoor'.

Afdeling proefdieren van het NKI, alle proefdierversorgers,
omdat jullie altijd voor me klaar stonden.

Al mijn lieve vrienden, voor alle leuke dingen die niets met werk te maken hebben.

Roy, wijze grote broer, voor het geven van het laatste zetje.
Paps en mams en de rest van de familie, voor alles!! Love you!

